UNIVERSITÀ DEGLI STUDI DI PADOVA

DIPARTIMENTO DI FISICA E ASTRONOMIA "GALILEO GALILEI"

CORSO DI DOTTORATO DI RICERCA IN ASTRONOMIA
Ciclo XXXVI

CHARACTERISATION OF HERSCHEL-SELECTED STRONG LENS CANDIDATES THROUGH HST AND SUB-MM/MM OBSERVATIONS

Coordinatore: Ch.mo Prof. Giovanni Carraro
Supervisore: Ch.mo Prof. Enrico Maria Corsini
Co-Supervisore: Ch.ma Prof.ssa Lucia Marchetti
Co-Supervisore: Ch.mo Prof. Mattia Negrello

Dottorando: Edoardo Borsato

Contents

Abstract

Dusty star-forming galaxies (DSFGs) are a population of high-redshift ($z > 1$), heavily dust-obscured sources that experience strong episodes of star formation. These galaxies emit most of their radiation between the mid/far-IR and mm wavelengths due to the dust heated by the UV radiation produced by the newly formed stars. DSFGs play a key role in the early mass assembly of the Universe. They significantly contribute to the cosmic star-formation history at high redshift, accounting for roughly half of the stars ever formed. Large samples of DSFGs have been gathered and characterised in the literature. However, spatially resolved analyses are still rare due to the high redshift of these sources ($1 < z < 6$). The situation worsens when observing these sources outside of the sub-mm range, where they become intrinsically fainter. A possible way to address these issues is to rely on the boost in flux and angular resolution produced by strong gravitational lensing.

Strongly lensed DSFGs can be identified using a simple cut at high flux density in wide area sub-mm/mm surveys like those carried out with *Herschel* due to the declining number density of intrinsically bright unlensed sources with increasing flux density. Moreover, the negative K-correction characteristic of such sub-mm observations aids in observing large volumes, making it possible to detect sources at high redshift with a similar flux density as to lower redshift ones. However, the angular resolution of *Herschel* is not good enough to resolve the lensing features of background sources. Hence, there is a need for high-resolution follow-up observations. In the past decade, the interstellar medium properties of strongly lensed DSFGs have been studied in great detail. However, one parameter the lensed sources are still missing is the stellar mass, which is fundamental in understanding how evolved these sources are.

This thesis focuses on a sample of 281 strongly-lensed DSFG candidates identified through *Herschel* and followed up with the *HST* in the near-IR. These kinds of follow-up observations can help achieve three goals: (i) confirm the strong lensing nature of the candidate; (ii) characterise the photometric properties and morphology of the lenses; and (iii) possibly detect and reconstruct the optical rest-frame surface-brightness distribution of the background sources.

We begin the analysis of our sample by classifying the observed candidates according to their likelihood of being strongly lensed. We combine a visual inspection of the *HST* images and available sub-mm observations, finding 130 systems that are either lensed or show a possible lensing galaxy. For these, we model and subtract the candidate lens surface-brightness distribution through three different codes, `GASP2D`, `GALFIT`, or `ISOFIT` in order to cover all the lensing galaxy morphologies. After the lens subtraction, we repeat the visual inspection of the residuals, producing a final lens classification. We confirm 65 systems to be strongly lensed, 30 of which are new discoveries. We characterise the lens morphology, finding that $\sim 90\%$ of them are single galaxies with only a few group lenses. Most of the lensing galaxies are consistent with early-type galaxies from both morphological and photometric analysis.

We successfully perform lens modelling and source reconstruction of 23 lensed DSFGs that are well detected by *HST* and lensed by isolated galaxies. We model all the lenses as singular isothermal ellipsoids using `PyAutoLens`. We find that the Einstein radii of the lenses and magnifications of the background sources are consistent with previous studies.

However, the background-source circularised radii (ranging between 0.34 kpc and 1.30 kpc) are ∼3 times smaller than those measured in the sub-mm/mm for DSFGs already studied in the literature. This finding might indicate the onset of inside-out quenching processes, clearing the dust from the central regions and causing the rest-frame optical emission to pass through. Nevertheless, further investigations are needed to strengthen this claim. We compare our lenses with those in the SLACS survey, confirming that our sub-mm selection is more effective at picking up fainter and more diffuse galaxies, as well as group lenses, compared to lens samples selected in the visible.

Lastly, we test a combined Keck K_s band and *Spitzer*/IRAC1 and 2 analysis of HATLASJ142414+022304 disentangling successfully the heavily blended lensing galaxies and lensed DSFG in the low-resolution *Spitzer* observations. We perform spectral energy distribution modelling to measure the stellar mass of the lensed DSFG, finding that it is a massive main sequence galaxy, possibly consisting of a minor merger system.

This sample represents the first step towards systematically characterising the near-IR properties and stellar masses of the gravitationally lensed DSFGs. These stellar masses could then complement the wealth of available studies, constraining their evolutionary stage and further consolidating their role in the early Universe mass assembly.

List of publications

This thesis work is based on the following papers.

1. Dye S., Eales S. A., Gomez H. L., Jones G. C., Smith M. W. L., **Borsato E.**, Moss A., Dunne L., Maresca J., Amvrosiadis A., Negrello M., Marchetti L., Corsini E. M., Ivison R. J., Bendo G. J., Bakx T., Cooray A., Cox P., Dannerbauer H., Serjeant S., Riechers D., Temi P. and Vlahakis C., **2022**, "*A high-resolution investigation of the multiphase ISM in a galaxy during the first two billion years*", MNRAS, 510, 3734

2. Liu Bin, Chartab N., Nayyeri H., Cooray A., Yang C., Riechers D. A., Gurwell M., Zhu Zong-hong, Serjeant S., **Borsato E.**, Negrello M., Marchetti L., Corsini E. M. and van der Werf P. **2022**, "*Massive molecular gas reservoir in a luminous submillimeter galaxy during cosmic noon*", ApJ, 929, 41

3. Urquhart S. A., Bendo G. J., Serjeant S., Bakx T., Hagimoto M., Cox P., Neri R., Lehnert M., Sedgwick C., Weiner C., Dannerbauer H., Amvrosiadis A., Andreani P., Baker A. J., Beelen A., Berta S., **Borsato E.**, Buat V., Butler K. M., Cooray A., De Zotti G., Dunne L., Dye S., Eales S., Enia A., Fan L., Gavazzi R., González-Nuevo J., Harris A. I., Herrera C. N., Hughes D., Ismail D., Ivison R., Jin S., Jones B., Kohno K., Krips M., Lagache G., Marchetti L., Massardi M., Messias H., Negrello M., Omont A., Perez-Fournon I., Riechers D. A., Scott D., Smith M. W. L., Stanley F., Tamura Y., Temi P., Vlahakis C., Weiß A., van der Werf P., Verma A., Yang C., Young A. J., **2022**, "*The bright extragalactic ALMA redshift survey (BEARS) I: redshifts of bright gravitationally lensed galaxies from the Herschel ATLAS*", MNRAS, 511, 3017

4. Hagimoto M., Bakx T., Serjeant S., Bendo G. J., Urquhart S. A., Eales S., Harrington K. C., Tamura Y., Umehata H., Berta S., Cooray A. R., Cox P., De Zotti G., Lehnert M. D., Riechers D. A., Scott D., Temi P., van der Werf P. P., Yang C., Amvrosiadis A., Andreani P. M., Baker A. J., Beelen A., **Borsato E.**, Buat V., Butler K. M., Dannerbauer H., Dunne L., Dye S., Enia A. F. M., Fan L., Gavazzi R., González-Nuevo J., Harris A. I., Herrera C. N., Hughes D. H., Ismail D., Ivison R. J., Jones B., Kohno K., Krips M., Lagache G., Marchetti L., Massardi M., Messias H., Negrello M., Neri R., Omont A., Perez-Fournon I., Sedgwick C., Smith M. W. L., Stanley F., Verma A., Vlahakis C., Ward B., Weiner C., Weiß A. and Young A. J. **2023**, "*Bright extragalactic ALMA redshift survey (BEARS) III: detailed study of emission lines from 71 Herschel targets*", MNRAS, 521, 5508

5. Bendo G. J., Urquhart S. A., Serjeant S., Bakx T., Hagimoto M., Cox P., Neri R., Lehnert M. D., Dannerbauer H., Amvrosiadis A., Andreani P., Baker A. J., Beelen A., Berta S., **Borsato E.**, Buat V., Butler K. M., Cooray A., De Zotti G., Dunne L., Dye S., Eales S., Enia A., Fan L., Gavazzi R., González-Nuevo J., Harris A. I., Herrera C. N., Hughes D. H., Ismail D., Jones B. M., Kohno K., Krips M., Lagache G., Marchetti L., Massardi M., Messias H., Negrello M., Omont A., Pérez-Fournon I., Riechers D. A., Scott D., Smith M. W. L., Stanley F., Tamura Y., Temi P., van der Werf P., Verma A.,

Vlahakis C., Weiß A., Yang C. and Young A. J., **2023**, "*The bright extragalactic ALMA redshift survey (BEARS) - II. Millimetre photometry of gravitational lens candidates*", MNRAS, 522, 2995

6. Cox P., Neri R., Berta S., Ismail D., Stanley F., Young A., Jin S., Bakx T., Beelen A., Dannerbauer H., Krips M., Lehnert M., Omont A., Riechers D. A., Baker A. J., Bendo G., **Borsato E.**, Buat V., Butler K., Chartab N., Cooray A., Dye S., Eales S., Gavazzi R., Hughes D., Ivison R., Jones B. M., Marchetti L., Messias H., Nanni A., Negrello M., Perez-Fournon I., Serjeant S., Urquhart S., Vlahakis C., Weiss A., van der Werf P. and Yang C., **2023**, "*z-GAL - A NOEMA spectroscopic redshift survey of bright Herschel galaxies: [I] Overview*", A&A, 678, A26

7. Ismail D., Beelen A., Buat V., Berta S., Cox P., Stanley F., Young A., Jin S., Neri R., Bakx T., Dannerbauer H., Butler K., Cooray A., Nanni A., Omont A., Serjeant S., van der Werf P., Vlahakis C., Weiss A., Yang C., Baker A. J., Bendo G., **Borsato E.**, Chartab N., Dye S., Eales S., Gavazzi R., Hughes D., Ivison R., Krips B. M. Jones M., Lehnert M., Marchetti L., Messias H., Negrello M., Perez-Fournon I., Riechers D. A. and Urquhart S., **2023**, "*z-GAL - A NOEMA spectroscopic redshift survey of bright Herschel galaxies: [II] Dust properties*", A&A, 678, A27

8. Berta S., Stanley F., Ismail D., Cox P., Neri R., Yang C., Young A. J., Jin S., Dannerbauer H., Bakx T. J., Beelen A., Weiss A., Nanni A., Omont A., van der Werf P., Krips M., Baker A. J., Bendo G., **Borsato E.**, Buat V., Butler K. M., Chartab N., Cooray A., Dye S., Eales S., Gavazzi R., Hughes D., Ivison R. J., Jones B. M., Lehnert M., Marchetti L., Messias H., Negrello M., Perez-Fournon I., Riechers D. A., Serjeant S., Urquhart S., Vlahakis C., **2023**, "*z-GAL – A NOEMA spectroscopic redshift survey of bright Herschel galaxies: [III] Physical properties*", A&A, 678, A28

9. **Borsato E.**, Marchetti L., Negrello M., Corsini E. M., Wake D., Amvrosiadis A., Baker A. J., Bakx T., Beelen A., Berta S., Clements D. L., Cooray A., Cox P., Dannerbauer H., de Zotti G., Dye S., Eales S. A., Enia A., Farrah D., Gonzalez-Nuevo J., Hughes D. H., Ismail D., Jin S., Lapi A., Lehnert M. D., Neri R., Pérez-Fournon I., Rodighiero G., Scott D., Serjeant S., Stanley F., Urquhart S., van der Werf P., Vaccari M., Wang L., Yang C., and Young A, **2023**, "*Characterisation of Herschel-selected strong lens candidates through HST and sub-mm/mm observations*", MNRAS, accepted for publication

Chapter 1

Introduction

In this thesis, we will report on our work about the study of a sample of strongly-lensed candidates selected with the *Herschel Space Observatory* and followed up with the *Hubble Space Telescope*. In this first chapter, we will introduce two topics that are closely relevant to this project. The first is the population of dusty star-forming galaxies that make up the strongly lensed candidates, while the second is the strong gravitational lensing. In Section 1.1, we briefly review recent results on dusty star-forming galaxies. Then, in Section 1.3, we introduce some fundamental notions on strong gravitational lensing. Lastly, in Section 1.4, we focus on how strong gravitational lensing can aid the study of dusty star-forming galaxies and present an effective method for the selection of large samples of these lensed sources. To conclude, we give a breakdown of the aim and structure of the thesis Section 1.5.

1.1 Dusty star-forming galaxies

At the beginning of the 1990s, observations coming from the *Cosmic Background Explorer* (*COBE*) measured the energy spectra above 150 μm, finding that the Universe emits a similar amount of energy in the far-IR/mm as it does in the optical/UV. These observations, combined with various optical galaxy surveys, opened up two possibilities: the existence of a dust-obscured, optically invisible population of galaxies and/or the presence of dust-obscured knots embedded in optically detected disks hosting the most intense episodes of star formation. Towards the end of the same decade, blank-field pointings obtained with the Submillimeter Common-User Bolometric Array (SCUBA), mounted on the *James Clerk Maxwell Telescope* (*JCMT*), detected a population of bright far-IR/sub-mm sources that showed little to no optical emission. In the following years, several observatories, namely the *Spitzer Space Telescope* (*Spitzer* for short), *Herschel Space Observatory* (*Herschel* for short) and *South Pole Telescope* (*SPT*), built upon the first *JCMT* sample reaching more than a million of such dust-obscured objects, with the *Herschel* detections alone accounting for $\sim 50\%$ of all stars ever formed (Casey et al., 2014).

These objects are referred to as dusty star-forming galaxies (DSFGs) and are a vital component contributing to the high-redshift galaxy assembly. The bulk of their IR radiation comes from dust heated by ongoing star formation. Dusty environments, enshrouding young

massive and bright stars, absorb and then reprocess almost all (up to $\sim 99\%$) of the light emitted by the inner stars (e.g., Buat et al., 2010). Then, the dust-enriched gas is expelled from the host as stellar and galactic winds and will eventually be recycled to fuel new star-formation (e.g., Tacconi et al., 2020). While the above heating mechanism characterizes DSFGs, it is not the only one active. The contribution of active galactic nuclei (AGNs) is often essential and can account for a significant fraction of the re-heated emission. The most luminous DSFGs can reach IR luminosities as high as $10^{13}\,L_{\odot}$, and star-formation rates (SFRs) in the thousands of solar masses per year, making them some of the brightest objects known.

The cosmic star-formation rate density (SFRD), that is, the star formation per unit volume and time of the Universe, evolves with redshift (see Madau &Dickinson, 2014, for details) increasing from the present date up to $z \sim 2-3$ where it shows a peak then decreasing again at higher redshifts. Various studies have shown that DSFGs contribute significantly to the cosmic SFRD evolution (see Casey et al., 2014, for details), with the brighter population of sources ($10^{11} < L_{\rm IR} < 10^{13}\,L_{\odot}$) accounting for up to 50% of the total SFRD at $z = 2$ (Le Floc'h et al., 2005). Interestingly, the SFRD caused by the bright population becomes negligible in the local Universe. In Figure 1.1, we show the contribution of DSFGs to the cosmic SFRD.

Before getting into some recent results on the properties of DSFGs, it might be helpful to look at the local Universe closest equivalents of these objects, the local (ultra-)luminous infrared galaxies (ULIRGs). It has been shown that the ULIRGs have a high infrared luminosity that correlates with the high star formation rates and major-merger rates (see, Sanders &Mirabel, 1996, for a review). This observation led to the widely accepted evolutionary picture of ULIRG formation first proposed by Sanders et al. (1988). Figure 1.2 shows a schematic diagram of this evolutionary scheme from Casey et al. (2014). According to this model, a ULIRG is a fixed stage in the evolutionary sequence of galaxies where two gas-rich disk galaxies collide, powering an intense phase of star formation due to the rapid compression and cooling of the gas. This strong peak in star formation produces large quantities of dust grains, which causes a spike in IR luminosity. During the final stages of the merger, when the two supermassive black holes coalesce, an AGN forms and feeds from an accretion disk produced by the infalling material propelled by the galaxy merger (Hopkins et al., 2012a,b). At some point, the gas provided to the AGN and available to the star formation ends, halting the ULIRG phase. The now inert, merged system can eventually relax into an early-type galaxy (ETG). da Cunha et al. (2015) found that the average properties and spectral energy distributions (SEDs) of DSFGs are similar to local ULIRGs, with the only difference being that the former displays a brighter and bluer stellar emission. This distinction can be explained by having lower average dust attenuation despite similar dust masses (e.g., da Cunha et al., 2010), and this could be the consequence of the DSFGs being more extended than ULIRGs and/or having the dust and stellar distributions not co-spatial (e.g. Negrello et al., 2014). Moreover, assuming that DSFGs, which get brighter and more numerous going back in time, are redshifted ULIRGs, then major mergers would be expected to dominate the star formation at high redshift, a conclusion that is still debated (e.g., Rizzo et al., 2022).

In recent years, the properties of DSFGs were characterized in detail by numerous studies

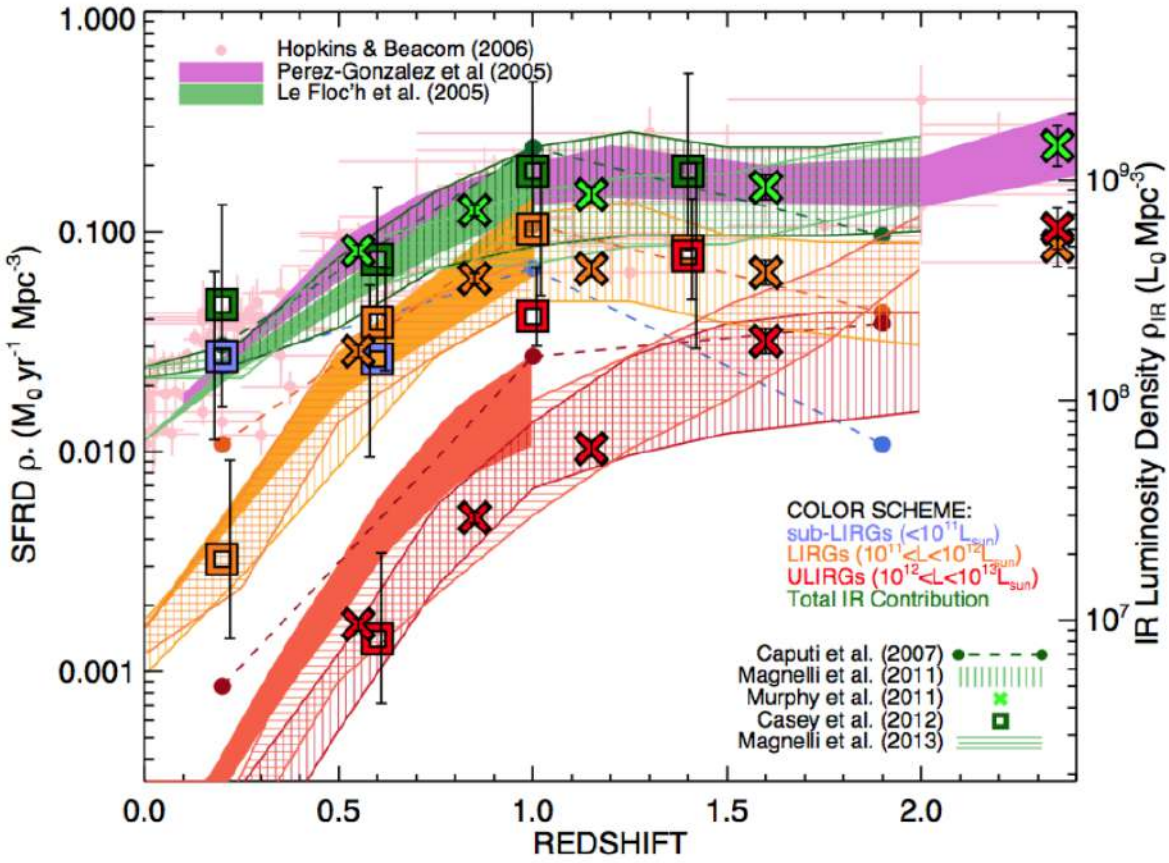

Figure 1.1: Estimate of the cosmic SFRD contribution of DSFGs divided into bins of infrared luminosity. The total integrated infrared contribution is shown in green, sub-LIRG population ($L < 10^{11}\,L_\odot$) in blue, LIRG population ($10^{11} < L < 10^{12}\,L_\odot$) in orange, and ULIRG population ($10^{12} < L < 10^{13}\,L_\odot$) in red. The different symbols or line types relate to the different sources of SFRD estimates (Le Floc'h et al., 2005; Pérez-González et al., 2005; Hopkins &Beacom, 2006; Caputi et al., 2007; Magnelli et al., 2011, 2013; Murphy et al., 2011; Casey, 2012). From Casey et al. (2014).

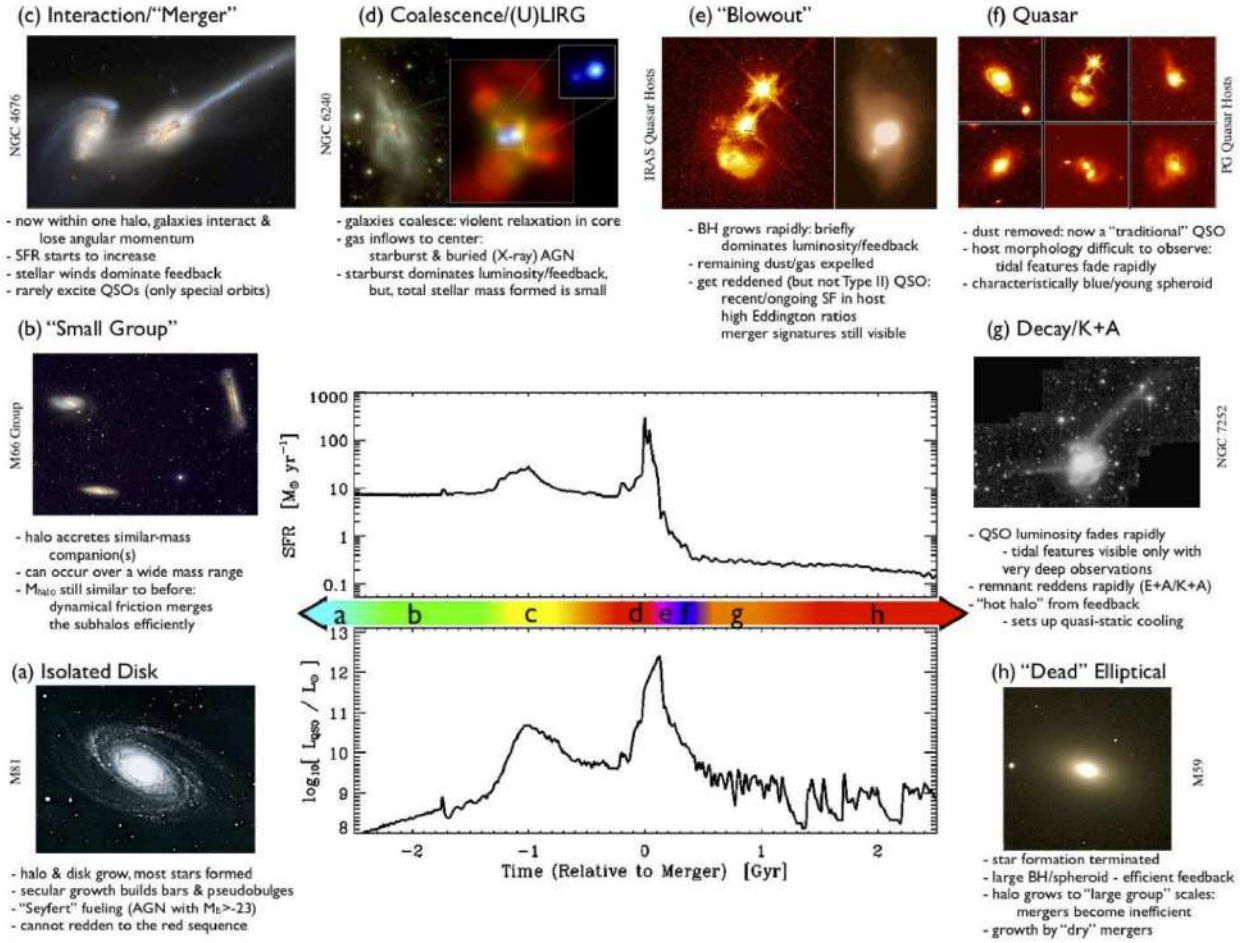

Figure 1.2: Formation scheme of a ULIRG. *Central panel:* SFH and IR luminosity of a galaxy as a function of the lookback time. *Surrounding panels:* Various snapshots characteristic of a specific ULIRG phase. From Casey et al. (2014), who adapted it from the version available in Hopkins et al. (2008). Image credits: (a) NOAO/AURA/NSF; (b) REU program/NOAO/AURA/NSF; (c) NASA/STScI/ACS Science Team; (d) Left: Optical, NASA/STScI/R. P. van der Marel & J. Gerssen; right: X-ray, NASA/CXC/MPE/S. Komossa et al.; (e) Left: J. Bahcall/M. Disney/NASA; Right: Gemini Observatory/NSF/University of Hawaii Institute for Astronomy; (f) J. Bahcall/M. Disney/NASA; (g) F. Schweizer (CIW/DTM); (h) NOAO/AURA/NSF.

confirming that DSFGs are massive (stellar masses $\sim 10^{10} - 10^{11} M_{\odot}$; e.g., Simpson et al. 2014) galaxies with high SFRs ($\sim 10^{2} - 10^{3}\,M_{\odot} yr^{-1}$) and dust reservoirs ($\geq 10^{8}\,M_{\odot}$; e.g., Swinbank et al. 2014; da Cunha et al. 2021), and a low fraction of X-ray AGN ($\sim 20\%$; e.g., Wang et al. 2013). The gas fraction of DSFGs is very high, reaching values of 40% and depletion times, defined as 1/SFR, between 1 and 0.1 Gyr (e.g., Scoville et al., 2017; Tacconi et al., 2018). The high obscurations found in these galaxies produce average V-band dust attenuation values of $A_V \sim 2$ mag (da Cunha et al., 2015), that if extrapolated from line-of-sight dust measurements in the infrared, can reach $A_V \sim 500$ (Simpson et al., 2017). Danielson et al. (2017) studied a sample of optically detected sources selected in the *Atacama Large Millimetre Array* (*ALMA*) LABOCA ECDFS Submm Survey (ALESS), finding star formation histories (SFHs) suggesting that DSFGs are young (100 Myr old) starbursts observed around 10 Myr after their birth. Moreover, da Cunha et al. (2015) showed that optically faint DSFGs have similar properties when compared to the optically brighter ones, except for the dust attenuation that displayed higher values. This observation suggests that these fainter sources are either more compact (Dudzevičiūtė et al., 2020) or disk-like aligned edge-on.

When placed in the SFR versus stellar mass plane, most star-forming galaxies occupy a narrow region called the star formation main sequence (SFMS, see Figure 1.3, Daddi et al., 2007; Elbaz et al., 2007). The SFMS shows a linear correlation when displayed logarithmically between the stellar mass and SFR, with the more massive systems having stronger star formation. The normalisation of the SFMS (i.e., the SFR for a given stellar mass) changes with time, with higher redshift MS galaxies forming more stars. SFMS galaxies are thought to be secular evolving disk galaxies whose star formation is fueled by gas accretion from the surrounding medium. A minority of sources are found to be above the SFMS. These systems, also known as starbursts, undergo intense episodes of star formation usually triggered by galaxy interactions and mergers not dissimilar from the ULIRG model above (e.g. Saintonge et al., 2013; Tacconi et al., 2018, 2020).

Alongside the SFR versus stellar mass location, another very useful quantity is the molecular gas depletion timescale that quantifies how long a galaxy can produce stars at its given SFR. Systems with short molecular gas depletion timescales build up their stellar masses very quickly. They are typically associated with star formation bursts, whereas longer molecular gas depletion timescales are indicative of steady secular evolution.

An alternative way to investigate the relation between the properties of DSFGs and their mode of star formation, other than the SFR versus stellar mass plot or the molecular gas depletion timescale, is through the kinematics of some tracer, such as ionized or cold gas. These kinematic data are able to distinguish between an orderly rotating disk, indicative of an SFMS galaxy, and a merger favouring the starburst scenario (e.g. Rizzo et al., 2022). Unfortunately, this kind of observation is very expensive.

It is still an open question whether DSFGs are starbursts or the more massive portion of the high redshift SFMS (Walter et al., 2020).

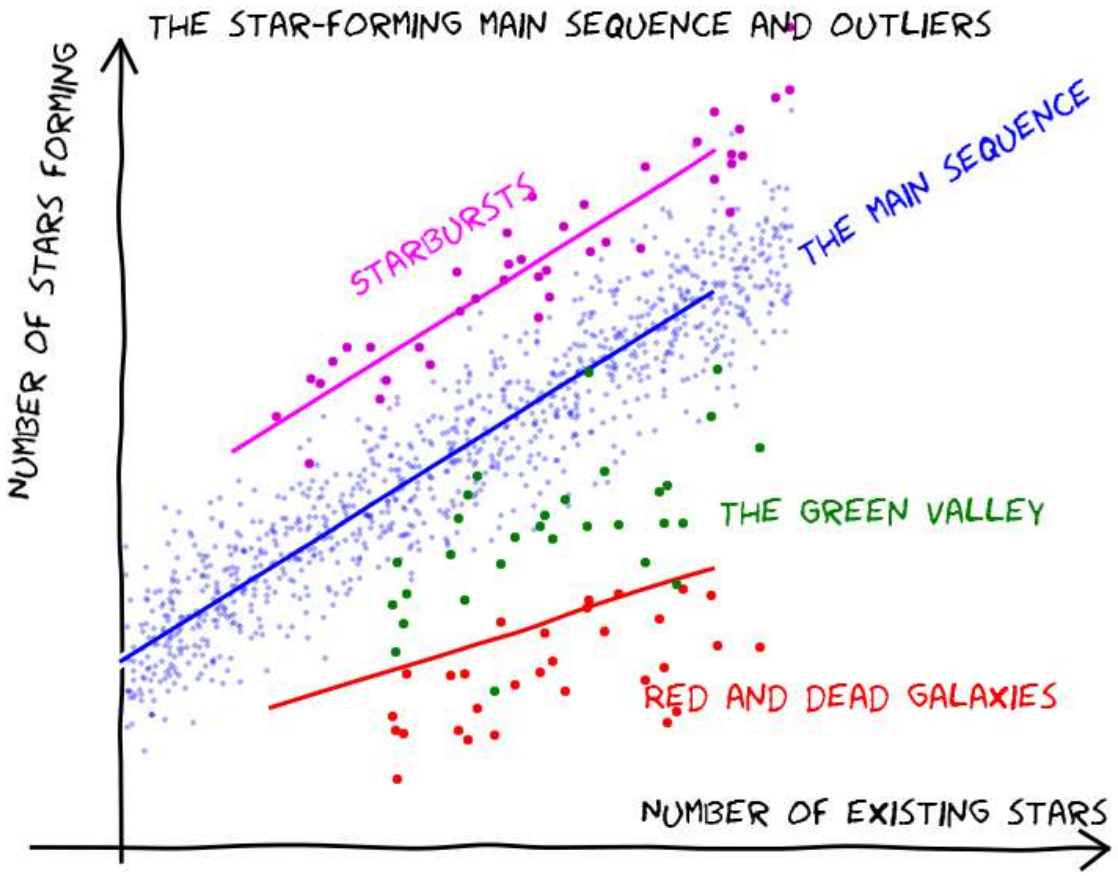

Figure 1.3: Schematics describing SFR versus stellar mass location of the population of SFMS (blue), starburst (magenta), green valley (green), and quiescent galaxies (red). Image credits: CANDELS collaboration.

1.2 *Herschel Space Observatory* and DSFGs

To understand the selection effects characteristic of samples of DSFGs, it is necessary to get into more detail on their dust emission properties. The dust grains mass buildup occurs mostly in the ejecta of supernovae (SNe) and the envelopes of asymptotic giant branch stars (see, Galliano et al., 2018, for details). These production mechanisms alone would require a top-heavy initial mass function (IMF) producing many massive stars and type II SNe (Nanni et al., 2020). Otherwise, to fully explain the massive amount of dust available in DSFGs, given the short timescales involved, it would be necessary to invoke some other production channel like the grain growth by accretion in the ISM itself (Michałowski, 2015).

Dust emission shows a strong peak in flux density that depends primarily on the dust temperature and is usually at $\lambda < 200\,\mu$m rest-frame. After which, the dust SED decreases steeply with the wavelength. When observing a galaxy at higher redshifts, its SED moves towards longer wavelengths and stretches while it becomes fainter due to the increasing distance. These two effects combine to change the flux density observed at a given wavelength. This phenomenon is known as K-correction. If the galaxy is dust-rich, and the observations are carried out in the sub-mm, the redshift increases the received flux density by moving the peak of the dust SED towards the covered wavelengths. For some combinations of wavelengths and redshifts, this increase can dominate over the dimming due to the distance, making the galaxy brighter the more distant it is. This is not the case in the optical/near-IR, where the incoming flux density strongly decreases with the distance from the galaxy. Figure 1.4 shows the effect of redshift on a characteristic DSFG SED.

DSFGs have dust temperatures ranging between 20 K and 50 K (Ismail et al., 2023). Note that this temperature range, which results from averaging the dust temperature over the whole galaxy, is intrinsic and not due to measurement uncertainties. The DSFG SEDs are further complicated by other parameters like the dust emissivity index, which relates to the dust grains composition (see, Galliano et al., 2018, for a review), or the optical depth of the dust column, that depends on the dust spatial distribution and the galaxy orientation. These intrinsic variations produce a large excursion in the sub-mm luminosities, significantly impacting the DSFG sample selection and completeness. From Figure 1.5, it is possible to note that the luminosity detection limits are greatly affected by the dust temperature, the colder objects being much more easily detected at longer wavelengths than the warm ones.

The combination of the redshift-dependent strong K-correction and intrinsic variations of the dust emission dominating the SEDs make for strong selection effects that complicate the definition of complete samples of DSFGs. Furthermore, when dealing with strong lensing, due to the rarity of these events, it is necessary to cover as much area of the sky as possible in order to gather large enough samples of lenses. However, this necessity is partially alleviated by the negative K-correction that increases the volume probed by the observations, allowing galaxies at different redshifts to be observed at similar flux densities.

Herschel was a spacefaring infrared and sub-mm observatory developed and operated by the European Space Agency, with an important participation of NASA, as part of the 'Horizon 2000' long-term plan. It was successfully launched on 14 May 2009, reaching its destination on the second Lagrange point of the Sun-Earth system L2 a few months later. *Herschel* operated until its cryostat ran out of Helium on 29 April 2013. *Herschel* followed

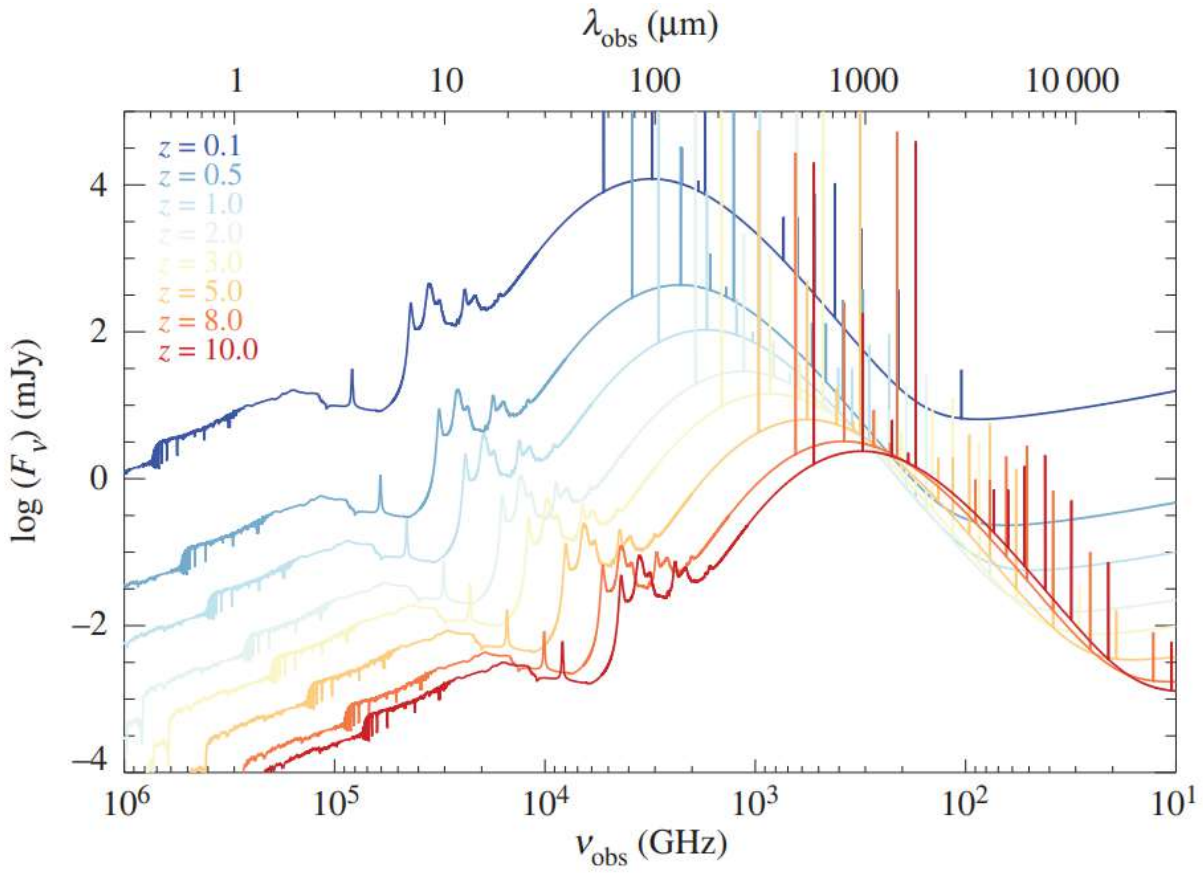

Figure 1.4: Median SED for a sample of ALESS detected sub-mm galaxies redshifted from $z = 0.1$ to $z = 10$ measured by da Cunha et al. (2015). From Hodge &da Cunha (2020).

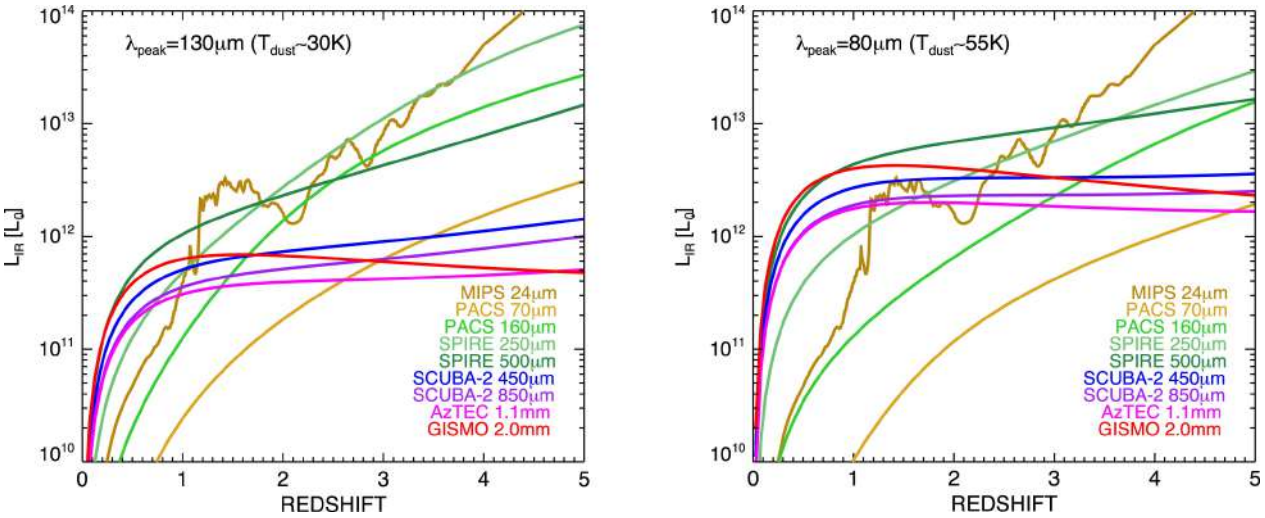

Figure 1.5: *Left panel:* Luminosity limits of different sub-mm bands as a function of redshift for a DSFG IR SED modelled as a modified blackbody peaking at 130 μm and having a temperature of 30 K. *Right panel:* Luminosity limits, we use a SED peaking at 80 μm with a temperature of 55 K. From Figure 7 in Casey et al. (2014).

a long tradition of the IR observatories *ISO*, *AKARI*, and *IRAS*, and more recently *Spitzer* Extending the spectral coverage from the far-IR ($\sim 60\,\mu$m) to the sub-mm ($\sim 600\,\mu$m). During its lifetime, *Herschel* carried out over 23,000 hours of successful science observations. The main area of interest of the satellite was the study of the dust and the ISM across the Universe. *Herschel* had a primary mirror of 3.5 m in diameter and mounts three science instruments: the Photoconductor Array Camera and Spectrometer (PACS), the Spectral and Photometric Imaging Receiver (SPIRE), and the Heterodyne Instrument for the Far Infrared (HIFI). The first two served as imaging cameras and spectrometers, whereas the latter consisted of a high-resolution spectrometer. The SPIRE camera was extensively used for the candidate lensed DSFG selection, thanks to its large field of view (FOV) and wavelength coverage. In its imaging mode, it had three bands centred at 250, 350 and 500 μm with widths such that $\lambda/\Delta\lambda \sim 3$. The FOV was of $4 \times 8\,\mathrm{arcmin}^2$, while the beams full widths at half maximum (FWHM) were 18.1, 25.2, and 36.6 arcsec for the three bands, respectively.

Due to the low *Herschel*/SPIRE angular resolution, its photometric measurements are heavily affected by source confusion, that is, the increase in noise caused by the blending together of faint, unresolved, point sources falling inside the same beam (e.g., Valiante et al., 2016). This effect is worsened by the negative K-correction (Casey et al., 2014). Source blending also applies to the brighter sources, boosting their fluxes, although the exact fraction of multiple blended sources in sub-mm surveys is still debated (e.g. Hodge et al., 2013; Bussmann et al., 2015; Hatziminaoglou et al., 2018).

The noise produced by the source confusion is strongly spatially correlated and has typical values that are comparable to, or even higher than, the instrumental noise (e.g. Oliver et al., 2012; Valiante et al., 2016).

An additional byproduct of the source confusion and steepness of the number counts distribution is a flux bias in the observed flux densities (Valiante et al., 2016). Since there are more faint sources to be scattered at higher flux densities than bright sources scattered at lower ones, the number of brighter sources gets overestimated. This bias has the effect of causing a systematic error on the number count distribution (known as Eddington bias, Eddington, 1913). This flux bias is stronger for the fainter sources and at shorter wavelengths, going from $\sim 20\%$ at 250 μm to $\sim 5\%$ and $\sim 4\%$ at 350 μm and 500 μm, respectively.

1.3 Strong gravitational lensing

Light rays are deflected as they propagate through a gravitational field. Given a luminous source sufficiently aligned with a massive object, its position, flux, and shape change. These distortions can range from a slight stretching of the source isophotes in the tangential direction to the gravitational potential, typical of weak lensing, to the production of multiple images, arcs, and rings characteristic of strong lensing (see, Meneghetti, 2021, for an introduction).

For a comprehensive treatment of gravitational lensing, it is necessary to refer to the theory of general relativity. However, the idea that a gravitational field can deflect light rays predates the development of Albert Einstein's (1879-1955) theory of gravitation. John Mitchell (1724-1793) first proposed a treatment of gravitational lenses in the context of Newtonian physics in 1784, followed by Johann Georg von Soldner (1776-1833) in 1804.

In 1963, the first quasars were discovered. These luminous, distant, and compact sources make for ideal extragalactic strongly lensed sources as Zwicky (1937) first laid out almost three decades earlier. However, it took around 20 years to achieve the first observations of a gravitationally lensed quasar. In an observational program aimed at identifying the optical counterparts of radio sources, Walsh et al. (1979) observed a system of two quasars, identified as QSO 9057+561, separated by approximately 6 arcseconds, which had nearly identical colours, redshifts, and spectra. Subsequently, a bright galaxy was identified between the two images, with a redshift much lower than that of the quasars, supporting the hypothesis of a phenomenon due to gravitational lensing. Further studies carried out with the *Very Large Baseline Interferometer* (*VLBI*) allowed for the characterisation of the structures of these radio sources, revealing two nuclear jets that exhibited the symmetry typical of what would be expected in a gravitationally lensed system.

In most extragalactic cases, the sizes of the foreground deflecting potential ('lens') and the lensed source ('background source') are much smaller than the other distances involved. In this regime, it is possible to define two planes. The first plane is the 'image plane' containing the projected surface brightness and mass distributions of the lens. Moreover, this plane hosts the distorted 'images' of the background source. The second plane is the 'source plane' containing the projected surface-brightness distribution of the background source. Notably, when multiple lenses are involved, it is possible to have multiple image planes, and the same is true for multiple background sources and source planes.

The number of images forming due to strong lensing depends on the mass profile and lens-source alignment. It can be shown that this number is odd with at least one image that is magnified. For certain configurations, some of these images could be superimposed, looking as if they were one. The magnification, similarly to the number of images, depends on both the lens and background source position. In some locations of the image plane, the magnification can diverge, reaching extremely high values. The curves formed by these locations are called 'critical curves'. By projecting the critical curves from the image plane to the source plane, it is possible to create another set of curves called 'caustic'. These curves are instrumental in determining the number of multiple images, their morphology and magnification. Another significant curve to take into account is the 'cut', which delimits the regions of the source plane where the background source must be located to form the first set of multiple images.

In Figure 1.6, it is possible to see how the alignment between the background source, lens, and observer changes the morphology of the lensed images for a given singular isothermal ellipsoid (SIE) mass distribution. When the background source is outside of the region defined by the caustic but inside the cut, a secondary fainter image of the background source begins to form. In contrast, the main image gets magnified and elongated. The more the background source gets closer to the caustics, the closer the images form to the critical curves, and the more they get distorted and magnified, reaching the maximum in correspondence with the caustic. Finally, an additional image forms when the background source crosses the caustic. If the background source is extended, it may fall inside the cut and caustic. In this case, the lens forms its maximum number of images for a SIE mass model corresponding to four. For flattened lenses, part of the caustic may be outside the cut, forming three images if the alignment is correct.

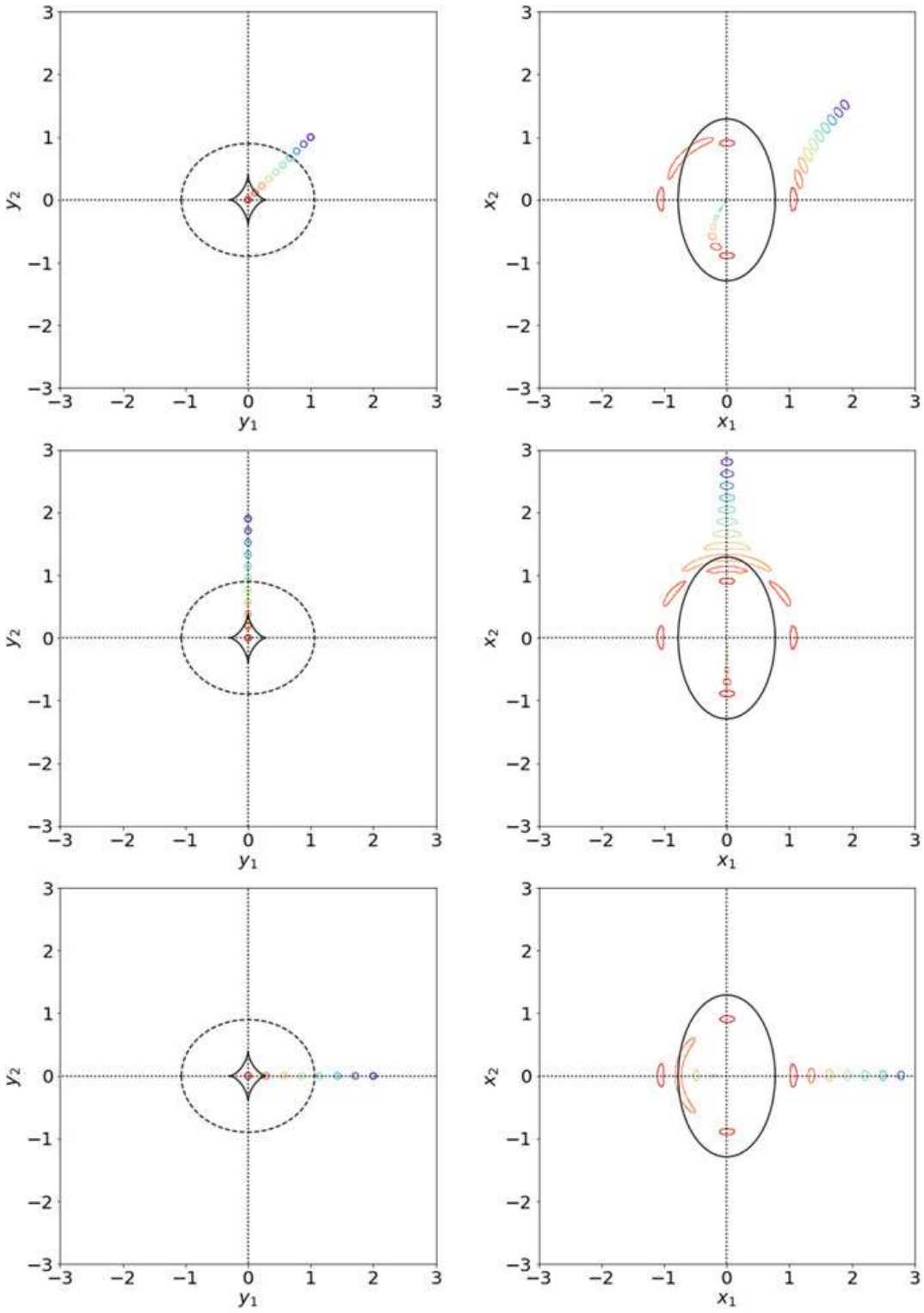

Figure 1.6: Lensing of circular sources by a SIE lens with an axis ratio of 0.6. *Left panels:* Background sources are located at several angular separations from the lens centre. Different sources are marked with different colours. The caustic and the cut are given by the black solid and dashed lines, respectively. *Right panels:* Lensed images (coloured contours) and critical line (solid black line). From Meneghetti (2021).

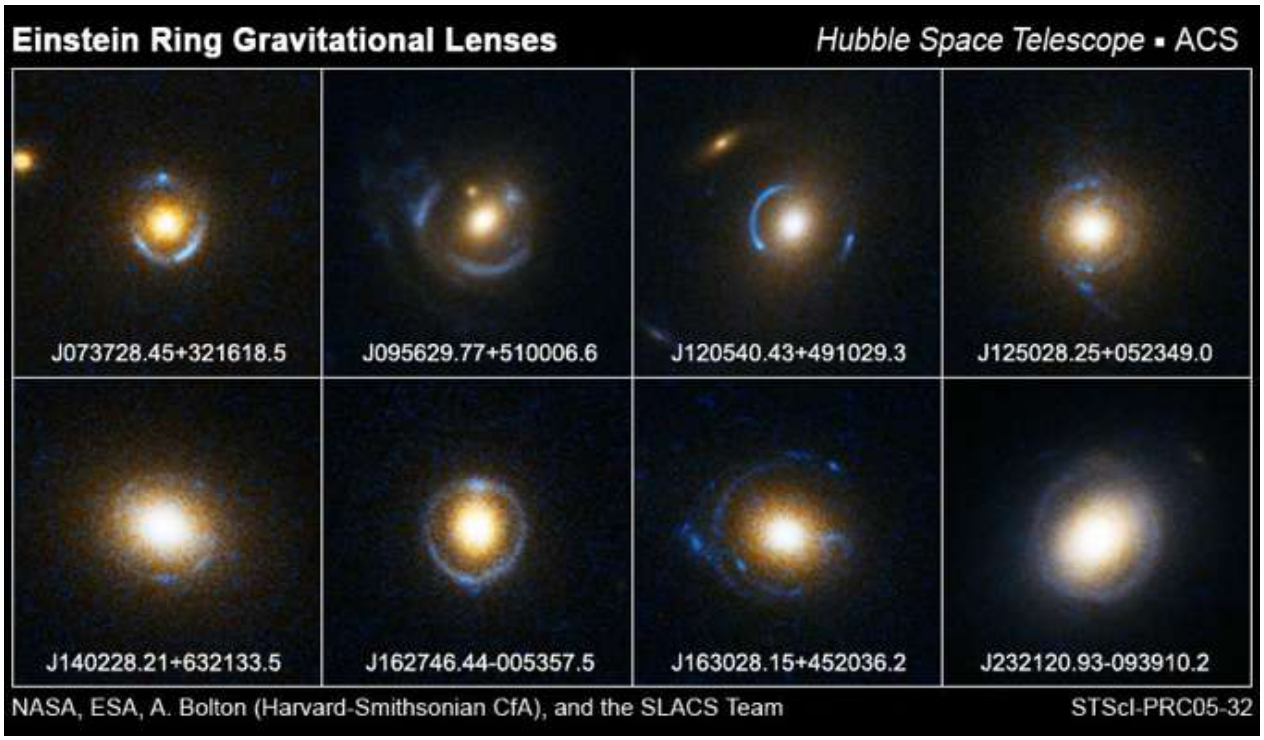

Figure 1.7: Eigth examples of strong lenses extracted from the SLACS survey. Image credits: NASA, ESA, A. Bolton (Harvard Smithsonian CfA), and the SLACS team.

The situation is complicated when dealing with extended and potentially very complex background source morphologies and lens mass distributions composed of multiple lenses. Figure 1.7 shows a gallery of strong lensing events extracted from the Sloan Lens Advanced Camera for Surveys Survey (SLACS; Bolton et al., 2004).

In a gravitationally lensed system, the fundamental observables are the relative positions, flux ratios, and distortion between images. These quantities are all functions of the deflection potential and its derivatives and, thus, can be exploited to infer the total mass distribution of the lens. In fact, strong lensing does not need any assumptions about the type of matter causing the deflection of light rays or its dynamical state. This property makes the study of gravitational lenses an effective tool to identify and characterise dark matter halos. The ΛCDM model predicts that galaxies form and evolve within dark matter halos (White &Rees, 1978; Blumenthal et al., 1984; Davis et al., 1985), making the study of these halos often complex. For non-lensed galaxies, the mass of the halo can be constrained by studying the dynamical state probed by various stellar or gaseous kinematic tracers. This has been done for elliptical and lenticular galaxies (e.g. Thomas et al., 2007), spiral galaxies (e.g. de Blok et al., 2008), dwarf and low surface-brightness galaxies (e.g. Zackrisson et al., 2006), and galaxy clusters (e.g. Nulsen et al., 2010).

In the case of elliptical and lenticular galaxies, the most commonly used dynamical tracer is represented by stars, which, however, presents two difficulties. The first is that their density decreases significantly beyond the effective radius, where dark matter dominates. The second is the degeneracy between mass and anisotropy of the stellar velocity distribution along the

line of sight (Binney &Tremaine, 1987). These two properties make the halos of ETGs challenging to characterise. The distribution of mass density derived from gravitational lens models can be used to validate the results obtained with traditional dynamical models based on photometry and stellar kinematics. The comparison between the distribution of total mass density and that associated with the stellar component places stringent constraints on the dark matter content and the mass-to-light ratio (Jiang &Kochanek, 2007), allowing for the derivation of the initial mass function (Treu et al., 2010) and reconstruction of the epoch and formation process of massive galaxies (e.g. Thomas et al., 2009). Furthermore, combining mass estimates obtained from both approaches makes it possible to break the degeneracy between mass and anisotropy that affects stellar kinematics studies, allowing for a detailed characterisation of halo mass profiles even in the central regions with high surface brightness (e.g. Barnabè et al., 2009).

Unlike ETGs, late-type galaxies exhibit a variety of dynamical tracers that extend to large distances from the galactic centre. The rotation curves of these tracers allow for accurate identification of dark matter halos (e.g. van Albada &Sancisi, 1986). Nevertheless, decomposing the total mass profile into its components is not straightforward (Corsini et al., 1999), mainly due to the presence of large uncertainties in the mass-to-light ratio M/L of the stellar component in young stellar populations obscured by dust (Bell &de Jong, 2001). Studies of gravitational lenses can be used, along with kinematic information, to distinguish between luminous and dark matter (e.g. Maller et al., 1997). Recently, Nightingale et al. (2023) have used the central image in the strong lens Abell 1201 to measure the mass of the supermassive black holes hosted at the centre of its lens.

The other immediate result obtained by lens modelling is the reconstruction of the intrinsic surface brightness distribution of the lensed background sources (Figure 1.8). By taking advantage of the magnification produced by lensing, which, in the case of massive galaxy clusters, can reach values up to ~ 100, it is possible to observe faint objects that would be otherwise undetectable. Resolutions of kiloparsecs or even less can be achieved at high redshifts, making it possible to determine morphology and kinematics (Marshall et al., 2007), resolve star-forming regions (Riechers et al., 2008), and study the distribution of chemical composition (Stark et al., 2008) of lensed sources. The magnification effect is particularly useful for studying DSFGs. When these galaxies are lensed, it becomes possible to characterise the morphological and dynamical properties of individual giant molecular clouds for objects at redshifts close to the peak of the cosmic star formation (e.g. Dye et al., 2015).

Another application of this magnification effect occurs in studying galaxies hosting distant AGNs. Accretion and feedback phenomena associated with the central black hole play a significant role in the formation and evolution of the host galaxy (e.g. Hopkins et al., 2009). Through strong gravitational lenses, it is possible to study how the properties of host galaxies evolve with redshift (e.g. Peng et al., 2006) while using microlensing effects produced by stars in the lens provides constraints on the characteristic sizes of the accretion disk of the black hole as a function of wavelength (Kochanek, 2004).

More recently, various studies managed to characterise caustic crossing events, consisting of the crossing of a caustic curve by star clusters (e.g. Vanzella et al., 2023), star-forming clumps (e.g. Meštrić et al., 2022) or even few stars (e.g. Welch et al., 2022) hosted by a background galaxy. During these crossings, the magnifications reach values of $\sim 10^6$, resolving

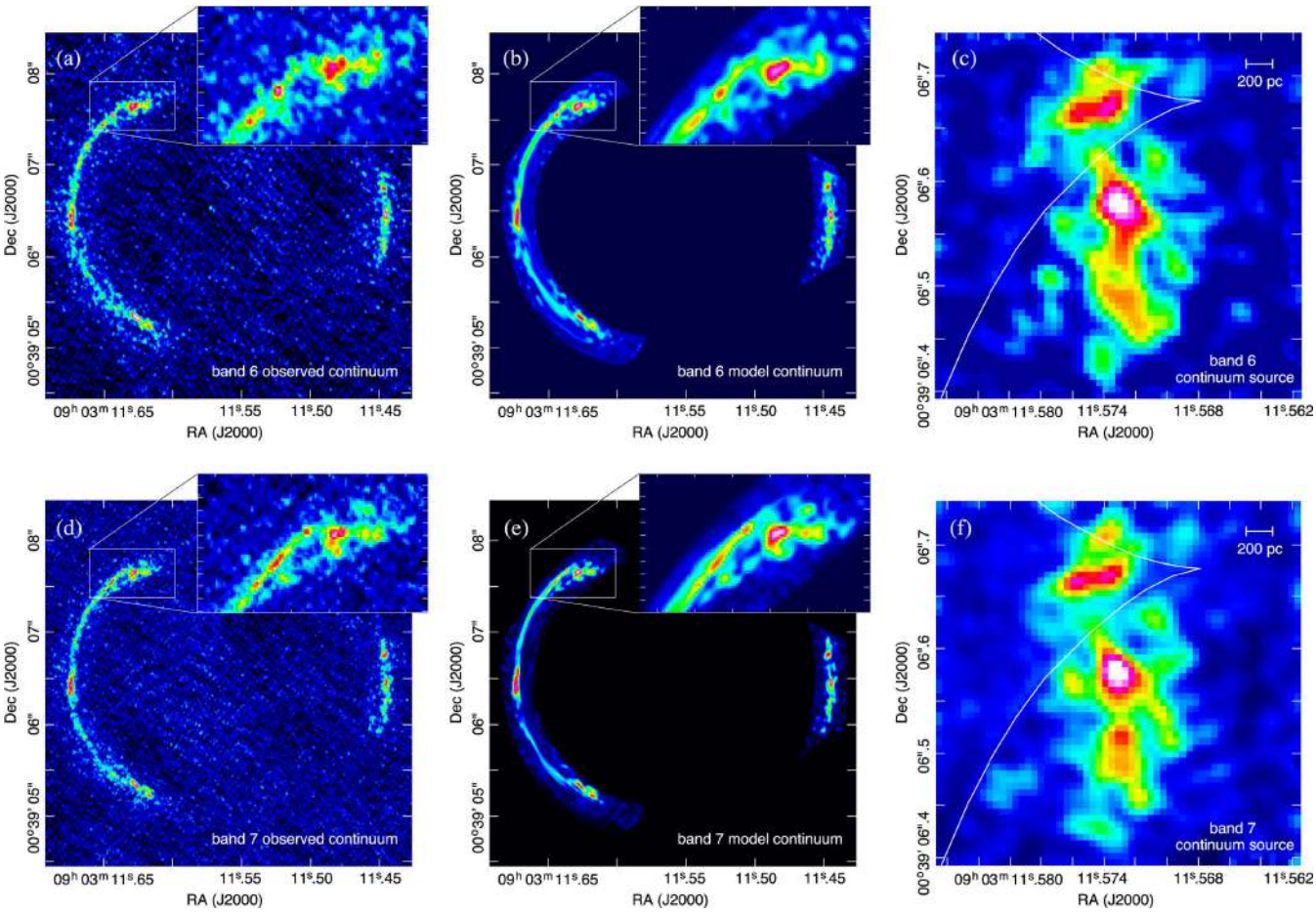

Figure 1.8: *Left panels:* Observed images of SDP.81 in bands 6 and 7. The top right inset highlights the clumpy substructure already visible in the arc. *Middle panels:* Best-fitting model image of the reconstructed background source. *Right panels:* Reconstruction of he background source. The white line in the source maps shows the position of the caustic. From Dye et al. (2015).

scales of the fraction of a parsec. These can be used to study stars directly and star clusters at high redshift and, at the same time, detail the properties of the lens mass distribution (see Oguri et al., 2018, for details).

1.4 Strongly lensed DSFGs

There are many benefits of lensing in the study of DSFGs. First of all, it boosts the background source flux density by a factor equal to the magnification of the system μ and the angular resolution by $\sim \sqrt{\mu}$. This magnification can reach values of $\sim 3-10$ for galaxy-scale lenses and $\sim 10-30$ for group-scale lenses. Even if the angular resolution of the observations does not allow for spatially resolving the DSFGs structure, knowing the fraction of lensed DSFG in a given sample is important, specifically when including the bright sources (Negrello et al., 2007). Measuring the magnification in sub-mm observations would allow breaking the degeneracy between various DSFG parameters, like the source size and optical depth of the dust (e.g. Ismail et al., 2023) and accurately place these systems in Kennicutt-Schmidt relation (e.g. Berta et al., 2021).

Over the years, a large sample ($\sim 30-50$) of lensed DSFGs has been collected and studied in great detail in relation to their dust and gas properties and, in some cases, kinematics. Notable works include the characterisation of the spatially resolved ISM properties with a focus on the molecular gas content (e.g. Dye et al., 2022), detection of multiple faint lines (e.g. Yang et al., 2019, 2020; Perrotta et al., 2023), characterisation of the photo-dissociation regions (e.g. Rybak et al., 2020), metallicity maps (e.g. De Breuck et al., 2019), and details about the dynamical structure (e.g. Rizzo et al., 2021). By using the boost in resolution produced by the strong lensing, these studies can probe the resolved properties listed above up to scales of $\sim 100\,\mathrm{pc}$ at redshifts of $z \sim 2-5$.

As noted above, a possible approach that, alongside the detailed ISM studies, would allow the characterisation of the star-formation properties of DSFGs is placing them in the SFR versus stellar mass relation. In order to do that, one must constrain the stellar mass that is unavailable for lensed DSFGs but for a few cases (e.g. Messias et al., 2014; Negrello et al., 2014; Dye et al., 2022). This lack of stellar masses is due to a combination of different reasons. On one side, there is the intrinsic faintness of the stellar emission caused by the massive attenuation operated by the high dust content. On the other side, we have to consider the presence of the lens blending with the lensed background source features that make photometry challenging and the uncertainty in deriving source properties. Moreover, in the observed optical/near-IR, the flux density of these sources strongly diminishes due to the K-correction, further complicating their detection.

The situation does not improve when approaching this issue from the side of the molecular gas depletion timescale. In fact, to estimate this parameter, it is necessary to know the total gas mass, which is hard to constrain due to the lack of any straightforward observation of both the molecular and neutral hydrogen at high-z and to the uncertainties of the tracer to gas conversion (e.g. Dye et al., 2022).

A viable technique to select candidate lensed DSFGs was presented by Negrello et al. (2007, 2010). It consists mainly of a flux density cut at a specific wavelength (i.e. $S_{500} \geq 100$

mJy at 500 μm, see Figure 1.9).

This approach exploits the steepness of the number count distribution of DSFGs as a function of the flux density. When a DSFG is lensed by a foreground system, its flux density gets boosted by a factor equal to the magnification. Given the very steep number count distribution of DSFGs, the population of the lensed ones forms a tail of bright objects that are otherwise much rarer. DSFGs are not the only sources detected in the sub-mm/mm. In fact, there is a significant contribution of dusty stars, local late-type galaxies (LTGs), and flat-spectrum radio sources like quasars (QSOs) or blazars. These other populations have their own characteristic number count distribution and can contaminate the bright tail of lensed DSFGs. That said, differentiating between DSFGs and other sources is relatively straightforward and can be done on shallow optical surveys for the first two classes of contaminants and radio surveys for the third class. While the contribution of unlensed DSFGs to the bright tail is unlikely, it is not impossible. Extreme objects, such as mergers or high-z protoclusters, might have a non-negligible contribution to the number counts bright tail depending on the flux density value at which the cut is taken.

1.4.1 H-ATLAS

H-ATLAS is the most extensive of the *Herschel* observational campaigns, covering an area of 570 deg^2 with 600 hours of observation time. Observations were conducted simultaneously using the SPIRE and PACS instruments, with a readout speed of 60 arcsec s^{-1} to maximise the observational coverage. The fields observed by H-ATLAS consist of a field near the North Galactic Pole (NGP) covering an area of 150 deg^2. Three fields $\sim$ 56 deg^2 each, coinciding with those surveyed in the Galaxy And Mass Assembly Redshift Survey (GAMA09, GAMA12, and GAMA15; Driver et al., 2009). Two fields totalling 250 deg^2 near the South Galactic Pole (SGP).

The results of H-ATLAS have been published in *Data Release 1* (DR1; Valiante et al., 2016; Bourne et al., 2016) for the GAMA fields, and in *Data Release 2* (Smith et al., 2017; Maddox et al., 2018; Furlanetto et al., 2018) for the NGP and SGP fields.

In these fields, the main strong lens searches were operated by Negrello et al. (2017) and Ward et al. (2022). They identified 80 and 11 candidate lensed galaxies with $S_{500} \geq 100$ mJy, respectively. Negrello et al. (2017) confirmed 20 of them through a combination of high-resolution imaging and spectroscopy. For the imaging data, they used *HST* and *Keck* data in the near-IR and *Submillimetre Array* (*SMA*) data in the sub-mm. Whereas for the near-IR spectroscopy, they used observations coming from the *William Herschel Telescope* (*WHT*), *Apache Point Observatory 3.5 Metre Telescope*, *New Technology Telescope*, *Gemini South Telescope*, and the*Anglo Australian Telescope* as part of the GAMA survey. For the background sources, they used the *Caltech Submillimeter Observatory*, *Green Banks Telescope*, *Plateu de Bure Interferometer* (*PdBI*), and the *Combined Array for Research in Millimeter-wave Astronomy* (*CARMA*) (see Negrello et al., 2017, for details). Ward et al. (2022), rather than focusing on confirming specific lensed candidates, studied the statistical properties of the associations between the *Herschel* detections and their optical counterparts. The authors used the Visible and Infrared Survey Telescope for Astronomy (VISTA) observations as part of the VIKING survey (Edge et al., 2013). Later on, Bakx et al. (2018) extended the selec-

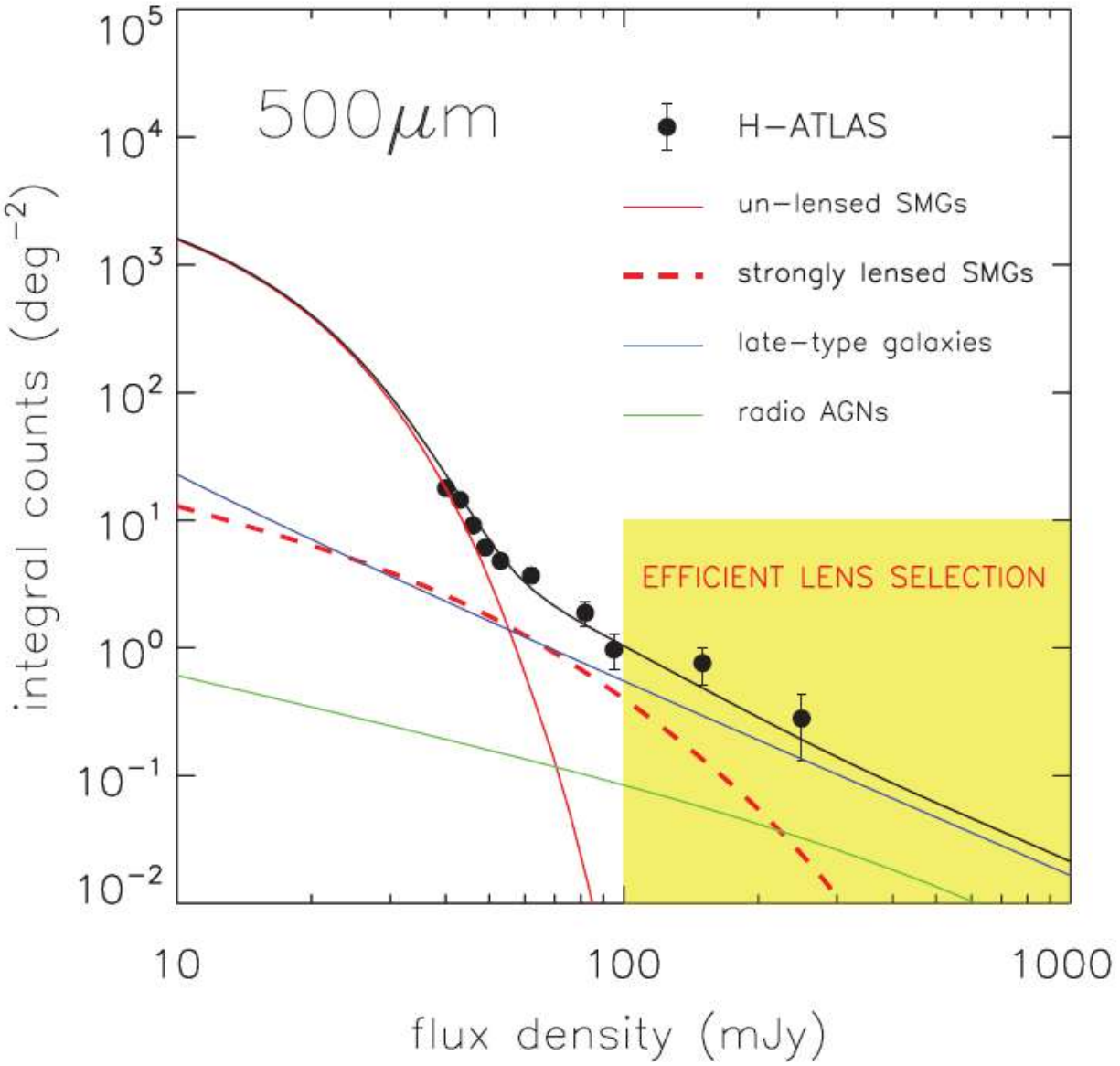

Figure 1.9: Example of the lens candidate selection applied by Negrello et al. (2010). The continuous and dashed red lines mark the number count distribution of the population of unlensed and lensed DSFGs, respectively. The green and blue lines mark the number count distribution of the flat-spectrum AGNs and late-type galaxies. Finally, the black line indicates the total number count distribution, while the black point corresponds to measures of the number count distribution in the H-ATLAS survey. The yellow shaded area marks the range of flux density where the lens selection is effective. From Negrello et al. (2010).

tion down to $S_{500} = 80$ mJy, and resticted to DSFGs with photometric redshift $z_{\rm phot} > 2$, as derived from the sub-mm colours (the *Herschel* bright sources – HerBS – sample), finding 200 candidates.

1.4.2 HerMES

The *Herschel* Multi-tiered Extragalactic Survey (HerMES; Oliver et al., 2012) is the second-largest observational campaign conducted with *Herschel*, covering an area of ~ 380 deg^2 with ~ 900 hours of observation time. The observations were divided into seven tiers, each obtained through a combination of SPIRE and PACS observations, utilising various observation modes and readout speeds. The fields were selected to overlap with as many observations as possible in different wavelengths covering legacy fields such as the Bootes, COSMOS, ECDFS, ELAIS North and South, EGS, FL2S, Lockman, and XMM fields. The largest HerMES field is the *HerMES Large-Mode Survey* (HELMS) field, which was added to the previous observations, positioned near the Sloan Digital Sky Survey (SDSS) Stripe 82 Region (Abazajian et al., 2009), covering an area of ~ 300 deg^2.

Regarding the strong lenses identification, HerMES was studied by Wardlow et al. (2013) who selected a sample of 13 candidates with $S_{500} > 100$ mJy and 29 with $80 < S_{500} < 80$ mJy in the HerMES fields, and, by using a combination of the morphology observed in near-IR and sub-mm observations confirmed nine as lensed. In the near-IR, they used *Keck*, *Spitzer*, and *HST* observations.

Bussmann et al. (2013) selected a sample of 30 candidates, confirming 21 to be strongly lensed, four moderately lensed, and the rest uncertain. They used a combination of follow-up observations both for imaging and spectroscopy. For the imaging, they used data coming from *HST*, *Keck*, and *SMA*. Whereas for the optical spectroscopy, they used data from the *MMT Observatory*, *Gemini South Telescope*, *WHT*, and *Very Large Telescope* (*VLT*). Calanog et al. (2014) presented a sample of 87 systems, confirming 12 of them as lensed. Some of these were already included in Bussmann et al. (2013, 2015). They used high-resolution *Keck* and *HST* data to characterise the near-IR morphology of the candidates and confirm them as lensed. Moreover, they applied lens modelling algorithms fitting the lenses and reconstructing the background sources. Later on, Bussmann et al. (2015) followed up with *ALMA* 29 candidates in the southern HerMES fields. Two were already presented in Bussmann et al. (2013), and eight were part of the sample of Wardlow et al. (2013). The authors utilised new shallow optical imaging with the Gemini South telescope to identify the possible lensing galaxies. Moreover, Bussmann et al. (2015) modelled all 29 systems with either weak or strong lenses, confirming six as strongly lensed.

1.4.3 HerS

The observational campaign HerS (Viero et al., 2014) consists of a series of observations obtained with SPIRE covering an area of ~ 79 deg^2, positioned in the Stripe 82 of the SDSS and partially overlapping with the HELMS field. HerS is intended to expand upon the results obtained with H-ATLAS and HerMES.

Nayyeri et al. (2017) studied both the HELMS and HerS fields identifying 77 candidates with $S_{500} > 100\,\mathrm{mJy}$ confirming three through available *HST* or *Keck* data. This study focused primarily on the unresolved sub-mm properties of the candidates with only a few available high-resolution observations.

The boundaries of the H-ATLAS, HerS, and HerMES are shown in Figure 1.10. The sample of lensed DSFG candidates was built by collecting sources from all the aforementioned observational campaigns. More details on the selection criteria and *HST* follow-up observations are given in Chapter 2.

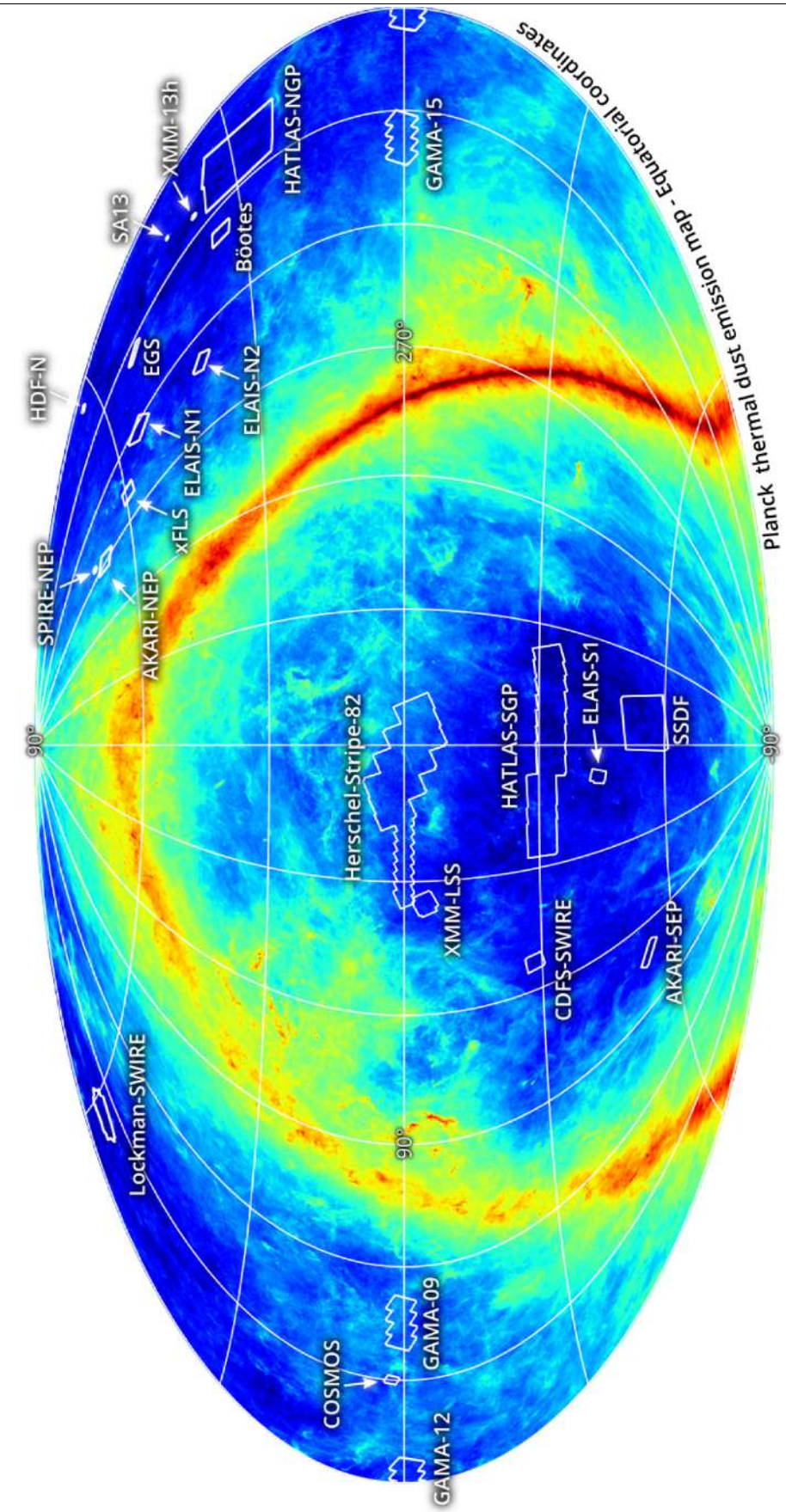

Figure 1.10: Boundaries of the H-ATLAS, HerS, and HerMES fields overlaid on the Planck Galactic thermal dust emission map. From Shirley et al. (2019).

1.5 Thesis aim and structure

In this thesis, we study a sample of strongly-lensed candidate DSFGs identified with *Herschel* and followed up with *HST*. In Chapter 1, we briefly introduce the topics of DSFGs and strong lensing, focusing specifically on the subpopulation of strongly lensed DSFGs. In Chapter 2, we present the sample of candidates and *HST* observations we used to classify and characterise our sample of lenses. In Chapter 3, we define the lens classification and present the multiwavelength follow-up observations we gathered from the literature. In Chapter 4, we describe the methods we adopted for the candidate lensing galaxies surface brightness modelling and subtraction. Later, we present the methods we adopted to perform lens modelling and reconstruct the background sources. In Chapter 5, we give a source-by-source description of the results obtained from the previous analysis and detail some interesting properties of both the lens population and background sources. Lastly, in Chapter 6, we present the spectral energy distribution fitting we performed for the case of the lensed DSFG ID141. A more detailed overview of the content of each chapter is the following.

- *Herschel* is able to produce large samples of strongly lensed candidates DSFGs. Unfortunately, its angular resolution and depth limit any detailed study of the spatially resolved properties of these candidates, thus not taking full advantage of the boost in resolution given by strong lensing. This highlights the need to follow up on these samples with some kind of high-resolution observations. In Chapter 2, we present the *HST* snapshot observations we use to try and address this issue. In Section 2.1, we describe the observational setup and data reduction of the *HST* observations. Then, we detail some additional corrections and measurements we performed on the whole sample candidates. In Section 2.2, we present the methods and results of an astrometric correction. Lastly, in Section 2.3, we estimate the depth of our snapshots that will be later used to give upper limits for non-detections.

- With a sample of strongly lensed candidates and high-resolution follow-up observations, it is necessary to find a way of distinguishing the clear lensing systems from the uncertain and the unlensed ones. While this process is straightforward in the sub-mm where these candidates are selected, it is more difficult in the near-IR, where the contamination of other sources is very high. In Chapter 3, we will present the classification methods we applied to our sample candidates. In Section 3.1, we define a first lens classification based on a visual inspection of the *HST* data. Then, in Section 3.2, we present a second complementary lens classification performed on available high-resolution sub-mm observations. For the two classifications, we detail a few possible statistical properties, mainly related to each class *Herschel* flux density distribution and colours. Lastly, we will combine the two lens classifications in the chapter summary, presented in Section 3.3.

- Having classified the candidates and identified possible lenses, the next issue is how to better study the lensing galaxies and background sources. To address them, it is necessary to identify and isolate the lenses from the background sources, which can be done by modelling and subtracting their surface brightness distribution. This

is described in Chapter 4. In Section 4.1, we present the methodology and fitting procedure we applied to model and subtract the surface-brightness distribution of the lensing galaxies. We then detail the set of Monte Carlo simulations we performed to estimate the uncertainties of the best-fitting parameters of the surface brightness models. To complement the surface-brightness fitting procedure, we give the modelling of HERSJ012620.5+012950 as an example. Lastly, we discuss an update to the lens classification consisting of a visual inspection after the removal of the lenses. Without the contamination of the lensing galaxies, it is then possible to focus on the background sources. These can be reconstructed by applying lens modelling techniques revealing their unlensed surface brightness distribution. This is a direct way of studying the DSFG morphology and stellar emission. In Section 4.2, we present the method and modelling approach used for the lens modelling. Specifically, we focus on how we computed the magnifications and reconstructed background-source sizes.

- Until now, we have presented the candidate lensed DSFGs, their classification, and the methods we applied in order to better characterise both the lensing galaxies and background sources in our *HST* snapshots. In Chapter 5, we present the results of this analysis, trying to address the following questions: *what are the photometric properties of our sample lenses? In what way does our background source-based selection impact the population of lensing galaxies? What are the properties and morphology of the lensed DSFGs?* In Section 5.1, we present the source-by-source description of the candidate systems, focusing both on each lens surface brightness model and background source reconstruction. This description is complemented by figures and tables containing the best-fitting models. In Section 5.2, we describe some general properties of the populations of lensing galaxies and lensed DSFGs. This is done by focusing primarily on the morphological characterisation of the lenses and background sources. Then, we perform a brief comparison of our sample with the one of SLACS.

- The measure of the stellar mass of a galaxy is of great importance in understanding its evolutionary stage and mode of star formation. Most star-forming galaxies follow a tight linear relation between the stellar mass and SFR. A systematic study of the location of lensed DSFGs in the SFR versus stellar mass plane is still missing. This is mainly due to the intrinsic faintness of these galaxies in the rest frame UV/optical and contamination from the lens surface brightness distribution. In Chapter 6, we provide a working example of how to constrain the stellar mass for one of the confirmed lensed galaxies in our sample. i.e., HATLASJ142414+022304. In Section 6.1, we discuss how to estimate the flux density of lensed sources in low-resolution *Spitzer* observations, which are crucial to the SED fitting and the measure of the stellar mass. Lastly, in Section 6.2, we give a brief summary of the possible implications of the same methodology to the full sample.

In Chapter 7, we review our findings, trying to answer the issues we set out on DSFGs.

The candidate has performed the analysis presented in Chapters 4 and 5 (published in Borsato et al., 2023), and obtained the Spitzer/IRAC flux density measurement, stellar mass estimate, and SED fitting detailed in Chapter 6 (published in Dye et al., 2022).

Chapter 2

HST follow-up

Herschel is able to produce large samples of strongly lensed candidate DSFGs. Unfortunately, its angular resolution and depth limit any detailed study of the spatially resolved properties of these candidates, thus not taking full advantage of the boost in resolution given by strong lensing. This highlights the need to follow up on these samples with some kind of high-resolution observations. In this Chapter, we present the *HST* snapshot observations we use to try and address this issue. In Section 2.1, we describe the observational setup and data reduction of the *HST* observations. Then, we detail some additional corrections and measurements we performed on the whole sample candidates. In Section 2.2, we present the methods and results of an astrometric correction. Lastly, in Section 2.3, we estimate the depth of our snapshots that will be later used to give upper limits for non-detections.

To determine whether a *Herschel*-selected sub-mm/mm bright galaxy is gravitationally lensed, high-resolution follow-up observations are essential. The distinctive features of lensing are the multiple images of a background source, which typically have separations of a few arcseconds. These angular scales are too small to be resolved by the large *Herschel* beam, even at its shortest wavelength ($50\,\mu$m $>\sim 9$ arcsec). Because lensed DSFGs emit mostly in the far-IR/sub-mm/mm (Negrello et al., 2014), the best way to detect and characterise the multiple images is via high-angular resolution observations at sub-mm/mm wavelengths obtained with interferometers, such as the *ALMA*, *SMA*, and the *Northern Extended Millimetre Array* (*NOEMA*) (e.g., Bussmann et al., 2013; Amvrosiadis et al., 2018). Interestingly, at these wavelengths, the object acting as the lens, which is usually a massive red-and-dead foreground elliptical galaxy with very low dust content, remains undetected, thus facilitating the lens identification and source reconstruction.

The lensing features of the lensed DSFGs have typical widths of ~ 0.3 arcsec (Amvrosiadis et al., 2018), measured along the radial direction from the lens centre. Therefore, achieving an angular resolution of at least 0.1 arcsec is essential to resolve the background source, at least partially.

Observatories that possess both high angular resolution and sensitivity are a few. The most notable among them include *HST*, the recently launched *James Webb Space Telescope* (*JWST*), and ground-based 8-meter class observatories aided by adaptive optics (AO), such as the *Keck* telescopes and the *VLT*. High-resolution near-IR observations are crucial for two

more reasons other than the simple morphological argument presented above. The first is characterising the properties of the lenses. Differently than optical/near-IR identified lens samples, lensed DSFGs often need dedicated follow-up campaigns to detect candidates for the lensing galaxies. Moreover, since the candidate selection is operated solely on sub-mm data, the resulting lens sample is only marginally biased through the redshift distribution of the background sources. The second aspect is the study of the stellar emission of DSFGs. These data can then be used to reconstruct the intrinsic morphology of the background DSFGs via lens modelling techniques (e.g., Dye et al., 2018; Maresca et al., 2022), which provide crucial information on the spatial distribution of the gas and dust and on the star-formation rate surface density (e.g., Cañameras et al., 2017; Yang et al., 2019; Sun et al., 2021; Jarugula et al., 2021; Dye et al., 2022). However, it is impossible to constrain all the physical properties of the lensed DSFGs with the long wavelength data alone. To constrain the stellar properties of both the lens and lensed DSFG, it is necessary to conduct rest-frame optical and near-IR observations. While works detailing the stellar content of unlensed DSFGs already exist in the literature, this information is still rare for the lensed population. This *HST* observations are able to detect the brighter end of the rest-frame optical emission of lensed DSFGs, allowing for some constraints for their stellar content (e.g., Negrello et al., 2014).

Following up these candidates with ground-based observatories can be challenging due to their dispersed locations in the sky and the required sensitivity. An alternative approach is to exploit the snapshot capabilities of *HST* (Negrello et al., 2014). This way, achieving the desired resolution with a few minutes of on-source integration time is possible, although at the cost of sensitivity.

The scheduling constraints imposed by *HST* low orbit are such that various gaps form between the General Observer (GO), Guaranteed Time Observer (GTO), Director's Discretionary (DD) and Calibration (CA) programs. These gaps can be efficiently filled by reasonably low exposure time (usually much less than 1 hour) and all-sky distributed targets. *HST* high angular resolution allows the study of the foreground lenses and, if bright enough, the detection of the background sources. Therefore, a series of snapshot proposals were conducted to characterise the population of *Herschel*-selected DSFGs. These proposals were observed in three observing cycles and are:

- Proposal ID 12488 (PI M. Negrello) in Cycle 19: 200 targets were proposed with $S_{500} \geq 85\,\mathrm{mJy}$, from the preliminary source catalogues of HerMES (63 targets) and H-ATLAS (137 targets). At that time, there were only *Herschel* data available for four out of the final five H-ATLAS fields (three fields on the Celestial Equator named GAMA09, GAMA12, and GAMA15, and one close to the North Galactic Pole named NGP), so the targets were spread across the Equatorial and Northern sky. The observations were carried out from October 2011 to August 2013.

- Proposal ID 15242 (PI L. Marchetti) in Cycle 25: 200 targets were proposed with $S_{500} \geq 100\,\mathrm{mJy}$ from the full *Herschel* coverage, in particular from HeLMS and HerS (Nayyeri et al., 2016) and with $S_{500} \geq 80\,\mathrm{mJy}$ from the H-ATLAS SGP field near the South Galactic Pole. The sample included some of the targets submitted for the Cycle 19 proposal, which had not been observed or for which the *HST* data obtained were

corrupted due to issues with the *HST* tracking system. The observations were carried out from October 2017 to June 2018.

- Proposal ID 16015 (PI L. Marchetti) in Cycle 26: this was a continuation of the Cycle 25 proposal. The observations were carried out from November 2019 to September 2020.

In summary, a total of 290 candidates were observed as part of these three snapshot programmes: 173 from H-ATLAS, 60 from HerMES, 42 from HeLMS, and 15 from HerS. Unfortunately, the data of nine systems were corrupted due to issues with the *HST* tracking system, so the final sample with available *HST* snapshot observations amounts to 281 systems. In Table 2.1, we report the full sample candidates, including their IAU identifiers, aliases, coordinates, lens classification, and *Herschel*/SPIRE flux densities that were used for the selection.

Table 2.1: Properties of the 281 systems classified as A, B, C, and D.

No.	IAU Name	Alt. Name	Ref.	RA	Dec	Lens classification[a]			S_{250}	S_{350}	S_{500}	Ref.
				[h m s]	[d m s]	Vis.	Multiw.	Final	[mJy]	[mJy]	[mJy]	
(1)	(2)	(3)	(4)	(5)	(6)	(7)	(8)	(9)	(10)	(11)	(12)	(13)
1	HATLASJ000330.6−321136	HERBS155	Ba18	00:03:31	−32:11:36.00	A	–	A	59.9 ± 5.8	94.2 ± 5.8	85.6 ± 7.2	Ba18
2	HATLASJ000912.7−300807	SD.v1.70	Zh18	00:09:13	−30:08:07.00	A	–	A	352.8 ± 5.4	272.6 ± 6.1	156.1 ± 6.8	Ne17
3	HELMSJ001353.5−060200	HELMS31	Na16	00:13:54	−06:02:00.00	A	–	A	178.0 ± 7.0	176.0 ± 6.0	120.0 ± 7.0	Na16
4	HELMSJ003619.8+002420	HELMS14	Na16	00:36:20	+00:24:20.00	A	–	A	251.0 ± 6.0	247.0 ± 6.0	148.0 ± 7.0	Na16
5	HELMSJ005841.2−011149	HELMS23	Na16	00:58:41	−01:11:49.00	A	–	A	391.0 ± 7.0	273.0 ± 6.0	126.0 ± 8.0	Na16
6	HERSJ011722.3+005624	HERS10	Na16	01:17:22	+00:56:24.00	A	–	A	105.0 ± 6.0	125.0 ± 6.0	117.0 ± 7.0	Na16
7	HERSJ012620.5+012950	HERS5	Na16	01:26:21	+01:29:50.00	A	–	A	268.0 ± 8.0	228.0 ± 7.0	133.0 ± 9.0	Na16
8	HERSJ020941.2+001558	9io9	Ge15	02:09:41	+00:15:58.00	A	A	A	826.0 ± 7.0	912.0 ± 7.0	718.0 ± 8.0	Na16
		HERS1	Na16									
		PJ020941.3	Hr16									
		ACT-S J0210+0016	Su17									
9	HERMESJ032637−270044	HECDFS05	Wa13	03:26:36	−27:00:44.00	A	–	A	155.0	131.0	84.0	Ca14
10	HERMESJ033732−295353	HECDFS02	Wa13	03:37:32	−29:53:53.00	A	–	A	133.0	147.0	122.0	Ca14
11	HATLASJ083051+013225	G09v1.97	Bu13	08:30:51	+01:32:24.87	A	A	A	248.5 ± 7.5	305.3 ± 8.1	269.1 ± 8.7	Ne17
		HERBS4	Ba18									
12	HERMESJ100144+025709	HCOSMOS01	Ca14	10:01:44	+02:57:08.62	A	A	A	86.0 ± 6.0	96.0 ± 6.0	71.0 ± 6.0	Bu15
13	HERMESJ103827+581544	HLock04	Wa13	10:38:27	+58:15:43.60	A	A	A	190.0	156.0	101.0	Ca14
14	HERMESJ110016+571736	HLock12	Ca14	11:00:16	+57:17:35.92	A	–	A	224.0	159.0	79.0	Ca14
15	HATLASJ114638−001132	G12v2.30	Bu13	11:46:38	−00:11:32.00	A	A	A	316.0 ± 6.6	357.9 ± 7.4	291.8 ± 7.7	Ne17
		HERBS2										
16	HATLASJ125126+254928	HERBS52	Ba18	12:51:26	+25:49:28.31	A	A	A	57.4 ± 7.4	96.8 ± 8.2	109.4 ± 8.8	Ne17
17	HATLASJ125760+224558	–	–	12:58:00	+22:45:57.82	A	–	A	272.4 ± 7.3	215.0 ± 8.1	137.8 ± 8.7	Ne17
18	HATLASJ133008+245900	NBv1.78	Bu13	13:30:08	+24:58:59.70	A	A	A	271.2 ± 7.2	278.2 ± 8.1	203.5 ± 8.5	Ne17
		HERBS12	Ba18									
19	HATLASJ133846+255057	HERBS29	Ba18	13:38:46	+25:50:56.84	A	A	A	159.0 ± 7.4	183.1 ± 8.2	137.6 ± 9.0	Ne17
20	HATLASJ142935−002837	G15v2.19	Ca14	14:29:35	−00:28:37.00	A	A	A	801.8 ± 6.6	438.5 ± 7.5	199.8 ± 7.7	Ne17
		H1429−0028	Me14									
21	HERMESJ171451+592634	HFLS02	Wa13	17:14:51	+59:26:34.12	A	–	A	164.0	148.0	87.0	Ca14
22	HERMESJ171545+601238	HFLS08	Ca14	17:15:45	+60:12:38.34	A	–	A	86.0	93.0	67.0	Ca14
23	HATLASJ225844.7−295124	HERBS26	Ba18	22:58:45	−29:51:25.00	A	–	A	175.4 ± 5.2	187.0 ± 5.9	142.6 ± 7.5	Ne17
24	HELMSJ232210.3−033559	HELMS19	Na16	23:22:10	−03:35:59.00	A	–	A	114.0 ± 6.0	160.0 ± 7.0	134.0 ± 8.0	Na16
25	HATLASJ233037.2−331217	HERBS123	Ba18	23:30:37	−33:12:18.00	A	–	A	106.2 ± 5.9	107.9 ± 6.0	90.0 ± 7.5	Ba18

a: the visual, multiwavelength, and final lens classifications are defined in Chapter 3 and Chapter 4, respectively. The first is defined by performing a visual inspection on the *HST* cutouts. The second utilizes high-resolution sub-mm observations when available. The third consists of a visual inspection of the B candidates after modelling and subtracting the surface brightness distribution of the candidate lensing galaxies.

Notes: Col. (1): Source reference number. Col. (2): IAU name of the *Herschel* detection. Cols. (3) and (4): Alternative name and reference. Cols. (5) and (6): ICRS right ascension (RA) and declination (Dec) coordinate (J2000.0) of the *Herschel* detection. Cols. (7), (8), and (9): Visual, multiwavelength, and final lens classifications. Col. (10), (11), (12), and (13): SPIRE flux density at 250 μm, 350 μm, 500 μm and reference. Al17: Albareti et al. (2017); Am18: Amvrosiadis et al. (2018); Ba18: Bakx et al. (2018); Be21: Berta et al. (2021); Bo06: Borys et al. (2006); Bu13: Bussmann et al. (2013); Bu15: Bussmann et al. (2015); Bu21: Butler et al. (2021); Ca14: Calanog et al. (2014); Co11: Cox et al. (2011); Dy18: Dye et al. (2018); Dy22: Dye et al. (2022); En18: Enia et al. (2018); Fa17: Falgarone et al. (2017); Ga11: Gavazzi et al. (2011); Ge15: Geach et al. (2015); Gi23: Giulietti et al. (2023); Hs12: Harris et al. (2012); Hr16: Harrington et al. (2016); Ik11: Ikarashi et al. (2011); Ma19: Ma et al. (2019); Ma22: Maresca et al. (2022); Me14: Messias et al. (2014); Na16: Nayyeri et al. (2016); Na17: Nayyeri et al. (2017); Ne17: Negrello et al. (2017); Om13: Omont et al. (2013); Su17: Su et al. (2017); Sh21: Shirley et al. (2021); Ur22: Urquhart et al. (2022); Va16: Valiante et al. (2016); Wa13: Wardlow et al. (2013); Ya17: Yang et al. (2017); Ya19: Yang et al. (2019).

Table 2.1 (cont.)

No.	IAU Name	Alt. Name	Ref.	RA	Dec	Lens classification			S_{250}	S_{350}	S_{500}	Ref.
				[h m s]	[d m s]	Vis.	Multiw.	Final	[mJy]	[mJy]	[mJy]	
(1)	(2)	(3)	(4)	(5)	(6)	(7)	(8)	(9)	(10)	(11)	(12)	(13)
26	HELMSJ001626.0+042613	HELMS22	Na16	00:16:26	+04:26:13.00	B	A	A	130.0 ± 15.0	180.0 ± 18.0	130.0 ± 15.0	Zh18
27	HATLASJ002624.8−341737	HERBS22	Ba18	00:26:25	−34:17:38.00	B	–	A	137.7 ± 5.2	185.9 ± 5.8	148.8 ± 6.8	Ne17
28	HELMSJ004723.6+015751	HELMS9	Na16	00:47:24	+01:57:51.00	C	A	A	398.0 ± 6.0	320.0 ± 6.0	164.0 ± 8.0	Na16
29	HERSJ012041.6−002705	HERS2	Na16	01:20:42	−00:27:05.00	B	–	A	240 ± 6	260 ± 6	189 ± 7	Na16
30	HATLASJ085112+004934	–	–	08:51:12	+00:49:33.83	B	–	A	125.1 ± 7.3	118.3 ± 8.3	77.7 ± 8.8	Va16
31	HATLASJ085359+015537	G09v1.40	Bu13	08:53:59	+01:55:37.21	B	A	A	396.4 ± 7.6	367.9 ± 8.2	228.2 ± 8.9	Ne17
32	HERMESJ104549+574512	HLock06	Wa13	10:45:49	+57:45:11.52	B	–	A	136.0	127.0	96.0	Ca14
33	HERMESJ105551+592845	HLock08	Wa13	10:55:51	+59:28:45.44	B	–	A	142.0	119.0	84.0	Ca14
34	HERMESJ105751+573026	HLSW−01	Ga11	10:57:51	+57:30:26.42	B	A	A	402.0	377.0	249.0	Ca14
		HLock01	Wa13									
35	HATLASJ132630+334410	NAv1.195	Bu13	13:26:30	+33:44:09.90	C	A	A	190.6 ± 7.3	281.4 ± 8.2	278.5 ± 9.0	Ne17
36	HATLASJ133543+300404	NA.v1.489	Na17	13:35:43	+30:04:03.66	B	A	A	136.6 ± 7.2	145.7 ± 8.0	125.0 ± 8.5	Ne17
		HERBS35	Ba18									
37	HATLASJ142140+000448	HerBS140	Ba18	14:21:40	+00:04:48.00	B	–	A	96.8 ± 7.2	98.5 ± 8.2	87.4 ± 8.7	Ba18
38	HERMESJ142824+352620	HBootes03	Wa13	14:28:24	+35:26:19.54	B	A	A	323.0	243.0	139.0	Ca14
39	HATLASJ223753.8−305828	HERBS68	Ba18	22:37:54	−30:58:28.00	B	–	A	139.1 ± 4.9	144.9 ± 5.1	100.6 ± 6.2	Ne17
40	HATLASJ225250.7−313657	HERBS47	Ba18	22:52:51	−31:36:58.00	B	–	A	127.4 ± 4.2	138.7 ± 4.9	111.4 ± 5.9	Ne17
41	HELMSJ233441.0−065220	HELMS1	Na16	23:34:41	−06:52:20.00	B	A	A	431.0 ± 6.0	381.0 ± 7.0	272.0 ± 7.0	Na16
42	HELMSJ233633.5−032119	HELMS41	Na16	23:36:34	−03:21:19.00	B	–	A	130.0 ± 6.0	131.0 ± 6.0	110.0 ± 7.0	Na16
43	HELMSJ001615.7+032435	HELMS13	Na16	00:16:16	+03:24:35.00	B	A	A	176.0 ± 13.0	210.0 ± 15.0	134.0 ± 11.0	Zh18
44	HELMSJ002220.9−015524	HELMS29	Na16	00:22:21	−01:55:24.00	B	A	A	66.0 ± 6.0	102.0 ± 6.0	121.0 ± 7.0	Na16
45	HELMSJ003814.1−002252	HELMS24	Na16	00:38:14	−00:22:52.00	C	A	A	73.35 ± 5.55	119.01 ± 6.01	122.87 ± 6.69	Su17
		ACT-S J0038−0022	Su17									
46	HELMSJ003929.6+002426	HELMS11	Na16	00:39:30	+00:24:26.00	C	A	A	140.0 ± 7.0	157.0 ± 7.0	154.0 ± 8.0	Na16
47	HELMSJ004714.2+032454	HELMS8	Na16	00:47:14	+03:24:54.00	C	A	A	312.0 ± 6.0	244.0 ± 7.0	168.0 ± 8.0	Na16
48	HELMSJ005159.4+062240	HELMS18	Na16	00:52:00	+06:22:41.00	B	A	A	163.0 ± 13.0	202.0 ± 15.0	142.0 ± 12.0	Zh18
49	HATLASJ005724.2−273122	HERBS60	Ba18	00:57:24	−27:31:22.00	B	A	A	73.3 ± 5.8	101.2 ± 6.1	103.6 ± 7.5	Ba18
50	HERMESJ021831−053131	SXDF1100.001 (Orochi)	Ik11	02:18:31	−05:31:31.00	B	A	A	78.0 ± 7.0	122.0 ± 8.0	99.0 ± 7.0	Bu15
		HXMM02	Wa13									
51	HERMESJ033211−270536	HECDFS04	Wa13	03:32:11	−27:05:36.00	C	A	A	56.0 ± 6.0	61.0 ± 6.0	55.0 ± 6.0	Bu15
52	HERMESJ044154−540352	HADFS01	Wa13	04:41:54	−54:03:52.00	B	A	A	76.0 ± 6.0	100.0 ± 6.0	94.0 ± 6.0	Bu15
53	HATLASJ083932−011760	HERBS105	Ba18	08:39:32	−01:18:00.00	C	A	A	73.8 ± 7.4	88.5 ± 8.1	93.2 ± 8.7	Ba18
54	HATLASJ091841+023048	G09v1.326	Ca14	09:18:41	+02:30:47.97	B	A	A	125.7 ± 7.2	150.7 ± 8.2	128.4 ± 8.7	Ne17
		HERBS32	Ba18									
55	HATLASJ113526−014606	G12v2.43	Bu13	11:35:26	−01:46:06.00	C	A	A	278.8 ± 7.4	282.9 ± 8.2	204.0 ± 8.6	Ne17
		HERBS10	Ba18									
56	HATLASJ115433.6+005042	HERBS177	Ba18	11:54:34	+00:50:42.30	B	A	A	53.9 ± 7.4	85.8 ± 8.1	83.9 ± 8.6	Ba18
57	HATLASJ120127.6−014043	HERBS61	Ba18	12:01:28	−01:40:44.00	B	A	A	67.4 ± 6.5	112.1 ± 7.4	103.9 ± 7.7	Ne17
58	HATLASJ131611+281220	HERBS89	Ba18	13:16:11	+28:12:20.39	C	A	A	71.8 ± 5.7	103.4 ± 5.7	95.7 ± 7.0	Ba18
59	HATLASJ134429+303036	NAv1.56	Bu13	13:44:29	+30:30:35.77	B	A	A	462.0 ± 7.4	465.7 ± 8.6	343.3 ± 8.7	Ne17
		HERBS1	Ba18									
60	HATLASJ141352−000027	G15v2.235	Bu13	14:13:52	−00:00:27.00	B	A	A	188.6 ± 7.4	217.0 ± 8.1	176.4 ± 8.7	Ne17
		HERBS15	Ba18									
61	HATLASJ142414+022304	ID 141	Co11	14:24:14	+02:23:03.62	B	A	A	112.2 ± 7.3	182.2 ± 8.2	193.3 ± 8.5	Ne17
		G15v2.779	Bu13									
		HERBS13	Ba18									

Table 2.1 (cont.)

No.	IAU Name	Alt. Name	Ref.	RA	Dec	Lens classification			S_{250}	S_{350}	S_{500}	Ref.
				[h m s]	[d m s]	Vis.	Multiw.	Final	[mJy]	[mJy]	[mJy]	
(1)	(2)	(3)	(4)	(5)	(6)	(7)	(8)	(9)	(10)	(11)	(12)	(13)
62	HERMESJ142826+345547	HBootes02	Wa13	14:28:26	+34:55:47.03	B	A	A	159.0	195.0	156.0	Ca14
63	HATLASJ230815.5−343801	HERBS28	Ba18	23:08:16	−34:38:01.00	B	A	A	79.4 ± 5.4	135.4 ± 5.7	140.0 ± 7.0	Ne17
64	HELMSJ232439.5−043936	HELMS7	Na16	23:24:40	−04:39:36.00	B	A	A	214.0 ± 7.0	218.0 ± 7.0	172.0 ± 9.0	Na16
65	HELMSJ233620.8−060828	HELMS6	Na16	23:36:21	−06:08:28.00	B	A	A	193.0 ± 7.0	252.0 ± 6.0	202.0 ± 8.0	Na16
66	HELMSJ000215.9−012829	HELMS3	Na16	00:02:16	−01:28:29.00	B	–	B	643.0 ± 7.0	510.0 ± 6.0	258.0 ± 7.0	Na16
67	HELMSJ001800.1−060235	HELMS21	Na16	00:18:00	−06:02:35.00	B	–	B	206.0 ± 6.0	186.0 ± 7.0	130.0 ± 7.0	Na16
68	HELMSJ002208.1+034044	HELMS38	Na16	00:22:08	+03:40:44.00	B	–	B	190.0 ± 6.0	157.0 ± 6.0	113.0 ± 7.0	Na16
69	HATLASJ002533.5−333825	HerBS87	Ba18	00:25:34	−33:38:26.00	B	–	B	114.7 ± 5.2	127.8 ± 6.1	96.0 ± 7.3	Ba18
70	HERMESJ002906−421419	HELAISS01	Wa13	00:29:06	−42:14:19.00	B	–	B	129.0	116.0	81.0	Ca14
71	HATLASJ003207.7−303724	HerBS56	Ba18	00:32:08	−30:37:24.00	B	–	B	80.3 ± 5.0	106.2 ± 5.2	105.8 ± 6.3	Ne17
73	HELMSJ004747.1+061444	HELMS26	Na16	00:47:47	+06:14:44.00	B	–	B	85.0 ± 7.0	119.0 ± 6.0	125.0 ± 8.0	Na16
74	HERSJ010301.2−003300	HERS6	Na16	01:03:01	−00:33:01.00	B	–	B	121.0 ± 7.0	147.0 ± 6.0	130.0 ± 8.0	Na16
75	HERSJ011640.1−000454	HERS4	Na16	01:16:40	−00:04:54.00	B	–	B	137.5 ± 6.75	196.11 ± 6.56	189.91 ± 7.81	Su17
76	HATLASJ012415.9−310500	HerBS69	Ba18	01:24:16	−31:05:00.00	B	–	B	140.4 ± 5.4	154.5 ± 5.7	100.3 ± 7.0	Ne17
77	HERSJ012521.0+011724	HERS13	Na16	01:25:21	+01:17:24.00	B	–	B	165.0 ± 8.0	153.0 ± 7.0	114.0 ± 10.0	Na16
78	HERSJ012546.3−001143	HERS12	Na16	01:25:46	−00:11:43.00	B	–	B	152.0 ± 8.0	135.0 ± 7.0	114.0 ± 9.0	Na16
79	HERSJ012754.1+004940	HERS3	Na16	01:27:54	+00:49:40.00	B	–	B	253.0 ± 6.0	250.0 ± 6.0	191.0 ± 7.0	Na16
80	HATLASJ012853.0−332719	HerBS73	Ba18	01:28:53	−33:27:19.00	B	–	B	117.1 ± 6.0	129.0 ± 6.2	99.6 ± 7.4	Ba18
81	HATLASJ013840.5−281855	HerBS14	Ba18	01:38:41	−28:18:56.00	B	Unc.	B	116.3 ± 5.7	177.0 ± 6.0	179.4 ± 7.1	Ne17
82	HATLASJ013951.9−321446	HerBS55	Ba18	01:39:52	−32:14:46.00	B	–	B	109.0 ± 4.9	116.5 ± 5.3	107.1 ± 6.2	Ne17
83	HERSJ021402.6−004612	HERS17	Na16	02:14:03	−00:46:12.00	B	–	B	110.0 ± 8.0	130.0 ± 8.0	105.0 ± 9.0	Na16
84	HERSJ021434.4+005926	HERS16	Na16	02:14:34	+00:59:26.00	B	–	B	110.0 ± 9.0	134.0 ± 8.0	109.0 ± 10.0	Na16
85	HERMESJ022017−060143	HXMM01	Wa13	02:20:17	−06:01:44.00	B	Unc.	B	179.0 ± 7.0	188.0 ± 8.0	134.0 ± 7.0	Bu15
86	HERMESJ022135−062617	HXMM03	Wa13	02:21:35	−06:26:17.00	B	Unc.	B	114.0 ± 7.0	134.0 ± 8.0	116.0 ± 7.0	Bu15
87	HERMESJ045058−531654	HADFS03	Ca14	04:50:58	−53:16:54.00	B	Unc.	B	119.0 ± 6.0	102.0 ± 6.0	63.0 ± 6.0	Bu15
88	HATLASJ084958+010713	G09v1.1259 HerBS157	Ca14 Ba18	08:49:58	+01:07:12.73	B	–	B	81.2 ± 7.3	98.9 ± 8.2	85.2 ± 8.7	Ba18
89	HATLASJ090453.2+022017	HerBS183 SDP.392	Ba18	09:04:53	+02:20:17.87	B	–	B	87.0 ± 7.2	98.2 ± 8.0	82.3 ± 8.8	Ba18
90	HATLASJ091331−003644	SDP.44		09:13:31	−00:36:44.00	B	–	B	175.5 ± 6.5	142.2 ± 7.4	85.8 ± 7.8	Va16
91	HATLASJ092136+000132	HerBS91	Ba18	09:21:36	+00:01:31.92	B	–	B	139.2 ± 7.3	128.8 ± 8.1	95.1 ± 8.6	Ba18
92	HATLASJ092409−005018	HerBS185		09:24:09	−00:50:18.00	B	–	B	71.8 ± 7.4	87.7 ± 8.2	82.2 ± 8.5	Ba18
93	HERMESJ103618+585454	HLock05	Wa13	10:36:18	+58:54:54.36	B	–	B	71.0	102.0	98.0	Ca14
94	HATLASJ113804−011736	HerBS96	Ba18	11:38:04	−01:17:36.00	B	–	B	85.1 ± 7.3	98.4 ± 8.2	94.8 ± 8.8	Ba18
95	HATLASJ113833.3+004909	HerBS100	Ba18	11:38:33	+00:49:09.68	B	–	B	96.8 ± 7.3	106.4 ± 8.1	93.4 ± 8.7	Ba18
96	HATLASJ113841−020237	–	–	11:38:41	−02:02:37.00	B	–	B	45.2 ± 7.0	72.7 ± 7.7	71.7 ± 8.1	Ma18
97	HATLASJ115112−012638	HerBS53	Ba18	11:51:12	−01:26:38.00	B	–	B	141.2 ± 7.4	137.7 ± 8.2	108.4 ± 8.8	Ne17
98	HATLASJ115120−003322	–	–	11:51:20	−00:33:22.00	B	–	B	146.9 ± 7.8	150.3 ± 8.5	88.0 ± 8.8	Ma18
99	HATLASJ120127.8−021648	–	–	12:01:28	−02:16:48.00	B	–	B	207.9 ± 7.3	160.9 ± 8.2	103.6 ± 8.7	Ne17
100	HATLASJ120319.1−011253	HerBS50	Ba18	12:03:19	−01:12:54.00	B	–	B	114.3 ± 7.4	142.8 ± 8.2	110.2 ± 8.6	Ne17
101	HATLASJ121301.5−004922	HerBS48	Ba18	12:13:02	−00:49:23.00	B	–	B	136.6 ± 6.6	142.6 ± 7.4	110.9 ± 7.7	Ne17
102	HATLASJ121334.9−020323	–	–	12:13:35	−02:03:23.00	B	–	B	211.0	197.9	129.9	Ne17
103	HATLASJ121542.7−005220	HerBS62	Ba18	12:15:43	−00:52:20.00	B	–	B	119.7 ± 7.4	135.5 ± 8.2	103.4 ± 8.6	Ne17
104	HATLASJ130054+260303	HerBS129	Ba18	13:00:54	+26:03:02.68	B	–	B	59.4 ± 5.9	85.4 ± 5.9	89.0 ± 7.0	Ba18
105	HATLASJ131322+285836	–	–	13:13:22	+28:58:35.61	B	–	B	160.8 ± 7.4	116.0 ± 8.4	68.0 ± 8.8	Ma18
106	HATLASJ134159+292833	–	–	13:41:59	+29:28:32.54	B	–	B	174.4 ± 6.7	172.3 ± 7.7	109.2 ± 8.1	Ne17

Table 2.1 (cont.)

No.	IAU Name	Alt. Name	Ref.	RA	Dec	Lens classification			S_{250}	S_{350}	S_{500}	Ref.
				[h m s]	[d m s]	Vis.	Multiw.	Final	[mJy]	[mJy]	[mJy]	
(1)	(2)	(3)	(4)	(5)	(6)	(7)	(8)	(9)	(10)	(11)	(12)	(13)
107	HATLASJ141833+010212	HerBS110	Ba18	14:18:33	+01:02:12.40	B	–	B	66.0	106.5	92.8	Ba18
108	HERMESJ142201+533214	HEGS01		14:22:01	+53:32:13.70	B	–	B	74.0	98.0	89.0	Ca14
109	HATLASJ142318.3+013913	–	–	14:23:18	+01:39:13.80	B	–	B	61.8 ± 7.5	83.0 ± 8.2	65.1 ± 8.8	Ma18
110	HATLASJ143203−005219	–	–	14:32:03	−00:52:19.00	B	–	B	160.6 ± 7.6	125.0 ± 8.3	76.1 ± 8.9	Ma18
111	HERMESJ143331+345440	HBootes01		14:33:31	+34:54:39.60	B	Unc.	B	158.0	191.0	160.0	Ca14
112	HATLASJ144243+015506	HerBS153	Ba18	14:42:43	+01:55:05.86	B	–	B	123.2 ± 7.2	133.4 ± 8.1	85.7 ± 8.8	Ba18
113	HATLASJ144715−012114	–	–	14:47:15	−01:21:14.00	B	–	B	132.7 ± 7.3	118.9 ± 8.2	74.7 ± 8.6	Ma18
114	HATLASJ223942.4−333304	HerBS111	Ba18	22:39:42	−33:33:04.00	B	–	B	105.9 ± 6.5	115.6 ± 6.2	92.7 ± 7.4	Ba18
115	HATLASJ224026.5−315154	HerBS148	Ba18	22:40:27	−31:51:55.00	B	–	B	120.6 ± 5.0	121.2 ± 5.5	86.3 ± 6.8	Ba18
116	HATLASJ224759.6−310134	HerBS141	Ba18	22:48:00	−31:01:35.00	B	–	B	122.1 ± 6.1	124.4 ± 6.5	87.3 ± 7.5	Ba18
117	HATLASJ224805.3−335820	HerBS33	Ba18	22:48:05	−33:58:20.00	B	–	B	122.3 ± 5.7	135.5 ± 6.3	126.9 ± 7.2	Ne17
118	HATLASJ225045.5−304719	HerBS168	Ba18	22:50:46	−30:47:19.00	B	–	B	65.5 ± 6.1	88.1 ± 6.1	84.0 ± 7.5	Na16
119	HATLASJ230546.2−331038	HerBS49	Ba18	23:05:46	−33:10:39.00	B	–	B	76.8 ± 5.6	110.9 ± 5.9	110.4 ± 7.0	Ne17
120	HELMSJ231447.5−045658	HELMS44	Na16	23:14:48	−04:56:58.00	B	–	B	220.0 ± 8.0	141.0 ± 7.0	106.0 ± 8.0	Na16
121	HATLASJ232210.9−333749	HerBS146	Ba18	23:22:11	−33:37:49.00	B	–	B	122.4 ± 5.2	134.6 ± 5.4	86.6 ± 6.8	Ba18
122	HATLASJ232531.3−302235	HerBS17	Ba18	23:25:31	−30:22:36.00	B	–	B	175.5 ± 4.3	227.0 ± 4.7	175.7 ± 5.7	Ne17
123	HELMSJ232617.5−025319	HELMS51	Na16	23:26:18	−02:53:19.00	B	–	B	86.0 ± 6.0	109.0 ± 6.0	104.0 ± 7.0	Na16
124	HELMSJ232831.8−004035	HELMS55	Na16	23:28:32	−00:40:35.00	B	–	B	95.0 ± 7.0	120.0 ± 6.0	102.0 ± 7.0	Na16
125	HELMSJ232833.6−031416	HELMS48	Na16	23:28:34	−03:14:16.00	B	–	B	49.0 ± 6.0	104.0 ± 6.0	105.0 ± 8.0	Na16
126	HELMSJ233420.4−003458	HELMS43	Na16	23:34:20	−00:34:58.00	B	–	B	156.0 ± 7.0	141.0 ± 5.0	109.0 ± 8.0	Na16
127	HELMSJ233721.9−064740	HELMS49	Na16	23:37:22	−06:47:40.00	B	–	B	173.0 ± 6.0	161.0 ± 7.0	105.0 ± 8.0	Na16
128	HELMS233728.8−045106	HELMS20	Na16	23:37:29	−04:51:06.00	B	–	B	162.0 ± 6.0	178.0 ± 7.0	132.0 ± 8.0	Na16
129	HELMSJ234314.0+012152	HELMS36	Na16	23:43:14	+01:21:52.00	B	–	B	115.0 ± 6.0	115.0 ± 6.0	113.0 ± 8.0	Na16
130	HATLASJ234955.7−330833	HerBS184	Ba18	23:49:56	−33:08:33.00	B	–	B	91.9 ± 5.9	107.6 ± 6.0	82.3 ± 7.1	Ba18
131	HELMSJ235101.7−024425	HELMS50	Na16	23:51:02	−02:44:26.00	B	–	B	112.0 ± 6.0	124.0 ± 6.0	105.0 ± 7.0	Na16
132	HATLASJ235121.9−332902	HerBS159	Ba18	23:51:22	−33:29:02.00	B	–	B	92.1 ± 5.9	98.3 ± 5.9	85.0 ± 7.1	Ba18
133	HELMSJ235331.7+031717	HELMS40	Na16	23:53:32	+03:17:18.00	B	Unc.	B	102.0 ± 6.0	123.0 ± 7.0	111.0 ± 7.0	Na16
134	HATLASJ001030.1−330621	HerBS98	Ba18	00:10:30	−33:06:22.00	C	–	C	56.3 ± 4.9	51.7 ± 5.0	94.4 ± 6.5	Ba18
135	HELMSJ001226.9+020810	HELMS45	Na16	00:12:27	+02:08:10.00	C	–	C	107.0 ± 6.0	142.0 ± 6.0	106.0 ± 7.0	Na16
136	HELMSJ001325.7+042509	HELMS56	Na16	00:13:26	+04:25:09.00	C	–	C	89.0 ± 6.0	98.0 ± 6.0	102.0 ± 7.0	Na16
137	HATLASJ002144.8−295217	HerBS156	Ba18	00:21:45	−29:52:18.00	C	–	C	103.7 ± 5.7	91.3 ± 6.1	85.4 ± 6.9	Ba18
138	HELMSJ002719.5+001204	HELMS34	Na16	00:27:20	+00:12:04.00	C	–	C	248.0 ± 6.0	206.0 ± 7.0	116.0 ± 8.0	Na16
139	HERMESJ002854−420457	HELAISS04	Ca14	00:28:54	−42:04:57.00	C	–	C	131.0	102.0	58.0	Ca14
140	HELMSJ003519.7+072806	HELMS57	Na16	00:35:20	+07:28:06.00	C	–	C	134.0 ± 7.0	135.0 ± 7.0	101.0 ± 8.0	Na16
141	HATLASJ003728.7−284124	HerBS174	Ba18	00:37:29	−28:41:25.00	C	–	C	95.6 ± 5.7	84.8 ± 5.9	83.2 ± 7.4	Ba18
142	HELMSJ004622.3+073509	HELMS46	Na16	00:46:22	+07:35:09.00	C	–	C	82.0 ± 9.0	113.0 ± 9.0	105.0 ± 10.0	Na16
143	HATLASJ005132.8−301848	HerBS45	Ba18	00:51:33	−30:18:48.00	C	–	C	164.6 ± 5.4	160.2 ± 5.8	113.0 ± 7.2	Ne17
144	HATLASJ005849.9−290122	HerBS181	Ba18	00:58:50	−29:01:22.00	C	–	C	92.5 ± 5.7	116.6 ± 6.0	82.6 ± 7.2	Ba18
145	HATLASJ011014.5−314813	HerBS160	Ba18	01:10:15	−31:48:14.00	C	Unc.	C	48.6 ± 5.6	84.2 ± 6.0	84.8 ± 7.1	Ba18
146	HATLASJ011730.3−320719	HerBS138	Ba18	01:17:30	−32:07:19.00	C	–	C	120.4 ± 5.8	111.2 ± 6.4	87.4 ± 7.8	Ba18
147	HATLASJ012209.4−273824	HerBS114	Ba18	01:22:09	−27:38:24.00	C	–	C	81.7 ± 5.9	93.8 ± 6.0	91.8 ± 7.7	Ba18
148	HERSJ013212.2+001754	HERS18	Na16	01:32:12	+00:17:54.00	C	–	C	176.0 ± 7.0	175.0 ± 6.0	104.0 ± 8.0	Na16
149	HATLASJ013239.9−330906	HerBS40	Ba18	01:32:40	−33:09:07.00	C	–	C	112.0 ± 5.5	148.8 ± 6.2	117.7 ± 7.0	Ne17
150	HERSJ014057.3−010547	HERS14	Na16	01:40:57	−01:05:47.00	C	–	C	136.0 ± 8.0	143.0 ± 8.0	112.0 ± 9.0	Na16
151	HATLASJ014520.0−313834	HerBS107	Ba18	01:45:20	−31:38:35.00	C	–	C	97.3 ± 6.1	99.1 ± 6.4	93.1 ± 7.8	Ba18
152	HERSJ020529.1+000501	HERS19	Na16	02:05:29	+00:05:01.00	C	–	C	89.0 ± 6.0	112.0 ± 6.0	102.0 ± 8.0	Na16

Table 2.1 (cont.)

No.	IAU Name	Alt. Name	Ref.	RA	Dec	Lens classification			S_{250}	S_{350}	S_{500}	Ref.
				[h m s]	[d m s]	Vis.	Multiw.	Final	[mJy]	[mJy]	[mJy]	
(1)	(2)	(3)	(4)	(5)	(6)	(7)	(8)	(9)	(10)	(11)	(12)	(13)
153	HERMESJ021632−053421	HXMM14	Ca14	02:16:32	−05:34:21.00	C	–	C	98.0	98.0	78.0	Ca14
154	HERMESJ021837−035315	HXMM13	Ca14	02:18:37	−03:53:15.00	C	–	C	55.0	88.0	94.0	Ca14
155	HERMESJ022213−070222	HXMM28	Ca14	02:22:13	−07:02:22.00	C	–	C	27.0	47.0	87.0	Ca14
156	HERMESJ022515−024707	HXMM19	Ca14	02:25:15	−02:47:07.00	C	–	C	43.0	67.0	70.0	Ca14
157	HERMESJ022518−044610	HXMM27	Ca14	02:25:17	−04:46:10.00	C	–	C	0.0	48.0	43.0	Ca14
158	HERMESJ023006−034153	HXMM12	Ca14	02:30:06	−03:41:53.00	C	Unc.	C	98.0 ± 7.0	106.0 ± 8.0	82.0 ± 7.0	Bu15
159	HERMESJ032434−292646	HECDFS08	Ca14	03:24:34	−29:26:46.00	C	–	C	104.0	67.0	54.0	Ca14
160	HERMESJ032443−282134	HECDFS03	Ca14	03:24:43	−28:21:34.00	C	–	C	83.0	118.0	113.0	Ca14
161	HERMESJ032713−285106	HECDFS09	Ca14	03:27:13	−28:51:06.00	C	–	C	77.0	66.0	51.0	Ca14
162	HERMESJ033118−272015	HECDFS11	Ca14	03:31:18	−27:20:15.00	C	–	C	45.0	52.0	42.0	Ca14
163	HERMESJ043341−540338	HADFS04	Ca14	04:33:41	−54:03:38.00	C	Unc.	C	74.0 ± 6.0	93.0 ± 6.0	84.0 ± 6.0	Bu15
164	HATLASJ083546+002804	–	–	08:35:46	+00:28:03.75	C	–	C	86.6 ± 6.6	94.5 ± 7.5	79.5 ± 8.0	Va16
165	HATLASJ083817−004134	HerBS108	Ba18	08:38:17	−00:41:34.00	C	–	C	84.5 ± 7.4	106.1 ± 8.2	93.0 ± 8.8	Ba18
166	HATLASJ083859.3+021325	HerBS169	Ba18	08:38:59	+02:13:25.87	C	–	C	95.2 ± 7.5	105.2 ± 8.2	84.0 ± 8.7	Ba18
167	HATLASJ083945+021023	HerBS171	Ba18	08:39:45	+02:10:22.83	C	–	C	71.3 ± 7.3	97.4 ± 8.1	83.4 ± 8.6	Ba18
168	HATLASJ084259.9+024959	HerBS188	Ba18	08:43:00	+02:49:59.02	C	–	C	84.2 ± 7.4	101.5 ± 8.1	81.8 ± 8.6	Ba18
169	HATLASJ085033+012914	–	–	08:50:33	+01:29:14.10	C	–	C	182.5 ± 6.9	131.6 ± 7.7	74.7 ± 8.0	Ma18
170	HATLASJ085126+014638	–	–	08:51:26	+01:46:38.37	C	–	C	66.4 ± 7.4	92.3 ± 8.1	79.1 ± 8.5	Va16
171	HATLASJ085309−005727	HerBS136	Ba18	08:53:09	−00:57:27.00	C	–	C	68.3 ± 7.5	97.5 ± 8.2	87.7 ± 8.6	Ne17
172	HATLASJ090953−010811	SDP.60		09:09:53	−01:08:11.00	C	–	C	152.1 ± 7.2	109.3 ± 8.1	83.5 ± 8.4	Va16
173	HATLASJ091809+001927	HerBS99	Ba18	09:18:09	+00:19:27.27	C	–	C	93.2 ± 7.4	116.6 ± 8.2	94.3 ± 8.7	Ba18
174	HATLASJ091857−000047	–	–	09:18:57	−00:00:47.00	C	–	C	171.6 ± 6.4	145.7 ± 7.4	85.1 ± 7.7	Va16
175	HATLASJ091949−005037	–	–	09:19:49	−00:50:37.00	C	–	C	150.7 ± 7.5	141.4 ± 8.4	90.4 ± 8.7	Va16
176	HATLASJ092141+005356	–	–	09:21:41	+00:53:55.58	C	–	C	71.2 ± 7.3	85.4 ± 8.2	79.6 ± 8.8	Va16
177	HERMESJ103958+563120	HLock17	Wa13	10:39:58	+56:31:19.92	C	–	C	62.0	82.0	67.0	Ca14
178	HERMESJ104051+560654	HLock02 LSW102	Wa13	10:40:51	+56:06:54.14	C	–	C	53.0	115.0	140.0	Ca14
179	HERMESJ104140+570859	HLock11	Wa13	10:41:40	+57:08:59.42	C	–	C	97.0	112.0	80.0	Ca14
180	HERMESJ105712+565458	HLock03	Wa13	10:57:12	+56:54:58.25	C	–	C	114.0 ± 7.0	147.0 ± 10.0	114.0 ± 8.0	Ca14
181	HATLASJ113243−005109	HerBS71	Ba18	11:32:43	−00:51:09.00	C	–	C	68.0 ± 7.0	106.0 ± 8.0	100.0 ± 9.0	Ma19
182	HATLASJ113834−014657	HerBS119	Ba18	11:38:34	−01:46:57.00	C	–	C	68.5 ± 7.2	85.6 ± 8.1	91.2 ± 8.6	Ba18
183	HATLASJ114753−005832	HerBS85	Ba18	11:47:53	−00:58:32.00	C	–	C	92.1 ± 6.6	104.2 ± 7.4	96.0 ± 7.7	Ba18
184	HATLASJ115820−013754	HerBS66	Ba18	11:58:20	−01:37:54.00	C	–	C	120.0 ± 7.0	124.0 ± 8.0	101.0 ± 8.0	Ma19
185	HATLASJ120600.7+003459	HerBS74	Ba18	12:06:01	+00:34:59.51	C	–	C	88.7 ± 7.4	104.1 ± 8.1	98.8 ± 8.7	Ba18
186	HATLASJ120709.2−014702	HerBS51	Ba18	12:07:09	−01:47:03.00	C	–	C	143.2 ± 7.4	149.2 ± 8.1	110.3 ± 8.7	Ne17
187	HATLASJ121348.0+010812	HerBS116	Ba18	12:13:48	+01:08:12.59	C	–	C	65.1 ± 7.4	96.6 ± 8.2	93.6 ± 8.5	Ba18
188	HATLASJ121416.3−013704	HerBS164	Ba18	12:14:16	−01:37:04.00	C	–	C	88.0 ± 6.4	99.3 ± 7.4	84.3 ± 7.7	Ba18
189	HATLASJ122034.2−003805	HerBS197	Ba18	12:20:34	−00:38:06.00	C	–	C	81.9 ± 7.5	93.8 ± 8.2	84.8 ± 8.7	Ba18
190	HATLASJ122117.0−014924	–	–	12:21:17	−01:49:24.00	C	–	C	146.6 ± 7.4	128.9 ± 8.2	87.2 ± 8.3	Va16
191	HATLASJ122158.5+003326	HerBS124	Ba18	12:21:59	+00:33:26.15	C	–	C	135.7 ± 7.3	116.1 ± 8.2	89.8 ± 8.6	Ba18
192	HATLASJ125105+261653	NGP.2070		12:51:05	+26:16:52.62	C	–	C	116.5 ± 5.5	125.3 ± 6.5	81.3 ± 7.7	Va16
193	HATLASJ125653+275903	HerBS31	Ba18	12:56:53	+27:59:02.98	C	–	C	133.9 ± 7.5	164.1 ± 8.2	131.8 ± 8.9	Ne17
194	HATLASJ125810+263710	–	–	12:58:10	+26:37:09.99	C	–	C	131.6 ± 7.3	122.9 ± 8.3	78.8 ± 8.5	Ma18
195	HATLASJ130601+231322	–	–	13:06:01	+23:13:21.65	C	–	C	86.0 ± 7.3	88.0 ± 8.2	76.5 ± 8.6	Va16
196	HATLASJ131001+264759	–	–	13:10:01	+26:47:59.05	C	–	C	142.1 ± 7.3	124.1 ± 8.2	81.2 ± 8.9	Va16
197	HATLASJ131020+253731	–	–	13:10:20	+25:37:31.47	C	–	C	186.4 ± 7.3	158.7 ± 8.1	93.7 ± 8.5	Va16

Table 2.1 (cont.)

No.	IAU Name	Alt. Name	Ref.	RA	Dec	Lens classification			S_{250}	S_{350}	S_{500}	Ref.
				[h m s]	[d m s]	Vis.	Multiw.	Final	[mJy]	[mJy]	[mJy]	
(1)	(2)	(3)	(4)	(5)	(6)	(7)	(8)	(9)	(10)	(11)	(12)	(13)
198	HATLASJ131609+254931	–	–	13:16:09	+25:49:31.15	C	–	C	121.4 ± 7.3	108.2 ± 8.1	76.8 ± 8.7	Va16
199	HATLASJ131642+251158	–	–	13:16:42	+25:11:58.38	C	–	C	62.7 ± 6.9	71.5 ± 7.7	63.9 ± 8.1	Ma18
200	HATLASJ131805+325018	HerBS173	Ba18	13:18:05	+32:50:18.05	C	–	C	73.3 ± 5.6	92.7 ± 6.0	83.3 ± 7.2	Ba18
201	HATLASJ132128+282023	HerBS127	Ba18	13:21:28	+28:20:22.74	C	–	C	110.0 ± 5.5	122.7 ± 6.1	89.5 ± 6.9	Ba18
202	HATLASJ132227+300723	–	–	13:22:27	+30:07:22.54	C	–	C	48.0 ± 7.3	78.6 ± 8.2	25.0 ± 8.8	Va16
203	HATLASJ132302+341650	HerBS30	Ba18	13:23:02	+34:16:49.66	C	–	C	124.2 ± 7.3	144.6 ± 8.2	137.0 ± 8.7	Ne17
204	HATLASJ132419+320754	HerBS43	Ba18	13:24:19	+32:07:54.43	C	–	C	84.5 ± 6.8	116.0 ± 7.6	115.4 ± 8.0	Ne17
205	HATLASJ132909+300958	HerBS204	Ba18	13:29:09	+30:09:58.23	C	–	C	57.9 ± 5.5	95.3 ± 6.1	80.1 ± 7.1	Ba18
206	HATLASJ133255+265529	–	–	13:32:55	+26:55:29.23	C	–	C	192.5 ± 7.4	167.4 ± 8.1	116.6 ± 8.6	Ne17
207	HATLASJ133256+342210	HerBS44	Ba18	13:32:56	+34:22:09.50	C	–	C	164.3 ± 7.5	186.8 ± 8.1	114.9 ± 8.7	Ne17
		NA.v1.267										
208	HATLASJ133440+353140	HerBS134	Ba18	13:34:40	+35:31:40.17	C	–	C	69.9 ± 5.9	97.3 ± 6.2	87.9 ± 7.3	Ba18
209	HATLASJ133534+341837	HerBS76	Ba18	13:35:34	+34:18:36.97	C	–	C	108.5 ± 5.9	124.3 ± 6.0	98.5 ± 7.0	Ba18
210	HATLASJ133623+343806	–	–	13:36:23	+34:38:05.88	C	–	C	78.8 ± 7.4	83.2 ± 8.3	79.1 ± 8.6	Ma18
211	HATLASJ133715+352058	–	–	13:37:15	+35:20:58.04	C	–	C	69.9 ± 7.5	88.1 ± 8.3	69.4 ± 8.8	Ma18
212	HATLASJ133905+340820	–	–	13:39:05	+34:08:20.20	C	–	C	59.3 ± 7.3	82.7 ± 8.2	70.1 ± 8.7	Va16
213	HATLASJ134124+354007	–	–	13:41:24	+35:40:06.58	C	–	C	62.9 ± 7.3	79.9 ± 8.2	82.2 ± 8.5	Va16
214	HATLASJ134139+322837	–	–	13:41:39	+32:28:37.34	C	–	C	39.8 ± 7.4	42.7 ± 8.1	80.1 ± 8.8	Va16
215	HATLASJ134403+242627	HerBS196	Ba18	13:44:03	+24:26:26.95	C	–	C	86.9 ± 5.7	92.3 ± 6.3	81.0 ± 7.1	Ba18
216	HATLASJ134442+240346	HerBS133	Ba18	13:44:42	+24:03:46.12	C	–	C	85.4 ± 5.5	98.5 ± 6.1	88.1 ± 7.3	Ba18
238	HATLASJ134654+295659	–	–	13:46:54	+29:56:59.06	C	–	C	85.0 ± 7.6	82.0 ± 8.3	77.8 ± 8.6	Va16
217	HATLASJ140422−001218	HerBS206	Ba18	14:04:22	−00:12:18.00	C	–	C	79.3 ± 7.4	102.6 ± 8.4	80.2 ± 8.8	Ba18
218	HATLASJ141810.0−003747	HerBS143	Ba18	14:18:10	−00:37:47.00	C	–	C	77.7 ± 6.5	97.3 ± 7.4	87.1 ± 7.9	Ba18
219	HATLASJ141955.5−003449	–	–	14:19:56	−00:34:49.00	C	–	C	76.4 ± 7.5	94.9 ± 8.0	80.2 ± 8.9	Va16
220	HERMESJ142549+345024	–	–	14:25:49	+34:50:23.57	C	–	C	48.0 ± 7.4	64.4 ± 8.3	52.9 ± 9.0	Ma18
221	HERMESJ142558+332549	HBootes09		14:25:58	+33:25:48.68	C	–	C	69.0	81.0	60.0	Ca14
222	HATLASJ142707+002258	HerBS130	Ba18	14:27:07	+00:22:57.60	C	–	C	119.4 ± 7.3	118.7 ± 8.1	88.8 ± 8.6	Ba18
223	HATLASJ143403.5+000234	HerBS147	Ba18	14:34:04	+00:02:34.34	C	–	C	103.3 ± 7.4	103.3 ± 8.1	86.6 ± 8.5	Ba18
224	HERMESJ143544+344743	HBootes12		14:35:44	+34:47:43.37	C	–	C	11.0	52.0	21.0	Ca14
225	HERMESJ144030+333843	HBootes07		14:40:30	+33:38:42.68	C	–	C	86.0	88.0	72.0	Ca14
226	HATLASJ144556.1−004853	G15v2.481		14:45:56	−00:48:53.00	C	Unc.	C	126.7 ± 7.3	132.6 ± 8.4	111.8 ± 8.7	Ne17
		HerBS46	Ba18									
227	HATLASJ144608.6+021927	HerBS38	Ba18	14:46:09	+02:19:27.01	C	–	C	73.4 ± 7.1	111.7 ± 8.1	122.1 ± 8.7	Ne17
228	HATLASJ145135.2−011418	HerBS126	Ba18	14:51:35	−01:14:18.00	C	–	C	81.9 ± 7.2	95.9 ± 8.2	89.8 ± 8.8	Ba18
229	HATLASJ145337.2+000407	HerBS137	Ba18	14:53:37	+00:04:07.94	C	–	C	86.0 ± 7.2	103.6 ± 8.0	87.7 ± 8.6	Ba18
230	HATLASJ145754+000017	HerBS195	Ba18	14:57:54	+00:00:17.07	C	–	C	70.3 ± 7.3	92.7 ± 8.1	81.0 ± 8.8	Ba18
231	HERMESJ161332+544358	HELAISN01		16:13:32	+54:43:57.76	C	–	C	123.0	129.0	88.0	Ca14
232	HERMESJ170508+594056	HFLS07	Ca14	17:05:08	+59:40:56.32	C	–	C	115.0	92.0	69.0	Ca14
233	HERMESJ170608+590921	HFLS03	Ca14	17:06:08	+59:09:21.28	C	–	C	98.0	105.0	81.0	Ca14
234	HERMESJ170818+582845	HFLS05	Ca14	17:08:18	+58:28:45.41	C	–	C	40.0	75.0	74.0	Ca14
235	HERMESJ172222+582611	HFLS10	Ca14	17:22:22	+58:26:10.82	C	–	C	52.0	50.0	32.0	Ca14
236	HERMESJ172612+583742	HFLS01	Ca14	17:26:12	+58:37:42.24	C	–	C	107.0	123.0	98.0	Ca14
237	HATLASJ222629.4−321111	HerBS144	Ba18	22:26:29	−32:11:12.00	C	–	C	98.9 ± 8.4	116.5 ± 8.2	87.0 ± 11.5	Ba18
238	HATLASJ224027.7−343134	HerBS97	Ba18	22:40:28	−34:31:35.00	C	–	C	96.1 ± 6.0	98.5 ± 6.3	94.4 ± 7.7	Ba18
239	HATLASJ224207.2−324159	HerBS67	Ba18	22:42:07	−32:41:59.00	C	Unc.	C	73.0 ± 5.5	88.1 ± 6.2	100.8 ± 7.7	Ne17
240	HATLASJ224400.8−340030	HerBS84	Ba18	22:44:01	−34:00:31.00	C	–	C	105.1 ± 5.9	123.0 ± 6.4	97.0 ± 7.6	Ba18

Table 2.1 (cont.)

No.	IAU Name	Alt. Name	Ref.	RA	Dec	Lens classification			S_{250}	S_{350}	S_{500}	Ref.
				[h m s]	[d m s]	Vis.	Multiw.	Final	[mJy]	[mJy]	[mJy]	
(1)	(2)	(3)	(4)	(5)	(6)	(7)	(8)	(9)	(10)	(11)	(12)	(13)
241	HATLASJ225324.2−323504	HerBS103	Ba18	22:53:24	−32:35:04.00	C	–	C	126.1 ± 5.3	131.2 ± 5.7	93.5 ± 7.0	Ba18
242	HATLASJ225339.1−325549	HerBS131	Ba18	22:53:39	−32:55:50.00	C	–	C	85.5 ± 5.2	99.7 ± 5.5	88.0 ± 6.9	Ba18
243	HATLASJ225611.6−325652	HerBS135	Ba18	22:56:12	−32:56:53.00	C	–	C	85.4 ± 5.5	96.7 ± 6.2	87.8 ± 7.5	Ba18
244	HATLASJ230002.6−315005	HerBS80	Ba18	23:00:03	−31:50:05.00	C	–	C	122.7 ± 5.7	122.1 ± 6.3	97.7 ± 7.6	Ba18
245	HATLASJ230538.5−312204	HerBS182	Ba18	23:05:39	−31:22:04.00	C	–	C	89.0 ± 5.7	109.1 ± 6.2	82.3 ± 7.9	Ba18
246	HATLASJ231205.1−295026	HerBS132	Ba18	23:12:05	−29:50:27.00	C	–	C	86.7 ± 5.8	102.6 ± 6.0	90.6 ± 7.8	Ba18
247	HELMSJ231857.2−053035	HELMS16	Na16	23:18:57	−05:30:35.00	C	–	C	143.0 ± 7.0	183.0 ± 7.0	146.0 ± 8.0	Na16
248	HATLASJ232419.8−323926	HerBS18	Ba18	23:24:20	−32:39:27.00	C	–	C	213.0 ± 4.4	244.2 ± 4.8	169.4 ± 5.8	Ne17
		SC.v1.128										
249	HELMSJ232558.3−044525	HELMS17	Na16	23:25:58	−04:45:25.00	C	–	C	190.0 ± 6.0	189.0 ± 6.0	142.0 ± 8.0	Na16
250	HATLASJ232623.0−342642	HerBS37	Ba18	23:26:23	−34:26:42.00	C	–	C	153.7 ± 4.4	178.3 ± 5.0	123.5 ± 6.2	Ne17
		SB.v1.202										
251	HELMSJ234014.6−070738	HELMS42	Na16	23:40:15	−07:07:38.00	C	–	C	158.0 ± 6.0	154.0 ± 6.0	110.0 ± 8.0	Na16
252	HELMSJ234951.6−030019	HELMS47	Na16	23:49:52	−03:00:19.00	C	–	C	186.0 ± 7.0	167.0 ± 6.0	105.0 ± 8.0	Na16
253	HATLASJ000455.3−330811	HerBS170	Ba18	00:04:55	−33:08:12.00	C	D	D	61.9 ± 5.4	78.8 ± 6.0	83.8 ± 7.0	Ba18
254	HERMESJ003824−433705	HELAISS02	Ca14	00:38:24	−43:37:05.00	B	D	D	115.0 ± 6.0	124.0 ± 6.0	108.0 ± 6.0	Bu15
255	HELMSJ005258.6+061319	HELMS10	Na16	00:52:59	+06:13:19.00	C	D	D	88.0 ± 6.0	129.0 ± 6.0	155.0 ± 7.0	Na16
256	HERSJ010911.7−011733	HERS9	Na16	01:09:12	−01:17:33.00	D	–	D	393.0 ± 8.0	220.0 ± 8.0	118.0 ± 9.0	Na16
257	HATLASJ012335.1−314618	HerBS145	Ba18	01:23:35	−31:46:19.00	C	D	D	54.7 ± 6.0	67.4 ± 6.2	86.8 ± 7.7	Ba18
258	HERMESJ021943−052433	HXMM20	Ca14	02:19:43	−05:24:33.00	C	D	D	85.0	79.0	67.0	Ca14
259	HERMESJ022022−015329	HXMM04	Wa13	02:20:22	−01:53:29.00	B	D	D	162.0 ± 7.0	157.0 ± 8.0	125.0 ± 11.0	Bu15
260	HERMESJ022029−064846	HXMM09	Wa13	02:20:29	−06:48:46.00	B	D	D	129.0 ± 7.0	118.0 ± 8.0	85.0 ± 7.0	Bu15
261	HERMESJ022206−070727	HXMM23	Ca14	02:22:06	−07:07:27.00	C	D	D	137.0	108.0	57.0	Ca14
262	HERMESJ022251−032414	HXMM22	Ca14	02:22:51	−03:24:14.00	C	D	D	101.0 ± 6.0	85.0 ± 6.0	61.0 ± 6.0	Bu15
263	HERMESJ022548−041750	HXMM05	Wa13	02:25:48	−04:17:50.00	B	D	D	103.0 ± 7.0	118.0 ± 8.0	97.0 ± 7.0	Bu15
264	HERMESJ043830−541832	HADFS02	Ca14	04:38:30	−54:18:32.00	C	D	D	19.0 ± 6.0	39.0 ± 5.0	52.0 ± 6.0	Bu15
265	HERMESJ044947−525427	HADFS09	Ca14	04:49:47	−52:54:27.00	C	D	D	98.0 ± 6.0	102.0 ± 6.0	72.0 ± 6.0	Bu15
266	HERMESJ045027−524126	HADFS08	Ca14	04:50:27	−52:41:26.00	B	D	D	142.0 ± 6.0	133.0 ± 6.0	90.0 ± 6.0	Bu15
267	HATLASJ083153+014014	–	–	08:31:53	+01:40:14.43	C	D	D	69.8 ± 7.3	93.0 ± 8.1	82.0 ± 8.6	Va16
268	HATLASJ083345+000109	HerBS88	Ba18	08:33:45	+00:01:09.41	D	D	D	71.0 ± 7.6	96.0 ± 8.1	95.9 ± 8.8	Ba18
269	HATLASJ084933+021443	G09-v1.124	Ca14	08:49:33	+02:14:43.14	B	D	D	216.7 ± 7.5	248.5 ± 8.2	208.6 ± 8.6	Ne17
		HerBS8	Ba18									
270	HATLASJ090613.8−010042	HerBS165	Ba18	09:06:14	−01:00:43.00	D	D	D	73.4 ± 7.4	80.2 ± 8.0	84.3 ± 8.7	Ba18
271	HATLASJ091238+020050	–	–	09:12:38	+02:00:49.71	D	–	D	173.2 ± 7.7	140.2 ± 8.2	97.6 ± 9.1	Ma18
272	HATLASJ091454−010357	HerBS142	Ba18	09:14:54	−01:03:57.00	C	D	D	69.0 ± 7.3	72.2 ± 8.1	87.2 ± 8.5	Ba18
273	HERMESJ100057+022014	HCOSMOS02	Ca14	10:00:57	+02:20:13.70	C	D	D	70.0 ± 6.0	85.0 ± 6.0	71.0 ± 6.0	Bu15
		COSBO3										
274	HATLASJ115521−021332	HERBS179		11:55:21	−02:13:32.00	C	D	D	67.3 ± 7.2	84.9 ± 8.1	75.7 ± 8.9	Va16
275	HATLASJ121812.8+011841	HerBS83	Ba18	12:18:13	+01:18:41.67	C	D	D	49.5 ± 7.2	79.7 ± 8.1	94.1 ± 8.8	Ba18
276	HATLASJ122407.4−003247	HerBS161	Ba18	12:24:07	−00:32:47.00	C	D	D	56.5 ± 7.3	75.7 ± 8.1	82.4 ± 8.8	Ba18
277	HATLASJ122459.1−005647	HerBS150	Ba18	12:24:59	−00:56:47.00	C	D	D	53.6 ± 7.2	81.3 ± 8.3	92.0 ± 8.9	Ba18
278	HATLASJ141118−010655	HerBS201	Ba18	14:11:18	−01:06:55.00	C	D	D	52.2 ± 7.2	78.6 ± 8.2	80.5 ± 8.7	Ba18
279	HATLASJ142004+014045	–	–	14:20:04	+01:40:44.73	D	–	D	191.7 ± 7.5	150.1 ± 8.3	65.2 ± 8.7	Ma18
280	HATLASJ222503.7−304847	HerBS166	Ba18	22:25:04	−30:48:48.00	B	D	D	32.4 ± 7.2	50.1 ± 8.5	84.3 ± 10.3	Ba18
		UR085S										
281	HATLASJ232200.0−355622	HerBS118	Ba18	23:22:00	−35:56:22.00	C	D	D	60.0 ± 6.3	84.3 ± 6.6	90.9 ± 7.7	Ba18

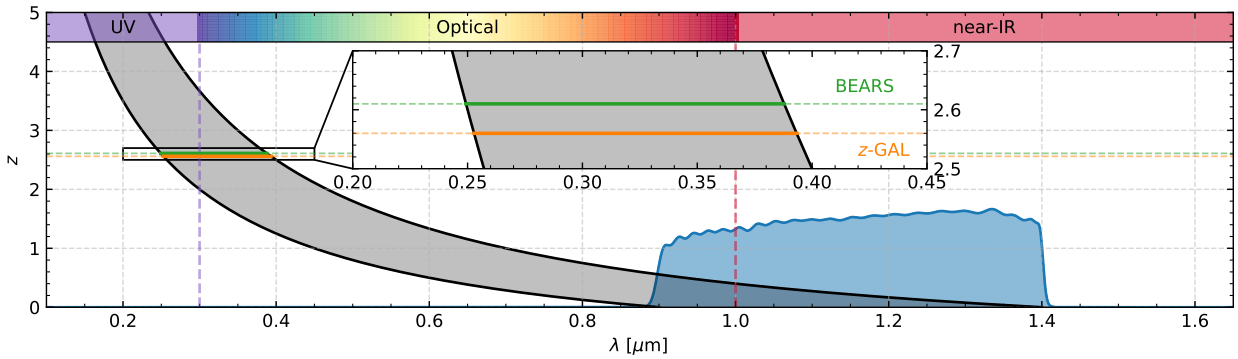

Figure 2.1: F110W wavelength coverage as a function of the redshift. The blue shaded area corresponds to the throughput of the filter, whereas the grey shaded stripe marks its footprint at increasing redshift. The orange and green lines indicate the z-GAL (Cox et al., 2023) and BEARS (Urquhart et al., 2022) median redshifts, respectively.

2.1 Observing setup and data reduction

All the *HST* snapshot proposals share the same observing strategy with short observations of $\sim$4 or $\sim$11 minutes on source performed with the wide-YJ (F110W) filter of the Wide Field Camera 3 (WFC3) IR channel (Dressel, 2022). The F110W filter has a pivot wavelength $\lambda_{\rm p} = 1153.4$ nm and a passband rectangular width of 443.0 nm, corresponding to a wavelength coverage between 883.2 nm and 1412.1 nm. This observing band was chosen to maximise the signal-to-noise ratio (SNR) for short exposures and efficiently covers the stellar emission from the foreground galaxy in the gravitational lensing system, usually an ETG (e.g., Auger et al., 2009).

In Figure 2.1, it is possible to see the wavelength coverage of the F110W filter as a function of the redshift. While locally, the F110W filter observes mostly in the near-IR, at $1 \leq z \leq 2$, it begins to sample the rest-frame optical part of the spectrum. At increasing redshift, the filter starts to cover the UV, thus probing the unobscured star-forming regions and youngest stars.

The IR channel of the WFC3 camera allows the detector to be read out with different samplings while the exposure accumulates. This observing mode is called `MULTIACCUM`, and it allows performing non-destructive consecutive read-outs of the WFC3/IR channel camera sensor during the same exposure. This approach has three advantages over a single read-out: it improves the dynamic range of the combined image, it allows to detection of cosmic rays (CR), and, lastly, it reduces the read-out noise (RON) of the image that quickly becomes a problem for IR observations.

The sampling strategy varies depending on the specific scientific case. Our snapshots were observed using either eight samplings with 10-s sampling intervals linearly spaced between one another (`SPARS10` sampling sequence) or nine samplings with 25-s sampling intervals linearly spaced between one another (`SPARS25` sampling sequence). Due to the filler nature of the snapshot programmes, the total exposure time was defined according to the available time slot. The snapshots were observed using a 4-point sub-pixel dithering pattern. Dithering

Table 2.2: Summary of the observing setup of the *HST* snapshots.

Camera	Filter	Wavelength range [Å]	Sampling sequence	$t_{\rm exp}$ [s]	Number of images	Pixel Size [arcsec]	FOV [arcsec×arcsec]
WFC3 IR	F110W	8832 – 14121	`SPARS10`	251.75	151	0.064	136 × 123
			`SPARS25`	711.74	130		

Notes: Cols. (1), (2), and (3): Camera, filter and central wavelength of the snapshots. Col. (4): Sampling intervals adopted for the read-out. Col. (5): Total exposure time. Col. (6): Number of observed candidates. Col. (7): Pixel scale of the drizzled observations. Col. (8): FOV of the camera.

consists of moving the telescope pointing by angle offsets between individual exposures on the same target. The amplitude of these offsets depends very much on the requirements of the observations. Large offsets, up to ~ 2 arcmin from the target, are commonly used to mosaic regions larger than *HST*/WFC3 FOV. Whereas smaller, sub-pixel offsets are performed to try and compensate for the detector artefacts by averaging them at slightly different positions on the image in order to catch CRs that were missed during the first rejection procedure and to improve the point-spread function (PSF) sampling since the WFC3/IR channel is undersampled of a factor ~ 2. We use the `AstroDrizzle` package (Hoffmann et al., 2021) to perform the following calibrations. For each dithering exposure and `MULTIACCUM` read, the pipeline rejects the pixels falling into the known detector artefacts, and then it removes the bias level and zeroth read exposure from the image. The exposures are corrected for the WFC3/IR channel non-linearity, and the saturated pixels are masked. Lastly, the dark currents are subtracted, and the CRs are removed. At this point, the `MULTIACCUM` read-outs are combined together into the four dithering exposures. Each exposure is then corrected for flat-field and geometric distortion and combined to form the drizzled image.

The resulting drizzled pixel size is 0.064 arcsec, roughly half of the original one. This reduced pixel scale improves the sampling of the PSF by a factor of 2, solving, at least partially, the undersampling. The total exposure times is $t_{\rm exp} = 251.75\,$s (~ 4 min) for the first sampling sequence and $t_{\rm exp} = 711.74\,$s (~ 11 min) for the second one. We report a summary of the observing setup in Table 2.2 and an example of drifted FOV in Figure 2.2.

Corrupted observations

We identify nine targets with corrupted observations, all associated with pointing failures. For eight targets, the observations are compromised by a fault during the guide star tracking during the read-outs. This issue leads to the generation of spurious tracks and blurs the sources, smearing all the relevant spatial information. In Figure 2.3, we show two 30×30 arcsec^2 cutouts, centred on *Herschel* target as an example of corrupted observations. In the first case (left panel), there is a relatively small drift during the read-outs. It is possible to see that the sources are smeared and distorted. In the second case (right panel), the tracking issues are strong enough to blur all spatial information, leaving only tracks corresponding

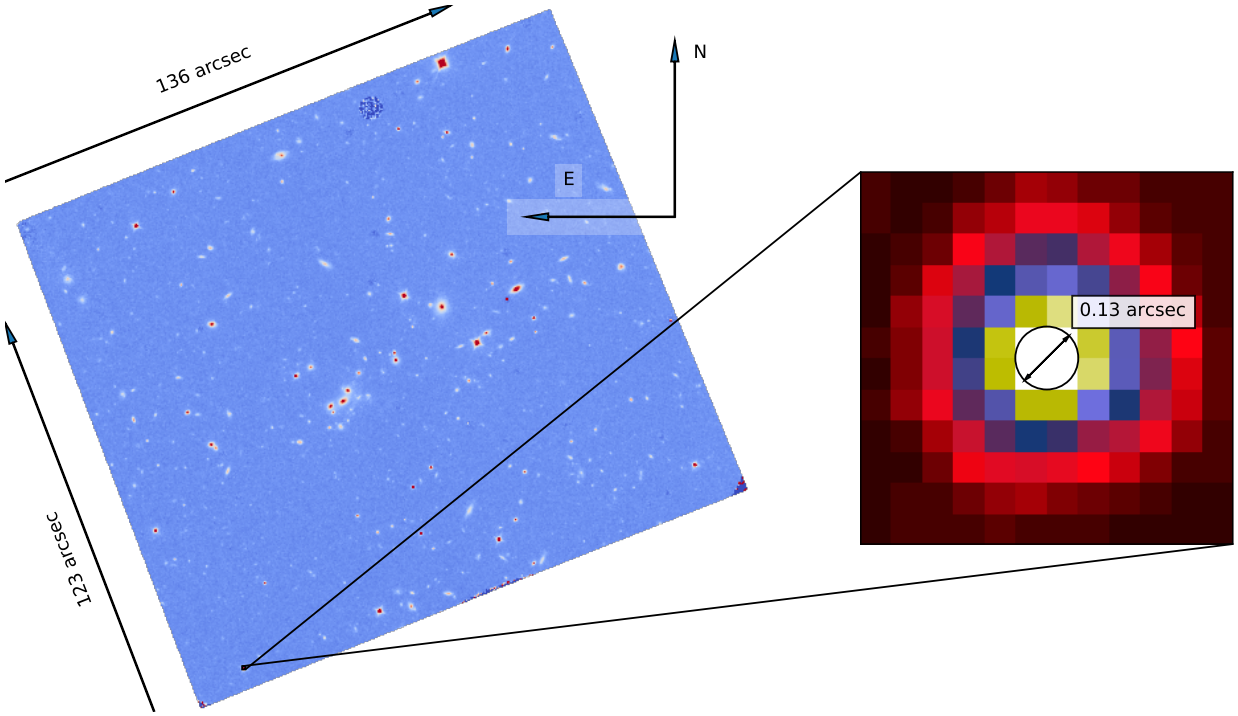

Figure 2.2: *Left panel:* Example of the drizzled *HST* FOV for a snapshot observation. Each image is oriented with the N up and the E left. *Right panel:* Example of an unresolved source where the ~ 0.13 arcsec pre-pixelisation FWHM encompasses two WFC3 pixels.

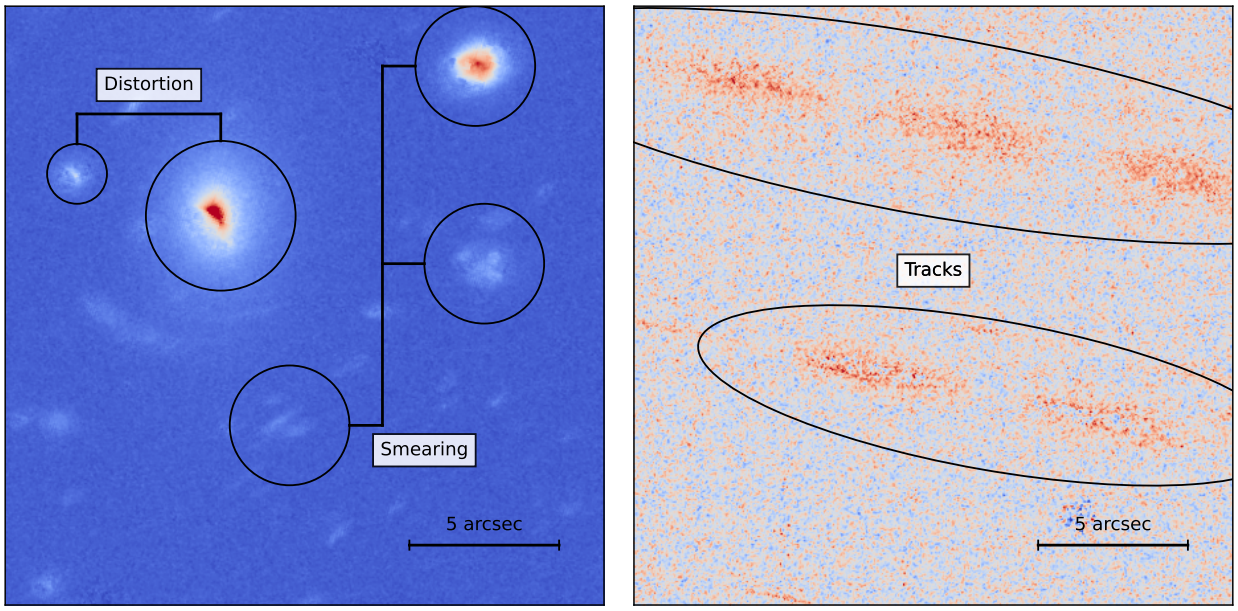

Figure 2.3: Examples of corrupted *HST* data. *Left panel:* Relatively small tracking errors smearing and distorting the sources. *Right panel:* Lrger tracking errors completely erase all the spatial information, leaving only tracks of the path of the bright sources moving through the camera detector.

to the path of the brightest sources that moved through the camera detector during the exposures.

For another target, the observations are affected by a pointing error such that *HST* observed a completely different FOV.

By removing the nine candidates with corrupted data, this sample reduces from 290 to 281 sources.

2.2 Astrometric correction

Accurate astrometry is crucial when comparing the multiwavelength observations of lensed DSFGs. It is not uncommon for these sources to exhibit offsets between the observed lensing features at different parts of the spectrum (e.g., SDP81, Negrello et al., 2010, 2014). This effect arises because multiwavelength observations capture distinct regions of the background source, which are then lensed in different positions onto the image plane.

To register the astrometry of each snapshot, we compare the positions of some reference sources having high astrometric accuracy with the positions of the same sources in the *HST* images. We primarily rely on the *Gaia* Early Data Release 3 (EDR3, Gaia Collaboration et al., 2021) catalogue. When the snapshot FOV has not been observed by *Gaia*, we utilise the *HST* Guide Star Catalog (GSC, Lasker et al., 1990). This is the case for six out of the 281 available snapshots.

To apply the astrometric correction, we follow the subsequent steps. Firstly, we conduct

a cone search centred on the *Herschel* target with a radius of 120 arcsecs to encompass most of the FOV. Reference sources near the image edges are excluded due to higher noise levels and numerous detector artefacts in these regions of the FOV. Next, we verify the position of each reference source, rejecting those for which the *HST* counterpart was close to detector artefacts. For detailed information on the WFC3 IR channel detector artefacts, we refer to Section 5.7.7 of Dressel (2022).

With the cleaned sample of reference sources, we proceed to estimate the centroids of the corresponding *HST* sources. To fit the centroid positions, we use the `Photutils` task `photutils.centroids.centroid_sources`. This task fits a user-defined function that calculates the centroid of a 2D array to a square or rectangular cutout of the image. For the centroid fitting function, we use a 2D Gaussian plus a constant, whereas, for the cutout, we use a box of 41×41 pixel centred on the reference source position projected to the detector footprint. We find that this box size is enough to pick up the reference sources counterparts in most cases. When that is not enough, we manually set a rough estimate for the *HST* centroid position and reran the centroid fitting procedure.

We decide to only account for the positional offset between the reference and their corresponding *HST* sources. Our targets are single galaxies or a few galaxies arranged in compact groups, typically small, having effective radii < 6 arcsec. Typical positional errors for the *Herschel* centroids are of ~ 2.5 arcsec at 5σ (Rigby et al., 2011). These centroids are then used as targets for the *HST* snapshots, implying that the strongly lensed candidates are located at most a few arcseconds from the *HST* pointing. The candidates closeness to the centre of the pointings and their relatively small sizes are such that the errors due to a rigid rotation and/or a distortion remain small with respect to the positional offsets,

After defining the shifts δx_i and δy_i between the i-th reference star and its *HST* counterpart as $\delta x_i = x_{\mathrm{ref,i}} - x_{HST,i}$ and $\delta y_i = y_{\mathrm{ref,i}} - y_{HST,i}$, we estimate the median shifts $\langle \delta x \rangle$ and $\langle \delta y \rangle$ for the snapshots as the middle value of the sorted δx_i and δy_i. We then correct the reference pixel of the image world coordinate system (WCS) for the measured $\langle \delta x \rangle$ and $\langle \delta y \rangle$. In Figure 2.4, it is possible to see an example of the astrometric correction.

Lastly, we measure the average shift length as $l = \sqrt{\langle \delta x \rangle^2 + \langle \delta y \rangle^2}$ and the standard deviation σ_{res} of the residual offsets (defined as $\delta x_{\mathrm{res,i}} = x_{\mathrm{ref,i}} - x_{HST,corr,i}$ and $\delta y_{\mathrm{res,i}} = y_{\mathrm{ref,i}} - y_{HST,corr,i}$) after correcting for median shifts. In Figure 2.5, we show the distribution of the offsets length l and of the ratio l/σ_{res} between the offsets length and the standard deviation of the residual offsets. Most snapshots have σ_{res} within 0.1 and 1 pixel, and, for a given value of σ_{res}, they span roughly two orders of magnitude in the median offsets that range between 0.1 and 10 pixels. High values of both l and l/σ_{res} identify large offsets that would be significant if not accounted for. Low values of l/σ_{res} identify the regions where the scatter of the $\delta x_{\mathrm{res,i}}$ and $\delta y_{\mathrm{res,i}}$ is high and the offset correction is less relevant. It is possible to see that there is an excess of high σ_{res} systems for the highest values of l. These are such that the ratio l/σ_{res} is close to 1, and the offsets may not be highly significant.

The number of reference sources available for the astrometric correction ranges between one and 17, with $\sim 68\%$ of the snapshots having between 3 and 7 reference sources. The median number of reference sources for the sample is 5 per snapshot.

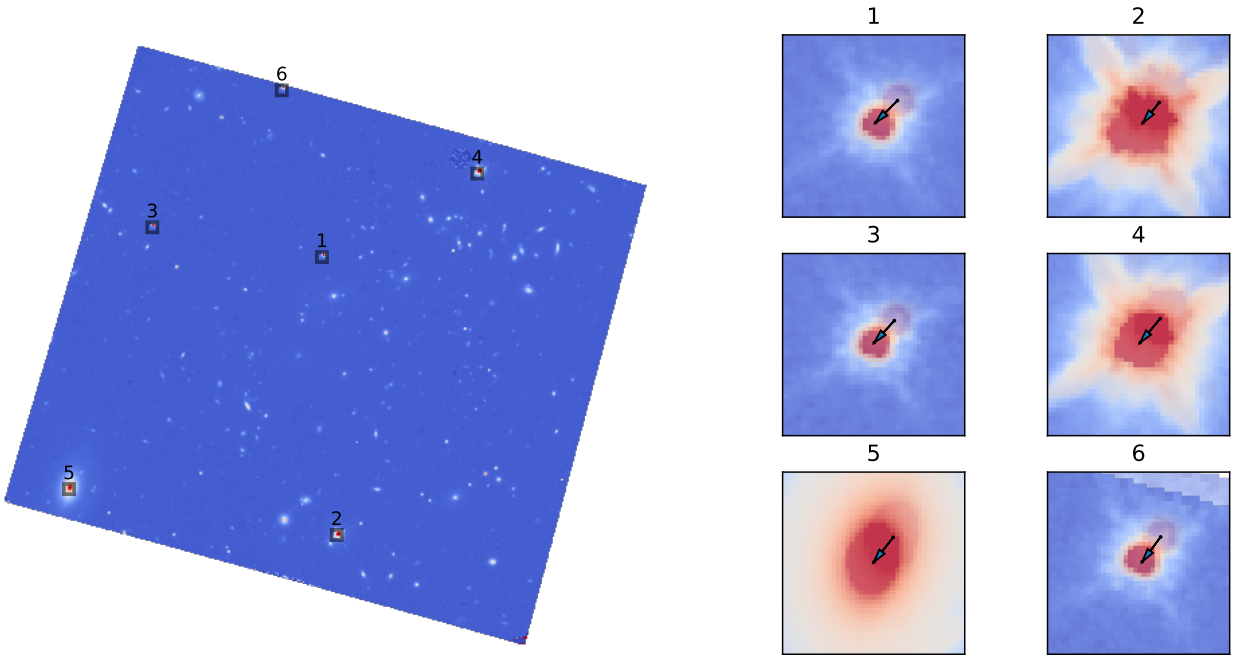

Figure 2.4: *Left panel:* FOV of the snapshot before updating the astrometry. The numbered black squares correspond to the 41×41 pixels boxes we used to fit the *HST* sources. *Right panels:* Zoom in on the boxes plotted in the left panel. In each zoom, we show the snapshot before and after updating the astrometry. An arrow connects the position of the *HST* counterpart before the correction with the position of the reference source.

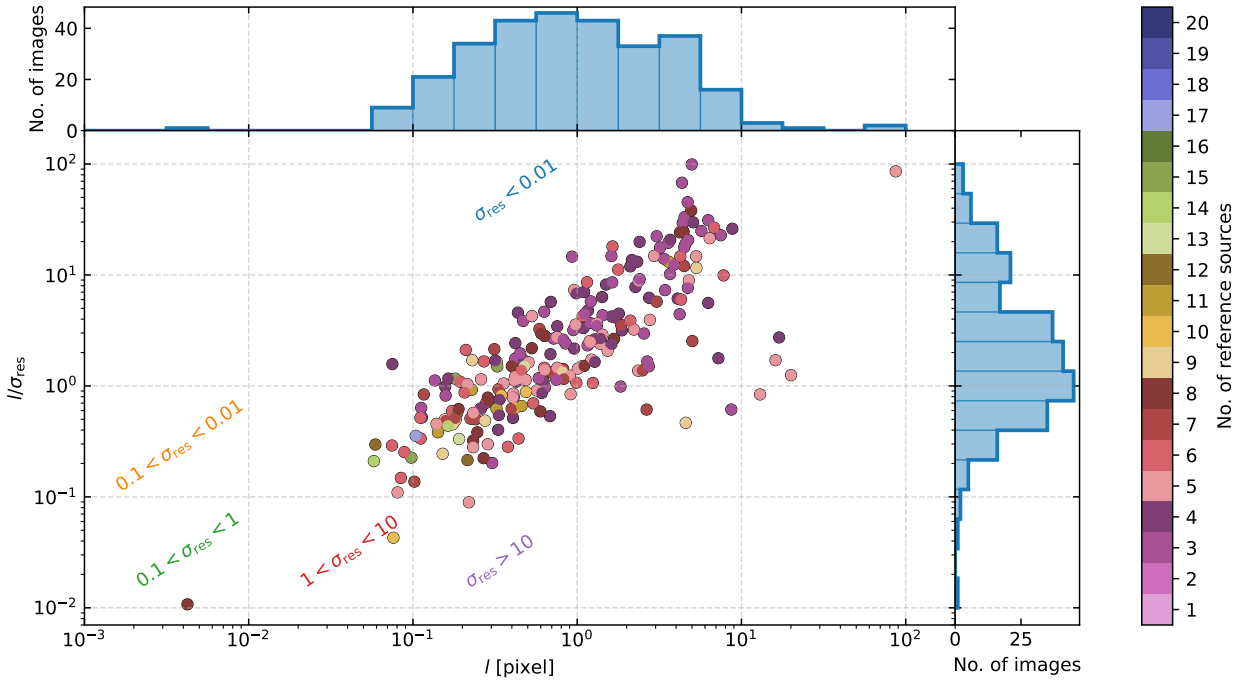

Figure 2.5: Ratio l/σ_{res} between the offset length and standard deviation of the residual offsets as a function of the offset length l. The colour of the markers corresponds to the number of reference sources. The coloured diagonal stripes identify the regions with $\sigma_{\mathrm{res}} > 10$ pixel (purple), $1 < \sigma_{\mathrm{res}} < 10$ pixel (red), $0.1 < \sigma_{\mathrm{res}} < 1$ pixel (green), $0.01 < \sigma_{\mathrm{res}} < 0.1$ pixel (orange), and $\sigma_{\mathrm{res}} < 0.01$ pixel (blue), respectively. The panels on the top and on the right show the distribution of l and l/σ_{res}, respectively.

2.3 Depth of the observations

With the reduced snapshots and corrected astrometry, we proceed to estimate the depth of our observations. We define that as the magnitude corresponding to a point source with a flux density equal to five times the total rms due to the sky and instrumental noise. These depths will be significant to give an upper limit to the flux density of candidate lensed DSFGs that remain undetected in the *HST* images.

We perform aperture photometry on randomly selected positions within the images. We estimate the rms as the standard deviation of the aperture flux density distribution obtained from this process. To avoid contamination from the sources in the images, we sigma-clipped the aperture flux density distributions before computing the rms. For the flux measurements, we adopted circular apertures of ~ 0.25 arcsec of diameter (~ 2 the FWHM of the PSF). Initially, we remove part of the edges of the images through a binary erosion with a square 10×10 pixels kernel to avoid including the noisier borders. We tile each FOV with the circular apertures separated by at least 1 pixel to prevent overlap. Then, we derive the aperture flux density in counts.

The aperture flux density distribution still includes apertures containing counts produced by the image sources. These create a tail of higher value counts on the aperture flux density distribution. For this reason, we sigma-clip the flux density distribution at 2.5σ. We use the biweight location and the standard deviation measured from the median absolute deviation (MAD) to approximate the central location and scale of the aperture flux density distribution, respectively. We define the standard deviation as $\sigma_{\rm Gauss} = {\rm MAD}/\Phi^{-1}(3/4)$, where $1/\Phi^{-1}(3/4) \approx 1.4826$ is the normal inverse cumulative distribution function evaluated at a probability of 3/4. Both the biweight location and standard deviation measured from the MAD are available in the `astropy.stats` package through the `astropy.stats.biweight_location` and `astropy.stats.mad_std` tasks, respectively.

For all but a few cases, the observed distributions are reasonably well reproduced by a Gaussian, meaning that our estimates for the rms are robust. The remaining cases show a bimodal flux density distribution. By visually inspecting the images, it is possible to see that the background level changes across the FOV (Figure 2.6, left panel). The regions with a lower/higher background level produce the left/right peak in the aperture flux distribution. In these cases, we adopted the rms of the background corresponding to the lens candidate location. This rms estimate was obtained after masking the regions producing the other peak in the background flux density distribution.

Finally, we convert the $5\,rms$ from counts to magnitudes by using the following:

$$m_{5\,rms} = -2.5\log_{10}\left(\frac{5\,rms\ [\rm counts]}{t_{\rm exp}\ [\rm s]}\right) - AB_{\rm zpt}\ [\rm mag]. \tag{2.1}$$

where $AB_{\rm zpt}$ is the AB magnitude system zeropoint that is calculated following Dressel (2022) with:

$$AB_{\rm zpt} = -2.5\log_{10}(photflam) - 5\log_{10}(photplam) + 18.692 + phot_{\rm zpt},$$

where $photflam = 1.5\,10^{-20}$ is the inverse sensitivity in units of ergs cm^{-2} Å^{-1} e^{-1}, $photplam = 11534.5$ is the pivot wavelength in Å, and $phot_{\rm zpt} = -21.1$ mag is the standard magnitude zeropoint.

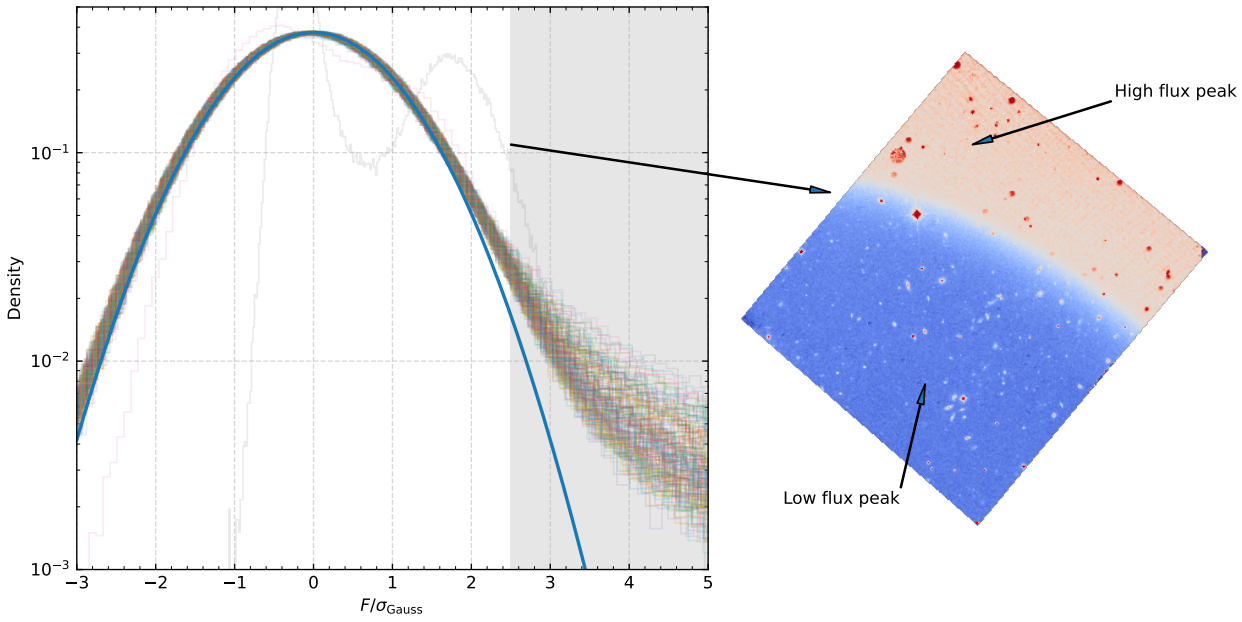

Figure 2.6: *Left panel:* Aperture flux density distributions scaled to the same location and size and normalised to unity. On top of the rescaled flux distributions, we plot the Gaussian with scale $\sigma_{\mathrm{Gauss}} = 1$ and location $\langle F \rangle = 0$ that corresponds to the measured scale and location in blue. The grey-shaded region corresponds to the part of the flux distributions that was sigma-clipped. *Right panel:* Example of snapshot observation that displays a bimodal flux distribution (grey line on the left panel).

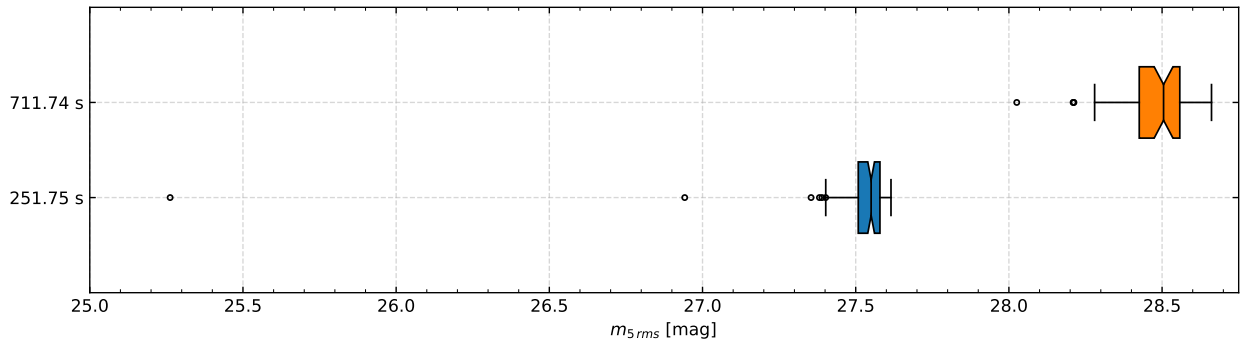

Figure 2.7: Distribution of the $m_{5\,\mathrm{rms}}$ depths for the two exposure times. The notch corresponds to the median of the distribution. The box edges define the 1st and 3rd quartiles, $Q1$ and $Q3$, respectively. The whiskers extend from the box edges to 1.5 in the inter-quartile range $Q3 - Q1$. The remaining outliers are plotted as empty dots.

In Figure 2.7 we show the distribution of the 5σ depth for the first exposure time ($t_{\mathrm{exp}} = 251.75\,\mathrm{s}$) in blue and for the second ($t_{\mathrm{exp}} = 711.74\,\mathrm{s}$) in orange. We find an average $\langle m_{5\,\mathrm{rms},1} \rangle = 27.55\,\mathrm{mag}$ and $\langle m_{5\,rms,2} \rangle = 28.50\,\mathrm{mag}$ for the two exposure times, respectively.

Chapter 3

Lens classification

With a sample of strongly lensed candidates and high-resolution follow-up observations, it is necessary to find a way of distinguishing the clear lensing systems from the uncertain and the unlensed ones. While this process is straightforward in the sub-mm where these candidates are selected, it is more difficult in the near-IR, where the contamination of other sources is very high. In this chapter, we will present the classification methods we applied to the sample candidates. In Section 3.1, we define a first lens classification based on a visual inspection of the *HST* data. Then, in Section 3.2, we present a second complementary lens classification performed on available high-resolution sub-mm observations. For the two classifications, we detail a few possible statistical properties, mainly related to each class *Herschel* flux density distribution and colours. Lastly, we will combine the two lens classifications in the chapter summary, presented in Section 3.3.

As already stated in Chapter 2, to deal with *Herschel*'s low ($\sim$ 18 arcsec at 250 μm) angular resolution, it is necessary to couple the candidate selection with some follow-up observations. One possibility is relying on higher angular resolution observations. In this way, it is possible to identify the characteristic features of strong lensing by simply looking at the morphology of the candidate.

As a consequence of the fact that the lenses and background sources are located at very different redshifts, observing in a given band would correspond to two, possibly very different, rest-frame regions of the spectrum. This raises the question of the choice of which kind of high-resolution follow-up observations. By observing in the sub-mm/mm, one would easily detect the background source without worrying about the lens, which is usually much fainter. This comes at the cost of not being able to characterise the optical properties of the lenses and background sources. On the other hand, observing in the optical/near-IR will allow the detection of the lens and usually very faint lensing features, which, in combination with the *Herschel*/SPIRE detection, will make a robust case for the lensing nature of the candidate.

A different approach would be that of obtaining spectroscopic observations for both the lens and background source, allowing them to measure their redshifts and confirming that they are at different distances along the same line of sight. One caveat is that one needs to be sure that the different redshifts correspond to the lensing system and not to unrelated objects, which are aligned by coincidence. The best way to classify and confirm these candi-

dates is to combine high-resolution optical/near-IR imaging with sub-mm/mm imaging and spectroscopy.

In previous works focusing on lensed DSFGs, the confirmation procedure was also required to assign the candidates a qualitative classification to quantify the likelihood of being lensed systems. Bussmann et al. (2013) combined high-resolution imaging in the near-IR and sub-mm with optical spectroscopy to classify 30 *Herschel* strongly-lensed candidates. The candidates showing an evident lens morphology in the *SMA* data and different redshifts for the lens and background source were confirmed to be strongly lensed and assigned to 'class A'. The candidates with an evident lens morphology in the *SMA* data but only a single redshift measurement for either the lens or background source were classified as 'class B'. Instead, the 'class C' candidates showed evidence for moderate lensing from the *SMA* map and different lens and source redshifts. Lastly, the authors grouped in a 'class X' all the candidates for which they found no concluding evidence of strong lensing.

The Bussmann et al. (2013) classification was adapted and expanded in Calanog et al. (2014), which defined 12 classes based on the combination of the observed high-resolution near-IR morphology and availability of redshifts. The latter was coded with a number ranging from 1 to 4 corresponding to the availability of the redshift for both the lens and background source (class 1), for the background source alone (class 2), for the lens alone (class 3), and for neither of them (class 4).

Bussmann et al. (2015) redefined their three original classes as A, C, and X. Differently from Bussmann et al. (2013), these classes were quantitatively defined, taking into account the results of the lens modelling.

Later on, Negrello et al. (2017) defined a system of four classes ranging from A to D. The authors combined the 'class B' and 'class C' used by Bussmann et al. (2013) into a new 'class B', renamed the 'class X' to 'class C', and added a 'class D' for the unlensed systems. The classes were defined as follows. The confirmed lensing systems of class A needed the detection of multiple images or arcs with *HST*/*Keck*/*SMA* and/or the presence of spectroscopic redshifts for both the lens and background source. The candidates likely to be lensed were identified based on the difference in redshift between the optical/near-IR identification and sub-mm detection, with at least one of the two redshifts being photometric. They were included in the B class. The unclear candidates were classified as C due to the lack of a reliable optical/near-IR counterpart, and, lastly, the D class included candidates confirmed to be unlensed.

3.1 *HST* data and visual lens classification

In this work, the primary source of high-resolution follow-up observations we adopt to assess the nature of the candidate lenses is the *HST* snapshot programmes presented in Chapter 2. We define a system of four classes, following the classification of Negrello et al. (2017), although we consider only the morphological properties of the candidate lens and background source and not the availability of their redshifts. The classes are defined as follows:

- Class A: the systems are confirmed as lensed by the presence of a multiply-imaged background source.

- Class B: the systems are likely to be lensed due to the presence of a possible lens and, in some cases, lensing features that are faint or heavily blended with the lens itself.
- Class C: the systems do not show a good candidate for the lens or background source.
- Class D: the systems are confirmed to be unlensed.

To allocate all 281 candidates to the four classes, we proceed by first carrying out a visual inspection of the *HST* data alone around the *Herschel*/SPIRE centroids. This lens classification defines what we will refer to as the 'visual lens classification'. In order to account for the low angular resolution of *Herschel*, we limited the analysis to a circular area of $\sim$ 20 arcsec in diameter (roughly equivalent to the *Herschel*/SPIRE beam at 250 μm) centred on the candidate centroid. This classification is the result of the visual inspections independently performed by E. Borsato, L. Marchetti, and M. Negrello.

The class A candidates

The *HST* image shows a near-IR object located close to the position of the *Herschel* detection with multiple images visible around it. In the case of galaxy-scale lenses, the lensing features consist of pairs of compact lensed images, arcs and compact images, multiple arcs, and rings. The complexity of these features increases significantly alongside that of the lenses, with group-scale systems producing more images with weirder configurations than their single-lens equivalents. The identification of the lens candidates is sometimes complicated by the number of near-IR sources that fall within the *Herschel*/SPIRE beam. For this reason, we consider all objects falling roughly within the observed lensing features as contributing to the lensing. In Figure 3.1, we show a representative subsample of the systems classified as A. The SNR of both the lens and lensing features varies significantly.

The class B candidates

A single galaxy or a group of galaxies is visible close to the position of the *Herschel* centroid, but there is no clear detection of multiple images. Hence, this class tags objects that are likely to be a lens, but the background source is too faint to be detected in the relatively shallow *HST* data. In Figure 3.2, we show a representative subsample of the systems classified as B.

The class C candidates

We can not detect any convincing lens or background source in the *HST* image. These candidates are likely to be either high-z unlensed DSFGs, lensing events where the lens is either at high redshift or has an intrinsically low luminosity, or both. We do not interpret the absence of a clear detection *HST* lens or background source as strong evidence of them being unlensed. Instead, they consist of the uncertain cases where *HST* and *Herschel* alone are insufficient to ascertain their nature. In Figure 3.3, we show a representative subsample of the systems classified as C.

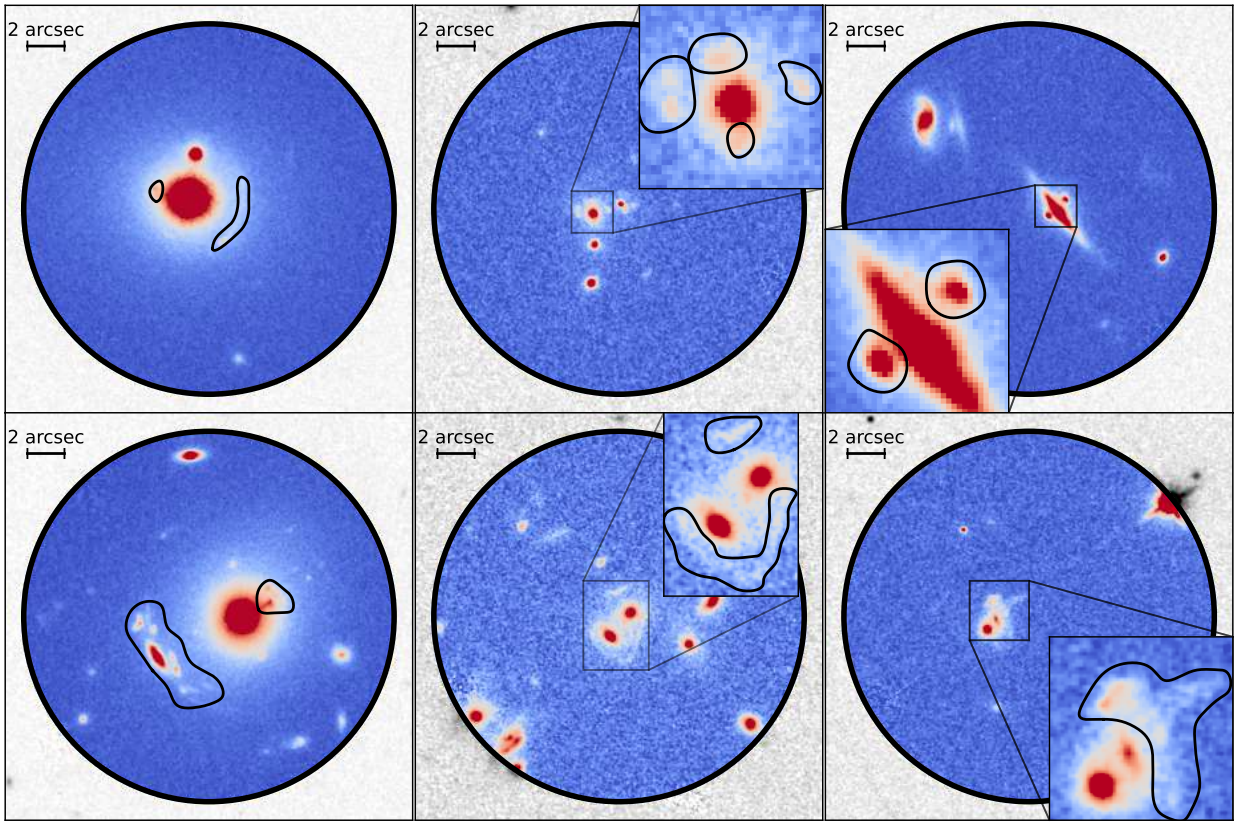

Figure 3.1: Six examples of strongly lensed candidates, which we visually classified as A. The black circle is centred on the *Herschel*/SPIRE centroid and has a diameter equal to ~ 20 arcsec (roughly corresponding to the beam FWHM at $250\,\mu$m). The thick black lines in the panels and zoomed insets highlight the lensing features used to confirm the candidates.

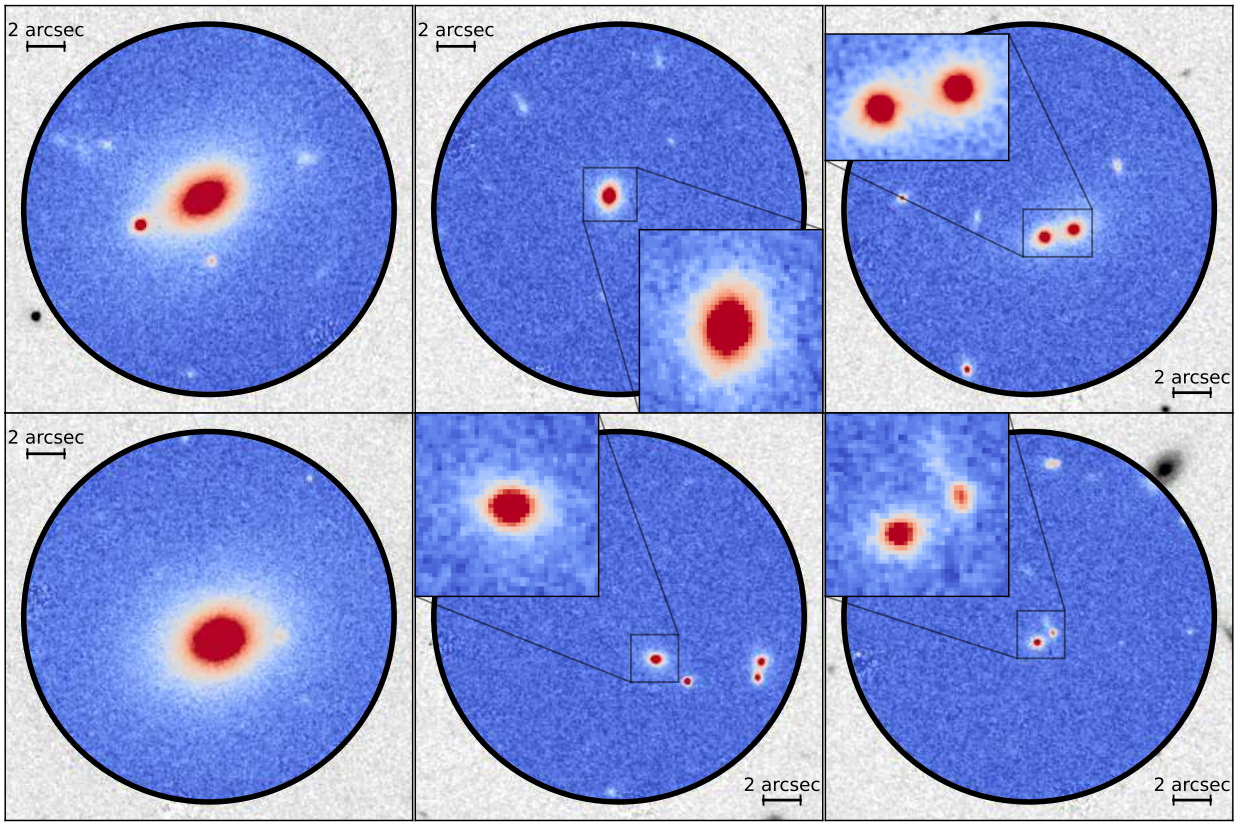

Figure 3.2: Six examples of strongly lensed candidates, which we visually classified as B. The black circle is centred on the *Herschel*/SPIRE centroid and has a diameter equal to $\sim$ 20 arcsec (roughly corresponding to the beam FWHM at 250 μm).

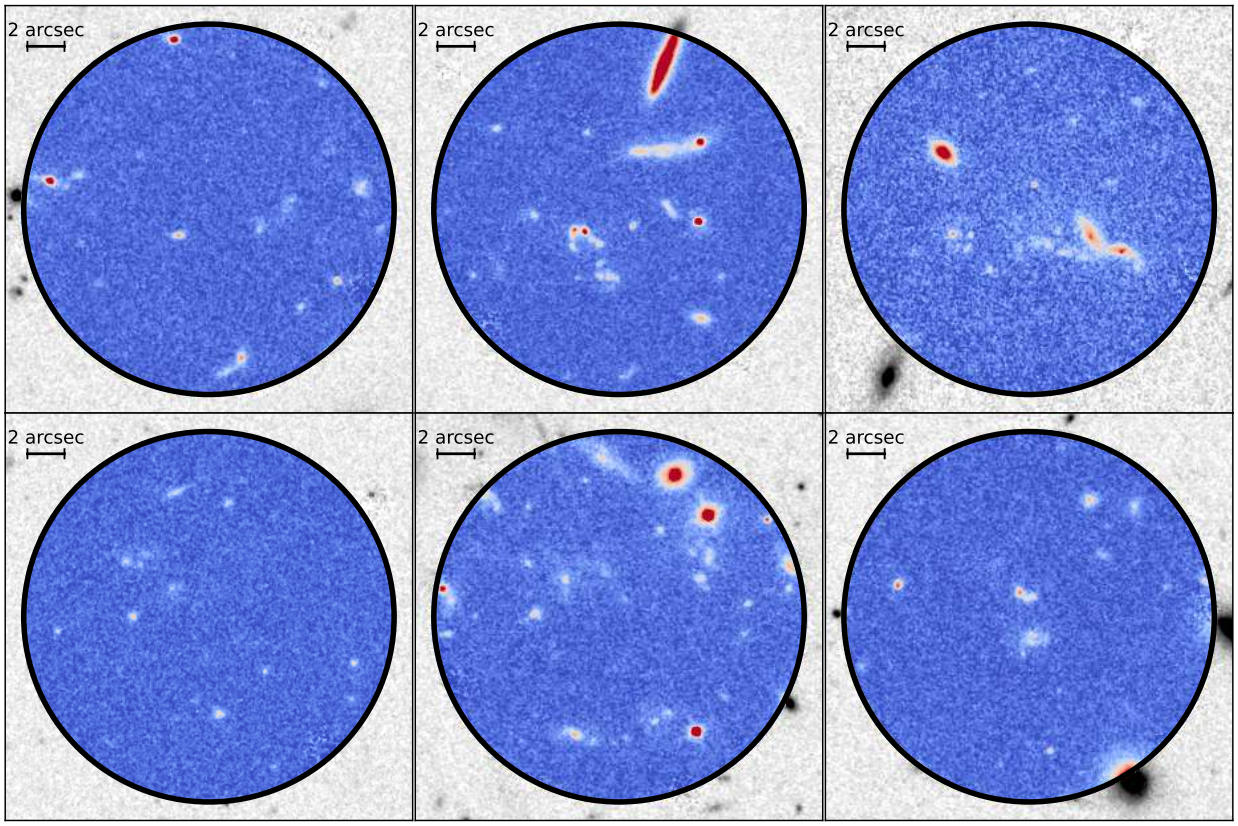

Figure 3.3: six examples of strongly lensed candidates, which we visually classified as C. The black circle is centred on the *Herschel*/SPIRE centroid and has a diameter equal to $\sim$ 20 arcsec (roughly corresponding to the beam FWHM at 250 μm).

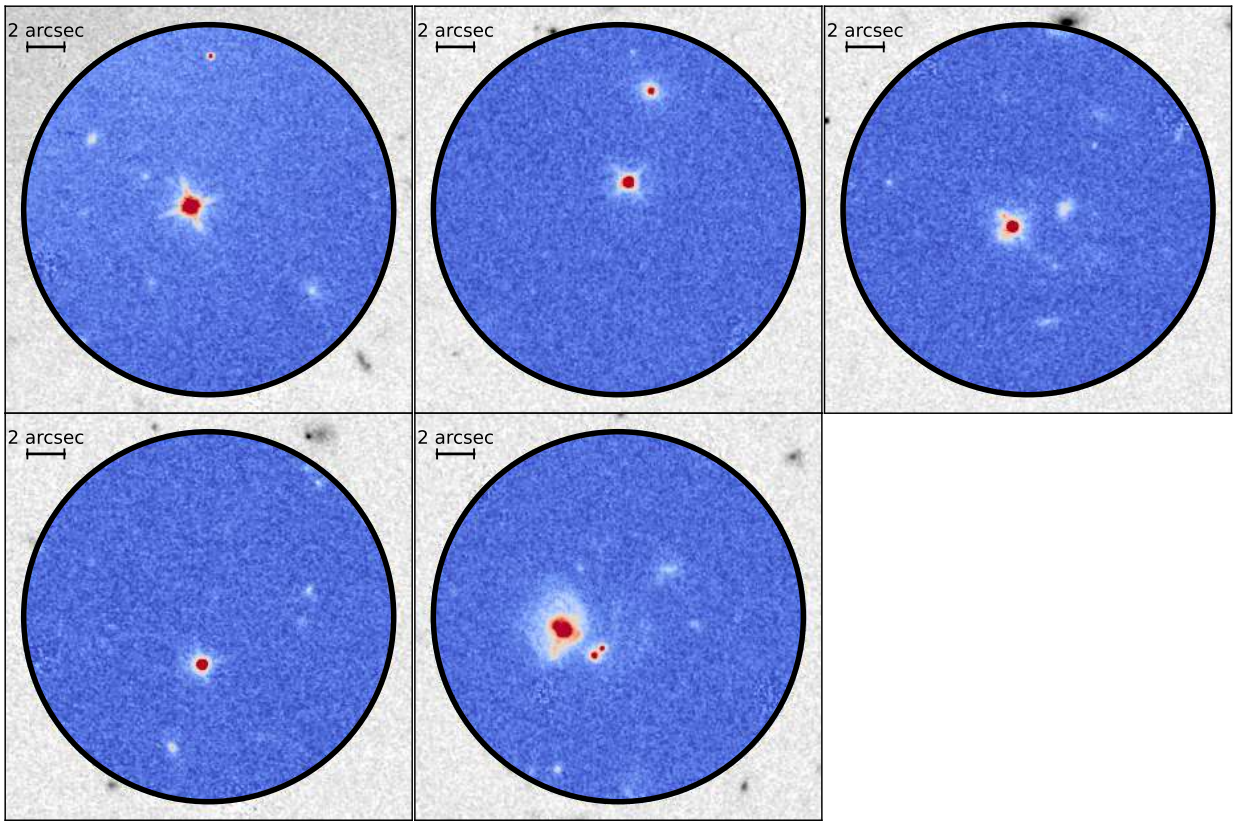

Figure 3.4: Five examples of strongly lensed candidates, which we visually classified as D. The black circle is centred on the *Herschel*/SPIRE centroid and has a diameter equal to ~ 20 arcsec (roughly corresponding to the beam FWHM at $250\,\mu$m).

The class D candidates

The source is a contaminant, e.g., a dusty star, an unlensed QSO, or a low redshift, sub-mm bright, spiral galaxy (previously misinterpreted as a lens candidate). At this stage, we use the *HST* source morphology alone to identify contaminants. For example, a single point-like source would have minimal image separations $\ll 0.1$ arcsec if it was associated with a lensing event, implying extremely small Einstein radii unlikely for typical galaxy-scale or group-scale strong lenses. In Figure 3.4, we show a representative subsample of the systems classified as D.

3.1.1 Results

Based on this simple visual analysis, we could assign 25 objects to class A, 105 to class B, 146 to class C, and 5 to class D. In Table 2.1, we report the visual lens classification of the strongly lensed candidates.

Due to the uneven coverage of the *HST* follow-up programmes, it is impossible to drive a conclusive statistical analysis on either the absolute number density of the lensed galaxies

above a certain flux density limit at 500 μm or the effectiveness of the *HST* lens searches. Hence, we only present and discuss the comparison of the occurrences of the different classes as a function of the flux density for our incomplete sample. We note that, as a consequence of the preliminary nature of the H-ATLAS catalogues used in Negrello et al. (2014), several systems ended up having $S_{500} < 80$ mJy in the final release of the H-ATLAS catalogues (Valiante et al., 2016; Maddox et al., 2018). We adopt the revised S_{500} values for the lens candidates.

In the bottom panel of Figure 3.5, we show the candidate flux density distribution at 500 μm as a function of the visual lens classification. The sample has a median flux density of $\langle S_{500} \rangle = 94.3$ mJy with half of the candidates having flux densities between $83.3 < S_{500} < 115.4$ mJy. In addition to the high flux density tail (that extends to ~ 700 mJy), there is a significant number of fainter flux density candidates ($S_{500} < 80$ mJy) caused mostly by the HerMES follow-up scheme. We include all the HerMES candidates for two reasons. Firstly, classifying all the candidates makes more simple possibile follow-up studies. Secondly, the different HerMES fields, although covering a small FOV, have many multi-wavelength observations making the fainter targets easier to confirm as lensed. Moreover, due to the incomplete coverage of the *HST* snapshots, trimming the sample by a homogeneous flux density cut would not significantly improve its completeness. As it can be seen from the top panel in Figure 3.5, the fraction of confirmed strong lenses increases as a function of the flux density, consistently with the expectations from the population models (e.g. Negrello et al., 2010, 2017; Wardlow et al., 2013). Below $S_{500} \simeq 300$ mJy, the B candidates and then the C candidates dominate the distribution. Interestingly, there is a significant fraction of C candidates above $S_{500} \simeq 100$ mJy, which could be due to either an excess of intrinsically bright unlensed DSFGs or the presence of a population of *HST*-faint or even *HST*-dark lenses, or a combination of the two.

The *Herschel*/SPIRE flux density ratios can be used as a proxy for the redshift. If we now look at the S_{250}/S_{350}, and S_{350}/S_{500} flux density ratios (Figure 3.6), we can see that the A candidates form a tight distribution, with most of the systems having SEDs peaking at 350 μm. This should be the case for galaxies with bright S_{500} flux densities, which are expected to be located at $1 < z < 4$ and potentially lensed (González-Nuevo et al., 2012). We note that the C and D systems tend to spread over a wider range of flux density ratios than the others, in line with them being mostly contaminants with a varying range of intrinsic properties. For reference, we plot the redshift track of the far-IR SED model of Pearson et al. (2013).

This template includes two Planck functions corresponding to two different dust temperatures:

$$S_\nu = A\big(B_\nu(T_\mathrm{h})\nu^\beta + a \cdot B_\nu(T_\mathrm{c})\nu^\beta\big), \tag{3.1}$$

where A is a normalisation factor, $B_\nu(T_\mathrm{h})$ and $B_\nu(T_\mathrm{c})$ are the hot and cold dust Planck functions, respectively, β is the dust emissivity index, and a is the cold-to-hot dust mass ratio. For the temperatures, dust emissivity index, and cold-to-hot dust mass ratio, we use the best fitting results obtained by Pearson et al. (2013) of $T_\mathrm{c} = 30$ K, $T_\mathrm{h} = 50$ K, $\beta = 2$, and $a = 30.1$. These parameters were measured for a sample of 40 H-ATLAS sources with measured spectroscopic redshifts between $0.5 < z < 4.2$.

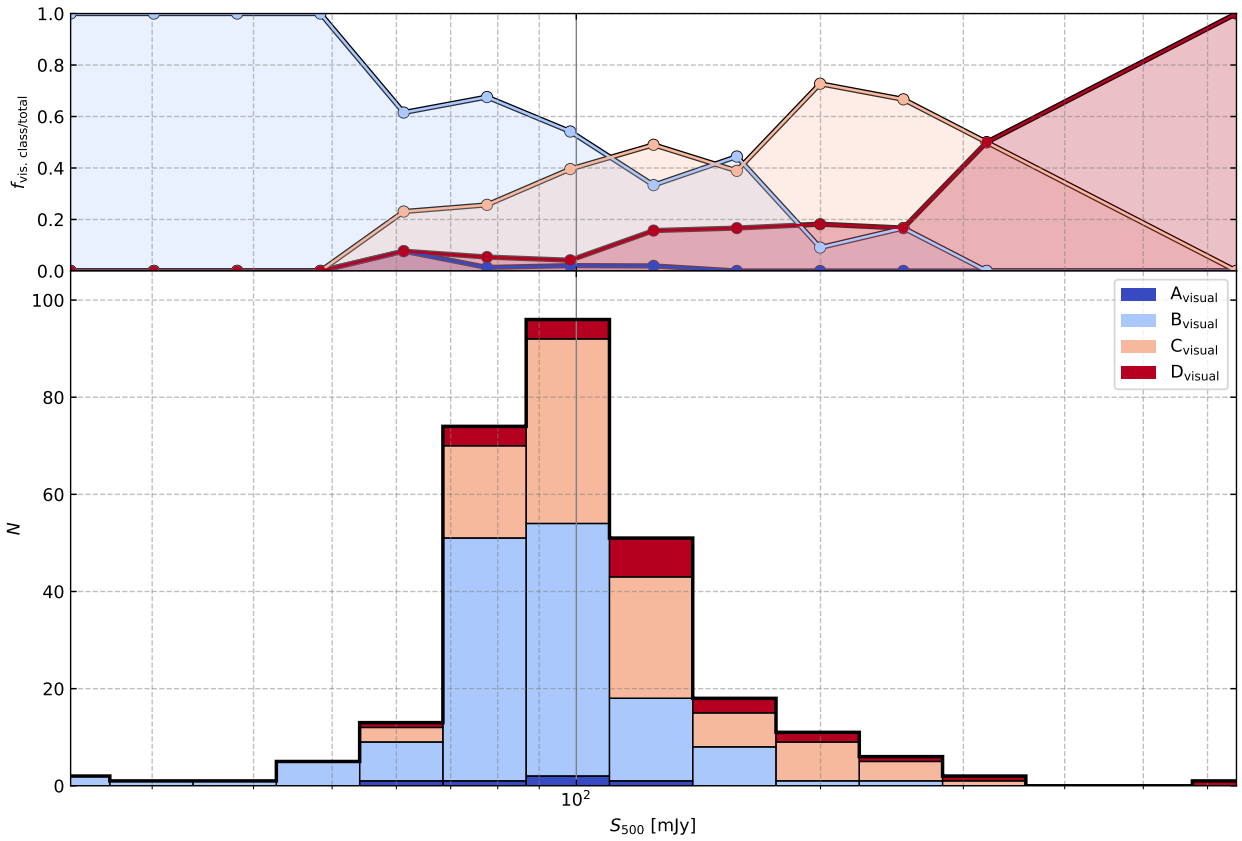

Figure 3.5: *Bottom panel:* Distribution of the background sources flux density at 500 μm as a function of the visual lens classification. *Top panel:* Fraction of candidates that fall into the bins used to compute the flux density distribution.

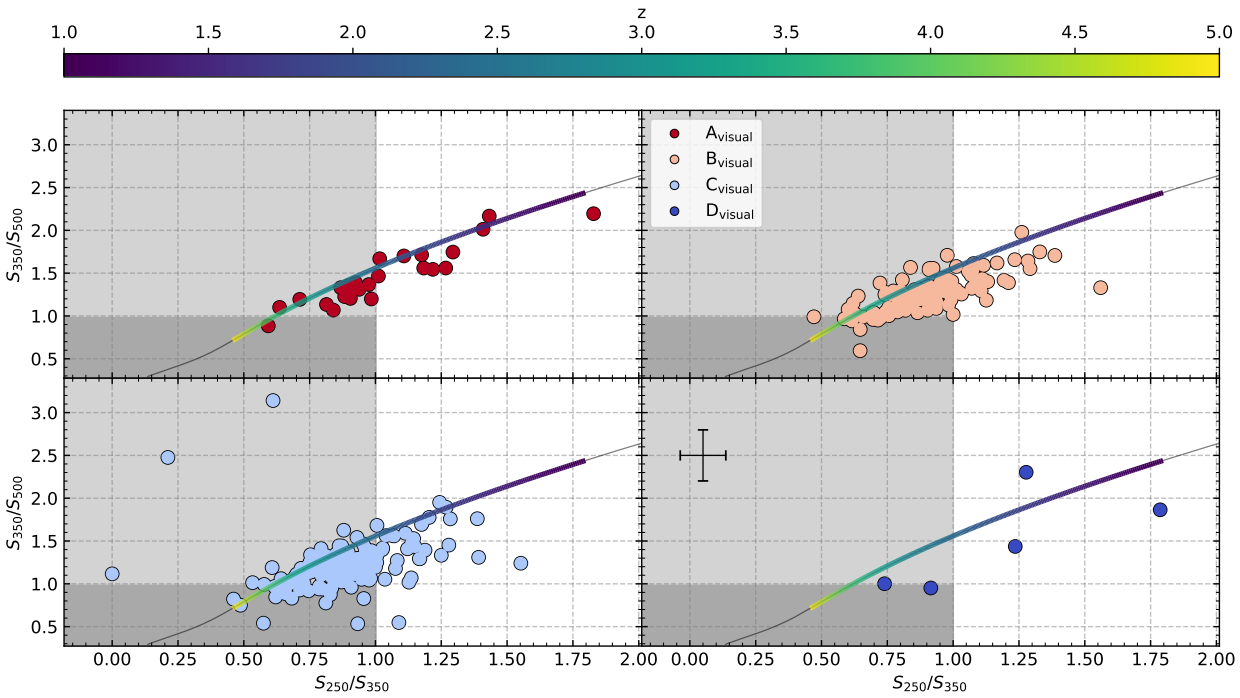

Figure 3.6: Distribution of the S_{250}/S_{350} and S_{350}/S_{500} flux density ratios of the background sources. Each panel corresponds to a different class in the visual classification, with the A, B, C, and D candidates colour-coded in red, pink, light blue, and blue, respectively. We overplot to the observed flux density ratio distributions the redshift track of the SED by Pearson et al. (2013). The redshift track is colour-coded as a function of the redshift. The light grey and grey shaded areas correspond to different SEDs peaking at 350 μm and 500 μm, respectively. The cross plotted in the bottom left panel corresponds to the mean measurement errors.

In the following, we plot the *HST* snapshot cutouts that we use for the classification of the candidate lenses. We show the candidates classified as A, B, C, and D in Figure 3.7, Figure 3.8, Figure 3.9, and Figure 3.10, respectively.

3.2 Sub-mm/mm data and lens classification

As a second step for the lens classification, we analyse archival high-angular resolution data in the sub-mm/mm to look for evidence of multiple images and arcs. We use archival *ALMA*, *SMA*, and *NOEMA* high-resolution multiwavelength observations for 77 systems and include them in our analysis. For the *ALMA* data, we download the Stokes I continuum images from the science archive[1]. For the *SMA* data, we either use the reduced continuum images from Enia et al. (2018), or we download the UV tables from the science archive[2] and we produce the continuum images with the Common Astronomy Software Applications[3] (`CASA`) software. HerBS-89a is the only source for which we use *NOEMA* data. The details of the data reduction are available in Neri et al. (2020, ; but see Berta et al. 2021 for a detailed study of this galaxy). These multiwavelength observations have an angular resolution ranging from 1.5 to 0.03 arcsec for *ALMA*, 0.5 arcsec for *SMA*, and 0.3 arcsec for *NOEMA*. We found that lower-resolution observations (> 2 arcsec) fail to effectively separate the lensing features and so are not generally useful for our morphological classifications. In Table 3.1, we summarise the observing setup of all the multiwavelength observations used in this lens classification.

The A and D classes defined in the visual lens classification are revised as follows.

- Class A: the candidates confirmed as lensed by the presence of a multiply imaged background source in *either the HST or multiwavelength follow-up*.
- Class D: the candidates confirmed as unlensed systems by the *either the HST or multiwavelength follow-up*.

Updating the lens classification results in visual B and C candidates moving to either the A or D classes. For 11 candidates, the multiwavelength follow-up observations are insufficient to address their nature. In these cases, the class remains unaltered.

Before visually classifying the multiwavelength follow-up observations, we build an SNR map of the interferometric observations. To do so, we compute a noise map by measuring the standard deviation in 5×5 pixels regions centred in each pixel of the continuum image. We mask the peaks in the noise map corresponding to ~ 10 times the standard deviation as they correspond to the source emission. These peaks are then replaced with values sampled from their neighbouring regions. We apply a similar procedure to measure the image background, in which case, we use the data instead of its standard deviation in the first two steps of the procedure. We calculate the SNR map by subtracting the background map from the data and dividing the residuals by the background noise map. In Figure 3.11, we show the sub-mm/mm SNR contours superimposed to the *HST* images for a representative subsample of the targets.

[1] https://almascience.eso.org/aq/?result_view=observations.
[2] https://lweb.cfa.harvard.edu/cgi-bin/sma/smaarch.pl.
[3] https://casa.nrao.edu/.

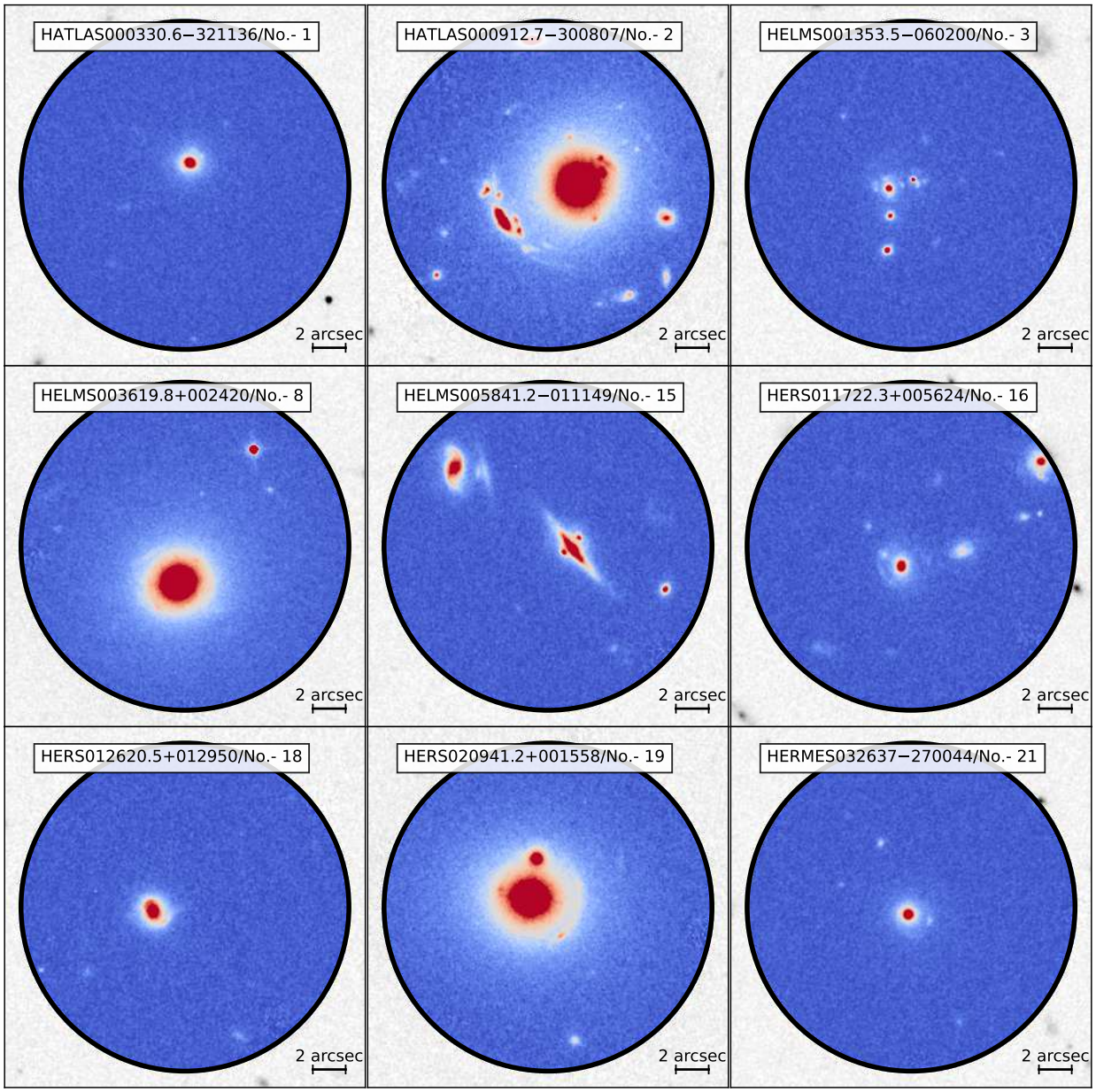

Figure 3.7: 22×22 arcsec^2 cutouts of the strongly lensed candidates classified as A. The black circle is centred on the *Herschel*/SPIRE centroid and has a diameter equal to ~ 20 arcsec ($\sim$ FWHM). All the panels share the same colour bar extending from -20 ADU, corresponding to blue, to 100 ADU in white, and then from white to red at 500 ADU.

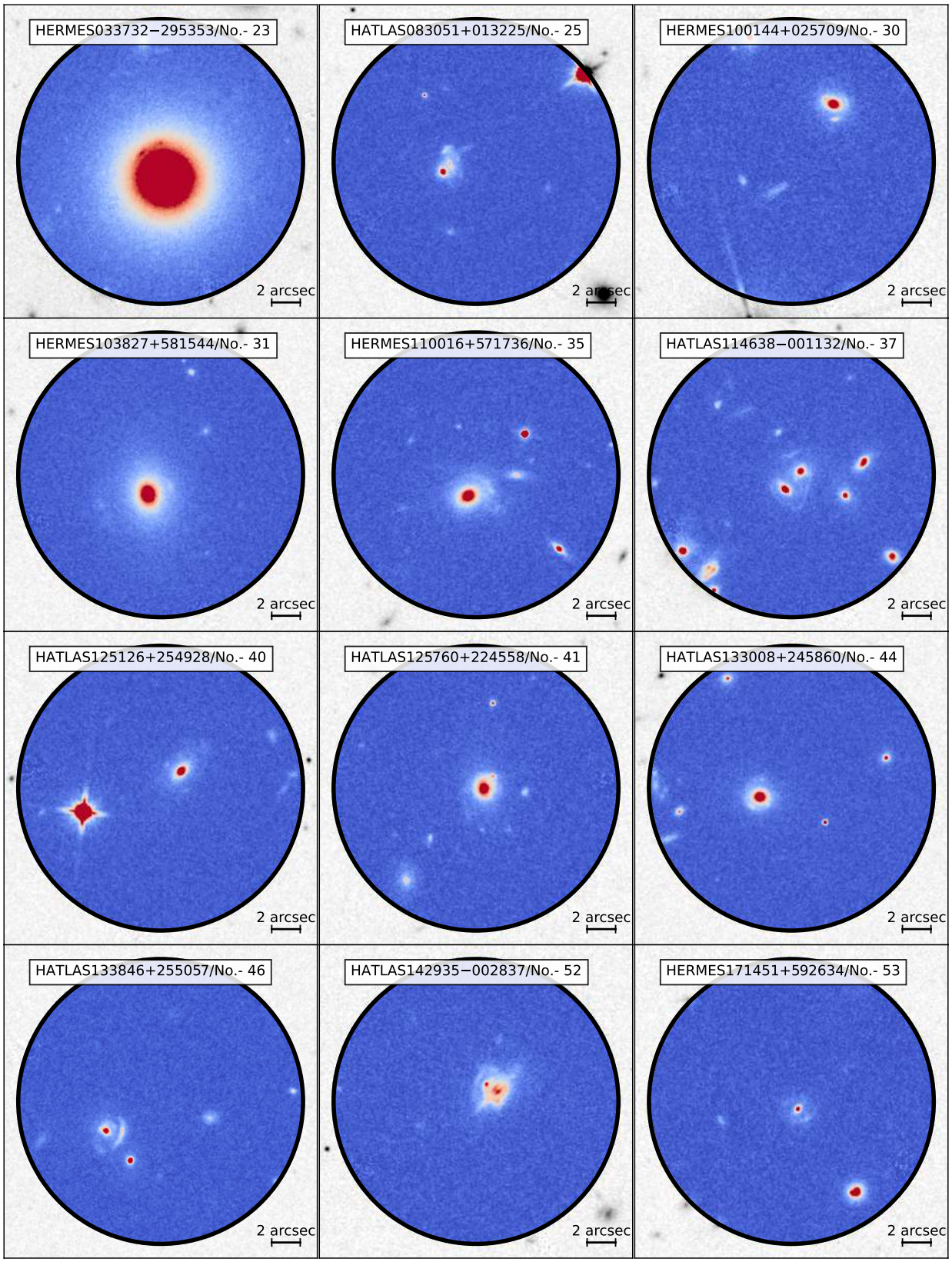

Figure 3.7 (cont.)

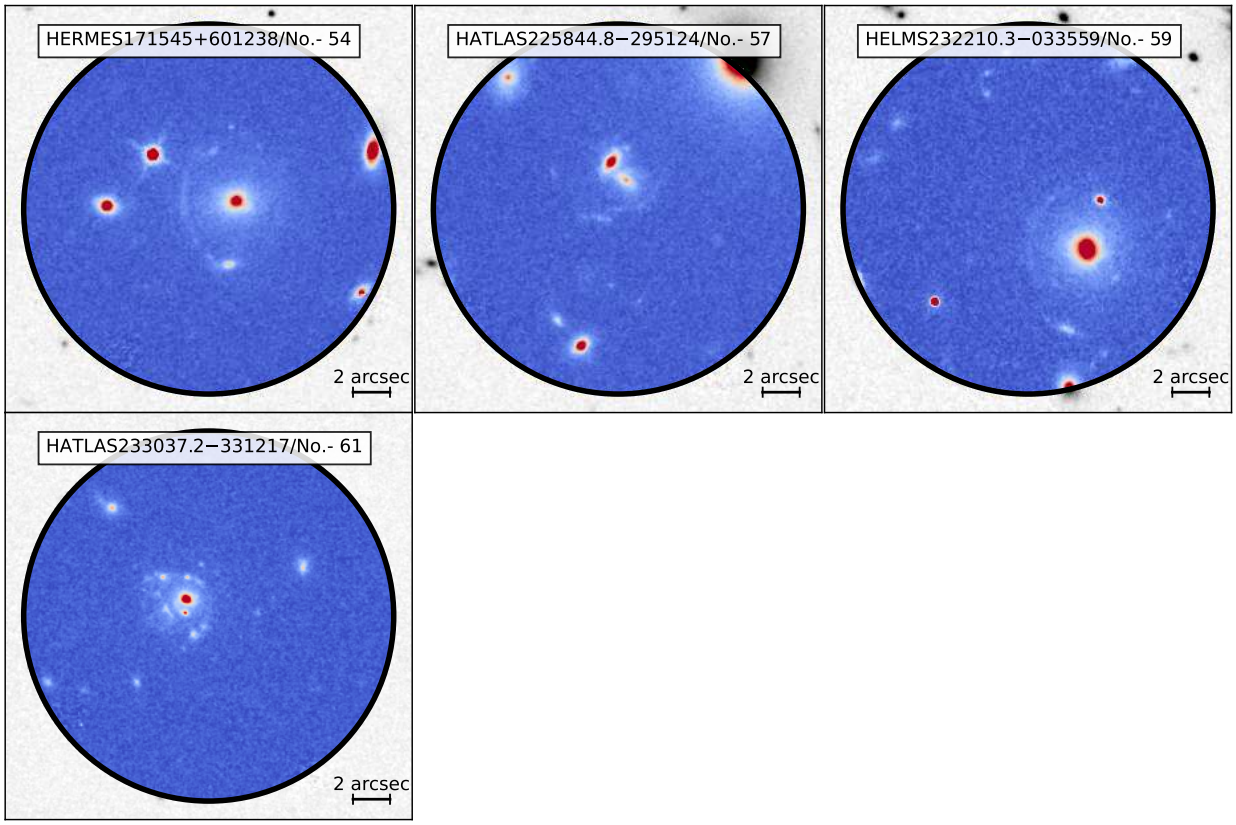

Figure 3.7 (cont.)

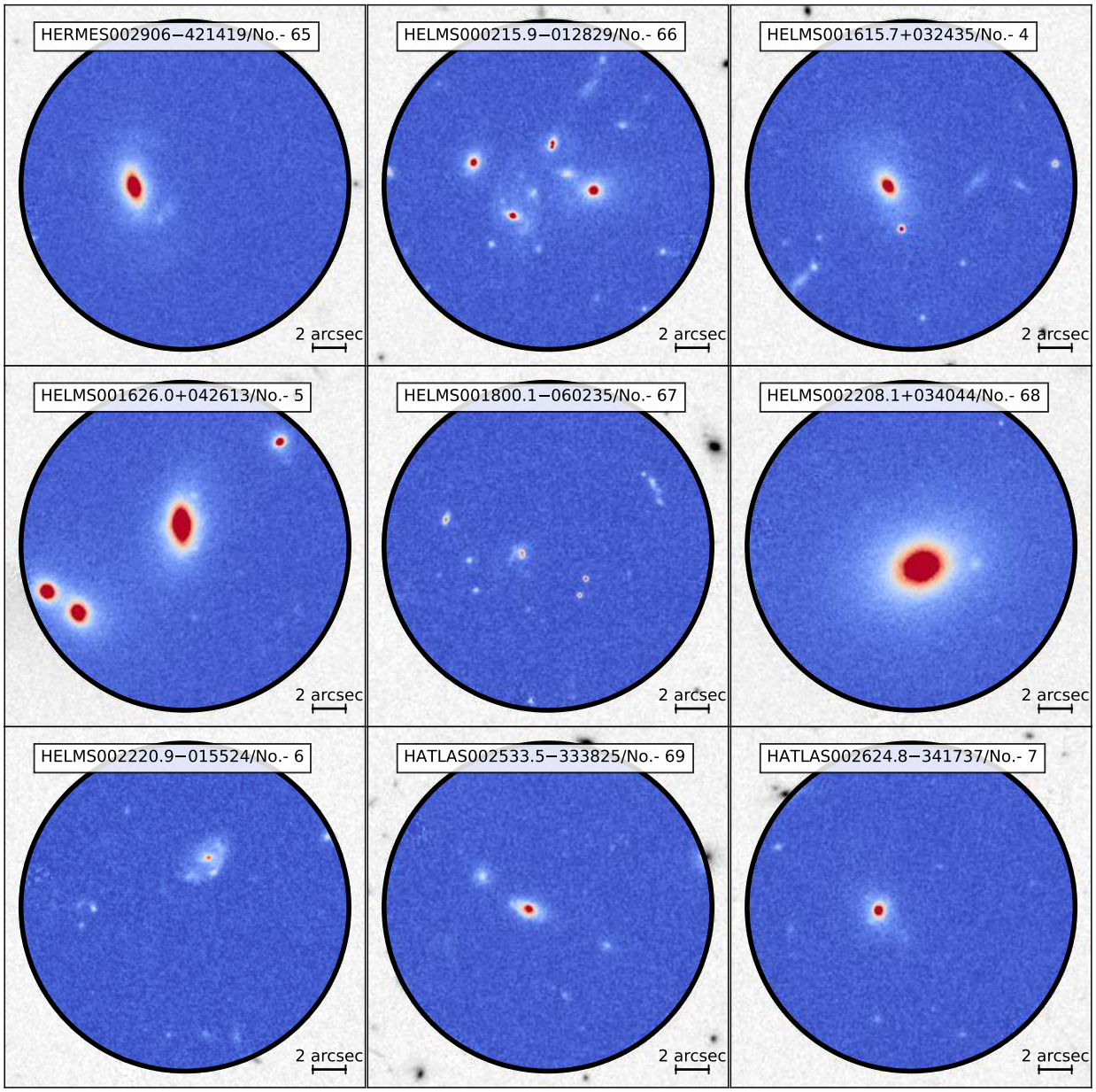

Figure 3.8: 22×22 arcsec^2 cutouts of the strongly lensed candidates classified as B. The black circle is centred on the *Herschel*/SPIRE centroid and has a diameter equal to ~ 20 arcsec ($\sim$ FWHM). All the panels share the same colour bar extending from -20 ADU, corresponding to blue, to 100 ADU in white, and then from white to red at 500 ADU.

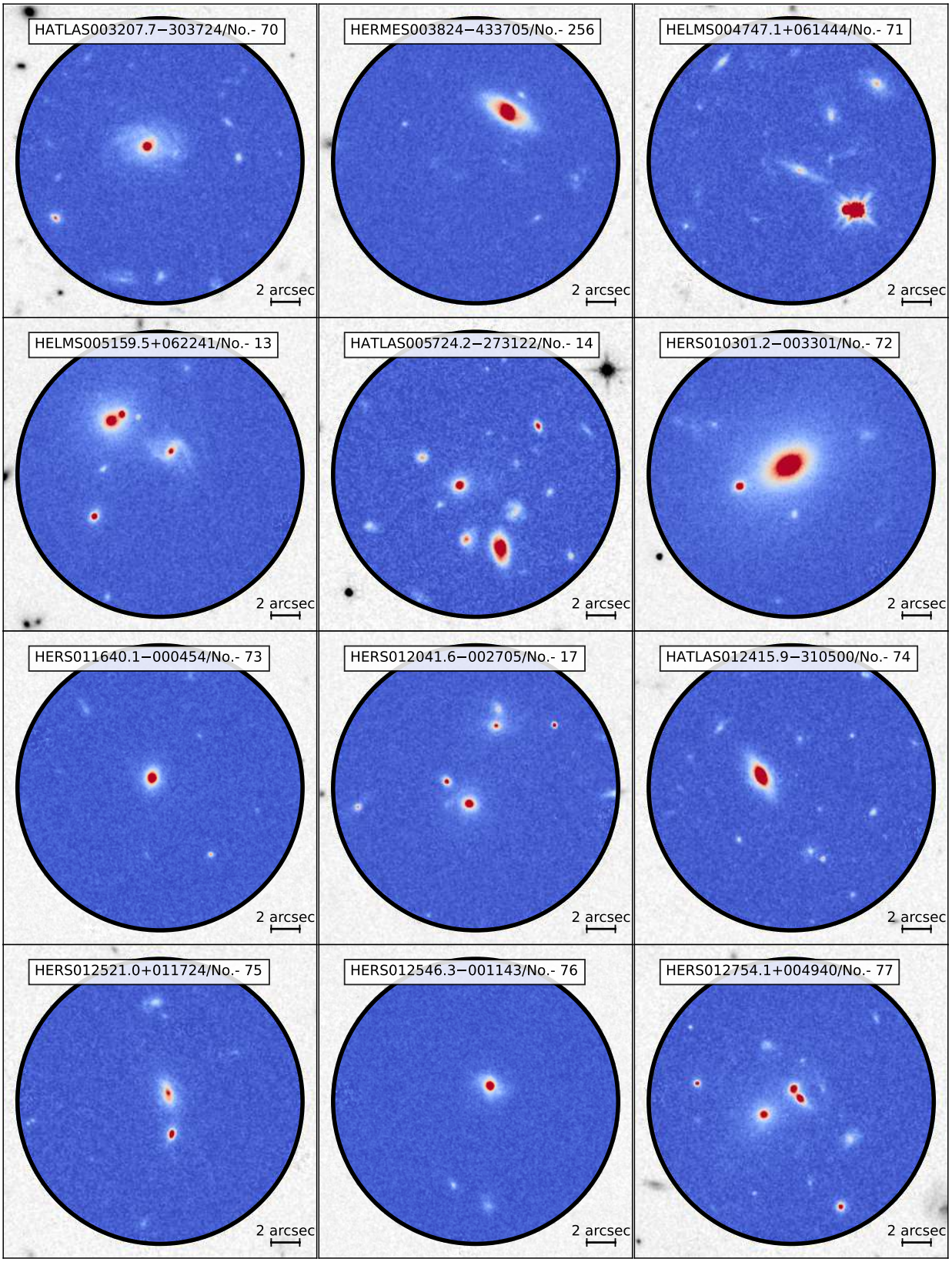

Figure 3.8 (cont.)

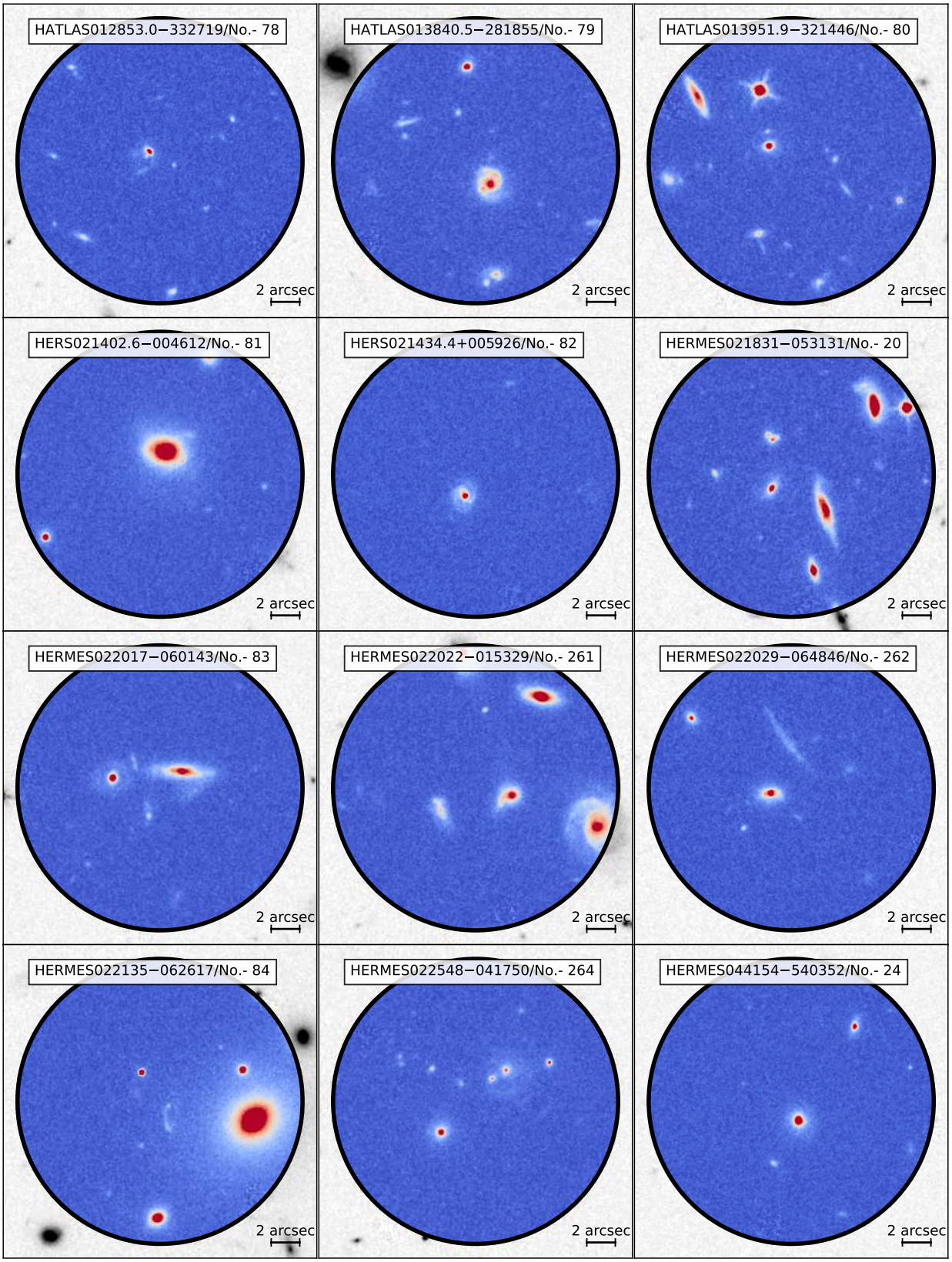

Figure 3.8 (cont.)

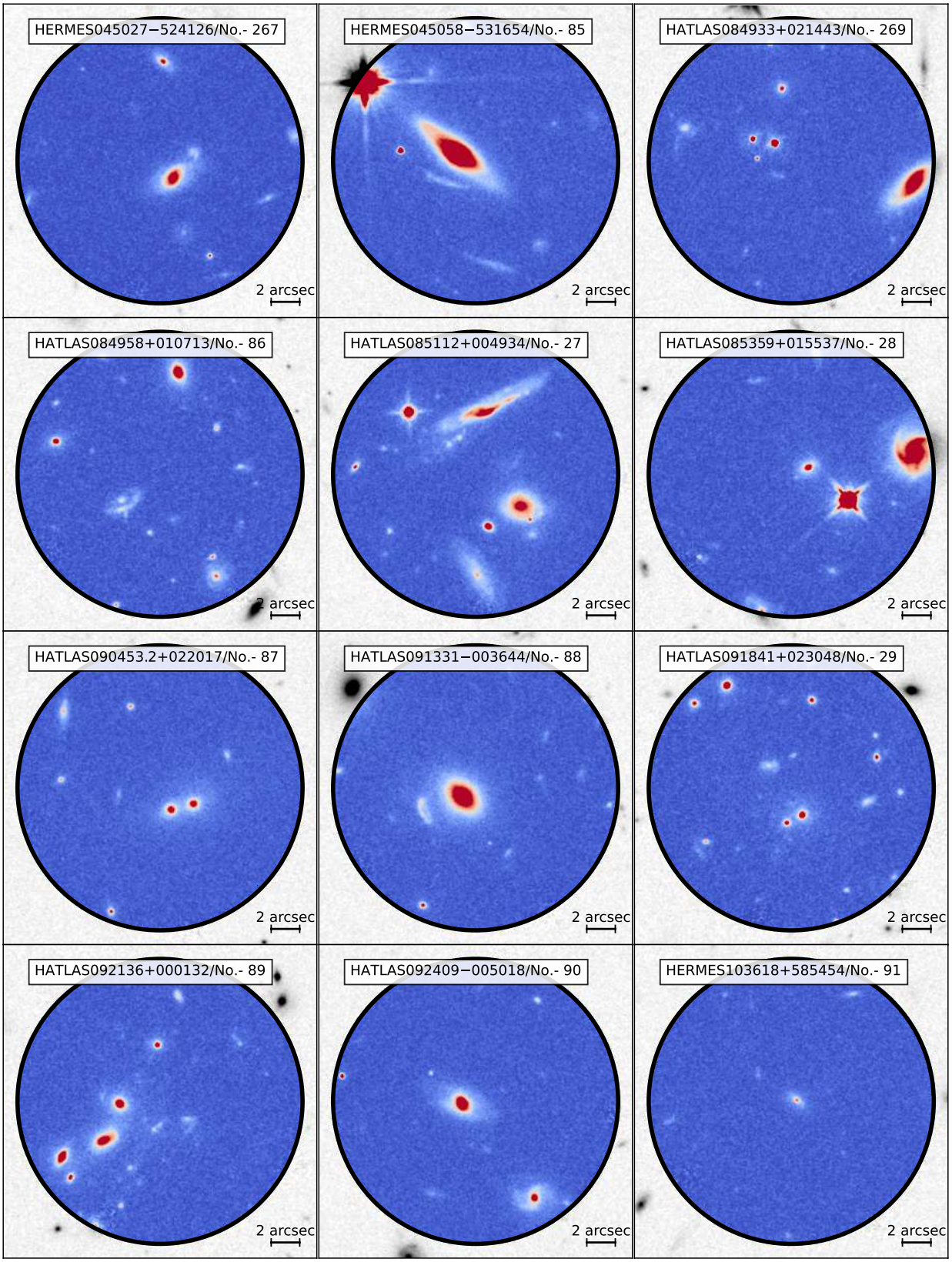

Figure 3.8 (cont.)

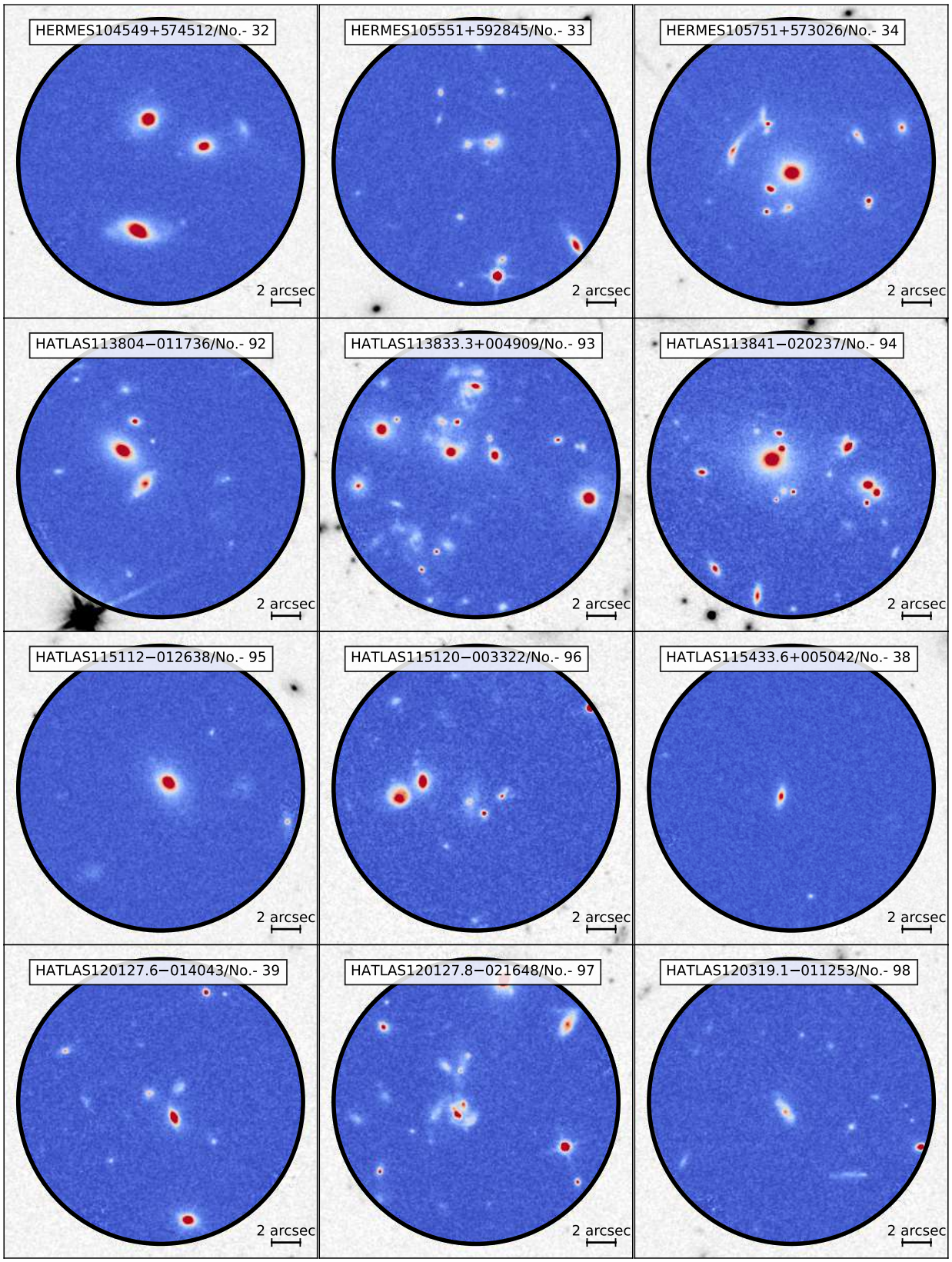

Figure 3.8 (cont.)

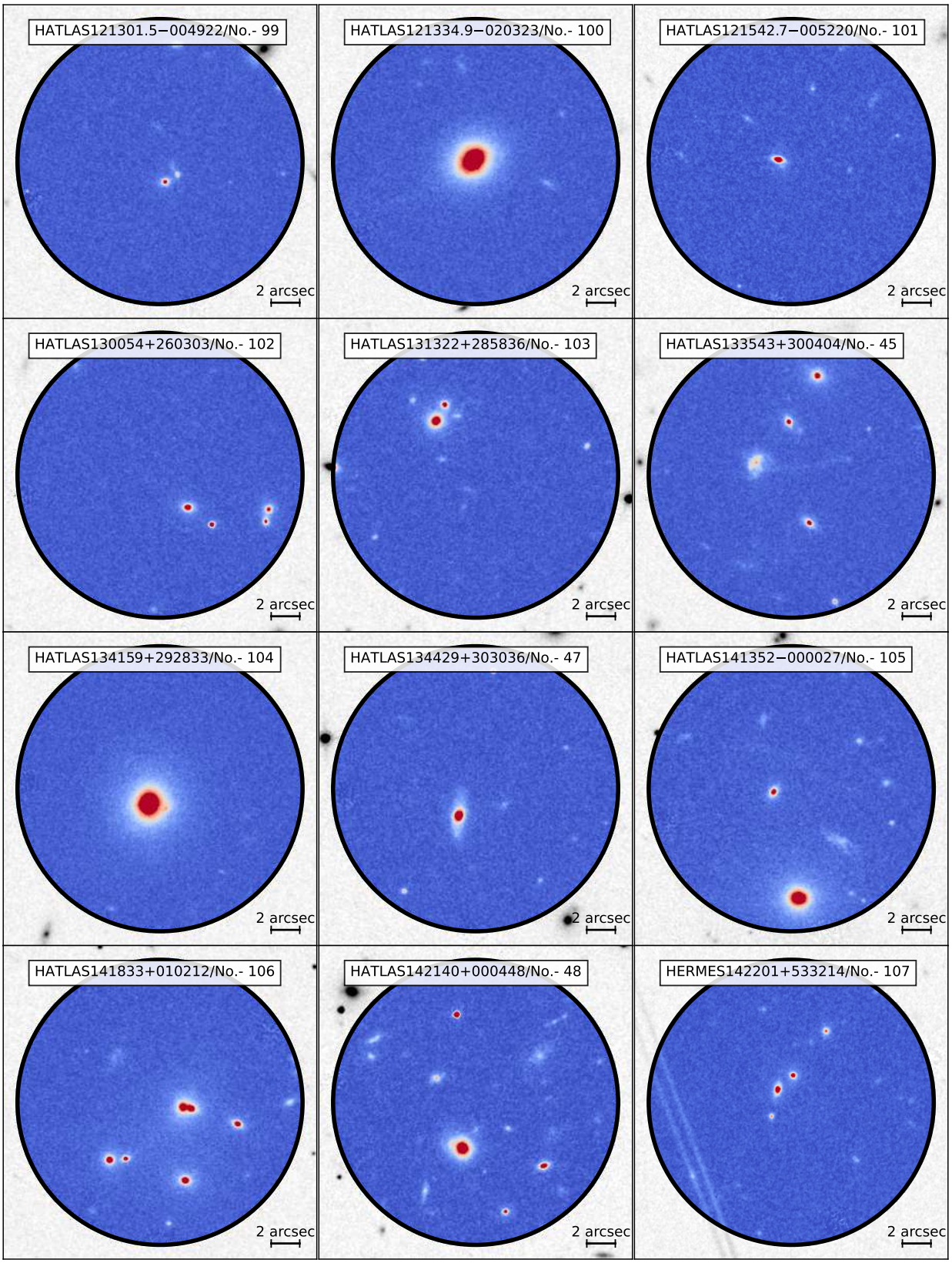

Figure 3.8 (cont.)

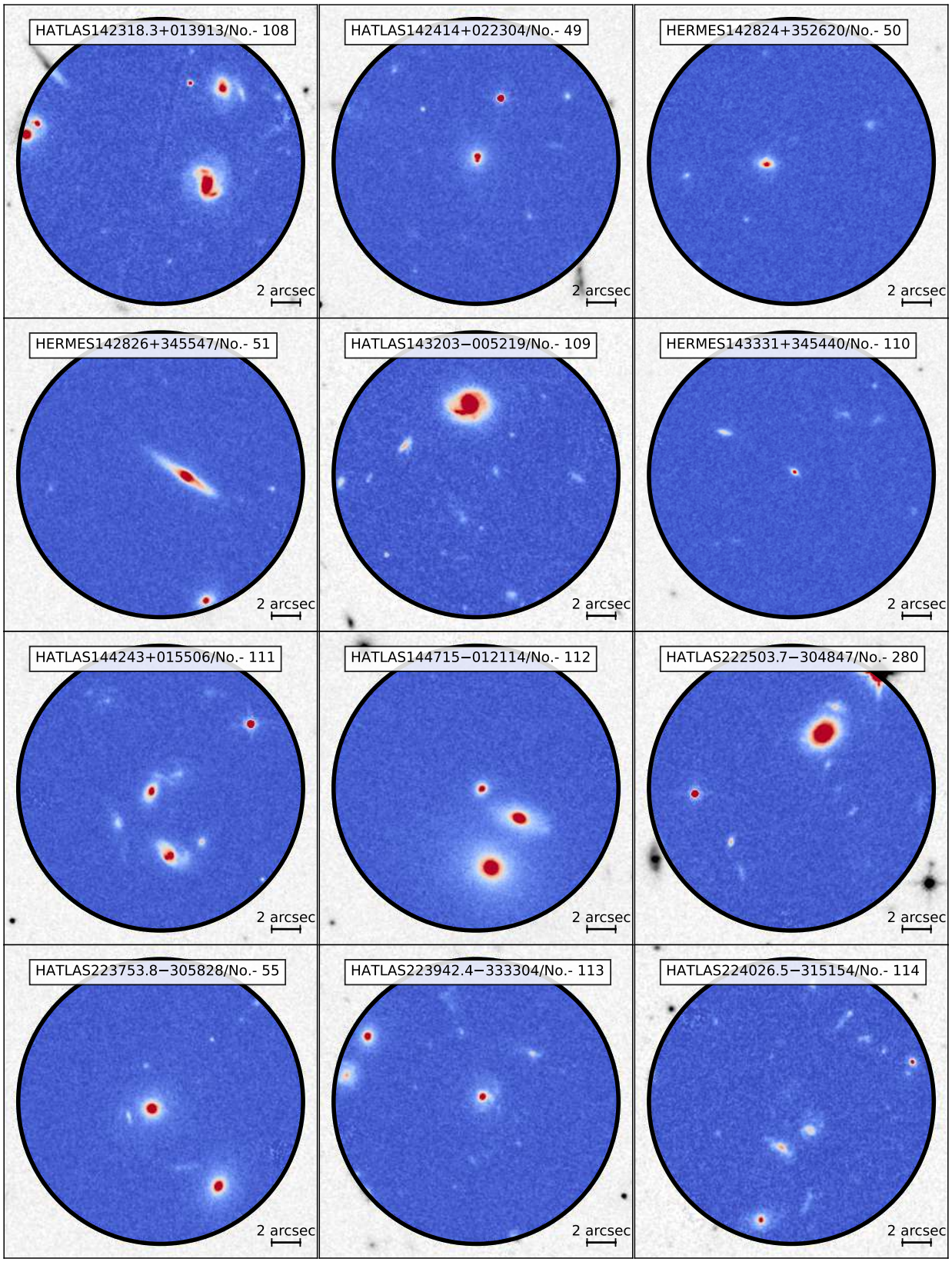

Figure 3.8 (cont.)

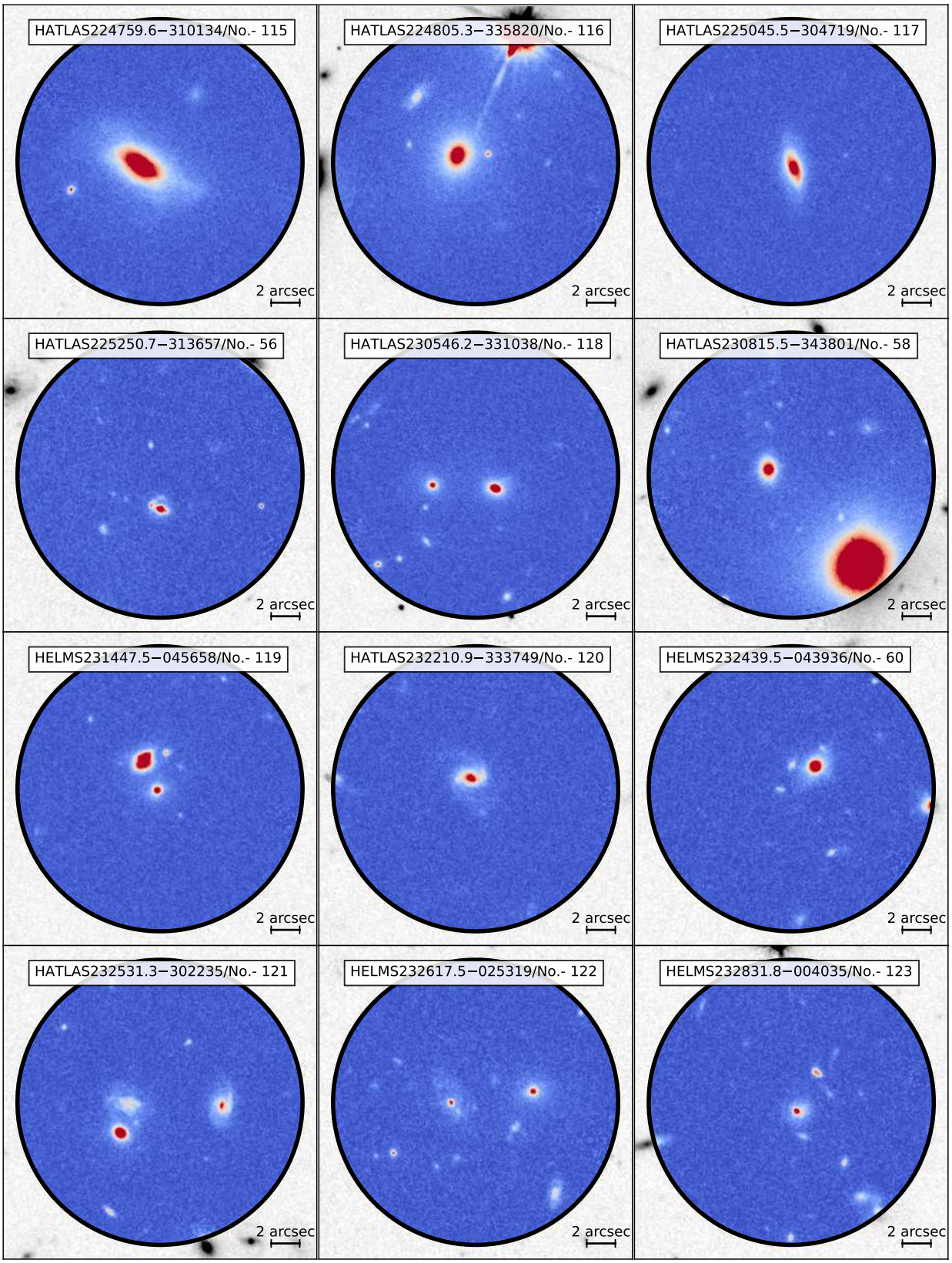

Figure 3.8 (cont.)

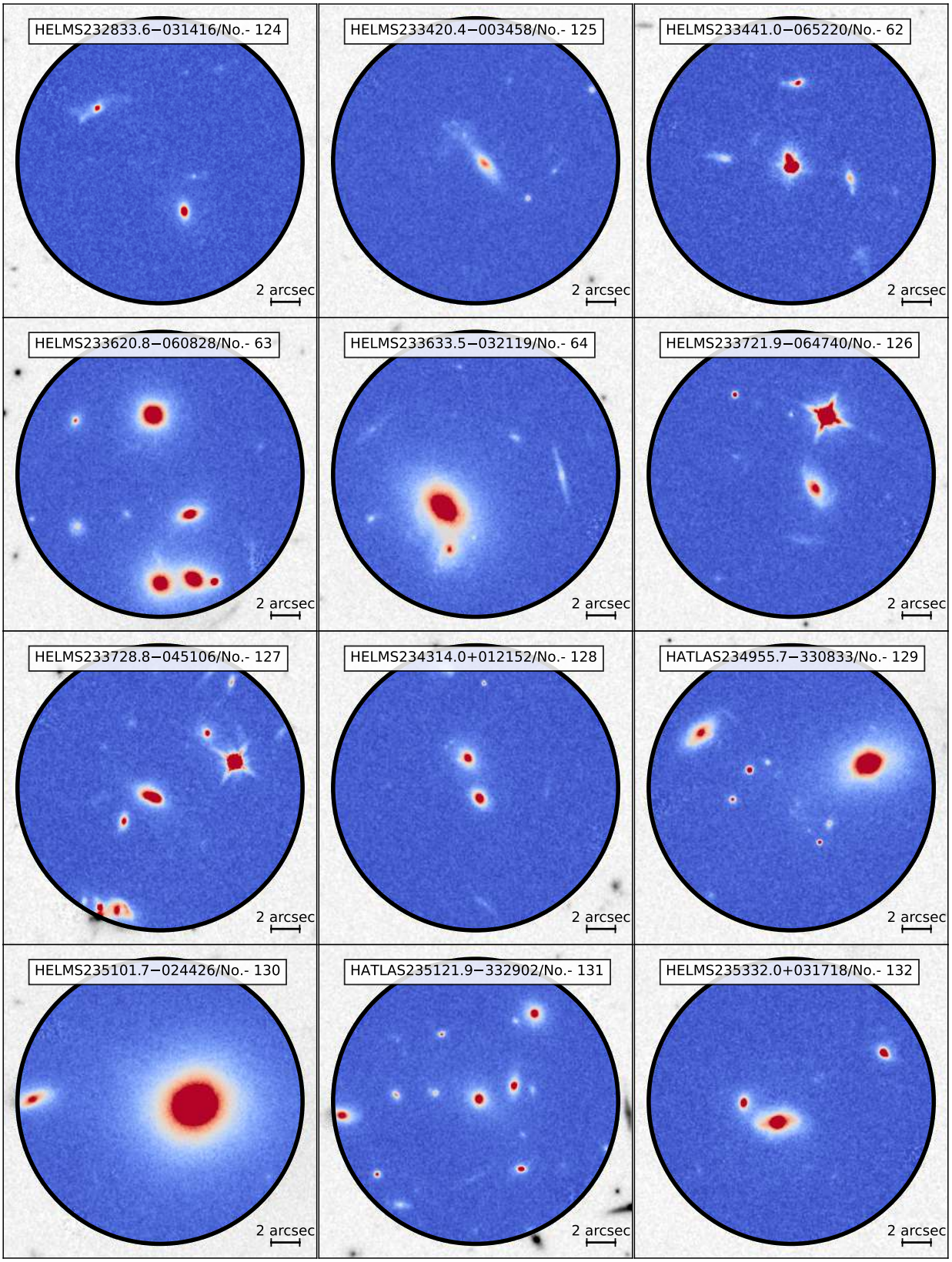

Figure 3.8 (cont.)

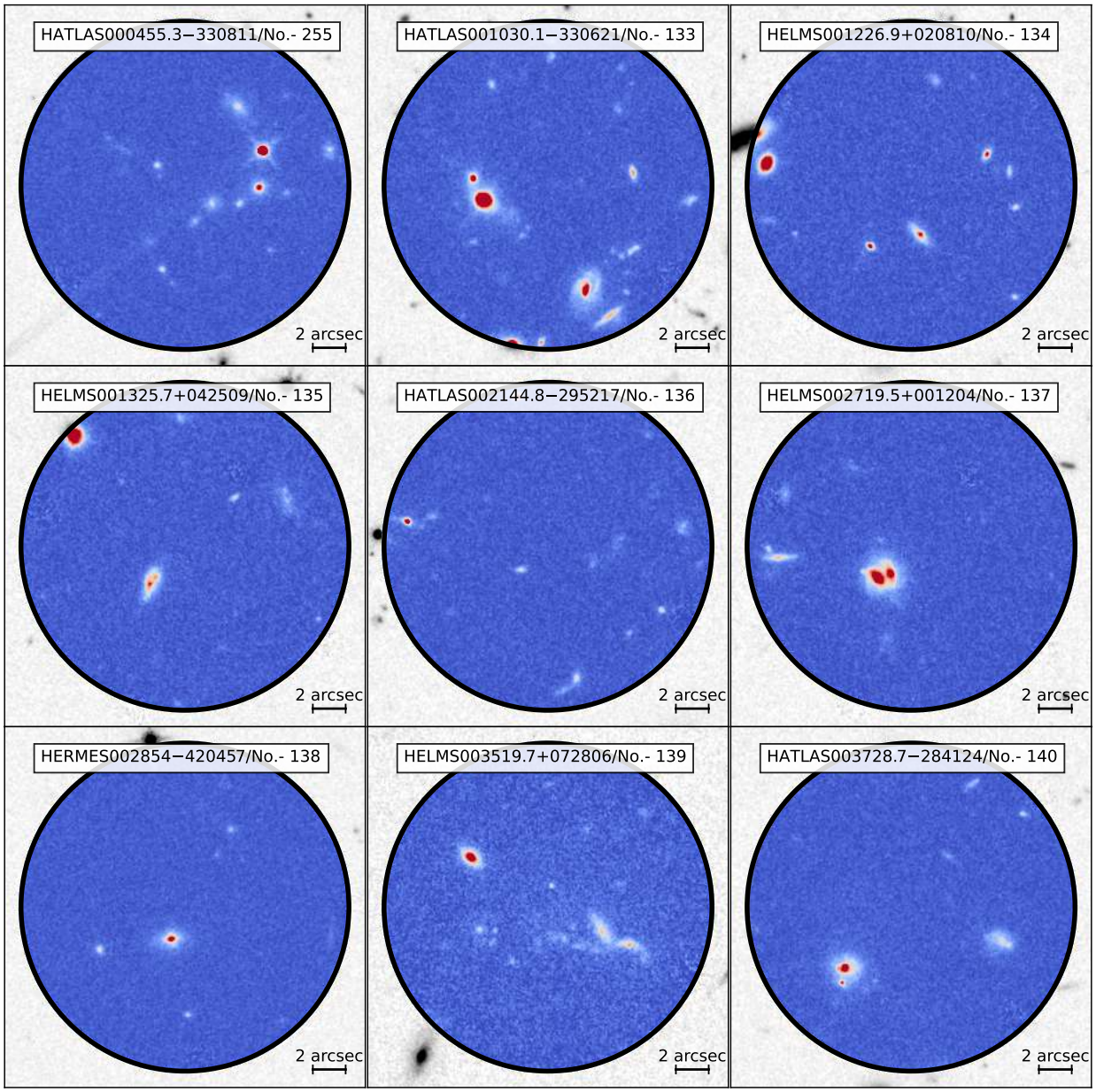

Figure 3.9: 22×22 arcsec^2 cutouts of the strongly lensed candidates classified as C. The black circle is centred on the *Herschel*/SPIRE centroid and has a diameter equal to ~ 20 arcsec ($\sim$ FWHM). All the panels share the same colour bar extending from -20 ADU, corresponding to blue, to 100 ADU in white, and then from white to red at 500 ADU.

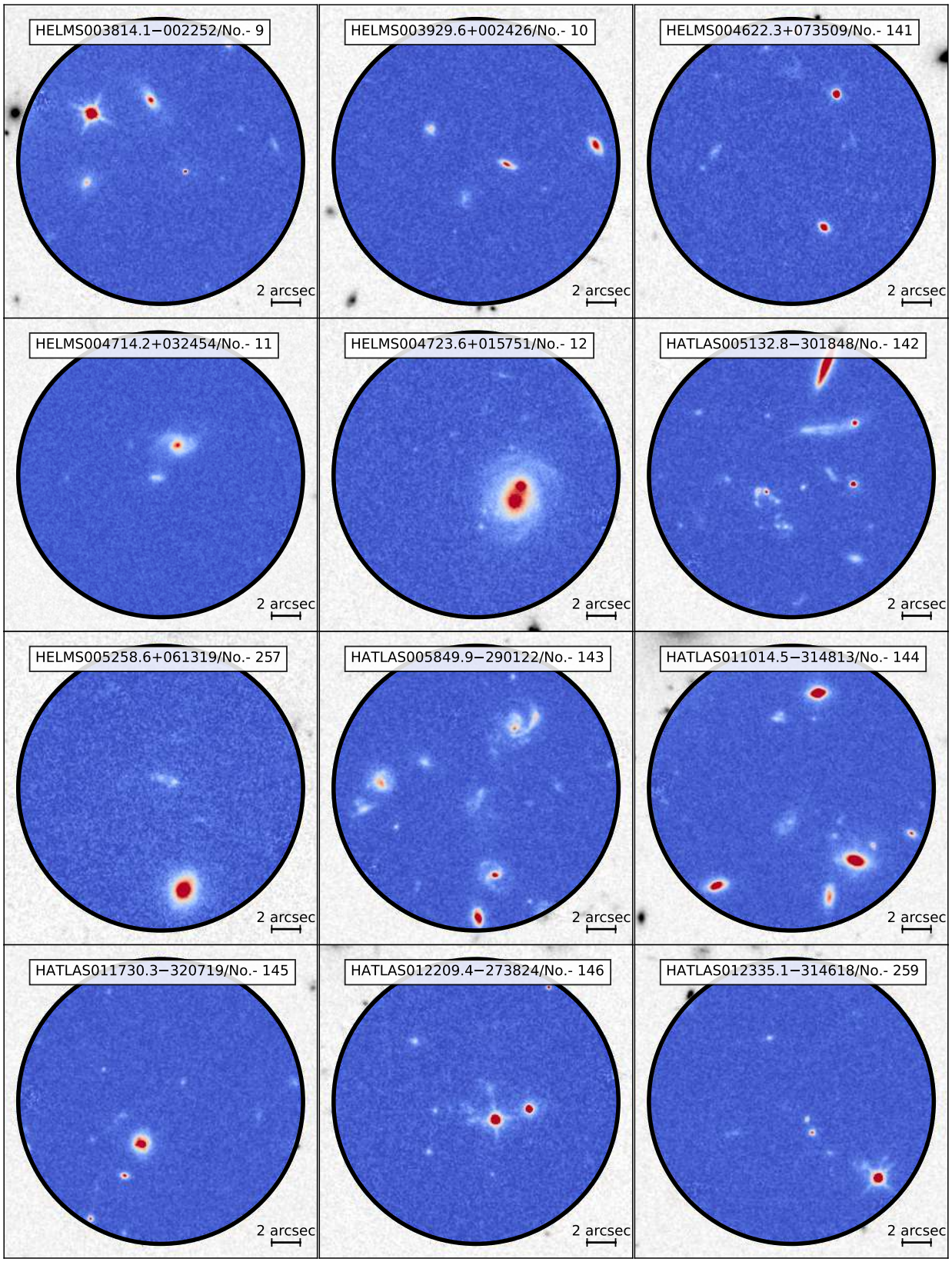

Figure 3.9 (cont.)

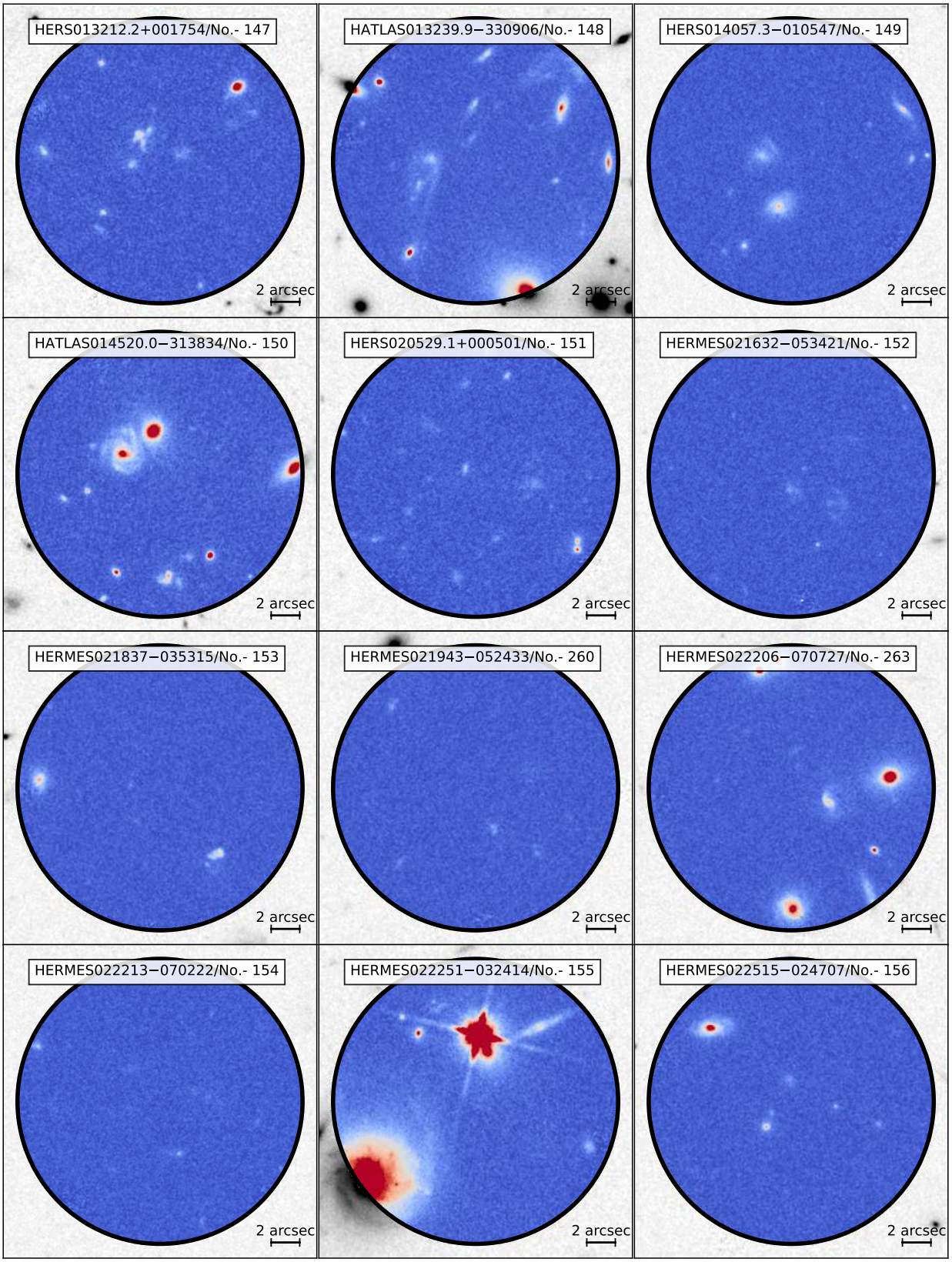

Figure 3.9 (cont.)

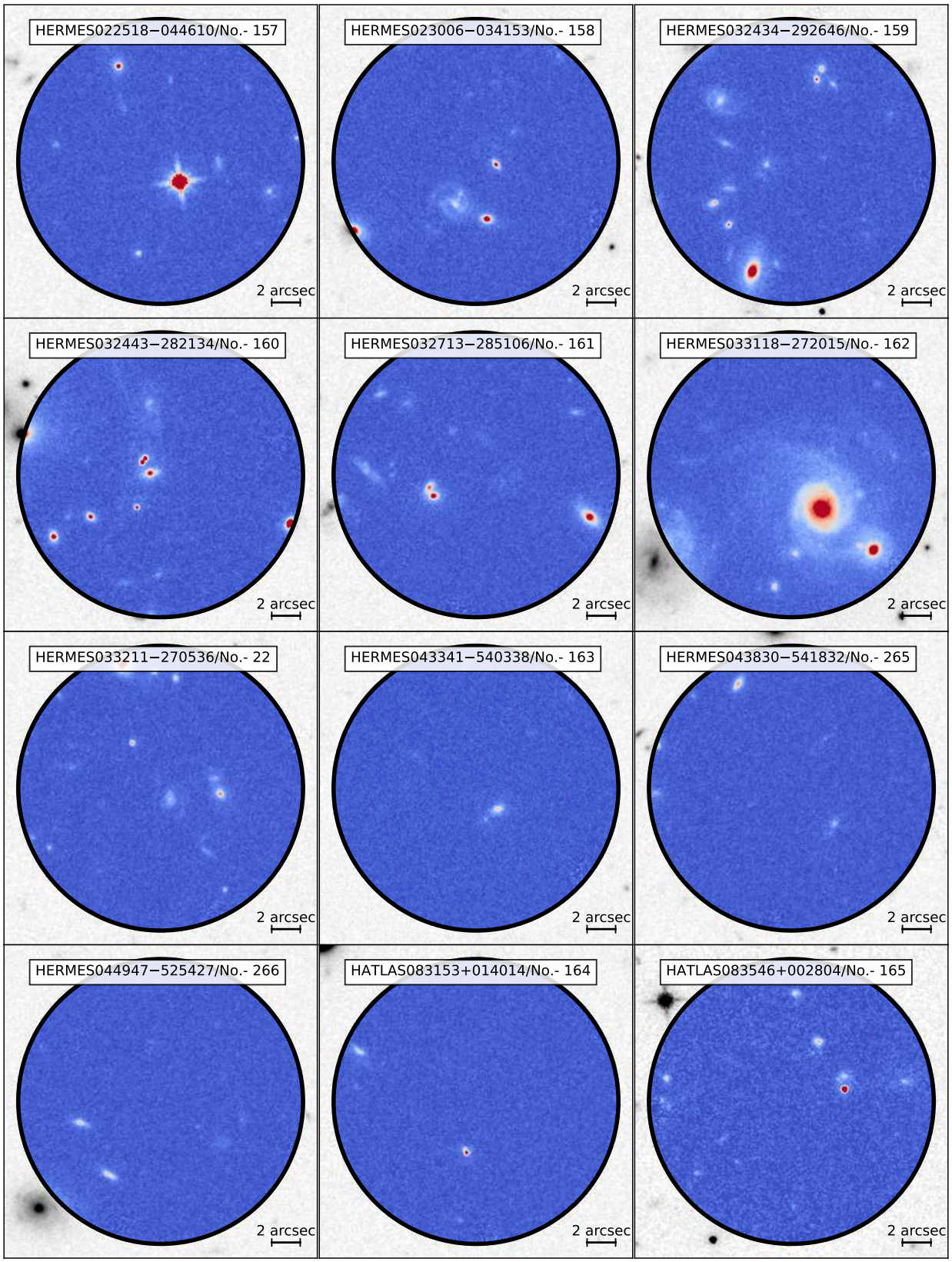

Figure 3.9 (cont.)

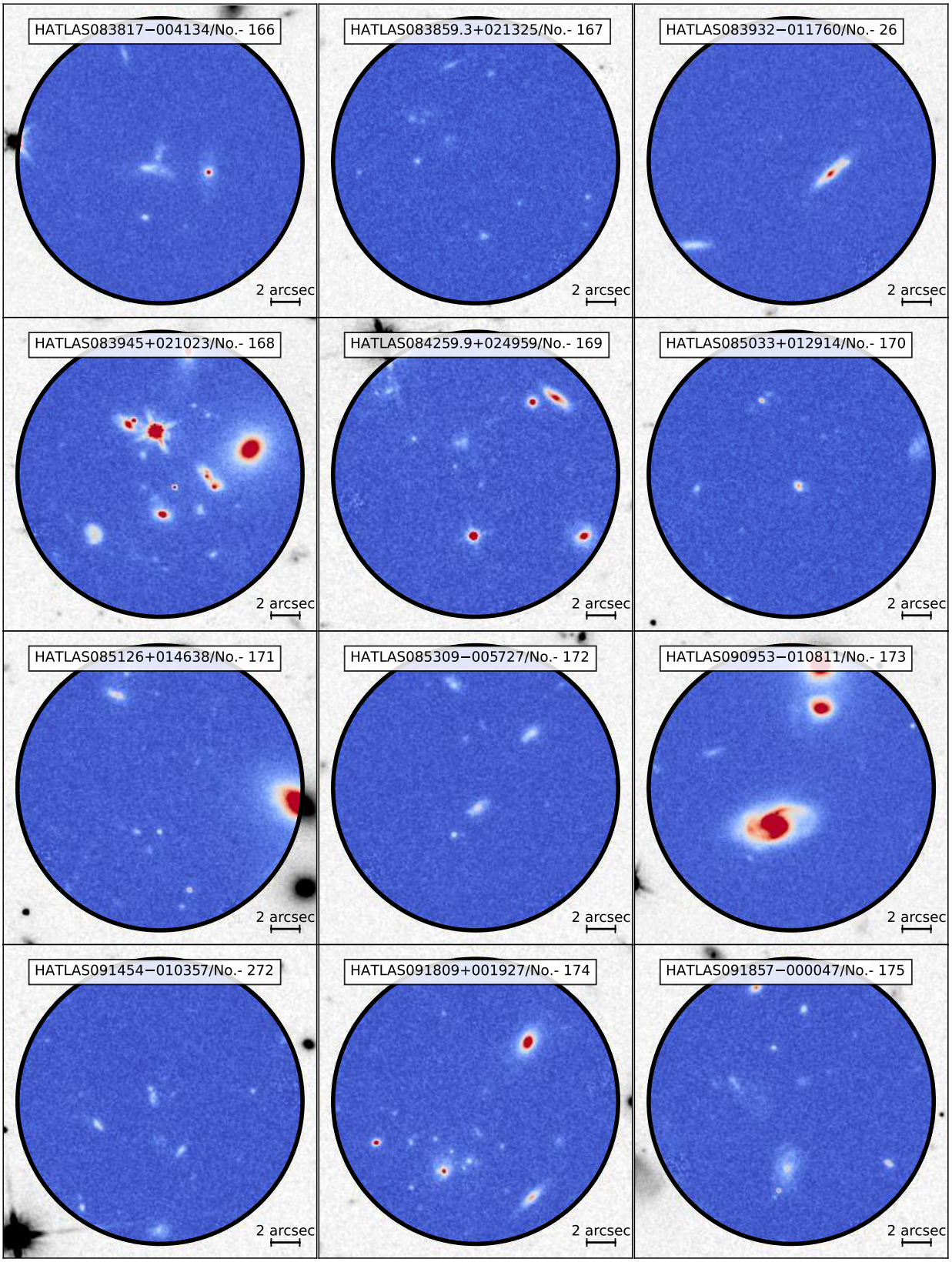

Figure 3.9 (cont.)

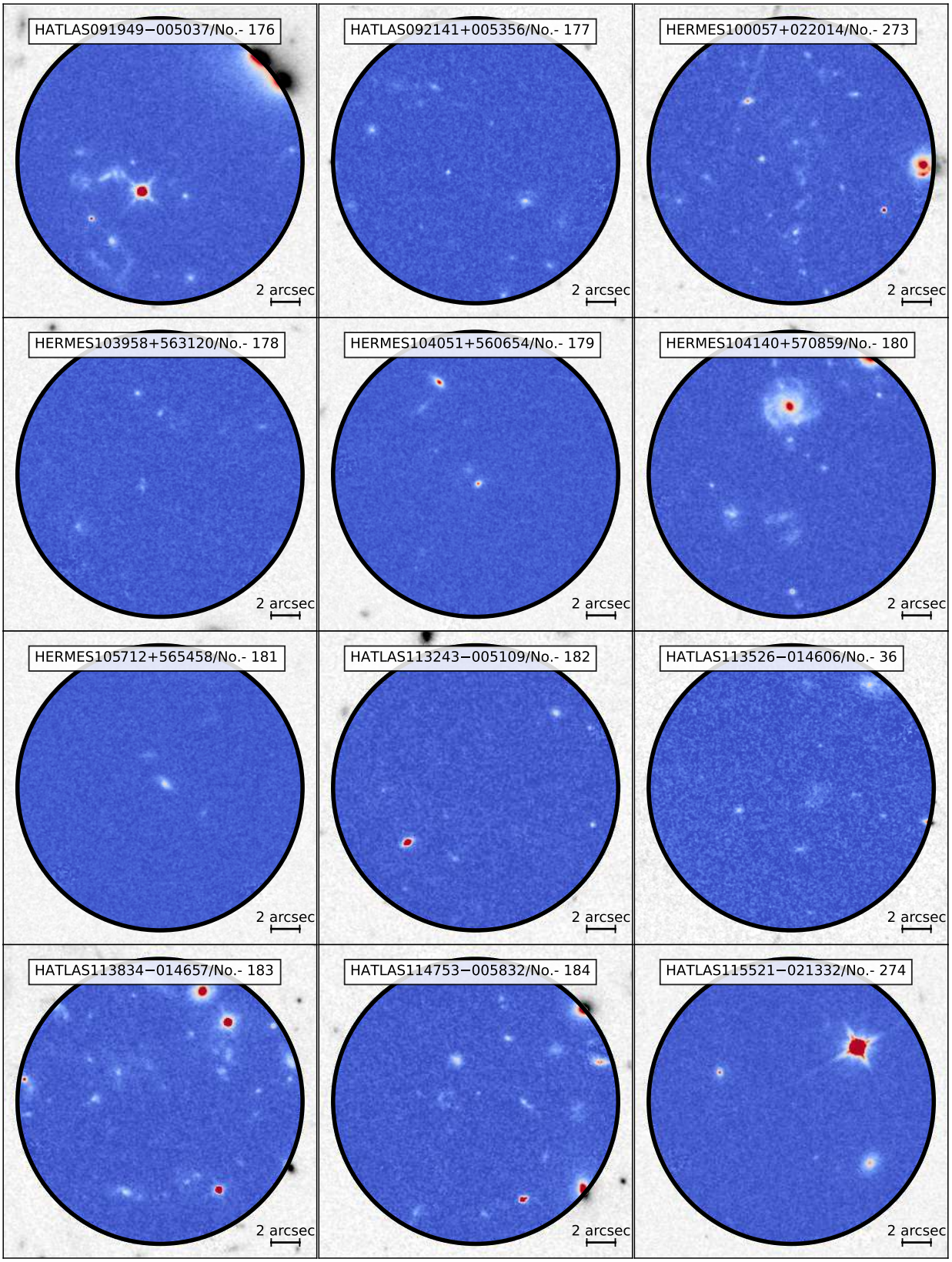

Figure 3.9 (cont.)

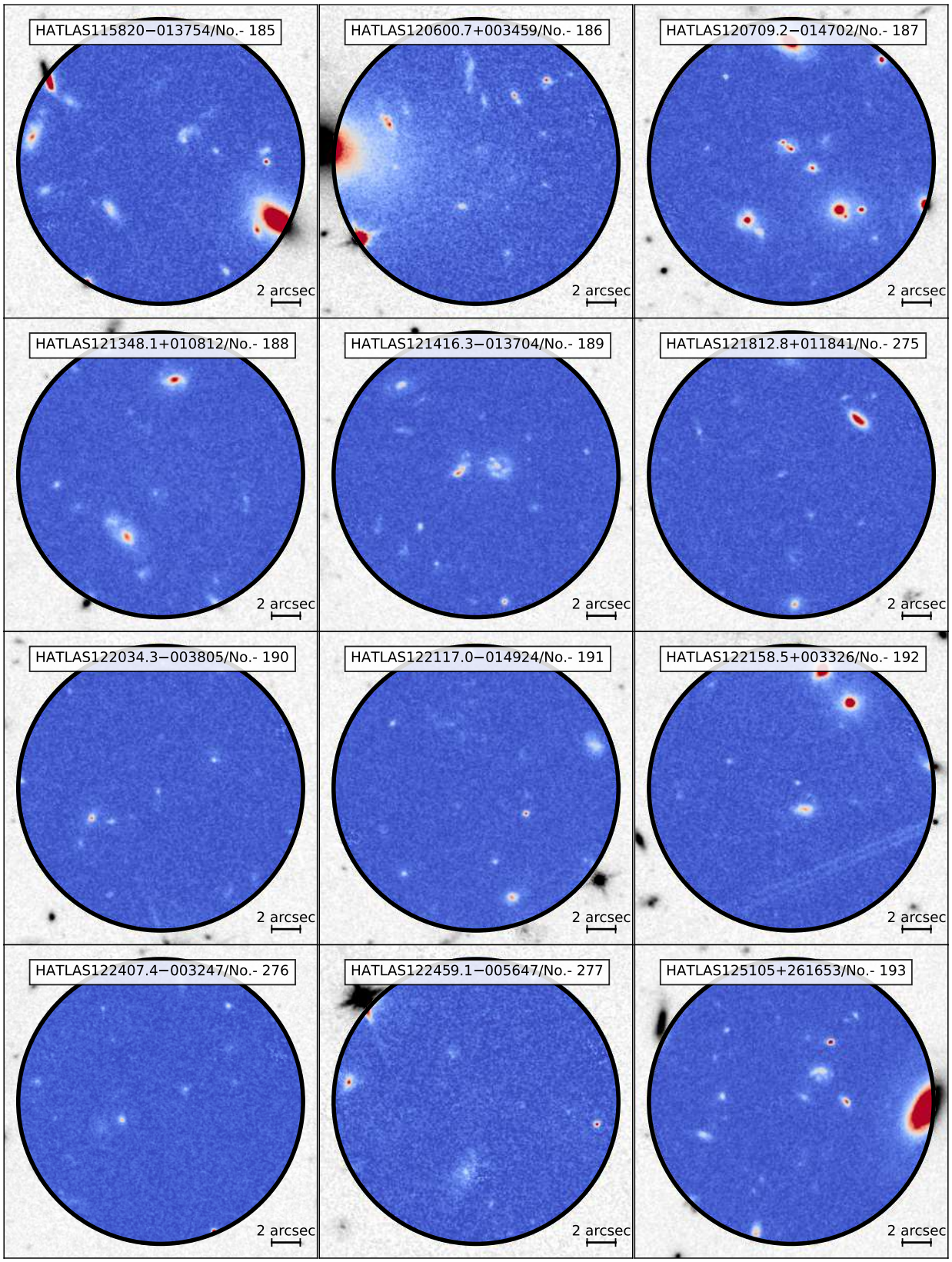

Figure 3.9 (cont.)

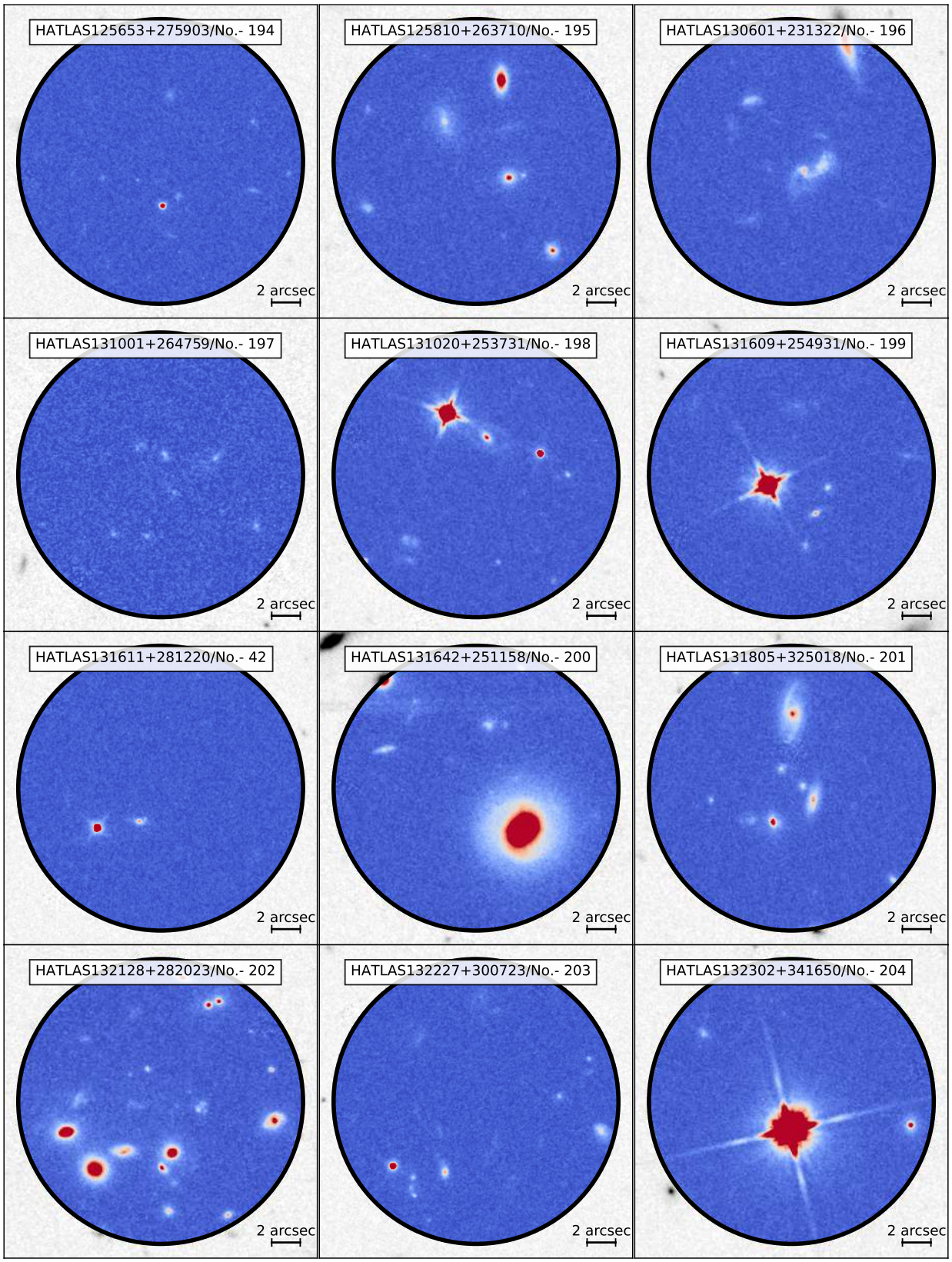

Figure 3.9 (cont.)

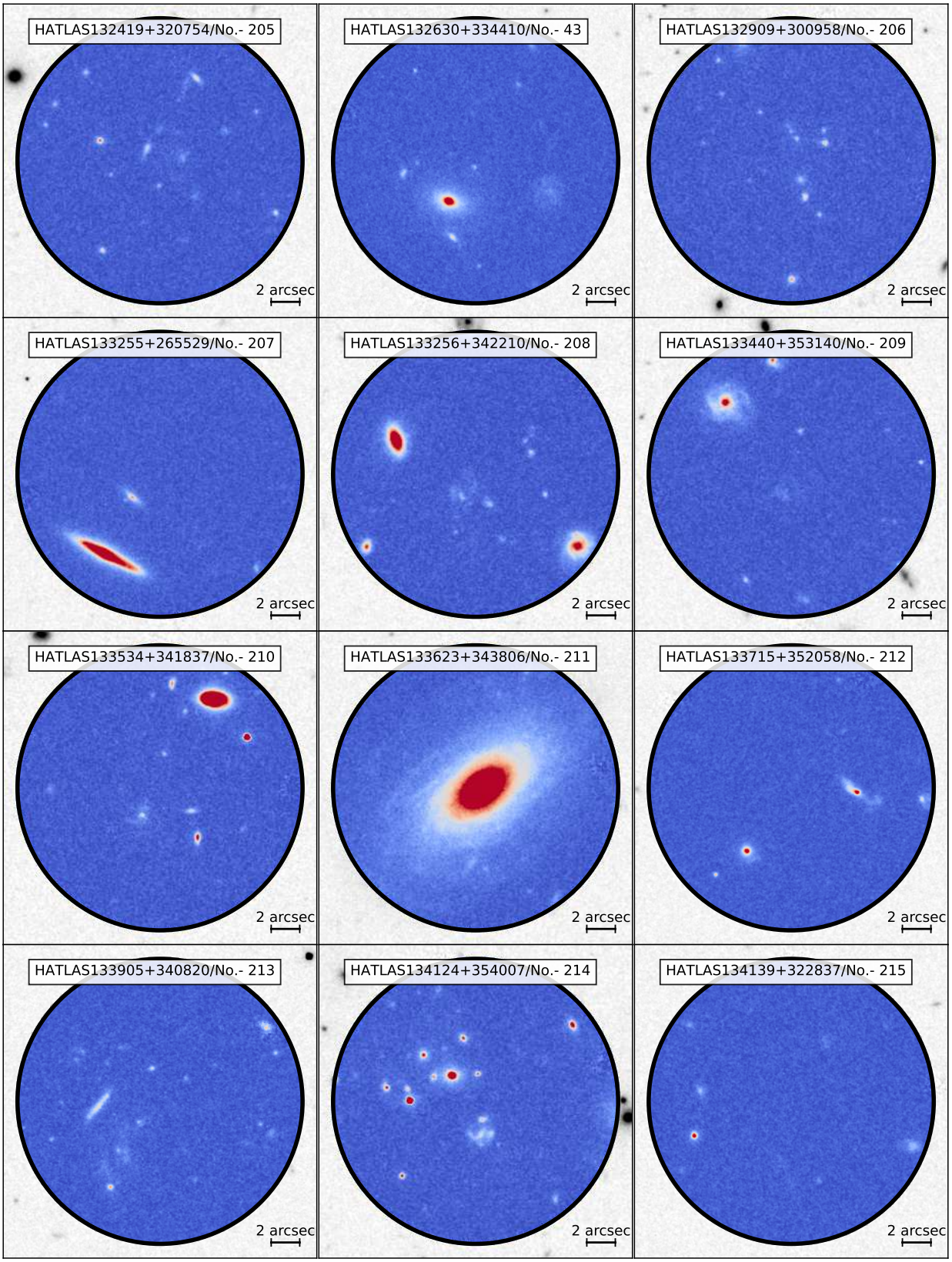

Figure 3.9 (cont.)

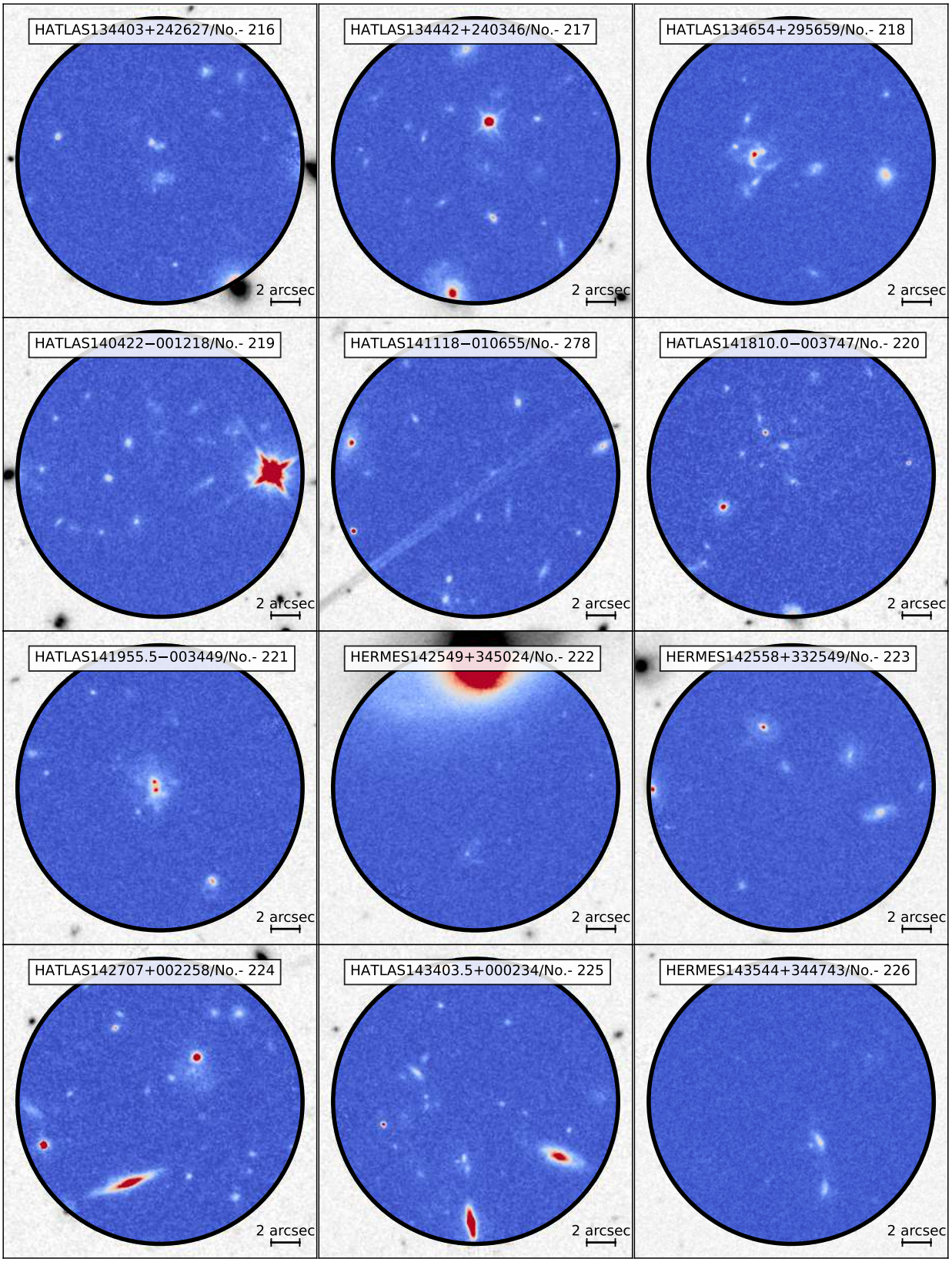

Figure 3.9 (cont.)

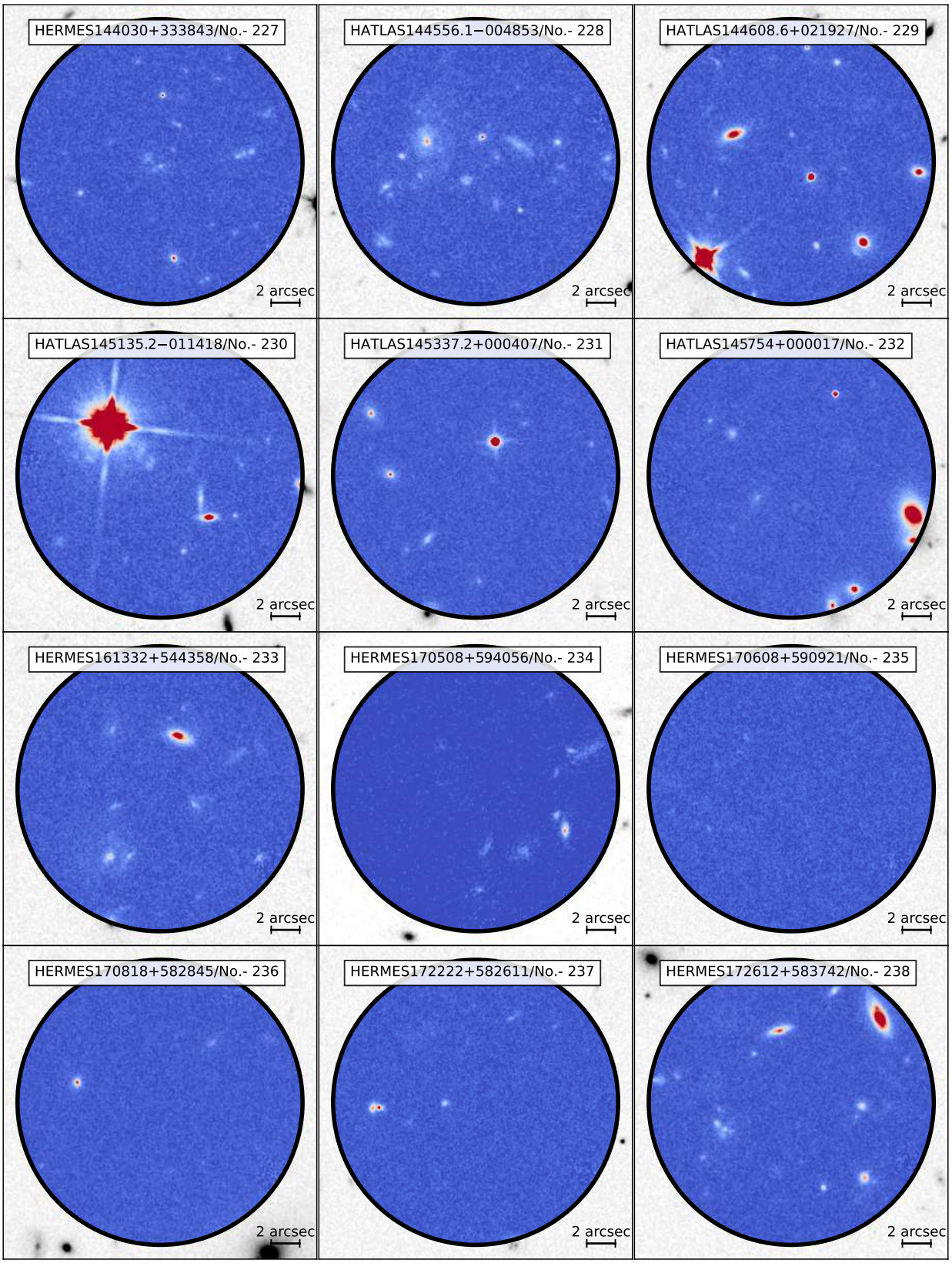

Figure 3.9 (cont.)

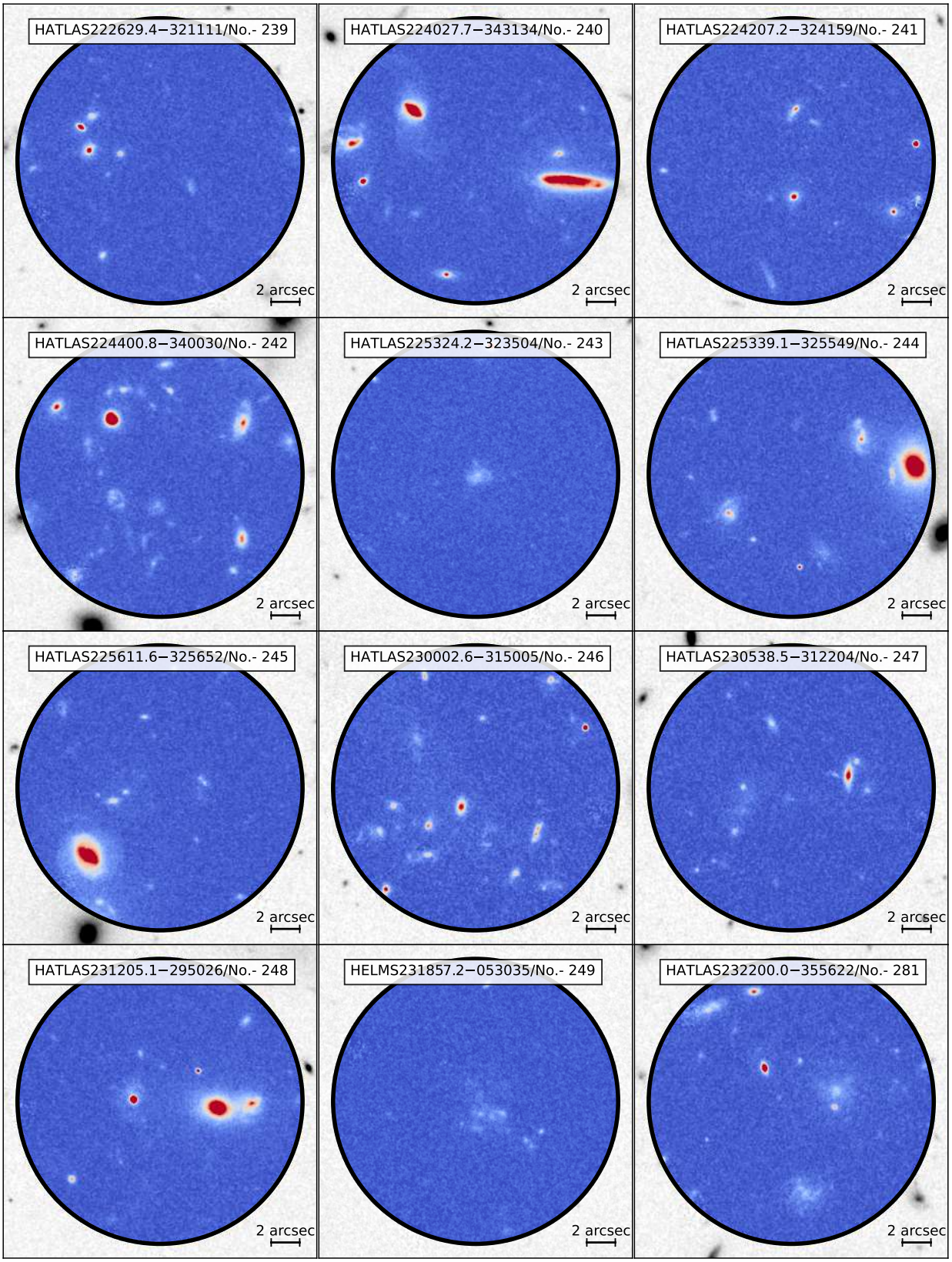

Figure 3.9 (cont.)

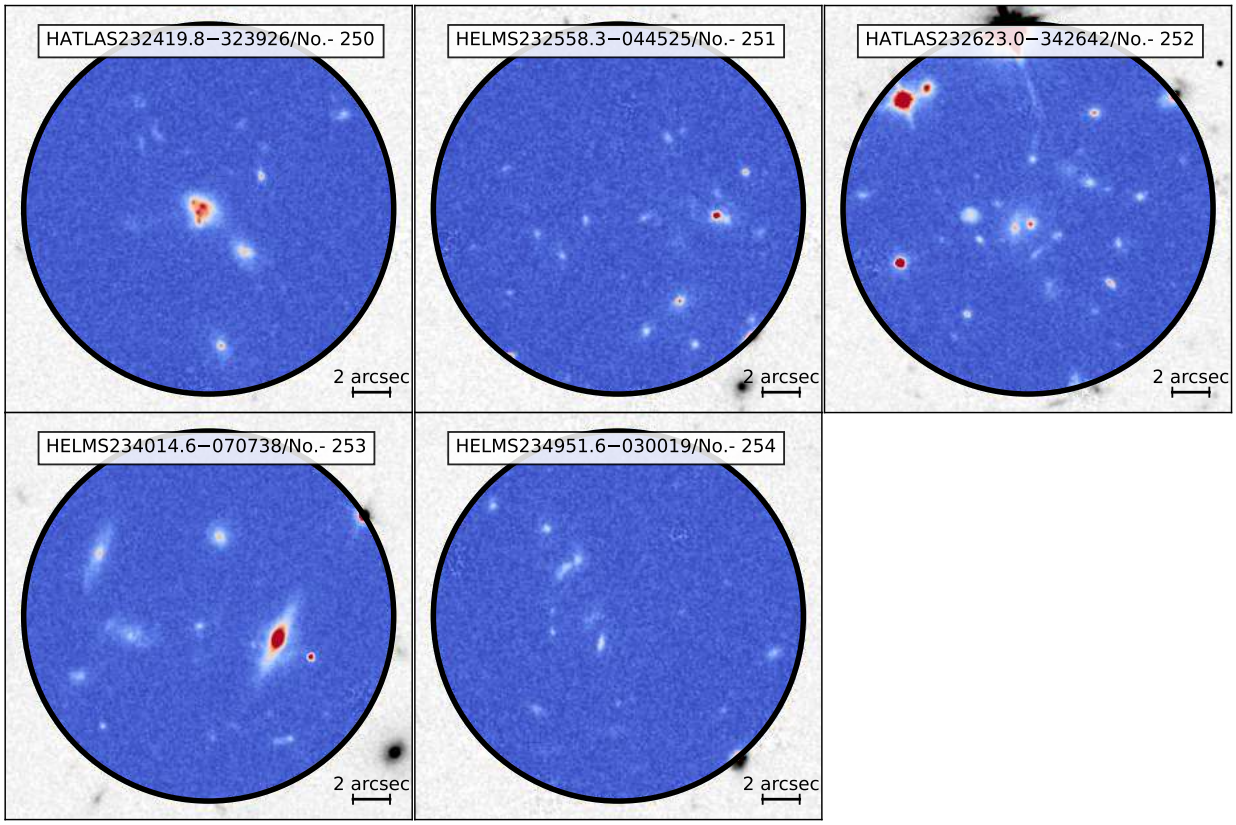

Figure 3.9 (cont.)

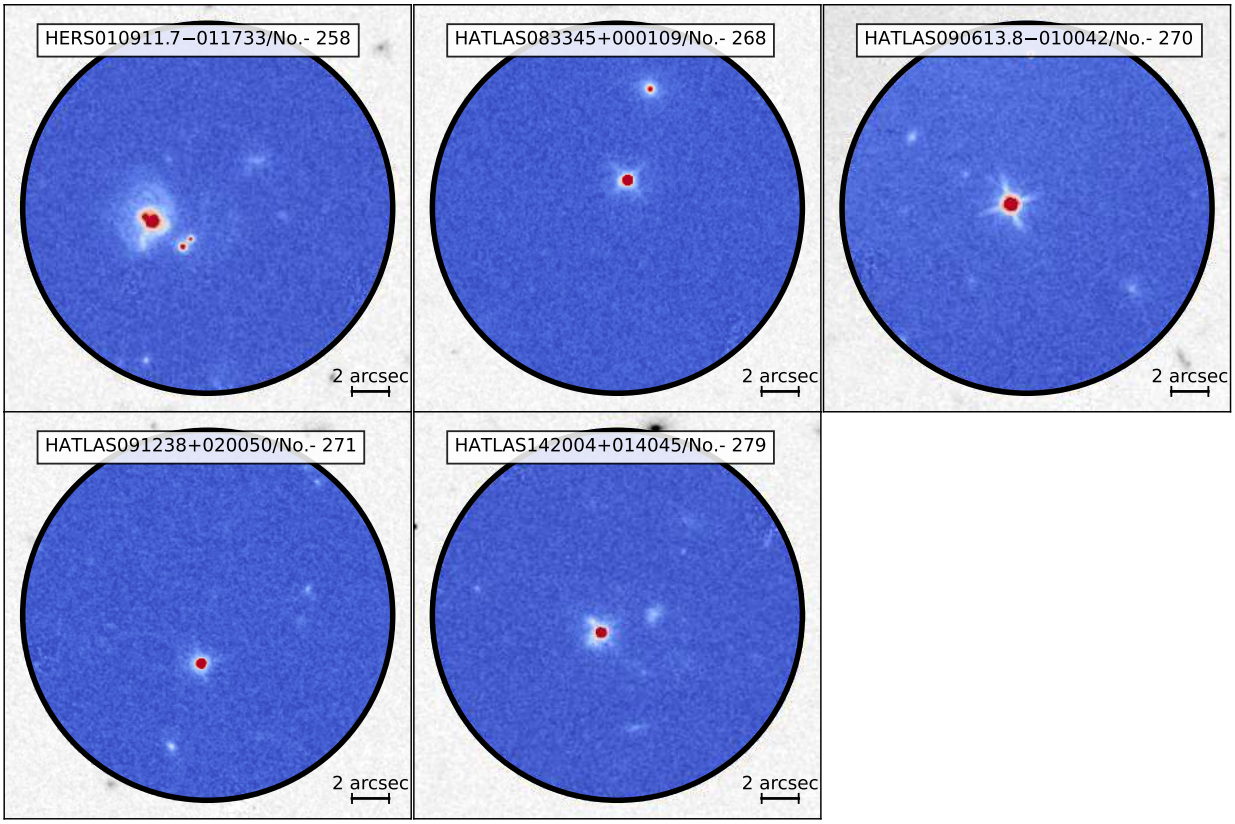

Figure 3.10: 22×22 arcsec^2 cutouts of the strongly lensed candidates classified as D. The black circle is centred on the *Herschel*/SPIRE centroid and has a diameter equal to ~ 20 arcsec ($\sim$ FWHM). All the panels share the same colour bar extending from -20 ADU, corresponding to blue, to 100 ADU in white, and then from white to red at 500 ADU.

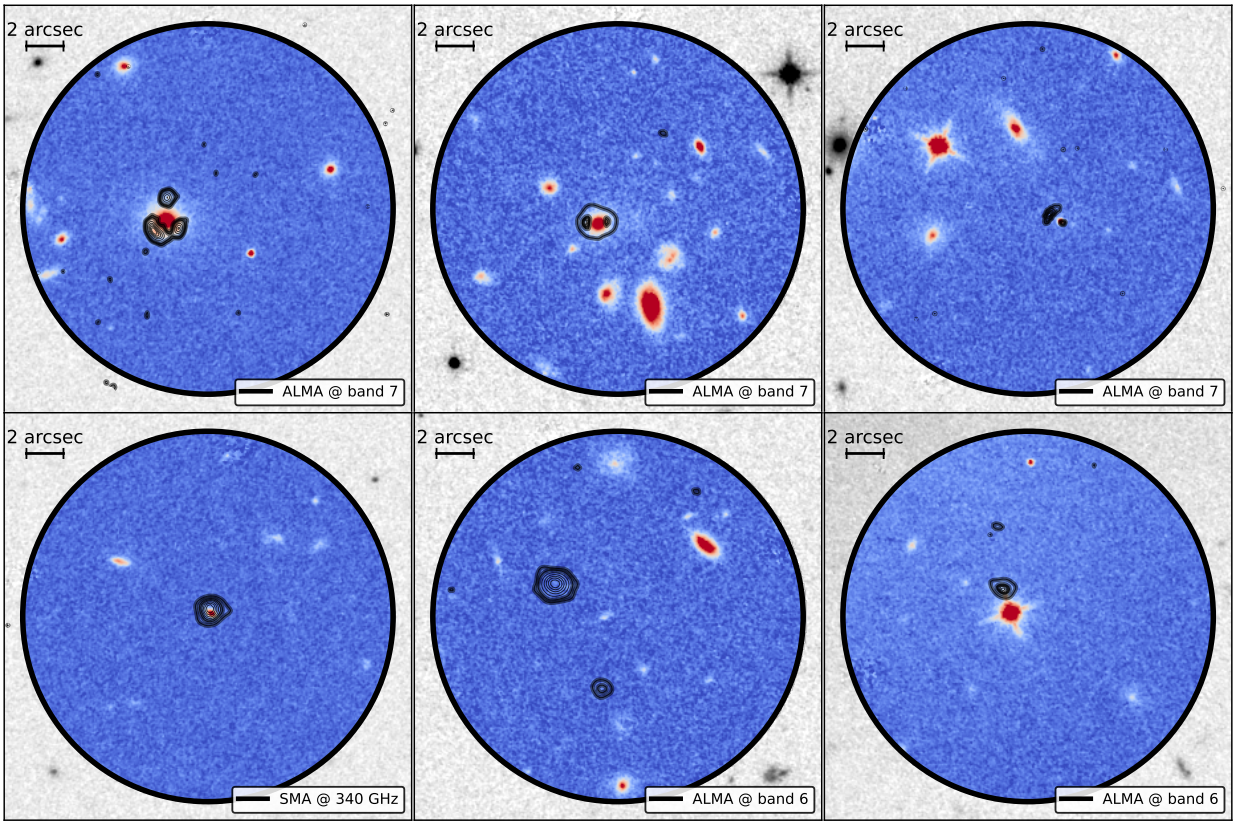

Figure 3.11: Six examples of strongly lensed candidates (top row), candidates of uncertain nature (first panel in the bottom row), and unlensed candidates (second and third panel in the bottom row) after including the multiwavelength follow-up observations. The black circle is centred on the *Herschel*/SPIRE centroid and has a diameter equal to ~ 20 arcsec (roughly corresponding to the beam FWHM at $250\,\mu$m). We show the contours of the high-resolution multiwavelength data taken at two levels corresponding to $SNR = 5$ and 10 respectively (thick lines) and five uniformly spaced levels between the $SNR = 10$ and maximum SNR in the multiwavelength image (thin lines).

Table 3.1: Observing setup for the high-resolution multiwavelength observations that were used for the classification.

No.	IAU Name	Observatory	Prop. ID	Band	Angular Res. [arcsec]	Cont. Sens. [mJy beam^{-1}]	Ref.
8	HERSJ020941.2+001558	ALMA	2017.1.00814.S	4	0.214	0.0119	
				8	0.256	0.0753	
				9	0.245	0.1984	
			2017.1.01230.S	3	0.064	0.0211	
			2017.1.01214.S	3	0.314	0.0123	
				6	0.420	0.0696	
			2019.1.01197.S	3	0.107	0.0128	
					0.397	0.0135	
				6	0.129	0.0417	
					0.400	0.0847	
			2019.1.01365.S	4	0.724	0.0105	
11	HATLASJ083051+013225	ALMA	2013.1.00358.S	7	0.147	0.1044	
			2015.1.01320.S	4	0.366	0.0117	
			2018.1.01710.S	4	0.061	0.0100	
				6	0.104	0.0145	
			2019.1.00663.S	6	0.335	0.0167	
			2019.1.00533.S	6	0.399	0.0121	
					0.484	0.0128	
12	HERMESJ100144+025709	ALMA	2011.0.00539.S	7	0.523	0.1221	
15	HATLASJ114638−001132	ALMA	2015.1.01042.S	6	0.488	0.0277	
			2018.1.00966.S	6	0.279	0.0317	
			2019.1.00426.S	4	0.032	0.0136	

Notes: Col. (1): Source reference number. Col. (2): IAU name of the *Herschel* detection. Col. (3): Facility used to observe the candidate. Col. (4): Proposal ID for the observations. Col. (5): Band or reference frequency of the observations. Col. (6): Angular resolution of the beam or configuration for the SMA observations. Col. (7): Continuum sensitivity per beam.

Table 3.1 (cont.)

No.	IAU name	Observatory	Prop. ID	band	Angular res. [arcsec]	Cont. sens. [mJy beam^{-1}]
16	HATLASJ125126+254928	ALMA	2018.1.00526.S	6	1.376	0.2035
18	HATLASJ133008+245900	ALMA	2018.1.00966.S	6	0.524	0.0214
				7	0.434	0.0185
19	HATLASJ133846+255057	SMA	2018B-S020	340 GHz	0.78	–
20	HATLASJ142935−002837	ALMA	2011.0.00476.S	6	0.589	0.0440
			2013.1.00358.S	7	0.143	0.0885
26	HELMSJ001626.0+042613	ALMA	2013.1.00358.S	7	0.140	0.1007
			2016.1.01188.S	6	0.031	0.0142
28	HELMSJ004723.6+015751	ALMA	2013.1.00358.S	7	0.138	0.1007
31	HATLASJ085359+015537	ALMA	2013.1.00164.S	6	0.452	0.0311
			2013.1.00358.S	7	0.152	0.1044
			2015.1.01042.S	7	0.469	0.0534
			2016.1.00282.S	6	0.155	0.0246
			2017.1.00027.S	6	0.026	0.0146
34	HERMESJ105751+573026	SMA	2010B-S049	340 GHz	0.38	–
35	HATLASJ132630+334410	ALMA	2017.1.01214.S	3	0.495	0.0122
			2013.1.00358.S	6	0.772	0.0455
38	HERMESJ142824+352620	ALMA	2012.1.00426.S	9	0.214	0.4610
			2021.1.00353.S	3	0.155	0.0302
				7	0.244	0.0688
				8	0.378	0.1586
41	HELMSJ233441.0−065220	SMA	2010B-S049	340 GHz	0.38	–
43	HELMSJ001615.7+032435	ALMA	2013.1.00358.S	7	0.140	0.1007
44	HELMSJ002220.9−015524	ALMA	2013.1.00001.S	7	0.098	0.1036
			2015.1.01486.S	6	0.476	0.0353
				8	0.262	0.1050

Table 3.1 (cont.)

No.	IAU name	Observatory	Prop. ID	band	Angular res. [arcsec]	Cont. sens. [mJy beam^{-1}]
45	HELMSJ003814.1−002252	ALMA	2016.1.00139.S	7	0.180	0.0675
46	HELMSJ003929.6+002426	ALMA	2016.1.00139.S	7	0.180	0.0675
47	HELMSJ004714.2+032454	ALMA	2013.1.00358.S	7	0.139	0.1007
48	HELMSJ005159.4+062240	ALMA	2013.1.00358.S	7	0.140	0.1007
			2017.1.00027.S	6	0.028	0.0156
49	HATLASJ005724.2−273122	ALMA	2018.1.00526.S	6	0.657	0.2117
50	ALMA	2013.1.00781.S		6	0.168	0.2002
			2013.1.00749.S	8	0.107	0.1210
			2015.1.01528.S	7	0.174	0.2537
51	HERMESJ033211−270536	ALMA	2011.0.00539.S	7	0.399	0.1373
52	HERMESJ044154−540352	ALMA	2011.0.00539.S	7	0.485	0.1934
53	HATLASJ083932−011760	ALMA	2018.1.00526.S	6	0.690	0.2372
54	HATLASJ091841+023048	ALMA	2016.1.00282.S	6	0.323	0.0168
			2017.1.01694.S	3	1.553	0.0191
55	HATLASJ113526−014606	ALMA	2016.1.01371.S	8	0.098	0.1739
			2018.1.00861.S	6	0.263	0.0208
				7	0.206	0.0192
			2019.1.00663.S	6	0.455	0.0209
56	HATLASJ115433.6+005042	ALMA	2019.1.01784.S	7	0.099	0.1679
57	HATLASJ120127.6−014043	SMA	2016B-S003	340 GHz	0.50	–
58	HATLASJ131611+281220	NOEMA		255 GHz		
59	HATLASJ134429+303036	SMA	2011B-S044	340 GHz	0.41	–
		ALMA	2013.1.00164.S	6	0.442	0.245
			2016.1.00285.S	7	0.388	0.321
					0.494	0.393
60	HATLASJ141352−000027	ALMA	2018.1.00861.S	6	0.146	0.0219
				7	0.306	0.0334

Table 3.1 (cont.)

No.	IAU name	Observatory	Prop. ID	band	Angular res. [arcsec]	Cont. sens. [mJy beam^{-1}]
		SMA	2011A-S050	340 GHz	0.37	–
61	HATLASJ142414+022304	ALMA	2013.1.00358.S	7	0.144	0.0855
			2016.1.00284.S	8	0.745	1.2634
			2016.1.00450.S	4	0.146	0.0088
			2017.1.00029.S	3	0.094	0.0118
62	HERMESJ142826+345547	SMA	2011A-S068	340 GHz	0.88	–
63	HATLASJ230815.5−343801	ALMA	2018.1.00526.S	6	0.685	0.2432
64	HELMSJ232439.5−043936	ALMA	2013.1.00358.S	6	0.137	0.1034
			2017.1.00027.S	7	0.040	0.0178
65	HELMSJ233620.8−060828	ALMA	2013.1.00749.S	8	0.109	0.1177
			2021.1.01116.S	6	0.120	0.161

3.2.1 Results

The 77 multiwavelength follow-up observations confirm 40 candidates as lensed and 26 as unlensed. Of these, nine and two were already classified as A and D, respectively. Consequently, we find 31 more lensed objects and identify 24 individual unlensed DSFGs or overdensities of unlensed DSFGs that were previously classified as B or C. As before, we can not draw meaningful statistical conclusions for the whole *HST* sample due to the incomplete and uneven coverage and quality of the multiwavelength observations. In this case, the situation worsens with only $\sim 1/3$ of the candidates having the high-resolution interferometric data.

The number and fraction of both A and D candidates increase overall by including the multiwavelength follow-up observations. The A systems now dominate the candidate's population above $S_{500} \simeq 105$, whereas the D candidates become significant below $S_{500} \simeq 100$. As before, a tail of C candidates remains present for high flux density. Focusing now on the subsample of candidates that have a multiwavelength follow-up, we notice that the distribution of the confirmed candidates (Figure 3.12, top panel) and one of the unlensed systems (Figure 3.12, bottom panel) has a different median flux density, with the confirmed lenses being brighter at $\langle S_{500} \rangle = 141.0\,\mathrm{mJy}$, and the unlensed systems having $\langle S_{500} \rangle = 85.9\,\mathrm{mJy}$. Interestingly, the distribution of unlensed systems shows a number of extremely bright objects. Of these, a total of three systems have flux densities at 500 μm significantly above the Negrello et al. (2010) selection, with values higher than 100 mJy by at least 3σ. These systems are HATLASJ084933+021443 with $S_{500} = 208.6 \pm 8.6\,\mathrm{mJy}$, HELMSJ005258.6+061319 with $S_{500} = 155.0 \pm 7.0\,\mathrm{mJy}$, and HERMESJ022022−015329 with $S_{500} = 124\,\mathrm{mJy} \pm 8\,\mathrm{mJy}$. The first is a protocluster (Ivison et al., 2013) at $z = 2.41$ with one of its members (on the SW of the cutout) being weakly lensed by a foreground object (Bussmann et al., 2013). The second is possibly a system of two intrinsically bright, unlensed DSFGs. Lastly, the third is a single bright source (Bussmann et al., 2015) at a photometric redshift of $z = 0.21 \pm 0.14$ (Wardlow et al., 2013).

A considerable fraction (55%) of the confirmed lenses were previously classified as B with a non-negligible contribution of C (23%) candidates. Notably, the fractions of visual B and C candidates confirmed by the multiwavelength observations do not change with the flux density. Moreover, the majority of unlensed systems were visually classified as C (63%), with a minority of visual B (29%) candidates.

In the following, we plot the cutouts of the multiwavelength follow-up observations we use for the final classification overplotted to the *HST* snapshots. We show the candidates that are confirmed as lensed in Figure 3.13, the uncertain cases in Figure 3.14, and the unlensed systems in Figure 3.15.

So far, we have not included the redshift of the lenses and background sources in the lens classification to avoid adding a further layer of complexity. Nevertheless, the distance information is necessary to investigate the intrinsic properties of the lensing galaxies and the background DSFGs. We try to recover the redshift information for the confirmed system by combining a literature search with a NASA Extragalactic Database cone search. We report the results in Table 3.2 and in Figure 3.16.

We are able to recover the redshifts of 68 galaxies distributed over the 65 confirmed lens systems; of these, 31 are spectroscopic, and 37 are photometric. For the background sources,

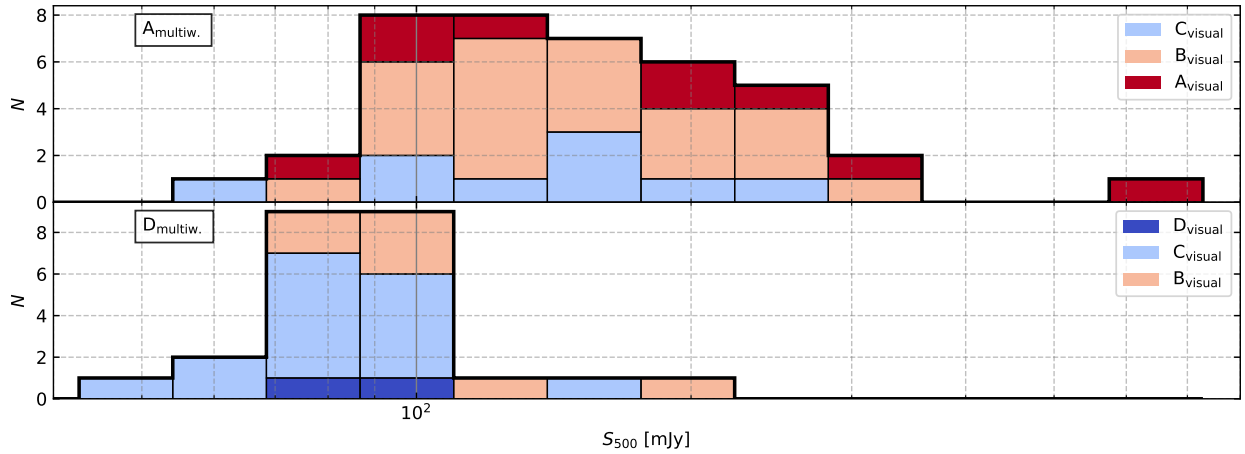

Figure 3.12: *Top panel:* Flux density distribution at 500 μm as a function of the visual + multiwavelength lens classification. *Bottom panel:* Flux density distribution at 500 μm as a function of the visual + lens classification of the systems confirmed as unlensed by multiwavelength follow-up.

we find 58 redshifts, 49 of which are spectroscopic. A fraction of these redshifts comes from recent dedicated redshift searches, like z-GAL (Cox et al., 2023) and BEARS (Urquhart et al., 2022), contributing to 12 and 4 measures, respectively.

In order to avoid further increasing the complexity of the lensed candidates classification, we decide not to use the spectroscopic information.

3.3 Summary

In summary, we classified the lens candidates on their likelihood of being lensed. To do so, we divided them into four classes, A, B, C, and D, for candidates that were lensed, likely to be lensed, uncertain, and unlensed, respectively. We performed this classification in two steps: the first one was an entirely visual inspection of the 281 *HST* snapshots around the *Herschel*/SPIRE detection, and the second one was the inclusion and visual inspection of 77 multiwavelength follow-up observations of the lensed candidates taken primarily with *ALMA*, *SMA*, and *NOEMA*. This way, we were able to find a total of 56 class A systems, 76 class B systems, and 120 class C systems, and lastly, we confirmed 29 objects belonging to class D. With the classification completed, the next step for the study of this lensed candidate sample is to try and isolate, model, and subtract the surface brightness distribution of the candidate lenses from the *HST* snapshots. To do so, we will focus on the A and B class candidates, for which we were able to guess a candidate for the lensing galaxies. When we have available high-resolution multiwavelength data, we use the position of the multiple images as an aid in identifying the possible lens location. This greatly improves the lens surface brightness modelling and subtraction in the case the candidates were classified as either visual B or C.

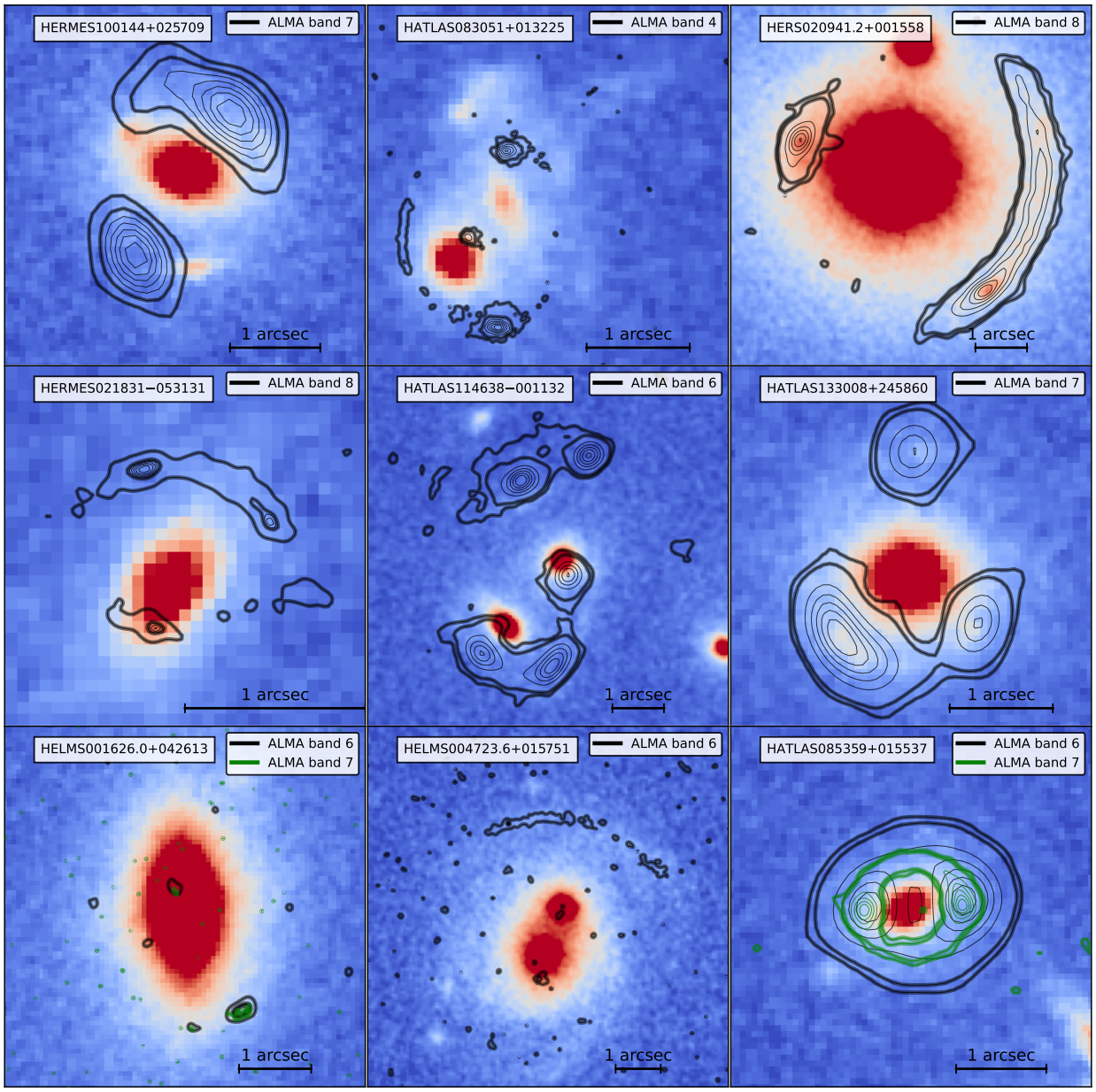

Figure 3.13: Cutouts of the strongly lensed candidates classified as A by multiwavelength follow-up observations. The black or green contours correspond to the high-resolution sub-mm observations used for the multi-wavelength lens classification. The contours are taken at two levels corresponding to $SNR = 5$ and 10 (thick curves), and five uniformly spaced levels between the $SNR = 10$ and the maximum SNR in the multiwavelength image (thin curves). All the panels share the same colour bar extending from -20 ADU, corresponding to the blue, to 100 ADU in white, and then from white to red at 500 ADU.

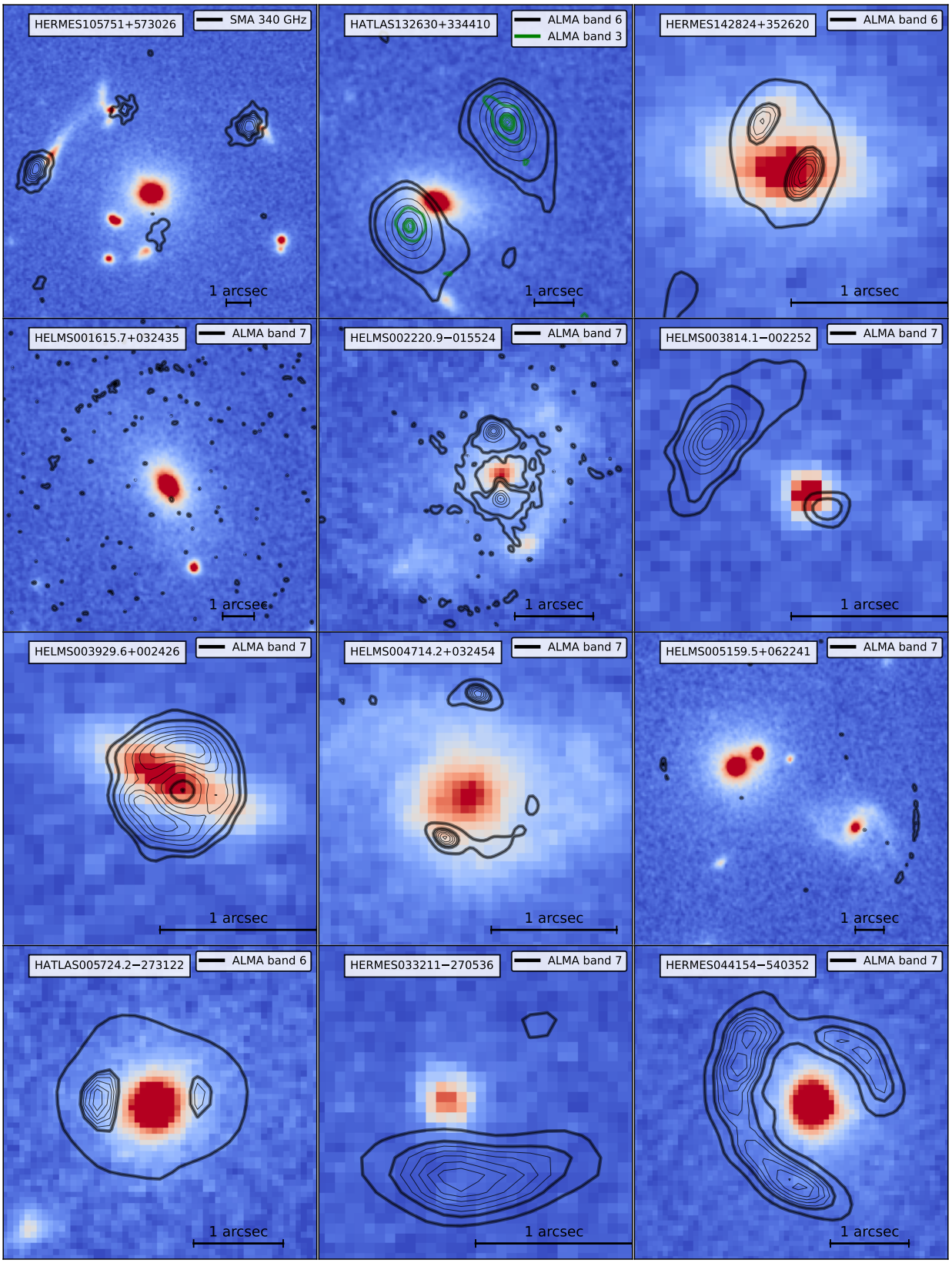

Figure 3.13 (cont.)

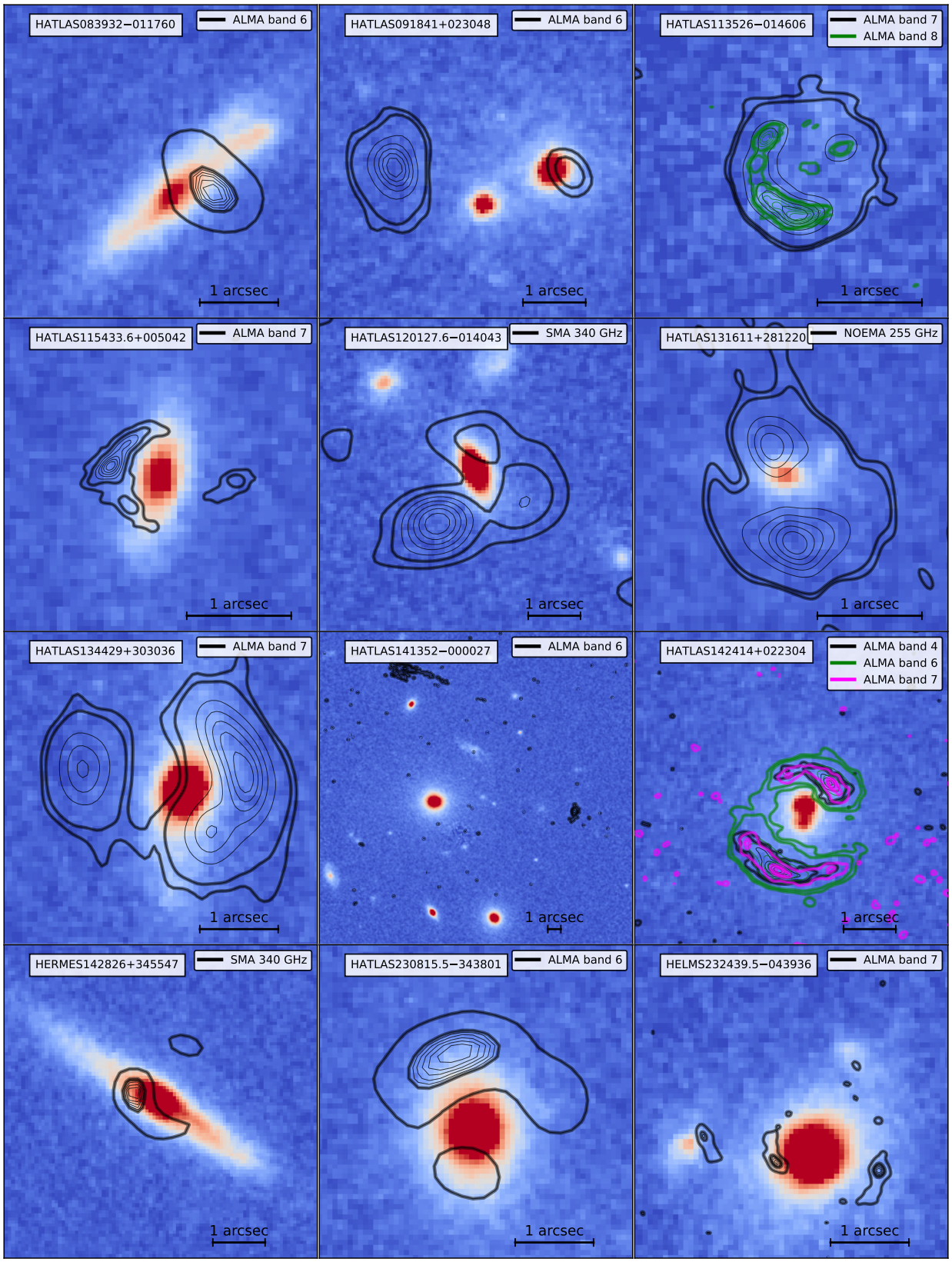

Figure 3.13 (cont.)

Table 3.2: Redshift of the candidate lenses and background sources of the confirmed lensing systems.

No.	Name	z_l	Ref.	z_s	Ref.
(1)	(2)	(3)	(4)	(5)	(6)
1	HATLASJ000330.6−321136	(0.38 ±0.10)	Sh21	3.077	Ur22
2	HATLASJ000912.7−300807	(0.28 ±0.08)	Sh21	(1.19 ±0.10)	Zh18
3	HELMSJ001353.5−060200	(0.60 ±0.18)	Na16	1.948	Co23
4	HELMSJ003619.8+002420	0.257573	Na16	1.617	Co23
5	HELMSJ005841.2−011149	(0.38 ±0.08)	Na16	1.498	Co23
6	HERSJ011722.3+005624	(0.87 ±0.05)	Na16	2.469	Co23
7	HERSJ012620.5+012950	(0.43 ±0.05)	Na16	1.449	Co23
8	HERSJ020941.2+001558	0.201854	Na16	2.55293	Ge15
9	HERMESJ032637−270044	–	–	–	–
10	HERMESJ033732−295353	(0.19 ±0.05)	Sh21	–	–
11a	HATLASJ083051+013225$_1$	0.626	Bu13	3.6345	Ya17
11b	HATLASJ083051+013225$_2$	1.002	Bu13	3.6345	Ya17
12	HERMESJ100144+025709	0.608	Ca14	–	–
13	HERMESJ103827+581544	0.591465	Al17	–	–
14	HERMESJ110016+571736	0.780518	Al17	–	–
15	HATLASJ114638−001132	1.2247	Bu13	3.2596	Y17
16	HATLASJ125126+254928	(0.62 ±0.10)	Ne17	3.4419	Ba20
17	HATLASJ125760+224558	0.555449	Al17	(1.53 ±0.30)	Ne17
18	HATLASJ133008+245860	0.4276	Bu13	3.112	Ca14
19	HATLASJ133846+255057	(0.42 ±0.10)	Ne17	(2.34 ±0.40)	Ba18
20	HATLASJ142935−002837	0.21844	Me14	1.0271	Me14
21	HERMESJ171451+592634	1.236	Sh21	3.17844	HC16
22	HERMESJ171545+601238	(0.40 ±0.09)	Sh21	2.264	Ca14
23	HATLASJ225844.7−295124	(0.69 ±0.21)	Sh21	(2.48 ±0.040)	Ba18
24	HELMSJ232210.3−033559	(0.14 ±0.09)	Na16	4.688	Co23
25$_1$	HATLASJ233037.2−331217$_1$	(0.66 ±0.17)	Sh21	2.170	Ur22
25$_2$	HATLASJ233037.2−331217$_2$	(0.66 ±0.17)	Sh21	2.170	Ur22
26	HELMSJ001626.0+042613	0.2154	Am18	2.509	Na16
27	HATLASJ002624.8−341737	(0.93 ±0.35)	Wa22	3.050	Ur22
28	HELMSJ004723.6+015751	0.3650	Am18	1.441	Na16
29	HERSJ012041.6−002705	(0.73 ±0.04)	Na16	2.0151	Co23
30	HATLASJ085112+004934	(0.66 ±0.32)	Sh21	(1.77 ±0.27)	MG19
31	HATLASJ085359+015537	(1.16 ±0.22)	Sh21	2.0925	Ya16

Notes: Col. (1): Source reference number. Col. (2): IAU name of the *Herschel* detection. Cols. (3) and (4): Redshift of the lens candidate and reference. Cols. (5) and (6): Redshift of the background source and reference. HerBS4 is a multiple-lens system with two lenses at different redshifts. The bracketed values are photometric redshifts. Following are the abbreviations used for the references that are not already included in Table 2.1: As16: Asboth et al. (2016); Ba20: Bakx et al. (2020); Co23: Cox et al. (2023); HC16: Hernán-Caballero et al. (2016); MG19: Manjón-García et al. (2019); Ne20: Neri et al. (2020); Ok21: Okido et al. (2021); St14: Stanford et al. (2014); Wa22: Ward et al. (2022); Ya16: Yang et al. (2016).

Table 3.2 (cont.)

No.	Name	z_l	Ref.	z_s	Ref.
(1)	(2)	(3)	(4)	(5)	(6)
32	HERMESJ104549+574512	(0.20 ±0.02)	Wa13	2.991	Wa13
33	HERMESJ105551+592845	(0.38 ±0.11)	Wa13	1.699[a]	Wa13
34	HERMESJ105751+573026	(0.60 ±0.04)	Ga11	2.9575	Ga11
35	HATLASJ132630+334410	0.7856	Bu13	2.951	Bu13
36_1	HATLASJ133543+300404$_1$	0.9825	St14	2.685	Ca14
36_2	HATLASJ133543+300404$_2$	0.9845	St14	2.685	Ca14
36_3	HATLASJ133543+300404$_3$	0.9815	St14	2.685	Ca14
36_4	HATLASJ133543+300404$_4$	0.9945	St14	2.685	Ca14
37	HATLASJ142140+000448	(1.11±0.41)	Sh21	2.781	Co23
38	HERMESJ142824+352620	1.034	Bo06	1.325	Bo06
39	HATLASJ223753.8−305828	(0.54±0.14)	Sh21	(2.13±0.38)	Wa22
40	HATLASJ225250.7−313657	(0.69±0.26)	Sh21	2.433	Ur22
41	HELMSJ233441.0−065220	–	–	1.9047	Co23
42	HELMSJ233633.5−032119	–	–	2.3353	Co23
43	HELMSJ001615.7+032435	0.663	Na16	2.765	Na16
44	HELMSJ002220.9−015524	(0.90±0.15)	Sh21	5.162	As16
45	HELMSJ003814.1−002252	(0.17±0.08)	Na16	4.9841	Co23
46	HELMSJ003929.6+002426	(0.72±0.23)	Sh21	2.848	Co23
47	HELMSJ004714.2+032454	(0.48±0.08)	Na16	1.19	Na16
48_1	HELMSJ005159.4+062240$_1$	0.60266	Ok21	2.392	Na16
48_3	HELMSJ005159.4+062240$_3$	0.59852	Ok21	2.392	Na16
49	HATLASJ005724.2−273122	(0.89±0.41)	Wa22	3.261	Ur22
50	HERMESJ021831−053131	1.350	Wa13	3.3950	Wa13
51	HERMESJ033211−270536	–	–	–	–
52	HERMESJ044154−540352	–	–	–	–
53	HATLASJ083932−011760	(0.42±0.12)	Sh21	2.669	Co23
54_1	HATLASJ091841+023048$_1$	(0.91±0.32)	Sh21	2.5811	Ha12
54_2	HATLASJ091841+023048$_2$	(0.91±0.32)	Sh21	2.5811	Ha12
55	HATLASJ113526−014606	–	–	3.1276	Ha12
56	HATLASJ115433.6+005042	(0.52±0.11)	Sh21	(3.90±0.50)	Ba20
57	HATLASJ120127.6−014043	(0.88±0.35)	Sh21	(4.06±0.38)	MG19
58	HATLASJ131611+281220	(0.90±0.13)	Be21	2.9497	Ne20
59	HATLASJ134429+303036	0.6721	Bu13	2.3010	Ha12
60_1	HATLASJ141352−000027$_1$	0.5478	Bu13	2.4782	Ha12
60_3	HATLASJ141352−000027$_3$	0.5494	Bu13	2.4782	Ha12
61_1	HATLASJ142414+022304$_1$	0.595	Bu13	4.243	Co11
61_2	HATLASJ142414+022304$_2$	0.595	Bu13	4.243	Co11
62	HERMESJ142826+345547	0.414	Wa13	2.804	Wa13
63	HATLASJ230815.5−343801	(0.72±0.21)	Wa22	(4.03±0.38)	MG19
64	HELMSJ232439.5−043936	(0.67±0.26)	Sh21	2.473	Na16
65	HELMSJ233620.8−060828	0.3958	Na16	3.434	Na16

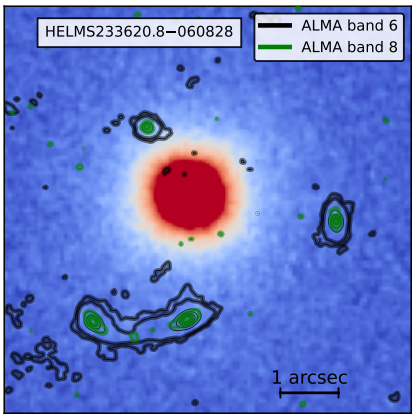

Figure 3.13 (cont.)

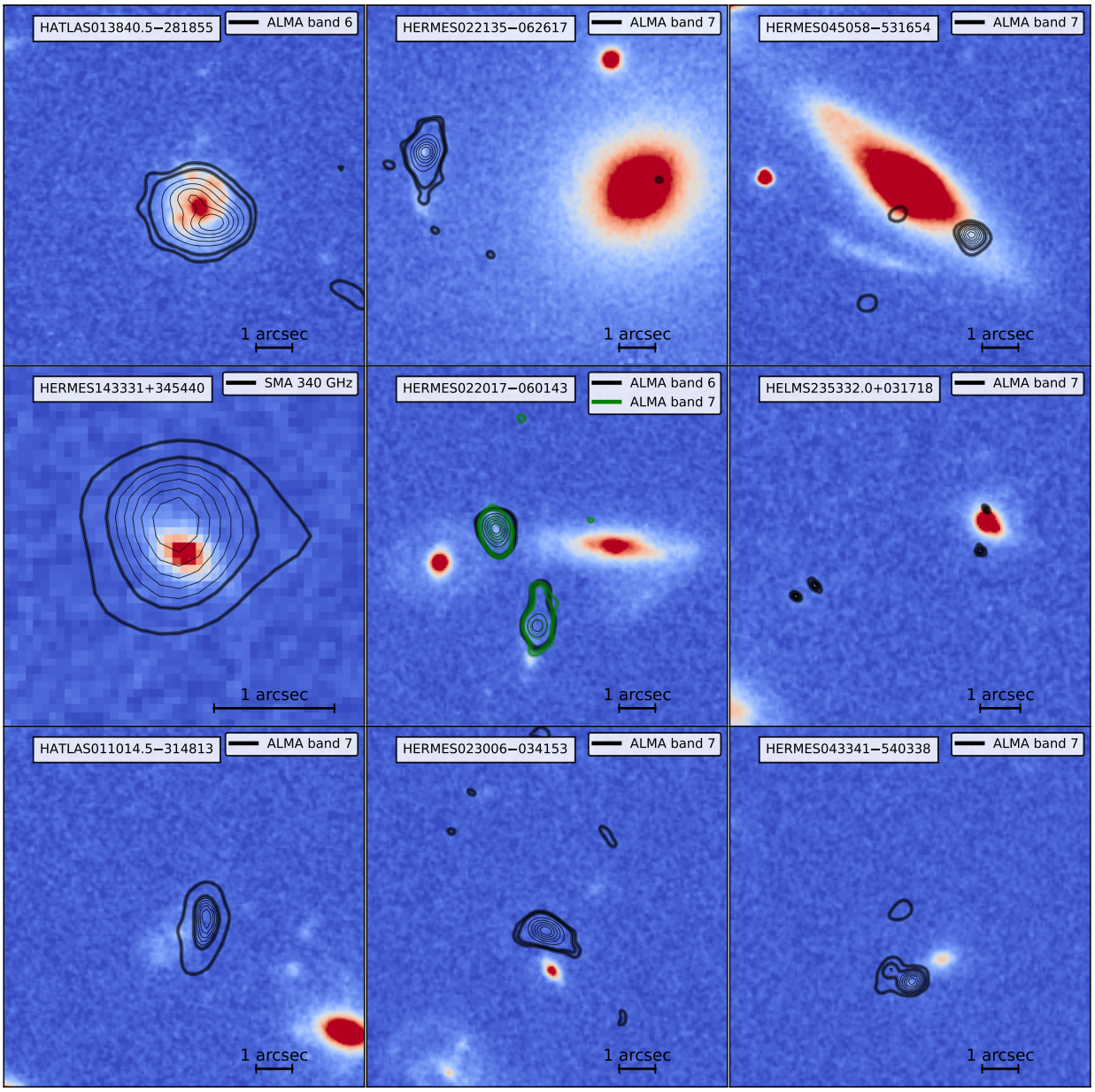

Figure 3.14: Cutouts of the strongly lensed candidates that are of uncertain nature after the inclusion of sub-mm follow-up observations. The black or green contours correspond to the high-resolution sub-mm observations used for the multi-wavelength lens classification. The contours are taken at two levels corresponding to $SNR = 5$ and 10 (thick curves), and five uniformly spaced levels between the $SNR = 10$ and the maximum SNR in the multiwavelength image (thin curves). All the panels share the same colour bar extending from -20 ADU, corresponding to the blue, to 100 ADU in white, and then from white to red at 500 ADU.

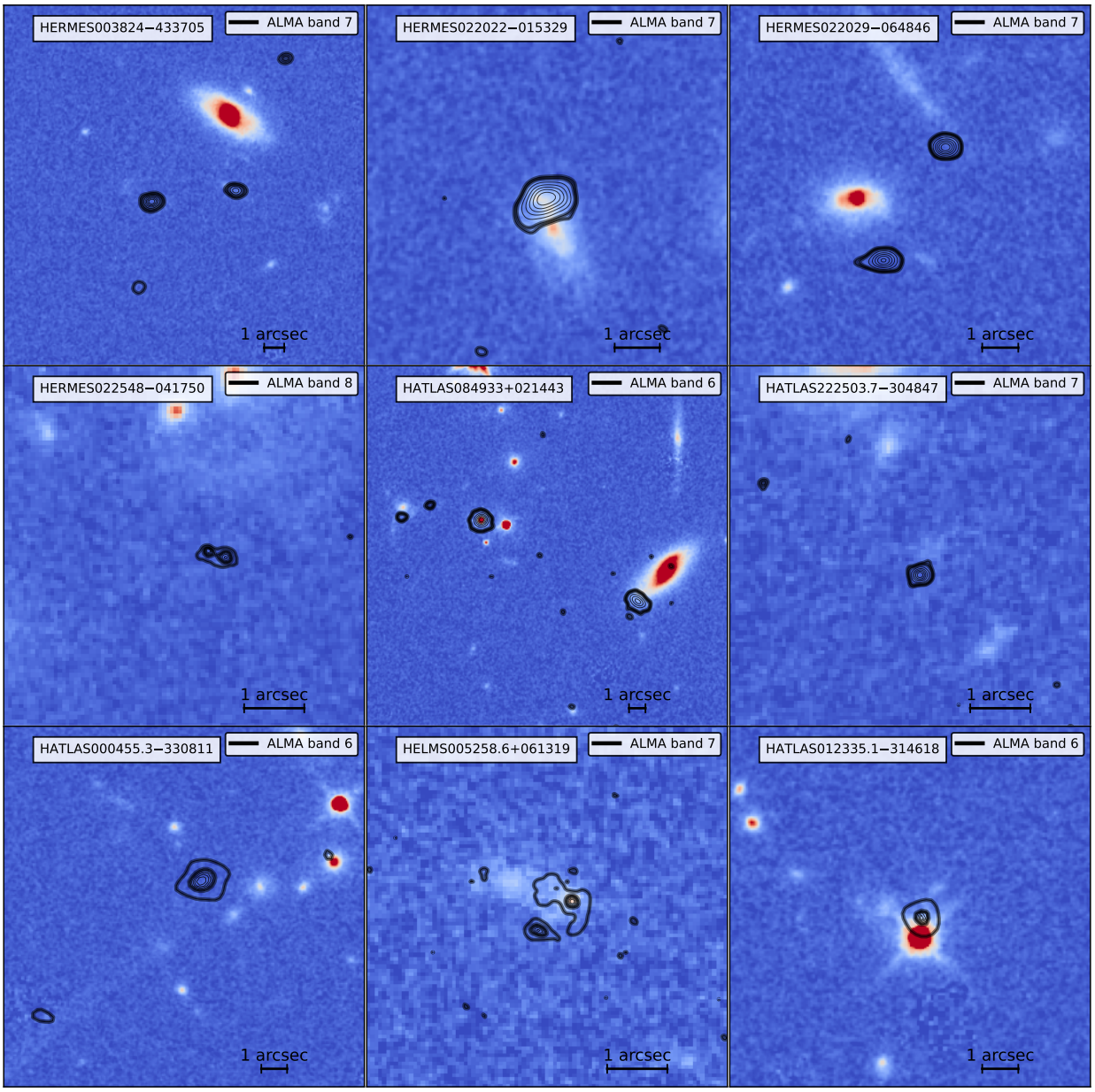

Figure 3.15: Cutouts of the strongly lensed candidates classified as D by multiwavelength follow-up observations. The black or green contours correspond to the high-resolution sub-mm observations used for the multi-wavelength lens classification. The contours are taken at two levels corresponding to $SNR = 5$ and 10 (thick curves), and five uniformly spaced levels between the $SNR = 10$ and the maximum SNR in the multiwavelength image (thin curves). All the panels share the same colour bar extending from -20 ADU, corresponding to the blue, to 100 ADU in white, and then from white to red at 500 ADU.

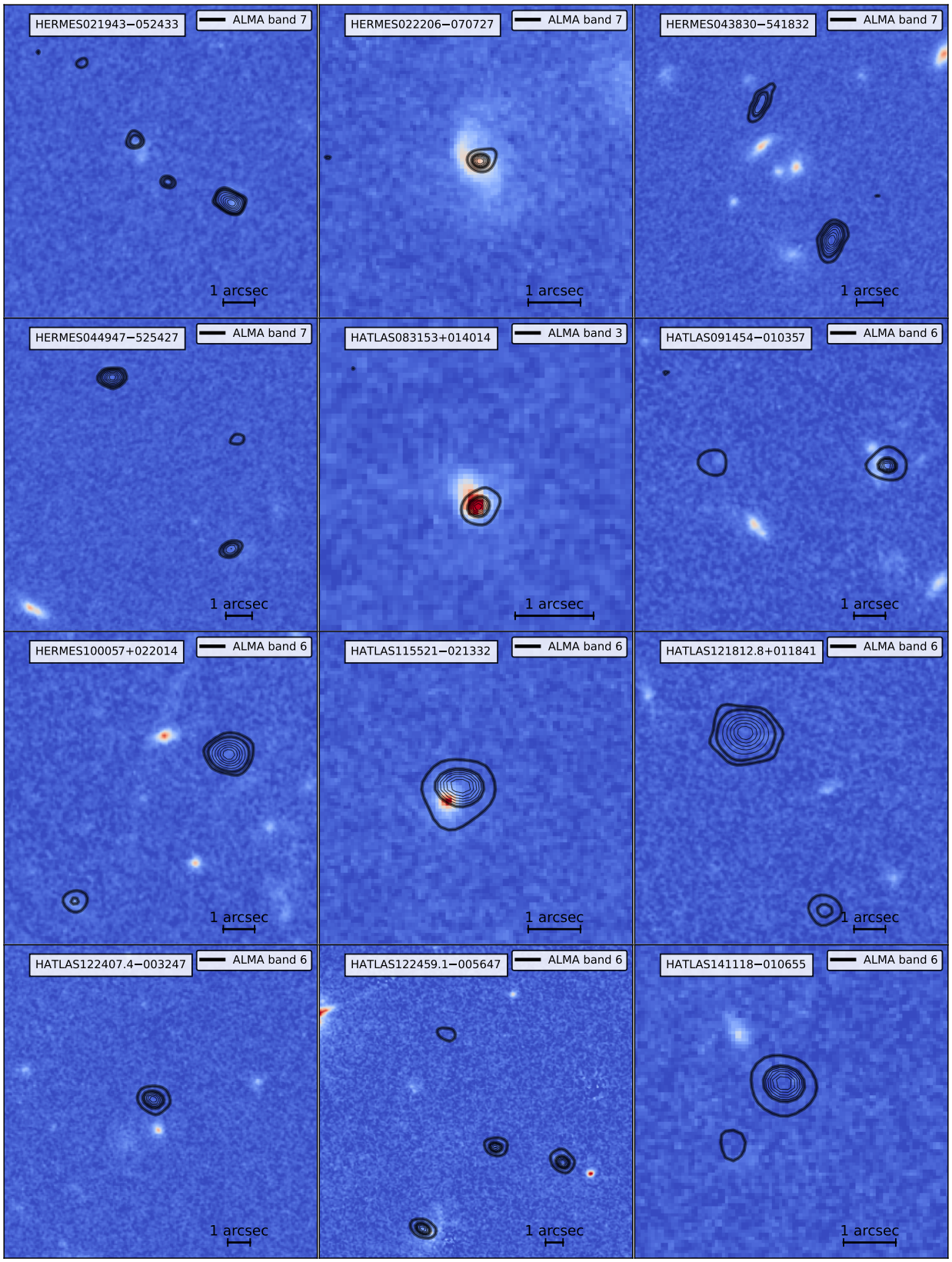

Figure 3.15 (cont.)

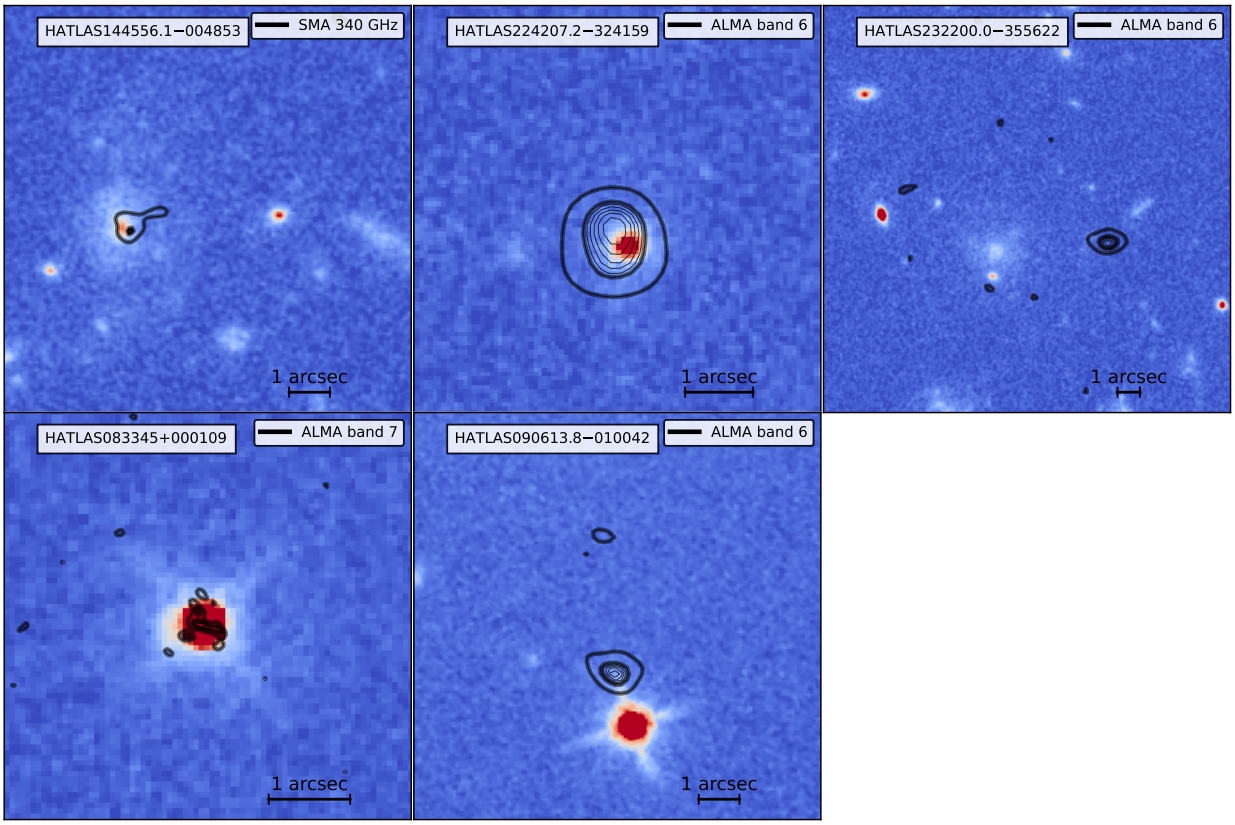

Figure 3.15 (cont.)

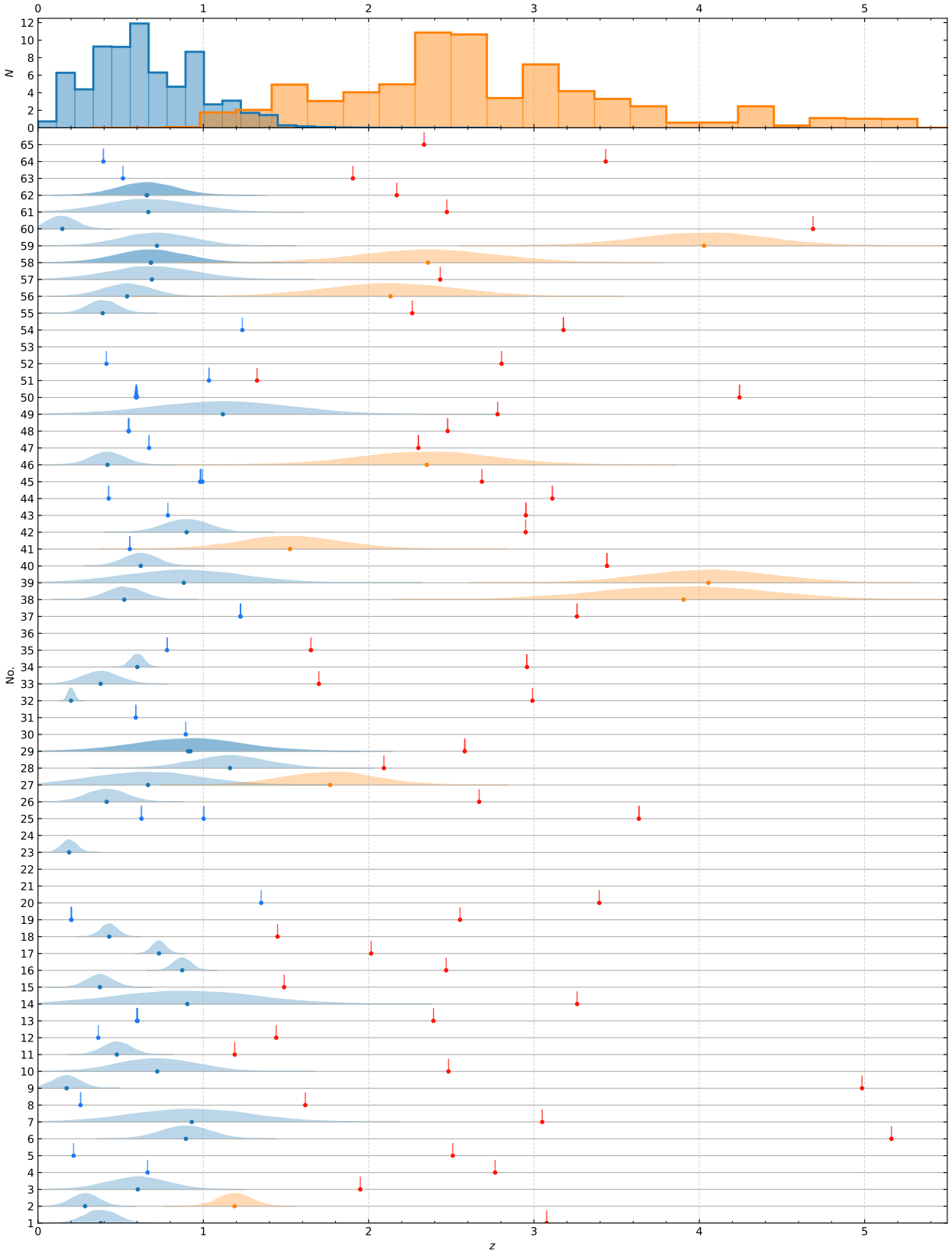

Figure 3.16: *Top panel:* Redshift distribution of the confirmed lenses (blue) and background sources (orange). *Bottom panel:* Redshift of the candidate lenses and background sources.

Chapter 4

Lens subtraction and lens modelling

Having classified the candidates and identified possible lenses, the next issue is how to better study the lensing galaxies and background sources. To address them, it is necessary to identify and isolate the lenses from the background sources, which can be done by modelling and subtracting their surface brightness distribution. This is described in this chapter. In Section 4.1, we present the methodology and fitting procedure we applied to model and subtract the surface-brightness distribution of the lensing galaxies. We then detail the set of Monte Carlo simulations we performed to estimate the uncertainties of the best-fitting parameters of the surface brightness models. To complement the surface-brightness fitting procedure, we give the modelling of HERSJ012620.5+012950 as an example. Lastly, we discuss an update to the lens classification consisting of a visual inspection after the removal of the lenses. Without the contamination of the lensing galaxies, it is then possible to focus on the background sources. These can be reconstructed by applying lens modelling techniques revealing their unlensed surface brightness distribution. This is a direct way of studying the DSFG morphology and stellar emission. In Section 4.2, we present the method and modelling approach used for the lens modelling. Specifically, we focus on how we computed the magnifications and reconstructed background-source sises.

In the case of gravitationally lensed systems observed in the optical or near-IR, the lens contribution generally dominates the system surface brightness and, in some cases, can cover or blend with the lensed images of the background source. Different surface brightness modelling approaches can be used to model the lens surface brightness contribution. The resulting best-fitting surface-brightness distribution can be subtracted from the images to reveal the background galaxies. This allows to: (i) revise the visual lens classification according to the structures previously hidden by the lens (e.g., Negrello et al., 2014); (ii) study of some photometric properties of the lens candidates such as their magnitudes, sizes and concentrations (e.g., Messias et al., 2014); (iii) reconstruct the surface brightness distribution of the background source (e.g., Dye et al., 2014).

4.1 Surface brightness modelling and subtraction

For the lens surface brightness analysis, we focus on the 65 A and 67 B candidates that represent the most promising systems for which we can identify a possible lensing galaxy. For the systems confirmed as lensed by multiwavelength data alone, we use the location of the background source sub-mm emission to identify the lenses in the *HST* observations. We group all the systems according to the following configurations:

- systems in which an isolated galaxy is acting as a lens. In this case, we model only this single object (type 1);
- systems in which two or three galaxies act as lenses (e.g., they are very close or even blended, and the lensing features are consistent with multiple lenses). In this case, we model all the galaxies at the same time (type 2);
- systems in which more than one galaxy is visible in the foreground, but they are either sufficiently small or distant with respect to each other that they can be separately modelled (type 3);
- one system which only shows lensed images but no lens, likely due to a combination of high redshift and obscuration (HATLASJ113526−014606; see Giulietti et al. 2023 for details). This system will not be included in the lens surface brightness modelling.

It is worth noticing that for type 2 and type 3 systems, we can not be sure whether all the galaxies are contributing to the lensing, as, in most cases, we do not know the redshift of all the galaxies. Therefore, we can not rule out the possibility that they are unrelated field objects.

4.1.1 Methods

For an extended light source, the surface brightness can be defined as the observed flux within a particular solid angle. The curves connecting the points with the same surface brightness are called isophotes. For a galaxy, it is possible to study how the surface brightness of the isophotes varies as a function of the distance from the centre. This can be done either along a specific direction, by means of 1D surface-brightness profiles, or onto the entire image by considering the 2D distribution of the surface brightness. In order to best characterise the galaxies acting as lenses and provide the best-fitting model of their surface brightness, we used either a parametric or a non-parametric approach depending on the lens morphology and configuration of the lensing system. Parametric models describe the radial behaviour of surface brightness using analytical functions that depend on various parameters. In contrast, non-parametric models describe the behaviour of the surface brightness without adopting an a priori parametrisation.

For the parametric modelling, we adopt the Galaxy Surface Photometry 2-Dimensional Decomposition algorithm (`GASP2D`; Méndez-Abreu et al. 2008, 2017) to model the type 1 and type 3 lensing systems and the Galaxy Fitting algorithm (`GALFIT`; Peng et al. 2002,

2010) for the type 2 lensing systems. GASP2D has the advantage of automatically setting the initial guess values needed to fit the galaxy image, whereas GALFIT allows us to perform the simultaneous fit of multiple systems. Both GASP2D and GALFIT algorithms are based on a χ^2 minimisation. Thus, it is essential to adopt initial guesses for the free parameters as close as possible to their actual values. This choice ensures that the iteration procedure does not stop on a local minimum of the χ^2 distribution.

We adopt the non-parametric Isophote Fitting algorithm (ISOFIT; Ciambur 2015) to model highly-inclined disk lenses for which GASP2D and GALFIT fail. We point out in the source-by-source descriptions the cases for which we made exceptions to the above prescriptions.

GASP2D

GASP2D is an algorithm developed in IDL[1] by Méndez-Abreu et al. (2008, 2017) that allows building parametric models of the surface brightness distribution of galaxies.

Each component of the galaxy is associated with a parametric profile characterised by elliptical and concentric isophotes with constant ellipticity, position angles, and a common centre. GASP2D allows modelling spheroids using the Sérsic (Sérsic, 1968), King (King, 1962), or de Vaucouleurs law (de Vaucouleurs, 1948). We model disks using a double exponential profile (Pohlen &Trujillo, 2006). We model bars using Ferrers ellipsoids (Aguerri et al., 2009), the Freeman (Freeman, 1966), or Prieto law (Prieto et al., 1997). We fit nuclear point sources (NPS) with a Moffat function (Moffat, 1969), and rings are modelled using a Gaussian profile. The surface brightness distribution of a galaxy can be written as the summation over all radii of such parametric components.

Since most of the lensing galaxies have an ETG-like morphology, we primarily use Sérsic profiles; in a few cases, we also adopt Gaussian and exponential profiles. The surface brightness of a Sérsic profile is a function of seven parameters and is defined as:

$$I(r) = I_{\rm e} e^{-b_n \left[\left(\frac{r}{R_{\rm e}}\right)^{\frac{1}{n}} - 1 \right]}, \tag{4.1}$$

where $I_{\rm e}$ is the effective surface brightness, $b_n = 1.9992n - 0.3271$, n is the Sérsic index, and $R_{\rm e}$ is the effective radius. For a 2D image the radius r is defined as a function of the position (x, y) as $r = \sqrt{(x'^2 + (y'/q)^2)}$ where $x' = -(x - x_0)\sin({\rm PA}) + (y - y_0)\cos({\rm PA})$ and $y' = (x - x_0)\cos({\rm PA}) + (y - y_0)\sin {\rm PA})$, with x_0 and y_0 being the centre coordinates, q and PA the axis ratio and position angle of the isophotes.

For $n = 1$ the Sérsic law corresponds to an exponential profile. Usually, the exponential profile can be written as:

$$I(r) = I_0 e^{-r/h}, \tag{4.2}$$

where h is the disk scale length, which is given by $h = R_{\rm e}/b_1$, while $I_0 = I_{\rm e} e^{b_1}$ is the central surface brightness.

For $n = 0.5$, the Sérsic law is equivalent to a Gaussian profile, usually defined as:

$$I(r) = I_0 e^{-\frac{r^2}{2\sigma^2}} \tag{4.3}$$

[1] IDL is distributed by *ITT Visual Information Solution*. It is available at http://www.ittvis.com.

where σ is the Gaussian standard deviation corresponding to $\sigma = R_e/\sqrt{2b_{0.5}}$, and $I_0 = I_e e^{b_{0.5}}$ is the central surface brightness.

Several free parameters define each parametric profile. To determine the best-fitting parameters that define the various components of a galaxy, `GASP2D` uses the Levenberg-Marquardt nonlinear least squares method (Press et al., 1992) to minimise the χ^2 defined as:

$$\chi^2 = \sum_{i=1}^{N} \frac{[I_{\rm model}(x_i, y_i) - I_{\rm galaxy}(x_i, y_i)]^2}{I_{\rm galaxy}(x_i, y_i) + I_{\rm sky}(x_i, y_i) + RON_i^2}, \tag{4.4}$$

where the summation $\sum_{i=1}^{N}$ is done over all pixels of the galaxy. $I_{\rm model}(x_i, y_i)$, $I_{\rm galaxy}(x_i, y_i)$, and $I_{\rm sky}(x_i, y_i)$ are the values of the model surface-brightness distribution, galaxy surface brightness, and the sky surface brightness, respectively, at the i-th pixel, and RON_i is the instrumental readout noise calculated at the i-th pixel.

The first step is the minimisation process to set initial estimates for the free parameters of the various components. We derive these initial values from a 1D surface brightness profile extracted from the image in order to reduce the complexity of the fitting process. If the galaxy exhibits a disk-like component, its values can be extrapolated by focusing on the behaviour of the surface brightness at large radii, where the contribution of the disk is expected to dominate the galaxy surface brightness and have an exponential profile. The resulting 1D profile of the disk is subtracted from that of the galaxy. The surface brightness profile must be visually inspected when dealing with a barred galaxy. The value of the surface brightness at the characteristic constant section, the distance to the 'knee' formed at the end of the constant section of the bar, the position angle, and the ellipticity calculated at the knee of the bar are used as initial parameter estimates.

We use all these estimates to initialise the minimisation process of the χ^2. The free parameters can vary until the convergence condition is met, i.e., where the χ^2 is minimum, and its variation between two successive steps is not larger than a certain threshold. The convolution of the galaxy model with the PSF is performed before calculating the χ^2 using the Fast Fourier Transform algorithm (Press et al., 1992). The galaxy model convolved with the PSF is then subtracted from the galaxy image to obtain a residual image.

`GALFIT`

`GALFIT` is an algorithm developed in `C`[2] by Peng et al. (2002, 2010) that allows building parametric models of the surface brightness distribution of galaxies.

In general, `GALFIT` resembles `GASP2D` as they are both parametric algorithms. Nevertheless, a few key differences exist. First of all, `GALFIT` does not estimate the initial parameters for the 2D surface brightness fitting. As such, the starting point of the fit needs to be given by hand during the component definition. Secondly, `GALFIT` allows to fit components with different centres. This property becomes very relevant when trying to model systems of blended galaxies simultaneously, where masking each separate component is not very effective. Moreover, leaving the centres free is helpful in a few lensing galaxies with off-centred

[2] https://users.obs.carnegiescience.edu/peng/work/galfit/galfit.html

surface brightness components. Finally, we prefer GALFIT when modelling the spiral structure of the lensing galaxies.

GALFIT definition of the Sérsic profile is very similar and easily comparable to the one used in GASP2D. Indeed, instead of using the effective surface brightness I_e, GALFIT adopts the total magnitude of the component. This magnitude can be written as a function of the parameters adopted by GASP2D, exposure time, and magnitude zero point of each snapshot. Hence, the conversion between the two definitions is immediate.

Firstly, GALFIT sets a parametric function to describe the radial dependence of the surface brightness (e.g., a Sérsic profile). Then, it rotates the coordinate system to allow the spiral structure to form. This coordinate rotation is also a function of the radius. In our case, we use a power law profile coupled with a hyperbolic tangent to generate a 'bar' extending into the centre of the lensing galaxy. A schematic description of the coordinate rotation can be given as:

$$\theta(r) = \theta_{\rm out}\ \tanh(r_{\rm in}, r_{\rm in}, \theta_{\rm incl}, \theta^{\rm sky}_{\rm PA}; r)\left[\frac{1}{2}\left(\frac{r}{r_{\rm out}}+1\right)\right]^{\alpha}, \tag{4.5}$$

where $\theta_{\rm out}$ is the angle rotation at $r_{\rm out}$, $r_{\rm in}$ is the 'bar' radius (i.e., the distance at which the rotation angle corresponds to 20 deg), α is the asymptotic power-law slope, $\theta_{\rm incl}$ is the inclination of the disk (where $\theta_{\rm incl} = 0$ deg corresponds to a face-on view and $\theta_{\rm incl} = 90$ deg to the edge-on view) and $\theta^{\rm sky}_{\rm PA}$ is the position angle of the spiral structure. Note that the 'bar' radius is a mathematical feature to give the rotation function as much flexibility as possible. So, it is not necessarily related to a physical component.

The thickness of the spiral structure is controlled by the axis ratio q of the profile being modified by the hyperbolic tangent or Fourier modes. More details on the exact definition of the hyperbolic tangent and related parameters are given in GALFIT user manual[3] and in Peng et al. (2010).

ISOFIT

ISOFIT (Ciambur, 2015) is a method that allows to build non-parametric models of the galaxy surface brightness, and it is an extension of the ELLIPSE module in IRAF[4].

The galaxy isophotes are interpolated with ellipses, adding perturbations in the form of a Fourier series expansion in terms of the azimuthal angle ϕ to describe variations from the simple ellipse shape. These perturbations are described through the coefficients of the Fourier harmonics A_n and B_n (Carter, 1978; Jedrzejewski, 1987).

In ELLIPSE, the galaxy isophotes, which are not necessarily concentric, are interpolated on a predefined set of points along the major axis. At each point, the starting isophote consists of a pure ellipse. The initial estimates of the centre coordinates, ellipticity, and position angle are manually given as input.

Subsequently, the galaxy is sampled along the elliptical path defined by the initial isophote, resulting in the variation of surface brightness as a function of the azimuthal angle. The difference between the actual isophote and this model is represented through a Fourier expansion,

[3] https://users.obs.carnegiescience.edu/peng/work/galfit/galfit.html
[4] https://iraf-community.github.io/

where only the $A_{1,2}$ and $B_{1,2}$ coefficients are considered non-zero, corresponding to the centre coordinates, ellipticity, and position angle. The best-fitting estimates of these coefficients are obtained by minimising the χ^2 value.

Higher-order harmonics are added by updating the model definition and recalculating the χ^2. Including these components improves the accuracy of the model. The model of the sampled surface brightness on the isophotes produced by `ELLIPSE` can be written in terms of the coefficients of the Fourier expansion as:

$$I_{\rm model}(\phi) = \langle I_{\rm ell} \rangle + \sum_n [A_n \cos(n\phi) + B_n \sin(n\phi)], \tag{4.6}$$

where $\langle I_{\rm ell} \rangle$ is the average surface brightness along an ellipse.

Unfortunately, when galaxies exhibit particularly complex shapes, such as edge-on disks or significant deviations from the elliptical shape, the resulting `ELLIPSE` model no longer converges to realistic solutions (see, Ciambur, 2015, for details). This effect is caused by the way `ELLIPSE` samples and parameterises the ellipses. The models are constructed based on uniformly spaced intervals in the azimuthal angle. For a circle, the lengths of the resulting sectors are uniform, while for an ellipse, these lengths depend on ϕ. Hence, the sectors defined close to the major axis are larger than those defined close to the minor axis.

To correct this effect, `ISOFIT` samples the isophotes using the 'eccentric anomaly' ψ, which is the natural angular parameter for the elliptical shape. The eccentric anomaly is related to the azimuthal angle as follows:

$$\psi = -\arctan\left(\frac{\tan\phi}{1-e}\right), \tag{4.7}$$

where $e = 1 - b/a = 1 - q$ is the ellipticity of the ellipse with major axis a and minor axis b. By uniformly sampling the ellipses in ψ, it is possible to obtain sectors of the same length along the entire curve. By substituting the eccentric anomaly to the azimuthal angle, the `ELLIPSE` model can be rewritten as:

$$I_{\rm model}(\psi) = \langle I_{\rm ell} \rangle + \sum_n [A_n \cos(n\psi) + B_n \sin(n\psi)]. \tag{4.8}$$

Furthermore, in `ISOFIT`, all harmonics of order ≥ 3 are simultaneously interpolated. In this way, all the orders contribute to the isophote model, whereas in `ELLIPSE`, each order corresponds to the best estimate of the component dominating the shape of the isophote. In `ELLIPSE`, the number of harmonics that can be included is practically unlimited, whereas in `ISOFIT`, the number of useful harmonics is limited since all the orders are simultaneously calculated.

The results of `ISOFIT` are reported in a table that includes, for each isophote, the values of the semi-major axis length in pixel, surface brightness I in ADU pixel^{-1}, ellipticity, position angle PA in deg, the centre coordinates x_0 and y_0 in pixel, local radial intensity gradient $\partial I/\partial sma$, and the values of AI_n and BI_n from which the dimensionless coefficients of the Fourier expansion A_n and B_n can be derived. Except for the major axis length, their respective errors are reported for each value.

Table 4.1: Input files adopted to perform the surface brightness modelling with the different fitting algorithms used in this work.

Algorithm	Noise Map	PSF Model	Isophote Table	Parametric Functions	Parameter Guesses	Pixel Mask
`GASP2D`	yes	yes	yes	yes	optional	yes
`GALFIT`	yes	yes	no	yes	yes	yes
`ISOFIT+CMODEL`	no	no	yes	no	no	yes

Regarding `ELLIPSE`, a procedure called `BMODEL` allows for the construction of 2D models of surface brightness by interpolating the surface brightness of isophotes as a function of the major axis. However, `BMODEL` only utilises the harmonics A_n and B_n with $n \leq 4$. In parallel with `ISOFIT`, Ciambur (2015) introduced an updated version of `BMODEL` called `CMODEL`, which utilises all the available harmonics parameterised through the eccentric anomaly rather than azimuthal angle. This enables the construction of more accurate models of the surface brightness.

4.1.2 Modelling procedure

Given this brief introduction to the methods that have been used in modelling the surface brightness, we can now focus on the fitting procedure. Firstly, before the actual fitting of the surface brightness distribution, it is necessary to compute some needed inputs. These are a noise map, a model of the PSF, a table containing the isophote parameters, the list of parametric functions to be used for the parametric methods, a set of guesses for such functions, and, lastly, a mask containing the list of pixels not to be considered during the fitting. The input files that are adopted by the different fitting algorithms are listed in Table 4.1. Details on the computation of these inputs are given in the paragraphs below.

Residual sky subtraction

The sky level provided by the image reduction consists of a global estimate across the FOV after automatically masking the luminous sources. This subtraction is unreliable in analysing the faintest lensing features since a residual sky level could still be present in the image. Therefore, we measure and subtract the residual sky level as follows.

We start by masking the candidate lensing system, foreground stars, and any other field galaxy using the `make_sources_mask` task of the `photutils.background python` package[5] (Bradley et al., 2021). The source segmentation algorithm identifies all the above sources and creates their footprints by selecting the $N_{\rm pixel}$ connected pixels with photon counts over a given threshold σ. Then, the algorithm enlarges the available footprints with binary dilation (e.g. Nadadur &Haralick, 2000) through an $m \times m$ pixels matrix to build the pixel mask of all the luminous sources in the image. We repeat this process twice to identify both the compact ($N_{\rm pixel} = 5$, $m = 11$, $\sigma = 2$) and extended ($N_{\rm pixel} = 10$, $m = 51$, $\sigma = 2$) sources. In both cases, we reiterate the source identification and footprint dilation until no more pixels

[5] https://photutils.readthedocs.io/en/stable/index.html

are added to the mask. The values of $N_{\rm pixel}$, m, and σ are chosen such that the resulting masks cover most of the sources and, at the same time, leave some background regions in the image. The final pixel mask combines the footprints built for compact and extended sources. We check the final pixel mask and manually edit it to remove any spurious source, such as residual cosmic rays and bad pixels, that were left unmasked earlier.

We calculate the residual sky level as the biweight location of the unmasked pixels. Then, we subtract it from the image. We derive the standard deviation of the sky-subtracted image as detailed in Section 2.3.

Pixel mask and noise map

We trim the sky-subtracted images to reduce the computing time for a reliable photometric decomposition. Each galaxy is centred in a FOV ranging from 200 × 200 pixels (corresponding to 12.8 × 12.8 arcsec^2) to 400 × 400 pixels (25.6 × 25.6 arcsec^2) to cover all the lensing features. We also trim the pixel mask to the same region. Then, we unmask the pixels corresponding to the source in the central circular region of ∼ 100-pixel (6.4 − arcsecs) radius. This choice allows us to set up the final pixel mask, which we use for the parametric fitting of the source surface brightness. The trimmed image and final pixel mask that we use to model the surface brightness distribution of HERSJ012620.5+012950 (HerS5) are shown in Figure 4.1 (right panel). In addition, we build the noise map of the images by calculating the variance (in units of electrons) of each pixel as $\sigma^2 = ({\rm RON}^2 + \sigma^2_{\rm sky} + \sigma^2_{\rm gal})/{\rm GAIN}^2$, where $\sigma^2_{\rm sky} = I_{\rm sky}{\rm GAIN}$ and $\sigma^2_{\rm gal} = I_{\rm gal}{\rm GAIN}$ with $I_{\rm sky}$ and $I_{\rm gal}$ being the surface brightness of the sky and of the galaxy in ADU, RON is the detector readout noise (in ADU) scaled for the number of samplings performed during the exposure (see Dressel 2022 for details), and GAIN is the detector gain (in e$^-$ ADU^{-1}). As the background noise we use $\sigma^2_{\rm bkg} = {\rm RON}^2 + \sigma^2_{\rm sky}$. Nevertheless, we estimate the expected variance of the sky from the equation above, verifying that $\sigma_{\rm sky} >$ RON.

PSF model

We build a PSF model for each image from the non-saturated point sources with the highest SNR available in the full WFC3/F110W FOV. For each point source, we identify the centroid with the `find_centroids` task of the `photutils` package, and we extract a cutout of 100 × 100 pixels (6.4 × 6.4 arcsec^2) corresponding to ∼ 20 × 20 FWHM^2. We get the stacked PSF by summing all the point-source cutouts. Before stacking, we normalise the total flux of each point source to unity after removing spurious sources and surface brightness gradient due to nearby bright and extended sources. The noise in the stacked PSF is filtered using a `python` 2D Savitsky-Golay filter[6] (e.g. Ratzlaff &Johnson, 1989). Then, we mask the smoothed PSF model using image segmentation and replace the background pixels with their mean value. We adopt the resulting stacked, smoothed, and background-subtracted PSF to model the surface brightness distribution of the source. The average number of point sources used to build the PSFs is 2 for each snapshot. We show in Figure 4.2 the PSF model we adopt for the parametric fit of HERSJ012620.5+012950.

[6] https://github.com/espdev/sgolay2

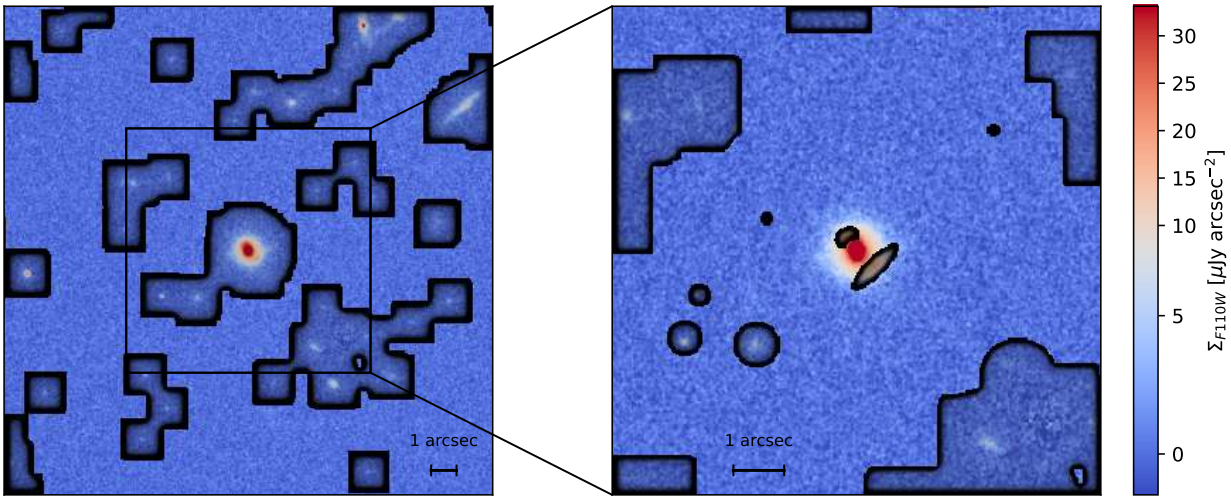

Figure 4.1: *Left panel:* Image of HERSJ012620.5+012950 with the pixel mask (corresponding to the regions with black contours) used to estimate the residual sky level and standard deviation of the background. The highlighted box marks the FOV of the image shown in the right-hand panel. *Right panel:* Trimmed sky-subtracted image and pixel mask used to fit the surface brightness distribution of the lensing galaxy of HERSJ012620.5+012950.

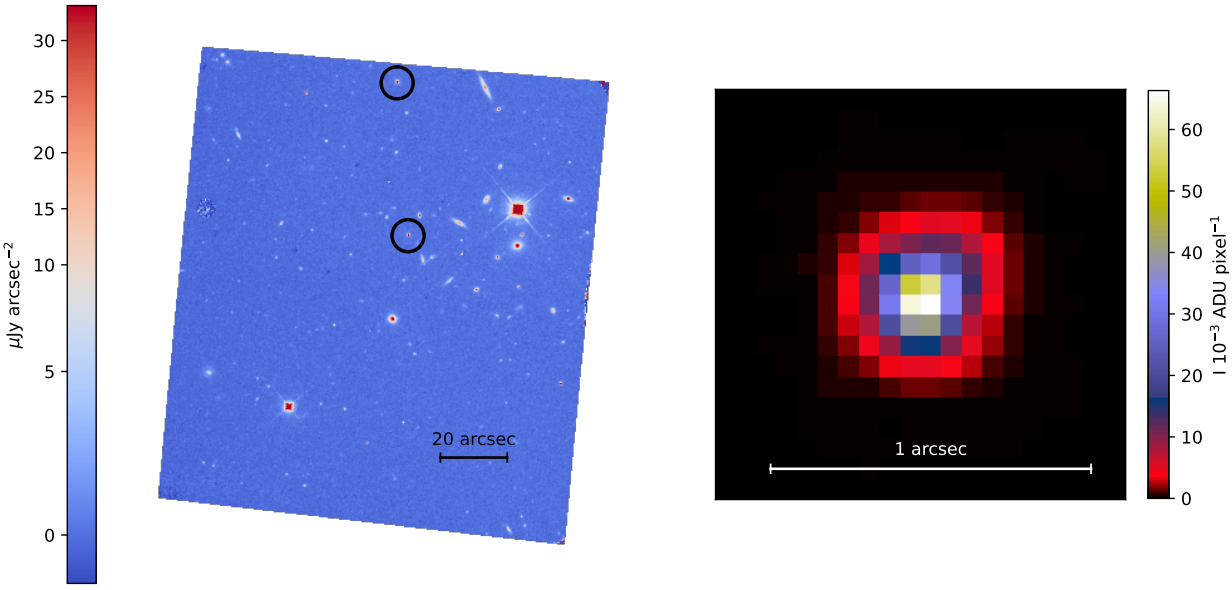

Figure 4.2: *Left panel:* Locations of the unresolved sources (marked with black circles) used to construct the PSF model. *Right panel:* Image of the normalised PSF model adopted to fit the surface brightness distribution of HERSJ012620.5+012950.

Parametric modelling

We perform the parametric modelling of the systems following the steps reported in the flowchart given in Figure 4.3, considering the PSF model, pixel mask, and noise map associated with the image. For `GALFIT`, we preliminarily fit a de Vaucouleurs law and adopt for the ellipticity and position angle the mean values of the azimuthally-averaged radial profiles. The best-fitting values of this preliminary decomposition are utilised as guess values for the actual parametric fitting of the source.

We always start by fitting a single Sérsic component. Then, we visually inspect the residual image to look for spurious sources and/or lensing features. We update the pixel mask to account for them and repeat the fit. If significant residuals are still visible, we add a second component and repeat the fit again. We check the new residual image and iterate the fitting procedure. The additional luminous components are included to remove the residual under/over-subtracted structures at scales similar to or larger than the PSF. As a final step, we double-check the best-fitting values to avoid hitting the boundaries of the allowed ranges for the structural parameters, for which we adopt the ones implemented in `GASP2D`, which are [0.3, 10] for the Sérsic index and $[0.5\,\mathrm{FWHM_{PSF}}, +\infty)$ for the effective radius (see, Méndez-Abreu et al., 2008, 2017, for details). This issue occurs mostly for the Sérsic index of a few surface brightness components, which we fix to 0.5, 1, or 4. If, instead, the best-fitting effective radius of the single Sérsic fit is smaller than the PSF FWHM or larger than the cutout radius, we add a nuclear point source (NPS) component or enlarge the cutout. When necessary, we mask out the dust patches and lanes as much as possible to recover a reliable model of the surface brightness distribution.

Non-parametric approach

We use `ISOFIT` to model the surface brightness distribution of the highly-inclined disk foreground lensing galaxies ($i > 80$ deg) for which `GASP2D` and `GALFIT` fail to recover the structural parameters.

Before fitting the isophotes, we subtract the residual sky level and build the pixel mask for the images of the systems to be fitted with the parametric approaches. Since `ISOFIT` models the observed surface brightness distribution of the galaxy through an isophotal fit and without disentangling the light contribution of its structural components, we do not need to account for the image PSF and noise map. The input files needed by `ISOFIT` are listed in Table 4.1. Unfortunately, we are not able to model HATLASJ142935−002837 (G15v2.19, Calanog et al., 2014) due to the low SNR of the image, which is heavily obscured by a complex pattern of dust that was not possible to mask successfully. For the analysis of HATLASJ142935−002837 (G15v2.19), we refer the reader to Calanog et al. (2014) and Messias et al. (2014) who managed to model this lens using Keck and ancillary ALMA observations.

Detailed example of HERSJ012620.5+012950

In the following section, we illustrate the detailed procedure of the fitting of the lens surface brightness distribution for the A candidate HERSJ012620.5+012950 (HerS5; Nayyeri et al.,

Figure 4.3: Flowchart describing the steps of the parametric surface-brightness modelling.

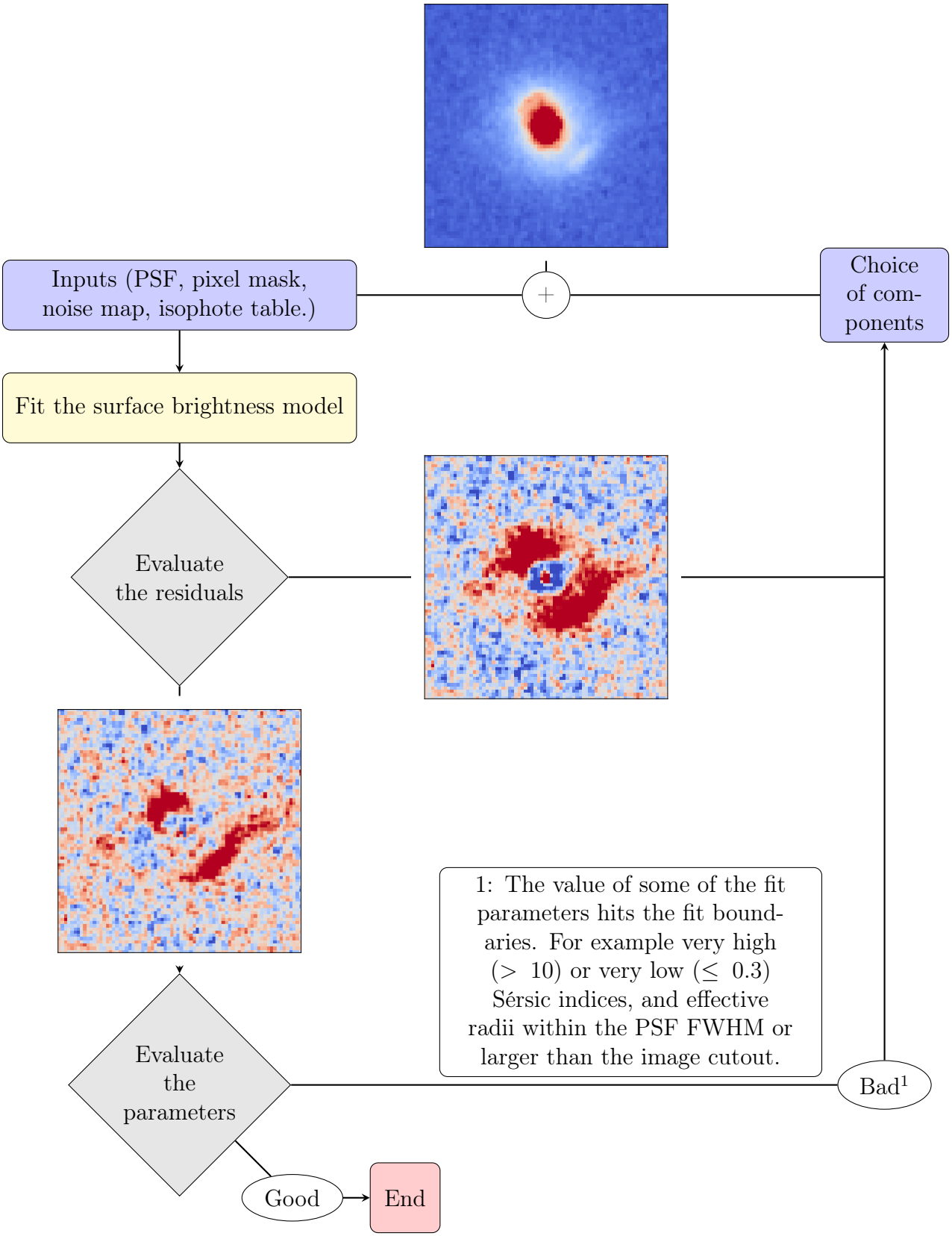

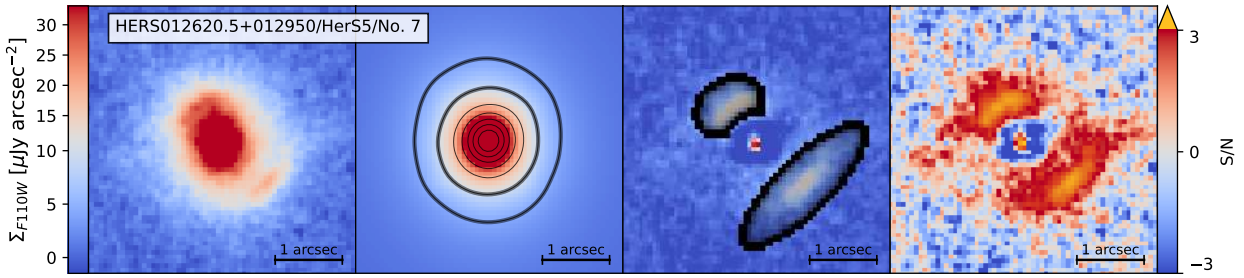

Figure 4.4: *From left to right panels:* Observed *F110W HST* image, single-Sérsic lens model, residual, and SNR residual map of HERSJ012620.5+012950. Contours in the model images are taken at two levels corresponding to $SNR = 5$ and 10 (thicker curves), and five uniformly spaced levels between the $SNR = 10$ and the maximum SNR in the model image (thinner curves). The residual map shows the pixel mask (corresponding to the black-shaded regions) adopted for the surface brightness modelling.

2016). This type 1 system comprises one compact lensing galaxy that we modelled using `GASP2D`.

In Figure 4.1, we show the masks we use for the estimate of the background properties (left panel) and surface brightness fitting (right panel).

The PSF is computed by stacking two point-like sources. In Figure 4.2, we present the positions of the point-like sources we use for the stacking and the final smoothed stack.

We start by fitting a single Sérsic profile to the 2D surface brightness distribution. The cutout of the image, model, residuals, and residuals in SNR are shown in Figure 4.4.

The best fitting single-Sérsic model has a reduced $\chi^2_{\rm red} = 1.10$, which is higher than unity, suggesting we are under-fitting the image. We can see that significant residuals are left at the position of the lensing galaxy. These structures only partially overlap with the lensing features that are masked during the fitting. They have a central symmetry, indicating that they might be related to the simple assumptions of a unique axis ratio, position angle, and shape we make for the lens.

To improve the residual, we try to add a second Sérsic component. This time we find a $\chi^2_{\rm red} = 1.04$. The advantages of adopting a more complex model are visible from the residual maps (Figure 4.5). The structures that were being seen for the single Sérsic model disappeared, leaving only the background source. Unfortunately, the resulting central Sérsic component gets very concentrated with a Sérsic index $n \simeq 10$. To alleviate this, we revise the choice of model components and try the combination of a Sérsic and a Gaussian profile. This choice removes the structures produced by the single-Sérsic fit, maintaining a similar χ^2 of the two-Sérsic one. Furthermore, the previously very concentrated Sérsic acquires a more realistic value of $n = 5.86^{+0.48}_{-0.47}$. Since our requirements are now fulfilled, we chose this model as the best-fitting one. One might still be wondering what would happen if we further increase the complexity of the surface brightness model. As a test, we show the results of a model obtained by adding to the best-fitting model a third Sérsic component (Figure 4.7). The residuals look very similar to what previously resulted from the two-Sérsic and Sérsic-and-Gaussian models. The decrease in the reduced χ^2 is negligible with only a

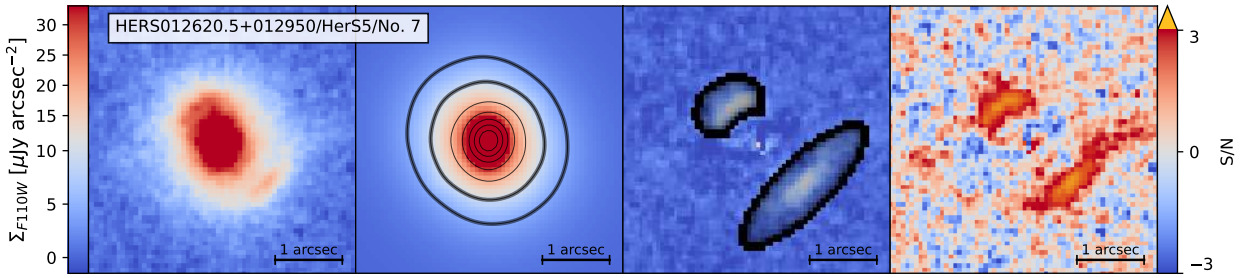

Figure 4.5: Same as Figure 4.4, but for the two-Sérsic lens model.

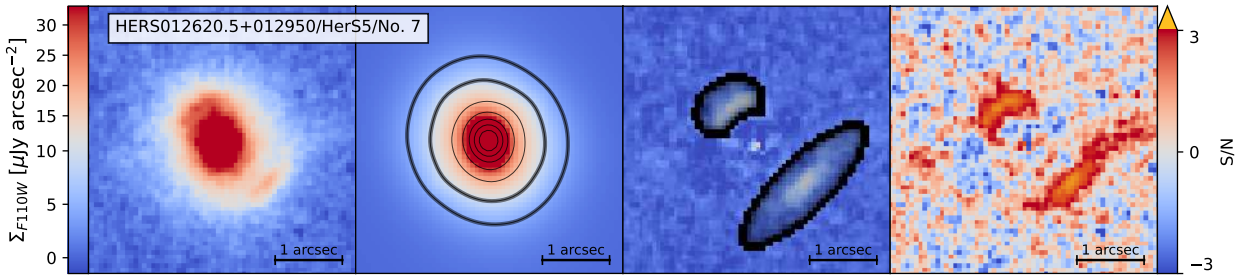

Figure 4.6: Same as Figure 4.4, but for the Sérsic-and-Gaussian lens model.

−0.20% change in front of the addition of seven new free parameters. We argue that there is nothing significant to improve by adding additional freedom.

4.1.3 Error estimate

The formal errors on the fitted parameters obtained from the χ^2 minimisation procedure usually underestimate the real errors of the structural parameters (e.g., Méndez-Abreu et al., 2008). Therefore, we compute the errors on the fitted parameters by analysing a sample of mock galaxies we build through a series of Monte Carlo (MC) simulations following the procedure of Dalla Bontà et al. (2018).

To mimic the observational setup, we carry out the MC simulations in two different exposure-time bins, corresponding to 251 s and 712 s. For each modelled galaxy, we build

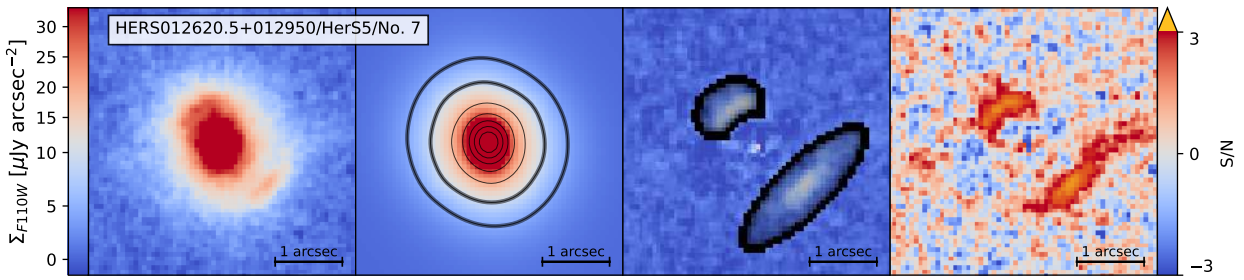

Figure 4.7: Same as Figure 4.4, but for the two-Sérsic-and-Gaussian lens model.

at least 70 mock galaxies by randomly choosing each component parameter p_i in the range $\langle p_i \rangle - 0.3\langle p_i \rangle < p_i < \langle p_i \rangle + 0.3\langle p_i \rangle$ where $\langle p_i \rangle$ is the best-fitting value. We created more than 7800 mock galaxies in total. The image size of each mock source ranged between 200 × 200 pixel (12.8 × 12.8 arcsec^2) and 400 × 400 pixel (25.6 × 25.6 arcsec^2) to enclose the largest fitted lens of that particular component combination. We convolve the mock galaxies with a PSF that is randomly chosen from those produced to fit the systems. We adopt the same pixel scale, detector gain and readout noise of the actual images. In addition, we add a background noise level corresponding to the median $\mathrm{rms_{bkg}}$ measured in the real images, and we add the photon noise in order to match the SNR of the mock and real images.

We run `GASP2D` or `GALFIT` with the appropriate combination of components to analyse the images of the mock galaxies. We then group the modelled galaxies according to their component combination (i.e. Sérsic, de Vaucouleurs, Sérsic-Sérsic, etc.). For each component of each modelled galaxy, we bin the different values of the mock galaxies in bins of one or two-magnitude width centred on the magnitude of the best-fitting model component. We study the distribution of the relative errors on the effective surface brightness I_e, effective radius R_e, and Sérsic index n as $\Delta p/p_\mathrm{input} = (p_\mathrm{output} - p_\mathrm{input})/p_\mathrm{input}$ and of the absolute errors on the position angle PA and axial ratio q as $\Delta p = (p_\mathrm{output} - p_\mathrm{input})$. All the distributions appear to be nearly Gaussian as a first approximation after removing all the systems for which the fit failed, e.g. when one of the fitted components goes to zero, or the model extends significantly more than the cutout. We measure each distribution biweight location and median absolute deviation to detect possible systematic effects and derive the errors on each parameter, respectively.

Discussion

By inspecting the distribution of the relative errors on the model parameters for all the components combination (Figure 4.8) we notice that the relative error distributions for I_e, R_e, and n have $\sigma_\mathrm{p} < 0.4$ while the error distribution of the axis ratio q and position angle PA have $\sigma_q < 0.05$, and $\sigma_\mathrm{PA} < 10\,\mathrm{deg}$, respectively. All error distributions are compatible with having no systematic errors with the median values $\langle p_{dist.} \rangle$ being consistent with zero $\langle p_{dist.} \rangle / \sigma_\mathrm{p} < 0.5$.

The parameters of the surface brightness components are correlated with each other, i.e. a larger profile that is also fainter and more concentrated at the effective radius provides a similarly good fit to the data as a smaller, brighter, and less concentrated profile (Figure 4.9). Interestingly, for some multi-component models, the effective surface brightness seems to be underestimated, whereas the effective radii (and, in some cases, the Sérsic indices) are overestimated. The fitting procedures tend to prefer larger profiles that are fainter at the effective radius and, sometimes, more concentrated than the true ones. By looking at the different rows in the same figure, it is possible to see that the errors associated with the parameters increase by using more complex models.

An additional factor determining the size of the error distributions is the magnitude of the component; we divide the error distributions into two equal-size bins in input magnitude by their median value. With the exception of the Sérsic-and-Exponential profile model, more luminous components have tighter error distributions and tend to be more symmetrical

around the median, implying that the trend mentioned above occurs preferentially in the case of the relatively faint components.

Detailed example of HERSJ012620.5+012950

In Figure 4.10, we illustrate the case of HERSJ012620.5+012950 as an example of the error computation procedure. The input magnitude distributions of both the Sérsic and Gaussian components are shown in blue and orange, respectively. Using the same colours, we also highlight the ranges of mock components that we used to compute the errors on the model parameters. The best-fitting GASP2D model magnitudes are reported as arrows on top of the input magnitude distributions.

In Figure 4.11, we show the distributions of the errors associated with the mock components extracted earlier. We mark with vertical lines the $\pm\sigma_{\rm p}$ errors on the best-fitting component parameters.

4.1.4 Measuring of the galaxy structural parameters

Often, the lensing galaxies are comprised of multiple components. Therefore, to describe the global properties of the surface brightness distribution in an independent way of the number and type of adopted components, we use the total effective radius R_{50} (i.e., the radius and surface brightness of the circularised isophote that contains half of the light of the galaxy), total effective surface brightness μ_{50}, and total magnitude m_{F110W}. For each galaxy, we sample 10^4 different combinations of its components considering the uncertainties on the best-fitting model of the surface brightness. This is done through a set of truncated normal distributions (one for each component parameter) with the central value being the best-fitting value from the surface brightness model, also the standard deviation being the uncertainty of the best-fitting value, and ranges $[0, \infty)$ ADU pixel^{-1}, $[0, \infty)$ pixel, $[0.3, 10]$, $[0, 1]$, and $[0, 360]$ deg for $\mu_{\rm e}$, $R_{\rm e}$, n, q, and PA, respectively. For all the combinations, we compute the curve of growth (COG) defined as:

$$\mathrm{COG}(R) = \int_0^R \sum_i I_i(p_i, r) dr \tag{4.9}$$

where $\mathrm{COG}(R)$ is the curve of growth computed up to the circularised radius R and $I_i(p_i, r)$ is the surface brightness profile of the i-th component as a function of its parameters p_i and radius r. We then estimated R_{50} by retrieving the radius within which half of the total flux is encircled.

The μ_{50} value is derived from the surface brightness profile at R_{50}, while the m_{F110W} value is obtained by summing the luminosities of all the components and substituting the result to the rms in Equation 2.1. We calculate the median and the 16% and 84% percentiles for each parameter from the cumulative distribution function. Additionally, we estimate the $C_{31} = R_{75}/R_{25}$ concentration index (e.g. Watkins et al., 2022) in order to compare our results with the literature. To derive the distributions of the R_{25} and R_{75} values, which correspond to radii containing 25% and 75% of the total luminosity, respectively, we applied the same procedure as done for R_{50}.

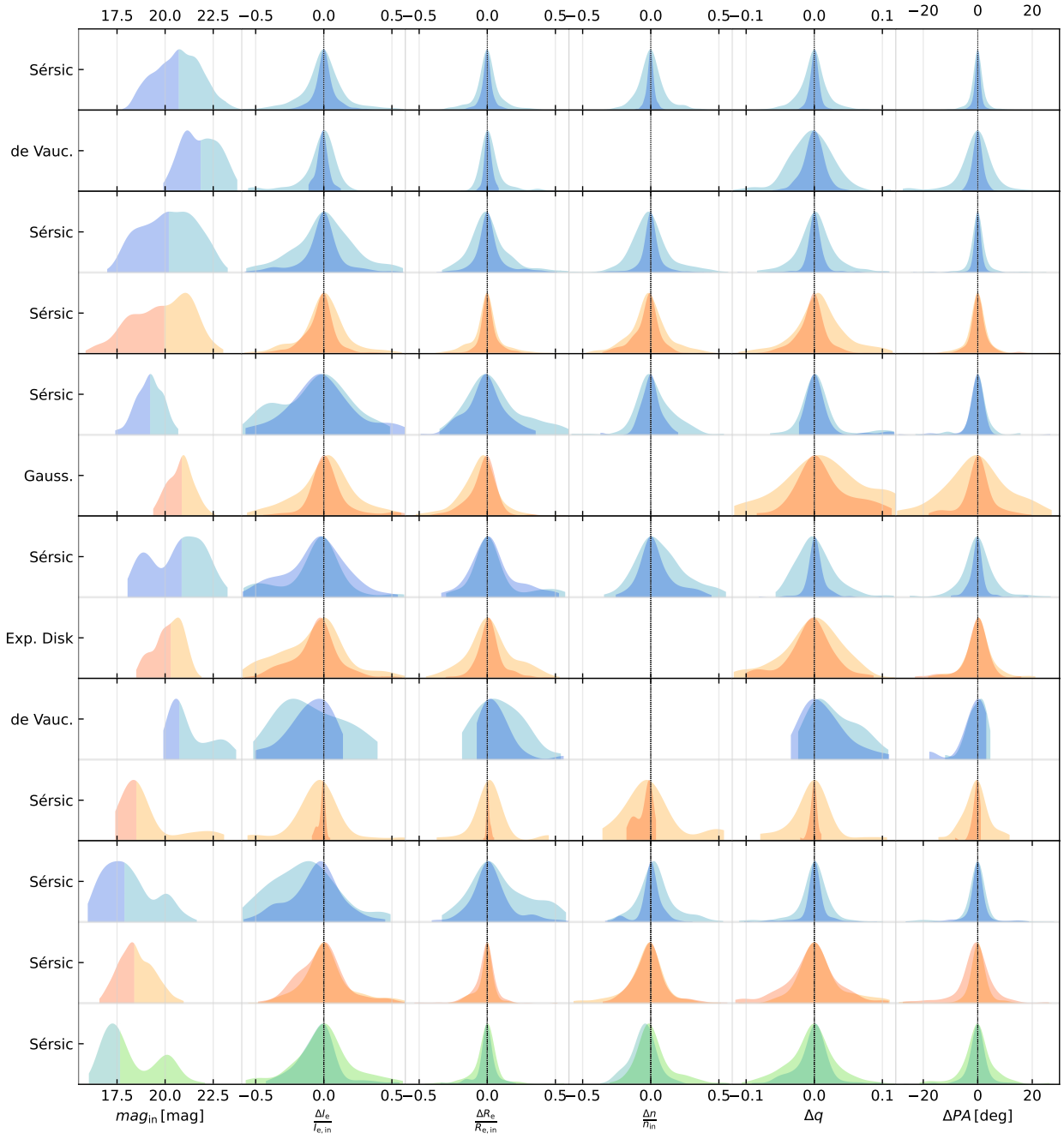

Figure 4.8: *From left to right panels:* Distributions for the mock galaxies of the component input magnitude, of the relative difference between the true and measured values for the mock galaxies of the effective surface brightness, effective radius, Sérsic index, and of the differences between the true and measured values of axis ratio and position angle. *From top to bottom panels:* Each row corresponds to a different surface brightness component. When one set of models has multiple components, we plot the different distributions with different colours: the first model component in blue, the second one in orange, and the third one in green. To highlight the effect of the input magnitude on the error distributions, we divide the input magnitudes into two bins so that each bin contains the same number of mock objects.

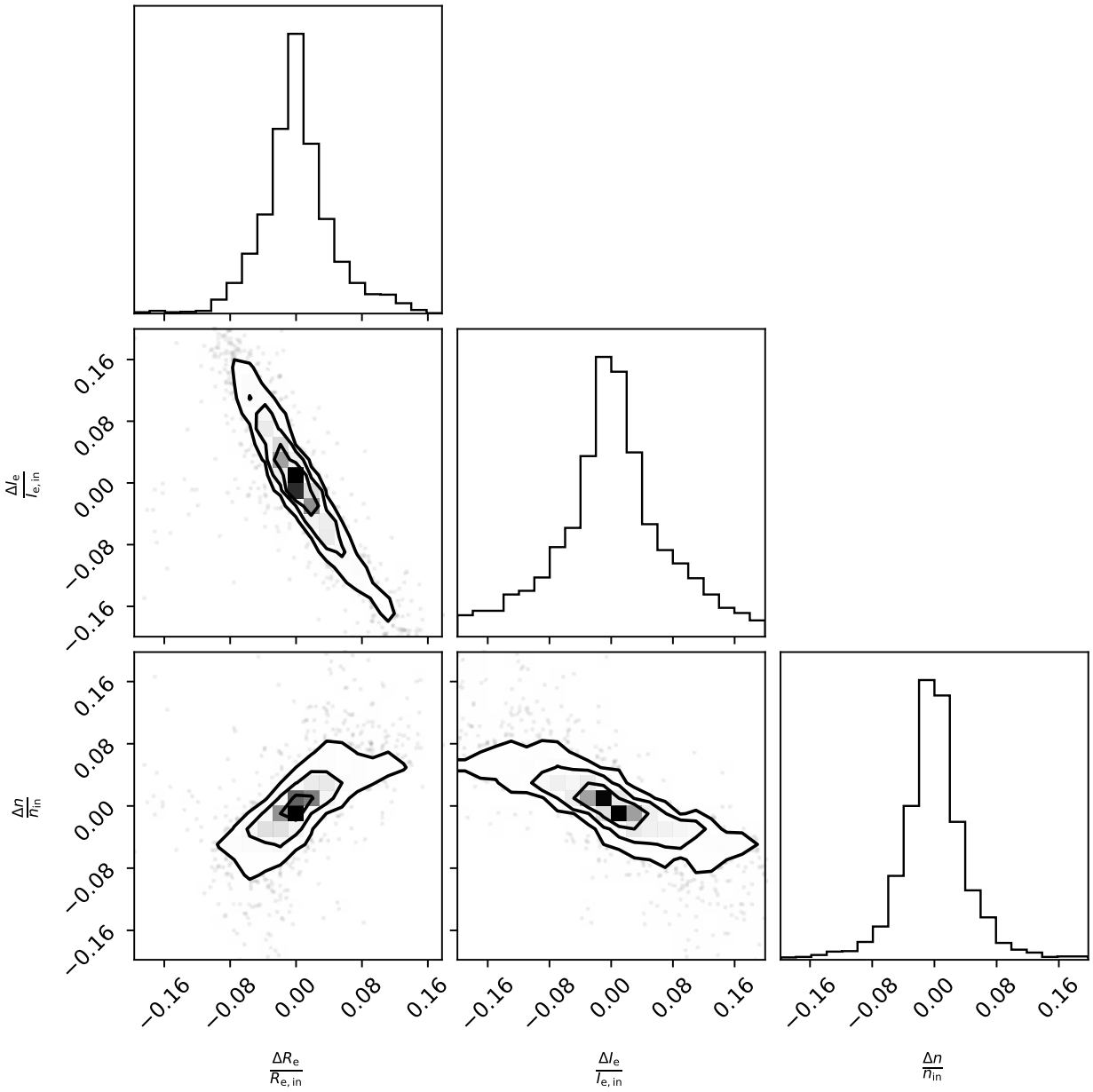

Figure 4.9: Corner plot for the parameters $\Delta R_{\rm e}/R_{\rm e,in}$, $\Delta I_{\rm e}/I_{\rm e,in}$, and $\Delta n/n_{in}$. the black contours correspond to the 0.5, 1, and 1.5 σ of the distribution.

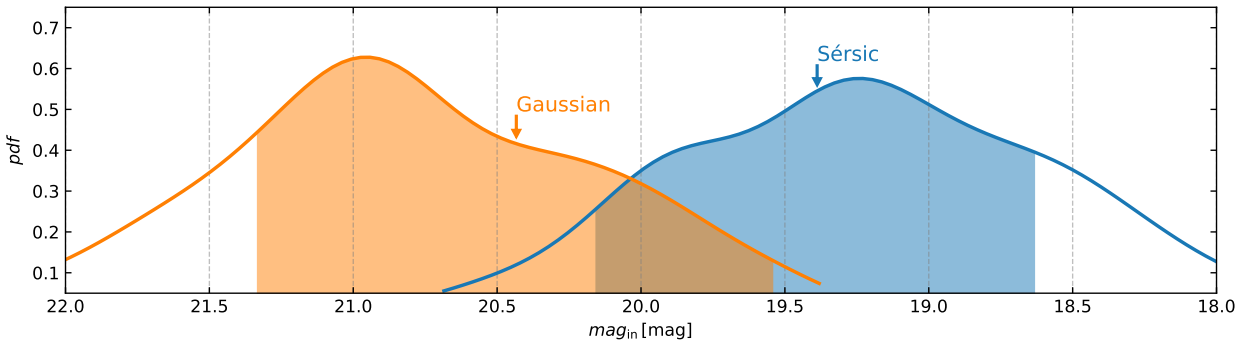

Figure 4.10: Distributions of the input magnitudes for the components of the Sérsic-and-Gaussian mock models. We show the Sérsic component distribution in blue and the Gaussian component distribution in orange. The range of magnitudes used for HERSJ012620.5+012950 are coloured following the same criteria. The best-fitting magnitudes for the Sérsic and Gaussian components are marked with an arrow.

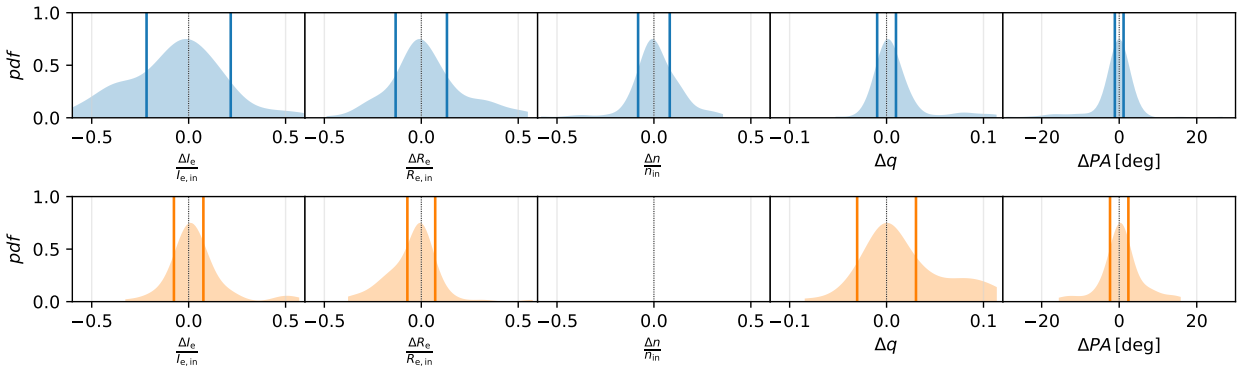

Figure 4.11: *Top panel:* Distributions of the relative errors for the I_e, R_e, and n, and distributions of the absolute errors for q and PA for the Sérsic component of HERSJ012620.5+01295 (blue). *Bottom panel:* Distributions of the relative errors for the I_e and R_e, and absolute error distribution for q and PA for the Gaussian component of HERSJ012620.5+01295 (orange). The values of the $\pm\sigma_p$ used for the final error computation are marked by the blue and orange vertical lines.

For the edge-on lenses, we run `ISOFIT` on the model image after deconvolving it with the PSF, and then we use the result to produce the COG. We also measure the surface brightness radial profile. We use the COG to estimate the values of R_{25}, R_{50}, and R_{75} and to assess their uncertainties; we build a set of 10^4 COGs for each galaxy. We sample the flux within each circularised radius with a Gaussian distribution centred on the measured flux value and standard deviation being the Poisson flux uncertainty. The circularised radius is sampled with a Gaussian distribution centred on the measured radius value and with standard deviation being the uncertainty on the ellipticity as measured by `ISOFIT`. We use the surface radial profile to estimate the values of μ_{50} and to assess its uncertainty. We build a set of 10^4 surface brightness radial profiles. At each radius, we adopt a Gaussian distribution centred on the measured value of surface brightness, with standard deviation being the uncertainty measured by `ISOFIT`.

4.1.5 Updated lens classification

We revise the lens classification of the A and B candidates for which we model and subtract the surface brightness distribution from the *HST* image. Some of the fainter multiple images of the lensed background sources might be heavily blended with their lenses and, as such, not recognisable in the visual lens classification. Hence, we inspect again the B candidates, looking this time at the lens subtracted residuals. In this way, we can identify nine new lensed DSFGs that have been previously assigned to class B (Figure 4.12).

The lens classification becomes the following: 65 class A systems, 67 class B systems, 118 class C systems, and 29 class D systems.

4.2 Lens modelling

In order to fully take advantage of the boost in resolution and depth offered by strong lensing, it is necessary to solve the lensing equation and reconstruct the intrinsic surface brightness distribution of the background sources. We focus on the confirmed lenses that can be modelled with a SIE and shear if needed and whose background sources are well detected in the *HST* observations. The first step is to gather the needed inputs for the fitting procedure: these are the lens-subtracted image, noise map, and PSF cutout. These were previously obtained from the modelling of the lensing galaxies surface brightness. To reduce the computation time, which can be significant for a lens modelling algorithm, we crop the images. To this aim, we also crop the PSF to $\sim 5 \times 5$ FWHM^2 cutouts. We then produce a mask containing the pixels to be ignored during the fitting. Since we are now interested in the background lensed source features, this pixel mask includes only spurious residuals associated with the lens subtraction or pixels belonging to field galaxies or stars. Hence, we can not use the pixel mask developed for the surface brightness modelling because it specifically masked the lensing features, but we needed to compute a new one.

We estimate the position of the lensing features by locating the brightest pixel in 5×5 pixels boxes encompassing each lensed image. The fitting algorithm will use these estimates to constrain the location of the background source in the source plane.

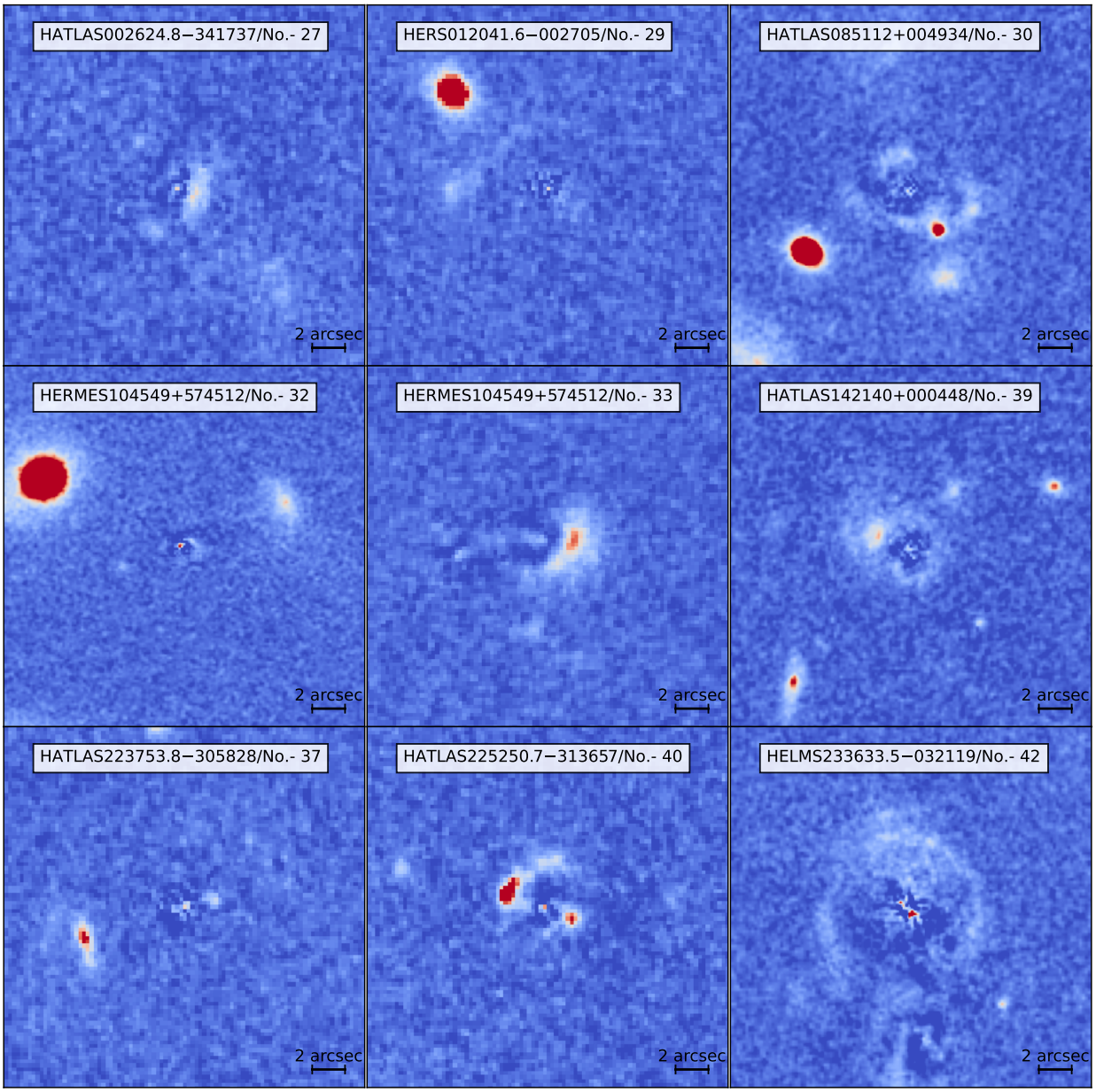

Figure 4.12: *From left to right panels:* B systems that were classified as lensed after the lens subtraction. The panels show $8 \times 8\,\mathrm{arcsec}^2$ cutouts of the lens subtraction residuals. All the panels share the same colour bar extending from -20 ADU, corresponding to the blue, to 120 ADU in white, and then from white to red at 200 ADU.

We produce a first rough estimate of the Einstein radius $\theta_{\rm E}$ from the residual images, which will then be used to define a prior in the lens modelling algorithm. Depending on the morphology of the lensing features, we define $\theta_{\rm E}$ as either the radius of the circle centred on the lens that best fits the Einstein ring (e.g. HELMSJ003619.8+002420) or as half of the separation between the multiple images (e.g. HATLASJ000912.7−300807; but see also Amvrosiadis et al. 2018). For the uncertainty on $\theta_{\rm E}$, we adopt the value corresponding to one-third of the observed width of the lensing feature.

4.2.1 PyAutoLens

The lens modelling is performed with `PyAutoLens`[7] (Nightingale et al., 2018, 2021b).

`PyAutoLens` is a `python` code that adopts the `PyAutoFit` (Nightingale et al., 2021a) probabilistic programming language to combine a light and/or a mass profile for the lens and a model for the background source light distribution. These models can be parametric, such as the Sérsic or Gaussian profiles for the surface brightness distributions or a Navarro-Frenk-White (NFW, Navarro et al., 1996) for the dark matter distribution. Alternatively, the surface brightness of the background source can be modelled through pixelisation, where the brightness of each pixel is free to vary except for a regularisation constant that sets some relative constraints between neighbouring pixels. `PyAutoLens` allows the use of various kinds of pixelisation schemes related to the choice of the grid on which the regularisation is calculated (e.g., a regular square grid, a Delaunay grid, or Voronoi grid) and the kind of regularisation constant that is used. Using pixelisation instead of a more classical parametric profile is useful for modelling more complex and irregular structures. For a given pixelisation, the size and distribution of the pixels become a significant factor when reconstructing the background sources surface brightness distribution. In the case of a simple regular grid, it is possible to evenly increase the resolution for the whole reconstructed source plane, but that comes at the expense of computational time. Luckily, we are not necessarily interested in evenly sampling the source plane. Instead, we want to sample it effectively. For example, in the case of a Delaunay triangulation or a Voronoi binning, one can choose the size and distribution of the bins to have a higher resolution when the SNR of the background source is high and a lower resolution when the SNR is low.

Combining a mass profile for the lens with a reasonable surface brightness distribution for the background source is necessary to begin the lens modelling. For the former, we adopt a SIE (see, Nightingale et al., 2018, for details)) that corresponds to a cored power law profile with the power index set to 2 and core radius to 0:

$$\kappa_{\rm SIE}(r) = \frac{3-\alpha}{1+q}\left(\frac{\theta_{\rm E}}{r+S}\right)^{\alpha-1}, \ \alpha = 2, \ S = 0, \tag{4.10}$$

where $\kappa_{\rm SIE}$ is the surface mass density distribution, q is the axis ratio of the mass distribution, $\theta_{\rm E}$ is the Einstein radius, $S = 0$ is the core radius, r is the radius in elliptical coordinates that is defined as $r = \sqrt{(x - x_{\rm SIE})^2 + (y - y_{\rm SIE})^2/q^2}$, and $x_{\rm SIE}$ and $y_{\rm SIE}$ are the centre coordinates of the mass component.

[7] https://github.com/Jammy2211/PyAutoLens

Instead of using the axis ratio and position angle, `PyAutoLens` defines two elliptical components $\epsilon_1 = f\sin(2PA)$ and $\epsilon_2 = f\cos(2PA)$, where $f = (1-q)/(1+q)$[8].

`PyAutoLens` works by simultaneously fitting the lens mass and background source. The algorithm adopts the semilinear inversion method when dealing with a pixelised background source (SLI, Warren &Dye 2003, Suyu et al. 2006, Nightingale &Dye 2015). The SLI method starts with a lens model and a pixelised source plane and then computes the linear combination of the source pixel values that, once mapped back to the image plane and convolved with the PSF, best fit the background lensed source. With the lensed model images computed, it is possible to produce the residuals and a merit function that, without a regularisation, would coincide with a χ^2 statistic to evaluate the goodness of the fit.

In order to prevent overfitting, the solution obtained from the pixelisation is regularised using a linear regularisation matrix (see Nightingale et al., 2018, for details). In fact, without it, the pixelisation could perfectly reconstruct the observed image and noise for any given mass model.

`PyAutoLens` maximises the Bayesian evidence ϵ defined as:

$$-2\ln\epsilon = \chi^2 + s^T H_\Lambda s + \ln\left[\det(F + H_\Lambda)\right] - \ln\det(H_\Lambda) + \sum_{j=1}^{J} \ln\left(2\pi\sigma_j^2\right), \tag{4.11}$$

where s is the source plane surface-brightness vector of the background source, H_Λ is the regularisation matrix that contains the regularisation coefficient λ defined by Nightingale &Dye (2015), F is the matrix that takes care of the ray tracing, mapping the image plane to the source plane, and σ_j is the uncertainty on the surface brightness of the image plane j-pixel. The Equation 4.11 is composed of three parts. The first part is the χ^2 that quantifies how well the model reproduces the data. The second part is composed of the regularisation terms (i.e., the second, third, and fourth terms of the right-hand side of the equation), while the third part boosts solutions that fit the higher SNR regions of the image plane.

Since most of our cases are compact and present multiple images at low SNR, we decide to use the simpler magnification-based regularisation presented in Nightingale &Dye (2015).

The regularisation terms, containing the parameter λ, act as a prior on the source reconstruction, imposing a smooth surface brightness distribution. A high value of λ produces a very smooth image, increasing the χ^2 and decreasing the Bayesian evidence. Conversely, a too-low λ produces a more complex reconstruction, increasing the regularisation terms and decreasing the Bayesian evidence. `PyAutoLens` allows for more complex realisations that can depend, in more sophisticated ways, on the source plane position and the background source surface brightness distribution.

The likelihood sampling is done through `dynesty` (Speagle, 2020), a nested sampling algorithm that effectively solves problems with a large parameter space. It performs the non-linear search that is used to determine the set of best-fitting model parameters. The non-linear search guesses many realisations of the mass model, using those that best fit the data to guide it where to guess subsequent models.

[8] see https://pyautolens.readthedocs.io/en/latest/index.html for details.

4.2.2 Modelling approach

We perform the lens modelling as follows. First, we fit the mass model and background source with parametric functions. We use a single Sérsic component for the background source. This fit has twelve free parameters, which are the centre coordinates relative to the surface brightness model $\delta x_{\rm SIE}$ and $\delta y_{\rm SIE}$, the Einstein radius $\theta_{\rm E}$, and the two elliptical components $\epsilon_{\rm SIE,1}$ and $\epsilon_{\rm SIE,2}$ for the mass model and seven for the background source consisting in the effective surface brightness $I_{\rm s,eff}$, effective radius $R_{\rm s,eff}$, Sérsic index $n_{\rm s}$ and the two corresponding elliptical components $\epsilon_{\rm s,1}$ and $\epsilon_{\rm s,2}$. The priors for the mass model are a Gaussian distribution centred on the cutout centre with $\sigma = 0.1$ arcsec for $\delta x_{\rm SIE}$ and $\delta y_{\rm SIE}$; a Gaussian distribution centred on the rough estimate obtained from the image separation with σ three times its error for $\theta_{\rm E}$; a Gaussian distribution centred on 0 with $\sigma = 0.3$ for $\epsilon_{\rm SIE,1}$ and $\epsilon_{\rm SIE,2}$, respectively. The priors for the background source are a Gaussian distribution centred on the cutout centre with $\sigma = 0.3$ arcsec for $x_{\rm s}$ and $y_{\rm s}$; a log-uniform distribution between 10^{-6} ADU and 10^{6} ADU for $I_{\rm s,eff}$; a uniform distribution between 0 arcsec and 30 arcsec for $R_{\rm s,eff}$; a uniform distribution between 0.8 and 5.0 for $n_{\rm s}$; a Gaussian distribution centred on 0 with $\sigma = 0.3$ for $\epsilon_{\rm s,1}$ and $\epsilon_{\rm s,2}$ (defined in a similar way as $\epsilon_{\rm SIE,1}$ and $\epsilon_{\rm SIE,2}$), respectively. As position threshold, we use a Gaussian distribution centred on the previously identified position with $\sigma = 0.5$ arcsec for all the systems, except for HELMSJ233441.0−065220. For the latter, we adopt $\sigma = 0.1$ arcsec due to the small angular separation of the lensed images. We then use the posteriors of the mass model obtained in this parametric fit and the priors on the position of the background sources on the image plane to initialise a Voronoi pixelisation with a constant regularisation coefficient λ. For the pixelisation, we use as priors a uniform distribution between 20 and 45 pixels for the size of the pixelisation and a log-uniform distribution between 10^{-6} and 10^{6} for λ. We do this initialisation fit by marginalising over the mass model and only fitting the pixelisation. Similarly, we marginalised the resulting pixelisation to fit the mass model with priors defined by the parametric fit posteriors. We consider this fit as the best guess for the lens model and source reconstruction.

In the analysis above we did not include the effects that different priors on the pixelisation or different choices of mass models have on the lens modelling. A detailed analysis of these systematics exceeds the scope of this work and will be given in future works.

In Figure 4.13, we report a flowchart detailing our adopted fitting approach.

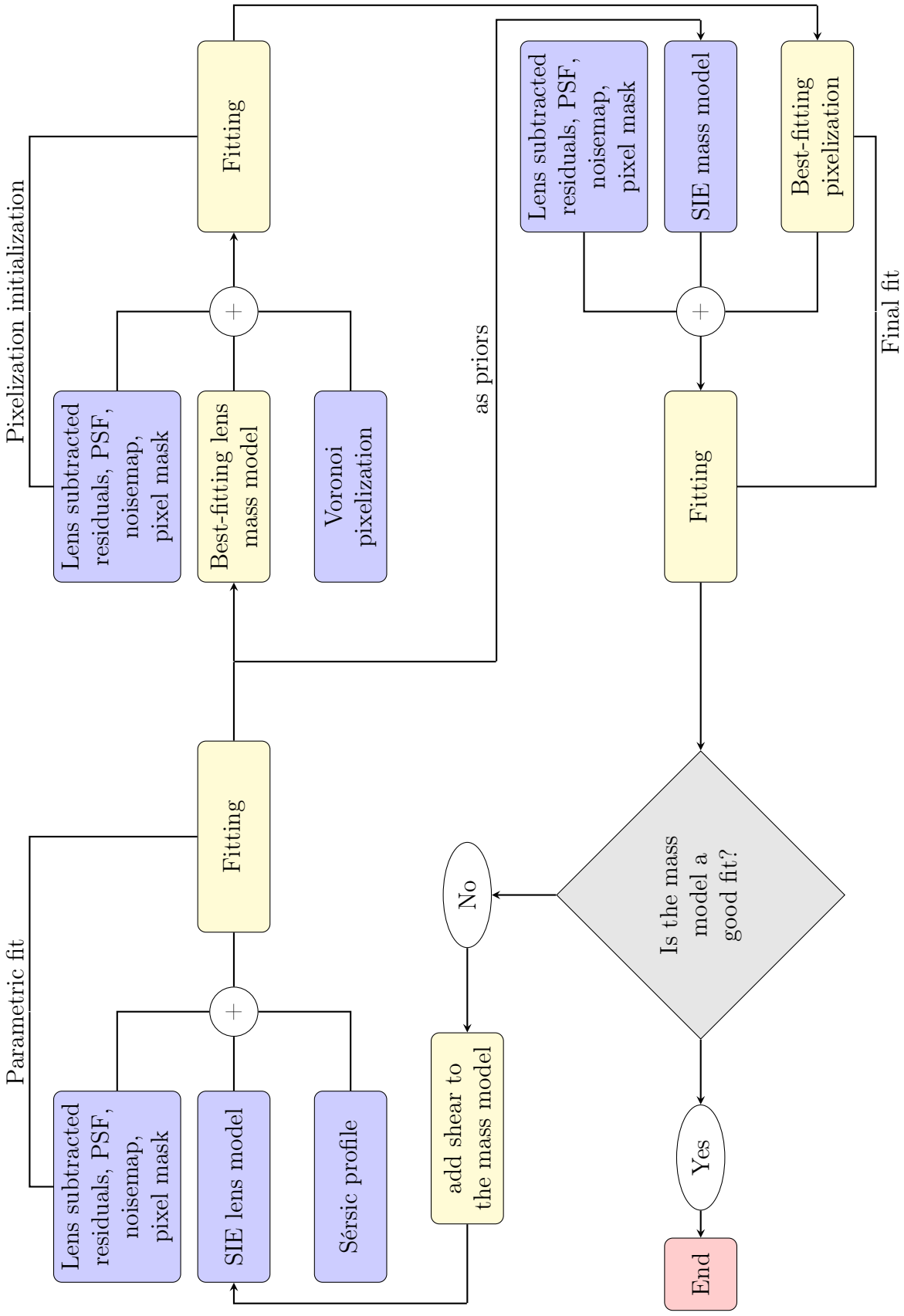

Figure 4.13: Flowchart describing the steps of the parametric surface-brightness modelling.

Magnification and source size computation

Since we are dealing with potentially irregular background sources, in order to estimate their sizes, we decide to follow Enia et al. (2018), who used the circularised radius of the source plane region with SNR above a given threshold to estimate the sizes. This choice is made for two reasons. The first is that it allows for a direct comparison between our findings and Enia et al. (2018) results. The second is that it allows us to estimate the sizes for more complex, multi-component sources (e.g. mergers) more naturally. It is important to remark that this size measurement does not compare straightforwardly to the effective radius obtained by fitting a regular profile to the background source surface-brightness distribution. Hence, caution must be used when comparing sizes obtained through the two different approaches.

For each modelled lens, we extract 500 fits from the lens modelling parameters posteriors, and, for each fit, we compute the regions of the source plane with SNR > 3. We measure the sizes of the lensed sources by computing the radii of the circularised regions in the source plane we use to compute the magnifications. This size estimate has the advantage of allowing a straightforward computation of the magnification. We set to zero all the pixel values in the source plane below the threshold SNR $= 3$ and mapped back the pixelised surface brightness distribution to the image plane. We compute the magnification by taking the ratio between the flux densities before and after the mapping.

Detailed example of HERSJ012620.5+012950

Here, we describe the procedure of fitting the lens mass distribution and background source surface-brightness distribution for the A candidate
HERSJ012620.5+012950 (HerS5; Nayyeri et al., 2016).

In Figure 4.14, we show the lens model and background source reconstruction when combining a SIE mass model and a Sérsic background source. The model nicely fits most of the lensed background source structure except for a westward elongated structure of the S arc. The critical curves and the background source surface-brightness distribution are flattened with a low axis ratio.

In Figure 4.15, we present the second step of the lens modelling. In this case, the lens mass model is the same as before, whereas the background source is the regularised Voronoi pixelisation. The background source, which before was symmetric, now shows a lopsided emission towards the SE of the cutout. However, the source appears roughly similar in size to that obtained from the parametric fit.

Lastly, in Figure 4.16, we show the results of the final fit having a combination of a SIE and the previously computed regularised pixelisation. It is possible to see that the critical curves get less flattened while both the caustics and reconstructed background source get smaller when compared to the earlier fits.

In Table 4.2, we compare the mass models of the first and third fit and the sizes and magnifications for background sources for all three fits. While the mass model remains consistent for the first and third fits, the background source becomes more compact, rounder, and magnified with each fit.

All the computed parameters computed (e.g., the effective and Einstein radii of the lenses, magnitudes and sizes of the background sources) are given in observed units of arcseconds

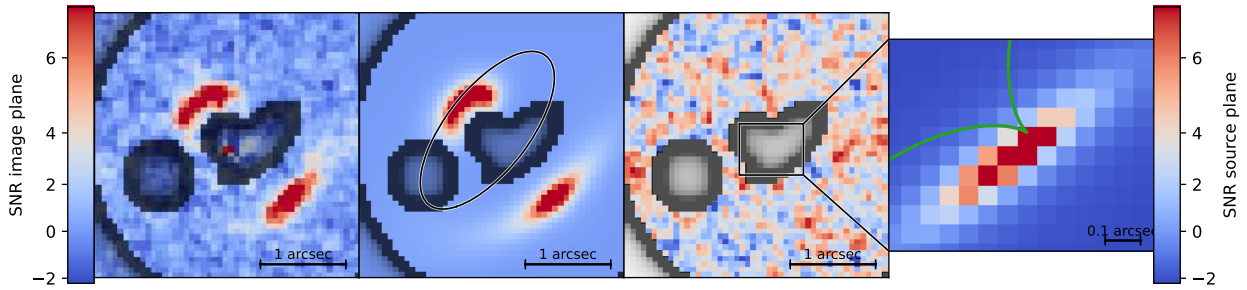

Figure 4.14: *First three panels:* Lens subtracted image, best-fitting background lensed source, and SNR residual map for parametric background source fit of HERSJ012620.5+012950. Each panel shows the pixel mask (corresponding to the black-shaded regions) adopted for the lens modelling. The second panel shows the critical curves (black line). The third panel shows the source plane region displayed in the last panel. *Right panel:* Source plane reconstruction of the background source and caustics curves (green line). We highlight with black and blue contours the SNR > 3 region adopted for computing the lensing magnification and source size, respectively.

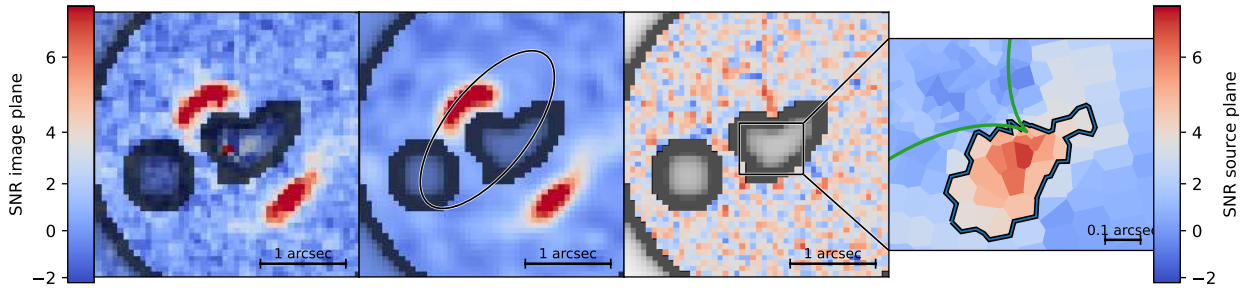

Figure 4.15: Same as in Figure 4.14, but for the regularised pixelisation initialisation background source fit.

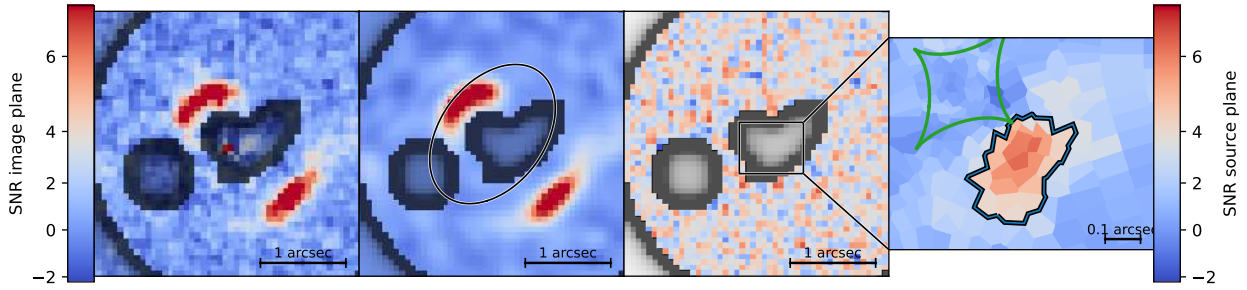

Figure 4.16: Same as in Figure 4.14, but for the regularised pixelisation background source fit.

Table 4.2: Physical properties of the lens mass models and background sources surface-brightness distribution for HERSJ012620.5+012950.

Model	δx [arcsec]	δy [arcsec]	$\theta_{\rm E}$ [arcsec]	q	PA [deg]	$R_{\rm bkg}$ [arcsec]	μ
(1)	(2)	(3)	(4)	(5)	(6)	(7)	(8)
SIE + Par. source	$-0.04^{+0.03}_{-0.02}$	$0.16^{+0.03}_{-0.04}$	0.79 ± 0.02	$0.47^{+0.08}_{-0.07}$	$52.51^{+0.84}_{-0.50}$	$0.214^{+0.024}_{-0.021}$	–
SIE + Pix. init.	–	–	–	–	–	$0.160^{+0.004}_{-0.006}$	$4.05^{+0.03}_{-0.02}$
SIE + Pix. final	$-0.006^{+0.015}_{-0.007}$	$0.14^{+0.01}_{-0.02}$	0.766 ± 0.004	$0.60^{+0.07}_{-0.03}$	$52.13^{+0.85}_{-0.58}$	$0.142^{+0.003}_{-0.010}$	$5.19^{+0.56}_{-0.20}$

Notes: Col. (1): Model combination. Cols. (2) and (3): RA and Dec. shifts between the lens mass and light distributions. Col. (4): Einstein radius. Col. (5): Axis ratio of the mass distribution. Col. (6): Position angle of the mass distribution. Col. (7): Size of the background source. The size is calculated as the effective radius for the Sérsic component for the first fit and as the radius of the equivalent circle to the regions of the source plane having SNR > 3 Col. (8): Magnification of the background source.

and apparent magnitudes. Hence, they are independent of the adopted distances. We address the conversion into physical units by taking into account the redshift PDF in Section 5.2. The concentration parameter C_{31} does not depend on the galaxy distance.

4.3 Summary

In this chapter, we present the methods and procedures necessary to model the surface brightness distribution of a galaxy. We fit and subtract the surface brightness distribution of the class A and B candidates. Lastly, we run Monte Carlo simulations to provide a robust estimate of the uncertainties on the surface brightness parameters. This analysis allows us to (i) update the lensing classification by visually inspecting the lens-subtracted residuals, reaching the final classification of 65 class A systems, 67 class B systems, 118 class C systems, and 29 class D systems; (ii) characterise some general properties of the sample lenses; and (iii) isolate the background sources so they can be modelled and reconstructed through lens modelling techniques.

With the candidate lensing galaxies modelled and structural parameters estimated, it is possible to study some general properties of the sample lenses. Lastly, focusing on the 65 A class lenses, it is possible to apply lens modelling techniques to extract the lensing mass properties and reconstruct the background sources. The analysis will be presented in Chapter 6.

With the lens surface brightness removed, we focus on the 65 confirmed strongly lensed DSFGs. We perform the lens modelling and source reconstruction for all the systems in which we could confidently identify a galaxy acting as the main lens as well as the background source in the *HST* images alone (34 systems). We adopt a SIE profile, adding shear when needed to model the mass distribution of the lens, whereas we use a magnification-based

Voronoi pixelisation to reconstruct the background sources. The results of this analysis and a comparison with similar works in literature are presented and discussed in Chapter 6. Along with describing the methods and fitting approach, we report, as an example, the case of HERSJ012620.5+012950.

Chapter 5

Results

Until now, we have presented the candidate lensed DSFGs, their classification, and the methods we applied in order to better characterize both the lensing galaxies and background sources in our *HST* snapshots. In this chapter, we present the results of this analysis, trying to address the following questions: *what are the photometric properties of the sample lenses? In what way does our background source-based selection impact the population of lensing galaxies? What are the properties and morphology of the lensed DSFGs?* In Section 5.1, we present the source-by-source description of the candidate systems, focusing both on each lens surface brightness model and background source reconstruction. This description is complemented by figures and tables containing the best-fitting models. In Section 5.2, we describe some general properties of the populations of lensing galaxies and lensed DSFGs. This is done by focusing primarily on the morphological characterisation of the lenses and background sources. Then, we perform a brief comparison of this sample with the one of SLACS.

We perform the lens surface-brightness modelling and subtraction for all 65 class A and 67 class B systems. Instead, for the lens modelling, we focus on those systems DSFGs having both a well-detected background source in the *HST* and a single lensing galaxy that could be adequately modelled by a SIE. This selection reduces the sample to 34 systems, of which we successfully model 23. A detailed account of the lens surface brightness and lens models is given in the following section.

5.1 Source-by-source description

The reference table of the lensed sources candidates containing the additional names, coordinates, *Herschel*/SPIRE flux densities, and references can be found in Table 2.1. The following source descriptions are ordered by lens classification and then by RA of the *Herschel*/SPIRE centroid following Table 2.1.

HATLASJ000330.6−321136 (HerBS155): We model this type 1 foreground lens at $z_{\rm l}^{\rm phot} = 0.38$ (Shirley et al., 2021) with two Sérsic components using `GASP2D`. The background lensed source is located at $z_{\rm s}^{\rm spec} = 3.08$, as measured by the BEARS survey (Urquhart et al.,

2022). It forms two regular arcs on the SE and NW sides of the lens. We model the mass distribution of the lens with a SIE profile. The background source is reconstructed in two components linked by a fainter ($SNR < 3$) S-shaped structure. These components are located on the NE side of the position of the mass centroid projected to the source plan.

HATLASJ000912.7−300807 (SD.v1.70): We model this type 1 foreground lens at $z_{\rm l}^{\rm phot} = 0.28$ (Shirley et al., 2021) with three Sérsic components using `GALFIT` to account for the different location of their centres. The background lensed source is located at $z_{\rm s}^{\rm phot} = 1.19$ (Zhang et al., 2018), and it forms a complex and multi-component arc-like main image on the SE side of the lens and a compact irregular secondary image on the NW side. We could not obtain a satisfactory model with a SIE and external shear due to the complex morphology of both the lens and background source.

HELMSJ003619.8+002420 (HELMS14): We model this type 1 foreground lens at $z_{\rm l}^{\rm spec} = 0.26$ (Nayyeri et al., 2016) with three Sérsic components using `GALFIT` to account for the different location of their centres. The background lensed source is located at $z_{\rm s}^{\rm spec} = 1.62$ (Cox et al., 2023) and forms an almost complete ring ($r \sim 2$ arcsec) consisting of a diffuse component and three brighter knots located on the SE, SW, and NW sides of the lens. Two additional faint NE and SW structures are visible close to the ring but do not have a clear lensed morphology. We model the mass distribution of the lens with a SIE profile. The background source is reconstructed in multiple irregular knots that are lensed into the various sections of the observed arc. The two main components of the background source overlap with the caustics of the mass model.

HELMSJ005841.2−011149 (HELMS23): The foreground lens is a type 1 edge-on galaxy at $z_{\rm l}^{\rm phot} = 0.38$ (Nayyeri et al., 2016), which we model with `ISOFIT`. The background lensed source is located at $z_{\rm s}^{\rm spec} = 1.50$ (Cox et al., 2023) and gives rise to two bright knots along the galaxy minor axis, opposite each other concerning the galaxy nucleus. We could not obtain a satisfactory model with a SIE and external shear due to the complex morphology of both the lens and background source.

HERSJ011722.3+005624$_{1,2}$ (HERS10): This type 3 foreground lensing system is formed by a main galaxy (labelled as '1' in Figure 5.1) at $z_{\rm l}^{\rm phot} = 0.87$ (Nayyeri et al., 2016) and possibly a secondary fainter galaxy (labelled as '2'), for which the redshift is not yet available. The lack of the redshift prevents us from being more conclusive about the lensing nature of the secondary galaxy. We model the two galaxies with `GASP2D` using one Sérsic and one Gaussian component for the brighter galaxy and a single Sérsic component for the fainter one. The background lensed source is located at $z_{\rm s}^{\rm spec} = 2.47$ (Cox et al., 2023) and forms an arc on the E side of the lens and a diffuse secondary image on the NW side. The reconstructed background source is too faint, having $SNR < 3$; hence, we exclude the resulting model.

HERSJ012620.5+012950 (HERS5): We model this type 1 foreground lens at $z_{\rm l}^{\rm phot} = 0.43$ (Nayyeri et al., 2016) with one Sérsic and one Gaussian component using `GASP2D`. The background lensed source is located at $z_{\rm s}^{\rm spec} = 1.45$ (Cox et al., 2023) and forms two arcs on the NE and SW sides of the lens. The SW arc shows an additional diffuse radial component, which extends westward. we model the mass distribution of the lens with a SIE profile and external shear to add further complexity to the mass model. The two arcs of the background source are reconstructed in a single flattened component located on the SW side of the position of the mass centroid projected to the source plane.

HERSJ020941.2+001558$_{1,2}$ (HERS1): This type 3 foreground lensing system is formed by a main galaxy (labelled as '1' in Figure 5.1) and a second fainter galaxy (labelled as '2'), which are both located at $z_{\rm l}^{\rm spec} = 0.20$ (Nayyeri et al., 2016; Liu et al., 2022). We used `GASP2D` to model the brighter galaxy with three Sérsic components and the fainter one with a single Sérsic component. The background lensed source at $z_{\rm s}^{\rm spec} = 2.55$ (Geach et al., 2015) forms a bright extended arc on the SW side of the lens and two knots on the E and SE sides. This system was studied in detail by Geach et al. (2015) and Liu et al. (2022), who measured an Einstein radius of $\theta_{\rm E} = 2.48^{+0.02}_{-0.01}$ arcsec. It has also been observed with *SMA* (340 GHz, Liu et al., 2022), *ALMA* (Band 7, Liu et al., 2022), JVLA (1.4 GHz and 5 GHz, Geach et al., 2015), *eMERLIN* (1.52 GHz, Geach et al., 2015) in the sub-mm/mm wavelength range and with *HST* (1.6 μm, Liu et al., 2022) and *Keck*/NIRC2 AO (H and $K_{\rm s}$ band, Liu et al., 2022) in the near-IR. The sub-mm/mm follow-up observations show no significant difference in morphology with those performed in the near-IR. We model the mass distribution of the lens with a SIE profile. The background source is reconstructed in two components elongated along the SW/NE direction and located on the SW side of the position of the mass centroid projected to the source plane. The same two-component morphology is seen in the reconstructed sub-mm/mm observations (e.g. Kamieneski et al., 2023a).

HERMESJ032637−270044 (HECDFS05): We model this type 1 foreground lens with a single Sérsic component using `GASP2D`. The background lensed source forms two compact images on the E and W sides of the lens, which is circled by a fainter incomplete ring. This system was studied in detail by Calanog et al. (2014), who measured an Einstein radius of $\theta_{\rm E} = 0.96^{+0.02}_{-0.03}$ arcsec. We model the mass distribution of the lens with a SIE profile. The background source is reconstructed in a compact flattened component located on the SW side of the position of the mass centroid projected to the source plane.

HERMESJ033732−295353 (HECDFS02): We model this type 1 foreground lens at $z_{\rm l}^{\rm phot} = 0.19$ (Shirley et al., 2021) with three Sérsic components using `GASP2D`. The background lensed source forms a bright extended arc (divided into two knots on the NE side of the lens) and an inner secondary image on the SW side. This system was studied in detail by Calanog et al. (2014), who measured an Einstein radius of $\theta_{\rm E} = 1.65^{+0.03}_{-0.05}$ arcsec. We model the mass distribution of the lens with a SIE profile. The background source is reconstructed into three components on the N side of the position of the mass centroid projected to the source plane. The two main knots are located on each side of the N cusp of the caustic, and when lensed, they form the two brighter knots that are visible on the arc.

HATLASJ083051+013225$_{1,2}$ (HerBS4): This type 2 foreground lens is formed by two galaxies, one (labelled as '1' in Figure 5.1) at $z_{\rm l}^{\rm spec} = 0.63$ and the other (labelled as '2') at $z_{\rm l}^{\rm spec} = 1.00$ (Bussmann et al., 2013). We deblended them with `GALFIT` by simultaneously modelling their surface brightness with a single Sérsic component each. The background lensed source at $z_{\rm s}^{\rm spec} = 3.11$ (Yang et al., 2017) shows a very complex structure with two intersecting arcs on the NW side of the lens. This system was studied in detail by Enia et al. (2018), Yang et al. (2019), and Maresca et al. (2022) which modelled high-resolution *SMA* (340 GHz, Bussmann et al., 2013), *ALMA* (Band 7, Amvrosiadis et al. 2018; Band 4 Yang et al. 2019) observations. This system was also observed with *Keck*/NIRC2 AO ($K_{\rm s}$ band, Calanog et al., 2014). The sub-mm/mm follow-up observations show a ring around both lenses that splits into two arcs on the SE and S sides of the system, a third compact image

on the N side of the second galaxy, and a further compact image between the two lenses. We could not obtain a satisfactory model with a SIE and external shear due to the complex morphology of both the lens and background source.

HERMESJ100144+025709 (HCOSMOS01): We model this type 1 foreground lens at $z_{\rm l}^{\rm spec} = 0.61$ (Calanog et al., 2014) with a single Sérsic component using `GASP2D`. The background lensed source forms three compact images on the lens NE, S, and NW sides, surrounded by a fainter ring. This system was studied in detail by Calanog et al. (2014), who measured an Einstein radius of $\theta_{\rm E} = 0.91^{+0.01}_{-0.01}$ arcsec. It was also observed with *ALMA* (Band 7, Bussmann et al., 2015) in the sub-mm/mm wavelength range and with *Keck*/NIRC2 AO ($K_{\rm s}$ band, Calanog et al., 2014) in the near-IR. The sub-mm/mm follow-up observations show only two images on the NW and SE sides of the lens, with the first one showing an arc-like shape. Bussmann et al. (2015) used the *ALMA* dataset to measure an Einstein radius of $\theta_{\rm E} = 0.956 \pm 0.005$ arcsec. We model the mass distribution of the lens with a SIE profile. The background source is reconstructed in a round component partially overlapping to the caustic, located on the SW side of the position of the mass centroid projected to the source plane. The difference in morphology between the near-IR and sub-mm image-plane emission (see Bussmann et al., 2015, for details) corresponds to a visible offset between the two components in the source plane, with dust emission being located on the SE side of the projected mass centroid.

HERMESJ103827+581544 (HLock04): We model this type 1 foreground lens at $z_{\rm l}^{\rm spec} = 0.59$ (SDSS DR13, Albareti et al., 2017) with two Sérsic components using `GASP2D`. The background lensed source forms two knots on the SE and NW sides of the lens, which is also surrounded by other fainter and more extended arcs. This system was studied in detail by Calanog et al. (2014), who measured an Einstein radius of $\theta_{\rm E} = 2.40^{+0.01}_{-0.05}$ arcsec and it was also observed with the *SMA* (340 GHz, Bussmann et al., 2013). The sub-mm/mm follow-up observations show no significant difference in morphology concerning the near-IR observations, except for a positional offset. Bussmann et al. (2013) used the *SMA* dataset to measure an Einstein radius of $\theta_{\rm E} = 2.0 \pm 0.2$ arcsec. We model the mass distribution of the lens with a SIE profile. The background source is reconstructed in an irregular component located on the E side of the position of the mass centroid projected to the source plane and caustic.

HERMESJ110016+571736 (HLock12): We model this type 1 foreground lens at $z_{\rm l}^{\rm spec} = 0.78$ (SDSS DR13, Albareti et al., 2017) with a single Sérsic component using `GASP2D`. The background lensed source gives rise to an extended arc on the NW side of the lens and a very faint compact secondary image on the SE side. This system was studied in detail by Calanog et al. (2014), who measured an Einstein radius of $\theta_{\rm E} = 1.14^{+0.04}_{-0.07}$ arcsec. We model the mass distribution of the lens with a SIE profile. The background source is reconstructed in two separate components, located on the E side of the position of the mass centroid projected to the source plane and caustic. The second farther component is weakly lensed by the foreground galaxy, showing no secondary image.

HATLASJ114638−001132$_{1,2}$ (HerBS2): This type 2 foreground lens is formed by two galaxies at $z_{\rm s}^{\rm spec} = 1.22$ (Bussmann et al., 2013), which we deblended by simultaneously modelling them with `GALFIT` using two Sérsic components each. The background lensed source at $z_{\rm s}^{\rm spec} = 3.26$ (Yang et al., 2017) shows a very complex structure with multiple

arcs and compact images. This system was studied in detail by Fu et al. (2012). It was also observed with *ALMA* (Band 6, Amvrosiadis et al., 2018), *SMA* (340 GHz, Fu et al., 2012), *PdBI* (232 GHz, Omont et al., 2013), and the *JVLA* (Ka-band, Fu et al., 2012) in the sub-mm/mm wavelength range and *Keck*/NIRC2 AO (J and K_s band, Fu et al., 2012) in the near-IR. The sub-mm/mm follow-up observations show three images: two arcs that split into two knots on the S and N sides of the lenses and a compact image between the two lenses. There is only a partial overlap between the near-IR and sub-mm/mm observations. We could not obtain a satisfactory model with a SIE and external shear due to the complex morphology of both the lens and background source.

HATLASJ125126+254928 (HerBS52): We model this type 1 foreground lens at $z_l^{phot} = 0.62$ (Negrello et al., 2017), with a single Sérsic component using `GASP2D`. The background lensed source at $z_s^{spec} = 3.44$ (Bakx et al., 2020) forms four knots located N, NE, S, and NW concerning the lens, three of which are connected by a fainter arc extending on the N side. This object was also observed with *ALMA* (Band 6, Prop. ID 2018.1.00526.S, PI I. Oteo). The sub-mm/mm follow-up observations show the counterparts of the N, NE, and S images. We model the mass distribution of the lens with a SIE profile. The background source is reconstructed in a compact flattened component located on the SW side of the position of the mass centroid projected to the source plane near the S cusp caustic. Faint and extended structures are visible around the main background source component.

HATLASJ125760+224558: We model this type 1 foreground lens at $z_l^{spec} = 0.55$ (SDSS DR13, Albareti et al., 2017) with a single Sérsic component using `GASP2D`. The background lensed source at $z_s^{phot} = 1.53$ (Negrello et al., 2017) forms a compact ring and a brighter knot on the NW side of the lens, which is slightly offset with respect to the ring. We model the mass distribution of the lens with a SIE profile. The background source is reconstructed in two separate components. The first smaller component is located near the E cusp of the caustic and forms the ring in the lensed image. The second larger component is located on the NW side of the mass centroid projected to the source plane, and it is lensed back into two separate images.

HATLASJ133008+245860 (HerBS12): We model this type 1 foreground lens at $z_l^{spec} = 0.43$ (Bussmann et al., 2013) with one Sérsic and one Gaussian component using `GASP2D`. The background lensed source at $z_s^{spec} = 3.11$ (Calanog et al., 2014) forms three compact images on the N, SE, and SW sides of the lens, which is also surrounded by a fainter incomplete ring. This system was studied in detail by Calanog et al. (2014), who measured an Einstein radius of $\theta_E = 0.944^{+0.002}_{-0.001}$ arcsec. It was also observed with *ALMA* (Band 7, Prop. ID 2018.1.00966.S, N. Indriolo), *SMA* (340 GHz, Bussmann et al., 2013), *PdBI* (240 GHz, Omont et al., 2013), and *NOEMA* (283 GHz, Yang et al., 2016) in the sub-mm/mm wavelength range and with *Keck*/NIRC2 AO (K_s band, Calanog et al., 2014) in the near-IR. The sub-mm/mm follow-up observations show no significant difference in morphology with respect to the near-IR observations. Bussmann et al. (2013) used the *ALMA* dataset to measure an Einstein radius of $\theta_E = 0.88 \pm 0.02$ arcsec. We model the mass distribution of the lens with a SIE profile. The background source is reconstructed in an irregular component located on the N cusp of the caustic and N of the position of the mass centroid projected to the source plane. A consistent morphology is seen in the reconstructed sub-mm/mm observations (see Bussmann et al., 2015, for details).

HATLASJ133846+255057 (HerBS29): We model this type 1 foreground lens at $z_{\rm l}^{\rm phot} = 0.42$ (Negrello et al., 2017) with a single Sérsic component using `GASP2D`. The background lensed source at $z_{\rm s}^{\rm phot} = 2.34$ (Bakx et al., 2018) forms two extended arcs with a sharp break on the S and N sides of the lens. This system was observed with *SMA* (340 GHz, Bussmann et al., 2013) too. The sub-mm/mm follow-up observations show no significant difference in morphology with respect to the near-IR ones. We model the mass distribution of the lens with a SIE profile and external shear to add further complexity to the mass model. The background source is reconstructed in a flattened component located on the SW side of the position of the mass centroid projected to the source plane, partially overlapping to the caustic.

HERMESJ171451+592634 (HFLS02): We model this type 1 foreground lens at $z_{\rm l}^{\rm spec} = 1.24$ (Shirley et al., 2021) with a single de Vaucouleurs component using `GASP2D`. The background lensed source at $z_{\rm s}^{\rm spec} = 3.18$ (Hernán-Caballero et al., 2016) forms two arcs on the NE and SW sides of the lens, which is surrounded by a fainter ring. This system was studied in detail by Calanog et al. (2014), who measured an Einstein radius of $\theta_{\rm E} = 0.87^{+0.02}_{-0.05}$ arcsec. We model the mass distribution of the lens with a SIE profile. The background source is reconstructed in two components linked by a fainter emission ($SNR < 3$), forming a thin elongated disk. This source is located on the S side of the position of the mass centroid projected to the source plane and partially overlapping to the caustic cusp.

HERMESJ171545+601238$_{1,2}$ (HFLS08): This type 3 foreground lensing system is formed by a main galaxy (labelled as '1' in Figure 5.1) at $z_{\rm l}^{\rm phot} = 0.40$ (Shirley et al., 2021) and possibly a secondary unresolved galaxy (labelled as '2'), for which the redshift is not yet available. The lack of redshift prevents us from being more conclusive about the lensing nature of the secondary galaxy. We used `GASP2D` to model the brighter galaxy with two Sérsic components and one PSF and the fainter one with a single Sérsic component. The background lensed source at $z_{\rm s}^{\rm spec} = 2.26$ (Calanog et al., 2014) forms an extended and irregular arc E of the lens and a compact secondary image on its W side. This system was studied in detail by Calanog et al. (2014), who measured an Einstein radius of $\theta_{\rm E} = 1.95^{+0.05}_{-0.04}$ arcsec. We could not obtain a satisfactory model with a SIE and external shear due to the complex morphology of both the lens and background source.

HATLASJ225844.8−295124 (HerBS26): This type 2 configuration is consistent with two blended galaxies at $z_{\rm l}^{\rm phot} = 0.69$ (Shirley et al., 2021), which we deblended by simultaneously fitting them with `GALFIT` using one and two Sérsic components, respectively. The background lensed source is located at $z_{\rm s}^{\rm phot} = 2.48$ (Bakx et al., 2018). It gives rise to an extended arc encircling the lens on the SW side without showing any clear secondary image. This morphology is likely due to the shear effect caused by the multiple-lens system. We could not obtain a satisfactory model with a SIE and external shear due to the complex morphology of both the lens and background source.

HELMSJ232210.3−033559$_{1,2}$ (HELMS19): This type 3 foreground lensing system is formed by a main galaxy (labelled as '1' in Figure 5.1) at $z_{\rm l}^{\rm phot} = 0.14$ (Nayyeri et al., 2016) and possibly a secondary fainter galaxy (labelled as '2'), for which the redshift is not yet available. The lack of redshift prevents us from being more conclusive about the lensing nature of the secondary galaxy. we model the two galaxies with `GASP2D` using two and one Sérsic components, respectively. The background lensed source is located at $z_{\rm s}^{\rm spec} = 4.69$

(Cox et al., 2023) and forms an extended irregular arc on the E side of the lens, a compact secondary image on the SW side, and possibly a third fainter image on the NW side. We could not obtain a satisfactory model with a SIE and external shear due to the complex morphology of both the lens and background source.

HATLASJ233037.2−331217$_{1,2}$ (HerBS123): This type 3 foreground lensing system is formed by a main galaxy (labelled as '1' in Figure 5.1) at $z_{\rm l}^{\rm phot} = 0.66$ (Shirley et al., 2021) and possibly a secondary unresolved galaxy (labelled as '2'), for which the redshift is not yet available. We deblended and modelled the two galaxies with `GALFIT` using two Sérsic components and a single unresolved component, respectively. The background lensed source is located at $z_{\rm s}^{\rm spec} = 2.17$, as measured by the BEARS survey (Urquhart et al., 2022). It shows a complex structure with multiple knots embedded into a main arc and a second inner elongated image on the SE side. This kind of morphology indicates strong shear, supporting the idea of a multiple lensing system. We could not obtain a satisfactory model with a SIE and external shear due to the complex morphology of both the lens and background source.

HELMSJ001626.0+042613 (HELMS22): We model this type 1 foreground lens at $z_{\rm s}^{\rm spec} = 0.22$ (Amvrosiadis et al., 2018) with two Sérsic components using `GASP2D`. The background lensed source at $z_{\rm s}^{\rm spec} = 2.51$ (Nayyeri et al., 2016) forms an arc on the S side of the lens. This system was observed with *ALMA* (Band 6, Amvrosiadis et al. 2018; Band 7, Prop. ID 2016.1.01188.S, S. Eales) in the sub-mm/mm wavelength range. The sub-mm morphology shows two compact images on top of the *HST* arc and a secondary image closer to the lens on its NE side. This system was studied in detail by Dye et al. (2018), who measured an Einstein radius of $\theta_{\rm E} = 0.98 \pm 0.07$ arcsec. The sub-mm/mm follow-up observations show both the S arc that splits into two images and a fainter secondary image on the NE side. The reconstructed background source is too faint, having $SNR < 3$; hence, we exclude the resulting model.

HATLASJ002624.8−341737 (HerBS22): We model this type 1 foreground lens at $z_{\rm l}^{\rm phot} = 0.93$ (Ward et al., 2022) with two Sérsic components using `GASP2D`. The background lensed source at $z_{\rm s}^{\rm phot} = 2.70$ (Zhang et al., 2018) forms an arc on the SW of the lens and a fainter secondary image on the opposite side. The SW arc splits into two components: a main and a fainter one, which are on the W and S side of the lens, respectively. The reconstructed background source is too faint, having $SNR < 3$; hence, we exclude the resulting model.

HELMSJ004723.6+015751$_{1,2}$ (HELMS9): This type 2 foreground lens is formed by two galaxies at $z_{\rm s}^{\rm spec} = 0.37$ (Amvrosiadis et al., 2018), which we deblended by simultaneously modelling them with `GALFIT` using two Sérsic components for the main galaxy (labelled as '1' in Figure 5.1) and one de Vaucouleurs component for the second galaxy (labelled as '2'). The background lensed source at $z_{\rm s}^{\rm spec} = 1.44$ (Nayyeri et al., 2016) shows a very complex structure with one confirmed arc on the N side of the lens and possibly multiple compact images. The background lensed source morphology is likely to be disturbed by additional features possibly related to the interaction with the two lenses. It was observed with *ALMA* (Band 6, Amvrosiadis et al., 2018) in the sub-mm/mm wavelength range. This system was studied in detail by Dye et al. (2018), who measured an Einstein radius of $\theta_{\rm E} = 2.16 \pm 0.10$ arcsec. The sub-mm/mm follow-up observations clearly show the N arc we detected in the *HST* image and some hints for further lensed images on the S side of the lens galaxies. We could not obtain a satisfactory model with a SIE and external shear due to the complex

morphology of both the lens and background source.

HERSJ012041.6−002705 (HERS2): We model this type 1 foreground lens at $z_{\rm l}^{\rm phot} = 0.73$ (Nayyeri et al., 2016) with two Sérsic components using `GASP2D`. The background lensed source forms an arc on the NE of the lens, a clump eastward of the arc and a fainter secondary image on the SW side of the lens. We model the mass distribution of the lens with a SIE profile. The background source is reconstructed in three components linked by a fainter emission ($SNR < 3$), forming an elongated disk-like structure. This source is located on the E side of the position of the mass centroid projected to the source plane and partially overlapping to the E cusp caustic.

HATLASJ085112+004934: We model this type 1 foreground lens at $z_{\rm l}^{\rm phot} = 0.66$ (Shirley et al., 2021) with three Sérsic components using `GASP2D`. The background lensed source at $z_{\rm s}^{\rm phot} = 1.77$ (Manjón-García et al., 2019) forms three arcs on the SW, SE, and NE sides of the lens. The SW arc is split roughly in half by a brighter clump. This morphology is likely due to the shear effect caused by nearby galaxies. We model the mass distribution of the lens with a SIE profile. The background source is reconstructed in two point-like components located in the caustic.

HATLASJ085359+015537 (G09v1.40): We model this type 1 foreground lens with two Sérsic components using `GASP2D`. The background lensed source at $z_{\rm s}^{\rm spec} = 2.09$ (Yang et al., 2016) forms a ring that splits into two arcs on the E and W sides of the lens. This system was studied in detail by Bussmann et al. (2013); Calanog et al. (2014), and Butler et al. (2021) with *ALMA* (Band 6, Butler et al. 2021 and Prop. ID 2017.1.00027.S, S. Eales; Band 7, Amvrosiadis et al. 2018 and Butler et al. 2021), and the *SMA* (340 GHz Bussmann et al., 2013) in the sub-mm/mm wavelength range and with *Keck*/NIRC2 AO ($K_{\rm s}$ band, Calanog et al., 2014) in the near-IR, respectively. These works measured an Einstein radius of $\theta_{\rm E} = 0.56^{+0.01}_{-0.02}$ arcsec from the *Keck* observations and $\theta_{\rm E} = 0.553 \pm 0.004$ arcsec from the *SMA* observations. The sub-mm/mm follow-up observations show no significant difference in morphology with respect to the near-IR ones. The reconstructed background source is too faint, having $SNR < 3$; hence, we exclude the resulting model.

HERMESJ104549+574512 (HLock06): We model this type 1 foreground lens at $z_{\rm l}^{\rm phot} = 0.20$ (Wardlow et al., 2013) with two Sérsic components using `GASP2D`. The background lensed source at $z_{\rm s}^{\rm spec} = 2.91$ (Calanog et al., 2014) forms two images on the NW and SE sides of the lens. Bussmann et al. (2013) used the *SMA* dataset to measure an Einstein radius of $\theta_{\rm E} = 0.10 \pm 0.03$ arcsec. We model the mass distribution of the lens with a SIE profile. The background source is reconstructed in two components which are linked by a fainter emission ($SNR < 3$), forming an elongated disk-like structure. This source is located on the E side of the position of the mass centroid projected to the source plane and caustic.

HERMESJ105551+592845 (HLock08): This type 2 foreground lens is formed by two (labelled as '1' and '2' in Figure 5.1) at $z_{\rm l}^{\rm phot} = 0.38$ (Wardlow et al., 2013), which we deblended by simultaneously modelling them with `GALFIT` using one Sérsic component each. The background lensed source at $z_{\rm s}^{\rm spec} = 1.70$ (Calanog et al., 2014) shows a complex morphology with a bright arc and a faint secondary image SW and NE of the galaxy 1 respectively, and a possible third image E of the galaxy 2. We could not obtain a satisfactory model with a SIE and external shear due to the complex morphology of both the lens and background source.

HERMESJ105751+573026$_{1,2,3,4,5,6}$ (HLock01): This type 2 foreground lens is formed by a group of six galaxies (labelled from '1' to'6' in Figure 5.1) at $z_{\rm l}^{\rm phot} = 0.60$ (Gavazzi et al., 2011), some of them needed to be deblended by simultaneously modelling them with `GALFIT` using respectively two Sérsic components, one de Vaucouleurs and one Sérsic component, one Sérsic component, one de Vaucouleurs component, one Sérsic component, and a PSF. Differently from Gavazzi et al. (2011), we divided galaxy 5 into two components. The background lensed source at $z_{\rm s}^{\rm spec} = 2.96$ (Gavazzi et al., 2011) forms a bright arc on the NE side of galaxy 1 that splits into two images in the proximity of galaxy 6, two additional bright compact images on the S and NW of galaxy 1, and, a faint counter image near the NE side galaxy 1 (which was predicted but not observed by Gavazzi et al. (2011)). This system was also observed with the *SMA* (340 GHz, Bussmann et al., 2013) and with *Keck*/NIRC2 AO (K_s band, Gavazzi et al., 2011). We could not obtain a satisfactory model with a SIE and external shear due to the complex morphology of both the lens and background source.

HATLASJ132630+334410 (NAv1.195): We model this type 1 foreground lens at $z_{\rm l}^{\rm spec} = 0.79$ (Bussmann et al., 2013) with one Sérsic component using `GASP2D`. The background lensed source at $z_{\rm s}^{\rm spec} = 2.95$ (Bussmann et al., 2013) forms two images on the NW and SE sides of the lens. This system was observed with *ALMA* (Band 3, Berman et al. 2022; Band 6, Prop. ID 2017.1.01214.S, PI Y. Min), and the *SMA* (340 GHz Bussmann et al., 2013). The sub-mm/mm follow-up observations show no significant difference in morphology with respect to the near-IR ones. Bussmann et al. (2013) and Kamieneski et al. (2023a) used the *SMA* and *ALMA* band 3 datasets, respectively, to measure an Einstein radius of $\theta_{\rm E} = 1.80 \pm 0.02$ arcsec and $\theta_{\rm E} = 1.78^{+0.21}_{-0.14}$ arcsec. We model the mass distribution of the lens with a SIE profile. The background source is reconstructed in an irregular component located on the NW side of the position of the mass centroid projected to the source plane and caustic.

HATLASJ133543+300404$_{1,2,3,4}$ (HerBS35): This type 2 foreground lens is formed by a cluster of galaxies (labelled as '1', '2', '3', and '4' in Figure 5.1) at $z_{\rm l}^{\rm spec} = 0.98$ (Stanford et al., 2014; Nayyeri et al., 2017), which we deblended by simultaneously modelling them with `GALFIT` using one Sérsic and one PSF component for galaxy 1 and one Sérsic component each for the remaining ones. The background lensed source at $z_{\rm s}^{\rm spec} = 2.69$ (Nayyeri et al., 2017) shows a complex morphology with a compact, bright arc and a faint secondary image NE and SW of the galaxy 1, one arc S of the galaxies 1 and 2, and another arc N of the galaxies 3 and 4. This system was observed with the *SMA* (228 GHz, Nayyeri et al., 2017), the *JVLA* (4 GHz, Nayyeri et al., 2017), and *Keck*/NIRC2 AO (H and K_s band, Nayyeri et al., 2017). The sub-mm/mm follow-up observations show a complex morphology with various arcs and images not detected in the near-IR observations. We could not obtain a satisfactory model with a SIE and external shear due to the complex morphology of both the lens and background source.

HATLASJ142140+000448 (HerBS140): We model this type 1 foreground lens at $z_{\rm l}^{\rm PHOT} = 1.11$ (Shirley et al., 2021) with a single Sérsic component using `GASP2D`. The background lensed source is located at $z_{\rm s}^{\rm spec} = 2.78$ (Cox et al., 2023) and forms a faint ring that splits on the N and S sides of the lens and a clump slightly offset of the ring on the NE side. We could not obtain a satisfactory model with a SIE and external shear due to the complex morphology of both the lens and background source.

HERMESJ142824+352620 (HBootes03): We model this type 1 foreground lens at $z_{\rm l}^{\rm spec} = 1.03$ (Borys et al., 2006) with two Sérsic components using `GASP2D`. The background lensed source at $z_{\rm s}^{\rm spec} = 1.33$ (Borys et al., 2006) forms a close arc on the NE of the lens and a diffuse secondary image on the SW side of the lens. It was observed with the *SMA* (340 GHz, Bussmann et al., 2013), and *ALMA* (Band 6, Amvrosiadis et al., 2018) in the sub-mm/mm wavelength range. The sub-mm/mm follow-up observations show no significant difference in morphology with respect to the near-IR observations. This system was studied in detail by Bussmann et al. (2013), who measured an Einstein radius of $\theta_{\rm E} = 2.46^{+0.01}_{-0.01}$ arcsec. We model the mass distribution of the lens with a SIE profile. The background source is reconstructed in an irregular component located on the N cusp of the caustic, N of the position of the mass centroid projected to the source plane.

HATLASJ223753.8−305828 (HerBS68): We model this type 1 foreground lens with one Sérsic component using `GASP2D`. The background lensed source at $z_{\rm s}^{\rm phot} = 2.13$ (Ward et al., 2022) or $z_{\rm s}^{\rm phot} = 2.26$ (Manjón-García et al., 2019)) forms an arc on the SE side of the lens and a faint secondary image on the E side. The SE arc shows a secondary faint farther arc extending from the main arc N tip. We model the mass distribution of the lens with a SIE profile. The background source is reconstructed in a flattened component located on the SE side of the position of the mass centroid projected to the source plane and caustic.

HATLASJ225250.7−313657 (HerBS47): We model this type 1 foreground lens with one Sérsic component using `GASP2D`. The background lensed source at $z_{\rm s}^{\rm phot} = 2.70$ (Manjón-García et al., 2019) forms a bright arc on the NW side of the lens and a faint secondary image on the SE side. Both the arc and the secondary image are split into two knots. We model the mass distribution of the lens with a SIE profile. The background source is reconstructed in a round component located on the NE side of the position of the mass centroid projected to the source plane and caustic.

HELMSJ233441.0−065220 (HELMS1): We model this type 1 foreground lens with two Sérsic components using `GASP2D`. For this case, we first modelled and subtracted the main images of the background lensed sources. Then, we masked around the residual signal of the source and modelled the lens. The background lensed source is located at $z_{\rm s}^{\rm spec} = 1.90$ (Cox et al., 2023) and forms an arc split into three bright unresolved images on the S side of the lens and a faint secondary image on the N side of the lens. We could not obtain a satisfactory model with a SIE and external shear due to the complex morphology of both the lens and background source.

HELMSJ233633.5−032119$_{1,2}$ (HELMS41): This type 2 foreground lens is formed by two galaxies, which we deblended by simultaneously modelling them with `GALFIT` using two Sérsic components for the first galaxy (labelled as '1' in Figure 5.1) and one Sérsic component for the second galaxy (labelled as '2'). The background lensed source is located at $z_{\rm s}^{\rm spec} = 2.34$ (Cox et al., 2023) and forms a ring (split into three arcs on the N, E, and W of the lens), as well as a secondary faint, more distant arc, and a more diffuse component, which are located close to the N arc. We model the mass distribution of the lens with a SIE profile. The background source is reconstructed in two separate components. The first is located on top of the E cusp of the caustic and forms the broken ring in the lensed image. The second component is located N of the mass centroid projected to the source plane and is lensed back into two separate images.

HELMSJ001615.7+032435 (HELMS13): We model this type 1 foreground lens at $z_{\rm l}^{\rm spec} = 0.66$ (Nayyeri et al., 2016) with one Sérsic component and one Gaussian using `GASP2D`. The background lensed source at $z_{\rm s}^{\rm spec} = 2.77$ (Nayyeri et al., 2016) is detected by *ALMA* (Band 7, Amvrosiadis et al., 2018), and forms a wide arc on the NE side of the lens. No secondary image is found. This system was studied in detail by Dye et al. (2018), who measured an Einstein radius of $\theta_{\rm E} = 2.79 \pm 0.10$ arcsec. We do not perform lens modelling since the background source is undetected in the *HST* image.

HELMSJ002220.9−015524 (HELMS29): We model this type 1 foreground lens with one Sérsic component using `GASP2D`. The background lensed source at $z_{\rm s}^{\rm spec} = 5.16$ (Asboth et al., 2016) was detected by *ALMA* (Band 6, Prop. ID 2015.1.01486.S, PI D. Riechers; Band 7, Prop. ID 2015.1.01486.S, PI D. Riechers; Band 8, Prop. ID 2015.1.01486.S and 2017.1.00043.S, PI D. Riechers). It forms a ring split into two brighter knots on the N and S sides of the lens. *HST* shows an arc-like structure at $\sim 1.5 - 2$ time the Einstein radius that is not detected in the sub-mm. We argued that it is part of the foreground galaxy. This system also has available deeper *HST*/WFC3 F105W (Prop. ID 14083, PI I. Pérez-Fournon), F125W (Prop. ID 15464, PI A. Long), and F160W (Prop. ID 14083, PI I. Pérez-Fournon) observations. After subtracting the lens, no counterpart was found in the *HST* image. We do not perform lens modelling since the background source is undetected in the *HST* image.

HELMSJ003814.1−002252 (HELMS24): We model this type 1 foreground lens at $z_{\rm l}^{\rm phot} = 0.17$ (Nayyeri et al., 2016) with one PSF using `GASP2D`. The background lensed source at $z_{\rm s}^{\rm spec} = 4.98$ (Cox et al., 2023) is detected by *ALMA* (Band 7, Ma et al., 2019). It forms an arc and a closer faint secondary image on the NE and SW sides of the lens, respectively. We do not perform lens modelling since the background source is undetected in the *HST* image.

HELMSJ003929.6+002426 (HELMS11): The foreground lens is a type 1 edge-on galaxy, which we model with `ISOFIT`. The background lensed source is located at $z_{\rm s}^{\rm spec} = 2.85$ (Cox et al., 2023) and was detected by *ALMA* (Band 7, Ma et al., 2019). It forms a ring with two brighter knots on the N and S sides of the lens. No *HST* counterpart is found after subtracting the lens. We do not perform lens modelling since the background source is undetected in the *HST* image.

HELMSJ004714.2+032454 (HELMS8): We model this type 1 foreground lens at $z_{\rm l}^{\rm phot} = 0.48$ (Nayyeri et al., 2016) with one Sérsic component and one exponential component using `GALFIT` including also the spiral structure. Additional $m = 2$, 3 Fourier components were added to the spiral arms to model their N-S asymmetry. The background lensed source at $z_{\rm s}^{\rm spec} = 1.19$ (Nayyeri et al., 2016) was detected by *ALMA* (Band 7, Amvrosiadis et al., 2018). It forms one arc on the S side of the lens and a compact secondary image on the N side. Near-IR counterparts of the background lensed source are visible only for the S arc. This system was studied in detail by Dye et al. (2018), who measured an Einstein radius of $\theta_{\rm E} = 0.59 \pm 0.03$ arcsec. We do not perform lens modelling since the background source is undetected in the *HST* image.

HELMSJ005159.4+062240$_{1,2,3}$ (HELMS18): This type 2 foreground lens is formed by a group of three galaxies, at $z_{\rm l}^{\rm spec} = 0.60$ (Okido et al., 2021), which we deblended by simultaneously modelling them with `GALFIT` using two Sérsic components for the first galaxy (labelled as '1' in Figure 5.1), one de Vaucouleurs component for the second galaxy (labelled as '2'), and one exponential profile, a PSF, and spiral arms for the third galaxy (labelled as

'3'). The background lensed source at $z_{\rm s}^{\rm spec} = 2.39$ (Nayyeri et al., 2016) was detected by *ALMA* (Band 6, Prop. ID 2017.1.00027.S, PI S. Eales; Band 7, Amvrosiadis et al. 2018). It forms an arc on the SW side of galaxy 3 and a secondary image on the E side of galaxies 1 and 2. This system was studied in detail by Maresca et al. (2022), who modelled the band 7 observations and measured the Einstein radii to be $\theta_{\rm E} = 3.80 \pm 0.02$ arcsec for the galaxies 1 and 2, and $\theta_{\rm E} = 1.46 \pm 0.02$ for the lens '3'. No *HST* counterpart is found after subtracting the lens. We do not perform lens modelling since the background source is undetected in the *HST* image.

HATLASJ005724.2−273122 (HerBS60): We model this type 1 foreground lens at $z_{\rm l}^{\rm phot} = 0.89$ (Ward et al., 2022) with one Sérsic component using `GASP2D`. The background lensed source at $z_{\rm s}^{\rm spec} = 3.26$ (Urquhart et al., 2022) is detected by *ALMA* (Band 6, Prop. ID 2018.1.00526.S, PI I. Oteo). It forms a ring that splits into two knots on the E and W sides of the lens, respectively. No *HST* counterpart is found after subtracting the lens. We do not perform lens modelling since the background source is undetected in the *HST* image.

HERMESJ021831−053131 (HXMM02): We model this type 1 foreground lens at $z_{\rm l}^{\rm spec} = 1.35$ (Wardlow et al., 2013) with one Sérsic component using `GASP2D`. The background lensed source at $z_{\rm s}^{\rm spec} = 3.40$ (Wardlow et al., 2013) is detected by *ALMA* (Band 6, Prop. ID 2013.1.00781.S, PI B. Hatsukade; Band 7, Prop. ID 2015.1.01528.S, PI I. Smail; Band 8, Prop. ID 2013.1.00749.S, PI D. Riechers), and *SMA* (340 GHz, Bussmann et al., 2013). It forms an arc that splits into two knots on the N side of the lens, an elongated second image on the S side, and a third elongated image on the W side. This system was studied in detail by Bussmann et al. (2013) and Bussmann et al. (2015), who modelled the *ALMA* band 6 and *SMA* observations, respectively. They measured an Einstein radius of $\theta_{\rm E} = 0.44 \pm 0.02$ and $\theta_{\rm E} = 0.507 \pm 0.004$, respectively. No *HST* counterpart is found after subtracting the lens. We do not perform lens modelling since the background source is undetected in the *HST* image.

HERMESJ033211−270536 (HECDFS04): We model this type 1 foreground lens with one PSF using `GASP2D`. The background lensed source is detected by *ALMA* (Band 7, Bussmann et al., 2015). It forms an arc and a faint secondary image on the S and the NW sides of the lens, respectively. This system was studied in detail by Bussmann et al. (2015), who measured an Einstein radius of $\theta_{\rm E} = 0.5$ arcsec. We do not perform lens modelling since the background source is undetected in the *HST* image.

HERMESJ044154−540352 (HADFS01): We model this type 1 foreground lens with one Sérsic component using `GASP2D`. The background lensed source was detected by *ALMA* (Band 7, Bussmann et al., 2015). It forms two arcs: one is more extended, splits into two knots and is located on the E side of the lens, and the other is on the W side. This system was studied in detail by Bussmann et al. (2015), who measured an Einstein radius of $\theta_{\rm E} = 1.006 \pm 0.004$ arcsec. No *HST* counterpart is found after subtracting the lens. We do not perform lens modelling since the background source is undetected in the *HST* image.

HATLASJ083932−011760 (HerBS105): The foreground lens is a type 1 edge-on galaxy, which we model with `ISOFIT`. The background lensed source is located at $z_{\rm s}^{\rm spec} = 2.67$ (Cox et al., 2023) and was detected by *ALMA* (Band 6, Prop. ID 2018.1.00526.S, PI I. Oteo). It forms two blended images separated by the disk of the lens. No *HST* counterpart is found after subtracting the lens. We do not perform lens modelling since the background source is undetected in the *HST* image.

HATLASJ091841+023048$_{1,2}$ (HerBS32): This type 2 foreground lens is formed by two galaxies which we deblended by simultaneously modelling them with `GALFIT` using two Sérsic components for the first galaxy (labelled as '1' in Figure 5.1) and one de Vaucouleurs component for the second one (labelled as '2'). The background lensed source at $z_{\rm s}^{\rm spec} = 2.58$ (Harris et al., 2012) is detected by *ALMA* (Band 3, Prop. ID 2017.1.01694.S, PI I. Oteo; and Band 7, Giulietti et al. 2022). It forms an arc on the E side of galaxy 1 and a secondary image on the W side of galaxy 2. An additional third *ALMA* detection is found E of the two galaxies near a *HST* clump and shows a faint near-IR counterpart. We do not perform lens modelling since the background source is undetected in the *HST* image.

HATLASJ113526−014606 (HerBS10): The background lensed source at $z_{\rm s}^{\rm spec} = 3.13$ was detected by *ALMA* (Band 3, 6, 7, and 8, Giulietti et al., 2023). It forms a wide arc on the SE and a secondary image on the NW. No foreground lens is detected in the near-IR, while there is a tentative detection for the background source. This system was studied in detail by Giulietti et al. (2023), who measured an Einstein radius of $\theta_{\rm E} = 0.4241^{+0.0005}_{-0.0005}$ arcsec. We do not perform lens modelling since the background source is undetected in the *HST* image.

HATLASJ115433.6+005042 (HerBS177): We model this type 1 foreground lens at $z_{\rm l}^{\rm phot} = 0.52$ (Shirley et al., 2021) with one Sérsic component using `GASP2D`. The background lensed source at $z_{\rm s}^{\rm phot} = 3.90$ (Bakx et al., 2020) is detected by *ALMA* (Band 7, Prop. ID 2019.1.01784.S, PI T. Bakx). It forms an arc on the E side of the lens and a secondary image on the W side. Potential near-IR counterparts of the background lensed source are visible on the S of the lens. We do not perform lens modelling since the background source is undetected in the *HST* image.

HATLASJ120127.6−014043 (HerBS61): We model this type 1 (or 2) foreground lens at $z_{\rm l}^{\rm phot} = 0.88$ (Shirley et al., 2021) with one Sérsic component and one exponential component using `GASP2D`. The background lensed source at $z_{\rm s}^{\rm phot} = 4.06$ (Manjón-García et al., 2019) is detected by the *SMA* (340 GHz, Enia et al., 2018). It forms an arc on the NW side of the lens and a bright secondary image on the SE side. This system was studied in detail by Enia et al. (2018), who measured an Einstein radius of $\theta_{\rm E} = 0.82 \pm 0.04$ arcsec. We do not perform lens modelling since the background source is undetected in the *HST* image.

HATLASJ131611+281220 (HerBS89): We model this type 1 foreground lens at $z_{\rm l}^{\rm phot} = 0.90$ (Berta et al., 2021) with one Sérsic component using `GASP2D`. The background lensed source at $z_{\rm s}^{\rm spec} = 2.9497$ (Neri et al., 2020) was resolved by *NOEMA* (255 GHz, Berta et al., 2021). It forms an arc on the S side of the lens and a compact image on the N side. This system was studied and modelled in detail by Berta et al. (2021), who measured an Einstein radius of $\theta_{\rm E} = 0.4832 \pm 0.0006$ arcsec. There is a tentative detection of the background lensed source in *HST* on the E and W sides of the lens. We do not perform lens modelling since the background source is undetected in the *HST* image.

HATLASJ134429+303036 (HerBS1): We model this type 1 foreground lens at $z_{\rm l}^{\rm spec} = 0.67$ (Bussmann et al., 2013) with one Sérsic component and one exponential component using `GASP2D`. The background lensed source at $z_{\rm s}^{\rm spec} = 2.30$ (Harris et al., 2012) was detected by *ALMA* (Band 6, Falgarone et al. 2017; and Band 7, Prop. ID 2016.1.00285.S, PI N. Indriolo) and by the *SMA* (340 GHz, Bussmann et al., 2013). It forms an arc on the W side of the lens and a more distant secondary image on the E side. This system was studied in detail by Bussmann et al. (2013) with the *SMA* data. They measured an Einstein radius of

$\theta_{\rm E} = 0.92 \pm 0.02$ arcsec. We do not perform lens modelling since the background source is undetected in the *HST* image.

HATLASJ141352−000027$_{1,2,3}$ (HerBS15): This type 3 foreground lens is formed by a cluster of galaxies at $z_{\rm l}^{\rm spec} = 0.55$ (Bussmann et al., 2013). We model three of the spectroscopically confirmed members, which are likely contributing to lensing, with GASP2D using one Sérsic and one exponential component for the main lens (labelled as '1' in Figure 5.1) and one Sérsic component for the second (labelled as '2') and the third (labelled as '3'). The background lensed source at $z_{\rm s}^{\rm spec} = 2.48$ (Harris et al., 2012) is detected by *ALMA* (Band 6, and 7, Prop. ID, 2018.1.00861.S PI C. Yang) and forms two arcs, one on the N of the galaxy 3 and the other on the E side of the galaxy 1. The background lensed source is only partly detected in *HST* images. We do not perform lens modelling since the background source is undetected in the *HST* image.

HATLASJ142414+022304$_{1,2}$ (HerBS13, ID 141): This type 2 foreground lens is formed by two galaxies at $z_{\rm l}^{\rm spec} = 0.60$ (Bussmann et al., 2012), which we deblended by simultaneously modelling them with `GALFIT` using one Sérsic component and a PSF for the first galaxy (labelled as '1' in Figure 5.1) and one Sérsic component for the second one (labelled as '2'). The background lensed source at $z_{\rm s}^{\rm spec} = 4.24$ (Cox et al., 2011) is detected by *ALMA* (Band 3 and 4, Dye et al. 2022; and 7, Dye et al. 2018; Band 8 Prop. ID 2016.1.00284.S, PI J. Bernard-Salas), and *SMA* (340 GHz, Cox et al. 2011). No *HST* counterpart is found after subtracting the lens. We do not perform lens modelling since the background source is undetected in the *HST* image.

HERMESJ142826+345547 (HBootes02): The foreground lens at $z_{\rm l}^{\rm spec} = 0.41$ (Wardlow et al., 2013) is a type 1 edge-on galaxy which we model with `ISOFIT`. The background lensed source at $z_{\rm s}^{\rm spec} = 2.41$ (Wardlow et al., 2013) was detected by the *SMA* (340 GHz, Bussmann et al., 2013) and by the *JVLA* (7 GHz, Wardlow et al., 2013). It forms an arc that splits into two knots and is located on the SE side of the lens, and a fainter secondary image is on the NW side. No *HST* counterpart is found after subtracting the lens. We do not perform lens modelling since the background source is undetected in the *HST* image.

HATLASJ230815.5−343801 (HerBS28): We model this type 1 foreground lens at $z_{\rm l}^{\rm phot} = 0.72$ (Ward et al., 2022) with two Sérsic components using `GASP2D`. The background lensed source at $z_{\rm s}^{\rm phot} = 4.03$ (Manjón-García et al., 2019) is detected by *ALMA* (Band 6, Prop. ID 2018.1.00526.S, PI I. Oteo). It forms an arc that splits into two knots and is located on the N side of the lens and a secondary image on the W side of the lens. No *HST* counterpart is found after subtracting the lens. We do not perform lens modelling since the background source is undetected in the *HST* image.

HELMSJ232439.5−043936 (HELMS7): We model this type 1 foreground lens with two Sérsic components using `GASP2D`. The background lensed source at $z_{\rm s}^{\rm spec} = 2.47$ (Nayyeri et al., 2016) is detected by *ALMA* (Band 6, Amvrosiadis et al. 2018; Band 7, Prop. ID 2017.1.00027.S, PI S. Eales). It forms three arcs: two are located close to the lens on its W and E sides, whereas the third arc is near an *HST* clump on the E side of the lens. This kind of morphology indicates multiple lenses, possibly the *HST* clump and a further one on the NW side of the main lens. This system was studied in detail by Maresca et al. (2022), who adopted two lenses and measured their Einstein radii to be $\theta_{\rm E} = 0.54 \pm 0.01$ arcsec and $\theta_{\rm E} = 0.40 \pm 0.01$, respectively. At the position of the second lens, there is no *HST* detection.

We do not perform lens modelling since the background source is undetected in the *HST* image.

HELMSJ233620.8−060828 (HELMS6): We model this type 1 foreground lens at $z_{\rm l}^{\rm spec} = 0.40$ (Nayyeri et al., 2016) with two Sérsic components using `GASP2D`. The lens is also part of the cluster that hosts other strong lensing events (see Carrasco et al. 2017 for details). The background lensed source at $z_{\rm s}^{\rm spec} = 3.43$ (Nayyeri et al., 2016) was detected by *ALMA* (Band 6, Prop. ID 2021.1.01116.S, PI D. Riechers; Band 8, Prop. ID 2013.1.00749.S, PI D. Riechers). It forms four images: two of them are on the S side of the lens and are connected by an arc, a third one on the W side, and a fourth on the NE side. Near-IR counterparts of the background lensed source are visible only for the S images. We do not perform lens modelling since the background source is undetected in the *HST* image.

HELMSJ000215.9−012829 (HELMS3): This type 2 foreground lens candidate is possibly formed by four galaxies, which we deblended by simultaneously modelling them with `GALFIT` using a Sérsic component for first(labelled as '1' in Figure 5.2), two Sersic components for the second galaxy (labelled as '2'), a de Vaucouleurs component for the third (labelled as '3'), and a Sérsic component and a PSF for the fourth one (labelled as '4'). There is no clear evidence of the lensed background source.

HELMSJ001800.1−060235 (HELMS21): We model this type 1 foreground lens candidate with a Sérsic component using `GASP2D`. Some elongated residuals are present towards the E side of the possible lens. However, the lack of a secondary image and the straight radially-elongated shape of the residuals make it impossible to confirm the lensing nature of the candidate.

HELMSJ002208.1+034044 (HELMS38): We model this type 1 foreground lens at a candidate with a Sérsic component using `GASP2D`. Some very faint and irregular ring-like residuals are present close to the centre of the possible lens. The irregularity and faintness of these residuals make it impossible to confirm the candidate lensing nature.

HATLASJ002533.5−333825 (HerBS87): We model this type 1 foreground lens candidate with a Sérsic component using `GASP2D`. Some elongated residuals are present, extending the centre of the lens towards the NE. Additionally, an oversubtraction and some residual emission are visible towards the centre and NW side of the possible lens. The shape and distribution of the residuals are consistent with a spiral structure and a dust lane viewed nearly edge-on. These residuals are not enough to confirm the lensing nature of the candidate.

HERMESJ002906−421419 (HELAISS01): We model this type 1 foreground lens candidate with two Sérsic components using `GASP2D`. Some arc-like residuals are present towards the SW side of the possible lens. However, the lack of a secondary image and follow-up observations makes it impossible to confirm the candidate lensing nature.

HATLASJ003207.7−303724 (HerBS56): We model this type 1 foreground lens candidate with two Sérsic components using `GASP2D`. Some residuals extending outwards from the centre are present towards the N, E and W sides of the possible lens. The shape and distribution of the residuals are consistent with the spiral structure viewed nearly face-on. These residuals are not enough to confirm the lensing nature of the candidate.

HELMSJ004747.1+061444 (HELMS26): The candidate foreground lens is a type 1 edge-on galaxy, which we model with `ISOFIT`. Some faint and irregular residuals are present towards the NE and SW sides of the possible lens. The irregularity and faintness of these

residuals make it impossible to confirm the candidate lensing nature.

HERSJ010301.2−003300 (HERS6): We model this type 1 foreground lens candidate with two Sérsic and a Gaussian component using `GASP2D`. No clear residuals are present after the candidate lens surface-brightness subtraction.

HERSJ011640.1−000454 (HERS4): We model this type 1 foreground lens candidate with a Sérsic component using `GASP2D`. No clear residuals are present after the candidate lens surface-brightness subtraction.

HATLASJ012415.9−310500 (HerBS69): We model this type 1 foreground lens candidate with a Sérsic and exponential components using `GALFIT` including also the spiral structure. Some residuals are present near the SE side of the possible lens. These residuals are not enough to confirm the lensing nature of the candidate.

HERSJ012521.0+011724 (HERS13): This type 3 foreground lens candidate is possibly formed by two galaxies which we model separately with `GASP2D` using a Sérsic component for first galaxy (labelled as '1' in Figure 5.2) and two Sersic components for the second (labelled as '2'). There is no clear evidence of the lensed background source. Some arc-like residuals are present towards the S side of the possible lens, although the lack of a clear secondary image makes it impossible to confirm the lensing nature of the candidate.

HERSJ012546.3−001143 (HERS12): We model this type 1 foreground lens candidate with a Gaussian and a de Vaucouleurs component using `GASP2D`. Some residuals are present, but they are likely associated with the lens subtraction.

HERSJ012754.1+004940 (HERS3): This type 2 foreground lens candidate is possibly formed by four galaxies, which we deblended by simultaneously modelling them with `GALFIT` using a Sérsic component for first and third galaxies (labelled as '1' and '2' in Figure 5.2), two Sersic components for the second galaxy (labelled as '3'), and a Sérsic component and a PSF for the fourth one (labelled as '4'). There is no clear evidence of the lensed background source.

HATLASJ012853.0−332719 (HerBS73): We model this type 1 foreground lens candidate with one Sérsic component using `GASP2D`. Some arc-like residuals are present towards the SE side of the possible lens. However, the lack of a clear secondary image and the complexity of the residuals are such that it is impossible to confirm the lensing nature of the candidate.

HATLASJ013840.5−281855 (HerBS14): It is unclear whether this source at $z^{\rm spec} = 3.78$ (Urquhart et al., 2022) is strongly lensed. It was detected by *ALMA* (Band 6, Prop. ID 2018.1.00526.S, PI I. Oteo) and shows one elongated component. Due to the ~ 0.6 arcsec resolution, it is impossible to exclude the presence of background lensed sources with very low angular separation. The candidate lens is a face-on spiral galaxy at $z^{\rm spec} = 0.61 \pm 0.28$. We modelled this candidate using a PSF and an exponential profile with `GALFIT` including also the spiral structure. Some residuals are present near the SE side of the possible lens. These residuals are not enough to confirm the lensing nature of the candidate.

HATLASJ013951.9−321446 (HerBS55): We model this type 1 foreground lens candidate with one Sérsic component using `GASP2D`. Some arc-like residuals are present towards the N and E sides of the possible lens. However, the lack of a clear secondary image and the complexity of the residuals are such that it is impossible to confirm the lensing nature of the candidate.

HERSJ021402.6−004612 (HERS17): We model this type 1 foreground lens candidate with three Sérsic components using `GASP2D`. Various arc-like residuals are present, although their configuration is not easily associated with strong lensing.

HERSJ021434.4+005926 (HERS16): We model this type 1 foreground lens candidate with a Sérsic and exponential components using `GALFIT` including also the spiral structure. Additional $m = 2$, 3 Fourier components were added to the spiral arms to model their NE-SW asymmetry. Some residuals extending outwards from the centre are present towards the SW side of the possible lens. The shape and distribution of the residuals are consistent with some leftover spiral structures viewed nearly face-on. These residuals are not enough to confirm the lensing nature of the candidate.

HERMESJ022017−060143$_{1,2}$ (HXMM01): This system is confirmed to be a DSFG pair that is weakly lensed by a pair of foreground galaxies. This type 3 foreground system is formed by an edge-on disk galaxy (labelled as '1' in Figure 5.2) at $z_{\rm l}^{\rm phot} = 0.87$ (Nayyeri et al., 2016) and a second-rounder and ringed galaxy (labelled as '2'). The sources at $z_{\rm s}^{\rm phot} = 0.87$ (Fu et al., 2012) were detected by *ALMA* (Band 6, Bussmann et al. 2015 and Prop. ID 2015.1.00723.S, PI I. Oteo; Band 7, Prop. ID 2011.0.00539.S, PI D. Riechers), *SMA* (340 GHz Fu et al., 2012), and *JVLA* (30 GHz Fu et al., 2012) in the sub-mm/mm and by *Keck*/NIRC2 AO ($K_{\rm s}$ Fu et al., 2012) in the near-IR. The background sources are located between the two lenses one on the S side and the other on the N side.

HERMESJ022135−062617 (HXMM03): It is unclear whether this background source at $z_{\rm s}^{\rm spec} = 2.72$ (Bussmann et al., 2015) is strongly lensed. we model the brightest cluster galaxy (BCG) of a candidate lensing cluster at $z_{\rm l}^{\rm spec} = 0.31$ (Albareti et al., 2017) with two Sérsic components using `GASP2D`. The source was detected by *ALMA* (Band 7, Bussmann et al., 2015). It forms a bright arc and is located on the E side of the lens. *ALMA* picked up no secondary image. Unfortunately, the W side of the potential lens, where the counter image is expected to be found, is outside the *ALMA* band 7 FOV. A near-IR counterpart of the *ALMA* arc is visible and shows a complex morphology with multiple knots. At the same time, the secondary image is not found even after subtracting the potential lens. One possibility is that the foreground structure weakly lenses the source.

HERMESJ045058−531654 (HADFS03): This system was proposed to be a group of three weakly lensed DSFGs by a foreground edge-on disk galaxy (Bussmann et al., 2015). It was detected by *ALMA* (Band 7, Bussmann et al., 2015) and forms three compact clumps near the candidate lens. All the *ALMA* clumps are on the S on the candidate lens and, as such, are not consistent with the usual strong lensing morphology.

HATLASJ084958+010713 (HerBS157): We model this type 1 foreground lens candidate with one Sérsic component using `GASP2D`. Bright arc-like residuals are present towards the SW side of the possible lens. However, the lack of a clear secondary image and the complexity of the residuals are such that it is impossible to confirm the lensing nature of the candidate.

HATLASJ090453.2+022017 (HerBS183): This type 2 foreground lens candidate is possibly formed by two galaxies (labelled as '1' and '2' in Figure 5.2), which we deblended by simultaneously modelling them with `GALFIT` using two Sérsic components each. No clear residuals are present after the candidate lens surface brightness subtraction.

HATLASJ091331−003644 (SDP.44): We model this type 1 foreground lens candidate

with two Sérsic components using GASP2D. Bright arc-like residuals are present towards the SW side of the possible lens. However, the lack of a clear secondary image and the complexity of the residuals are such that it is impossible to confirm the lensing nature of the candidate.

HATLASJ092136+000132 (HerBS91): This type 2 foreground lens candidate is possibly formed by four galaxies, which we deblended by simultaneously modelling them with GALFIT using two Sérsic components for the first (labelled as '1' in Figure 5.2), a Sérsic the second and third (labelled as '2' and '3'), and a de Vaucouleurs component for the fourth (labelled as '4'). These residuals are not enough to confirm the lensing nature of the candidate.

HATLASJ092409−005018 (HerBS185): We model this type 1 foreground lens candidate with a Sérsic component using GASP2D. Faint lens-shaped residuals are present after the lends subtraction, although their morphology is not easily associated with strong lensing.

HERMESJ103618+585454 (HLock05): We model this type 1 foreground lens candidate with a Sérsic component using GASP2D. No clear residuals are present after the candidate lens surface brightness subtraction.

HATLASJ113804−011736 (HerBS96): This type 2 foreground lens candidate is possibly formed by three galaxies, which we deblended by simultaneously modelling them with GALFIT using a Sérsic component for the first and third galaxy (labelled as '1' and '3' in Figure 5.2), and a Sérsic and spiral structure for the second (labelled as '2'). No clear residuals are present after the candidate lens surface brightness subtraction.

HATLASJ113833.3+004909 (HerBS100): This type 2 foreground lens candidate is possibly formed by four galaxies which we deblended by simultaneously modelling them with GALFIT using a Sérsic component for each (labelled as '1', '2', '3', and '4' in Figure 5.2). Various residuals are present, although, due to the system complexity, it is impossible to easily interpret them as multiple images of a strongly lensed galaxy.

HATLASJ113841−020237: This type 2 foreground lens candidate is possibly formed by two galaxies which we deblended by simultaneously modelling them with GALFIT using two Sérsic components for the first (labelled as '1' in Figure 5.2) and a Sérsic component for the second (labelled as '1'). A very faint arc is present on the S side of the possible lens. However, the lack of a clear secondary image and the faintness of the residuals make it impossible to confirm the lensing nature of the candidate.

HATLASJ115112−012638 (HerBS53): We model this type 1 foreground lens candidate with two Sérsic components using GALFIT to account for the different locations of their centres. Residuals are present on the SE side of the possible lens, although, due to the lack of a clear secondary image, it is impossible to confirm the lensing nature of the candidate.

HATLASJ115120−003322: This type 2 foreground lens candidate is possibly formed by three galaxies which we deblended by simultaneously modelling them with GALFIT using two Sérsic components for the first (labelled as '1' in Figure 5.2) and a Sérsic component for the other two (labelled as '2', '3'). Various residuals are present, although, due to the system complexity, it is impossible to easily interpret them as multiple images of a strongly lensed galaxy.

HATLASJ120127.8−021648: This type 2 foreground lens candidate is formed possibly by a group of three galaxies, which we deblended by simultaneously modelling them with GALFIT using a Sérsic and a de Vaucouleurs component for the first (labelled as '1' in

Figure 5.2) and a Sérsic component for the other two (labelled as '2', '3'). Various residuals are present, although, due to the system complexity, it is impossible to easily interpret them as multiple images of a strongly lensed galaxy.

HATLASJ120319.1−011253 (HerBS50): We model this type 1 foreground lens candidate with a Sérsic component using `GASP2D`. Residuals are present on the NE and SW sides of the possible lens. The shape and distribution of the residuals are consistent with the spiral structure viewed nearly edge-on. These residuals are not enough to confirm the lensing nature of the candidate.

HATLASJ121301.5−004922 (HerBS48): We model this type 1 foreground lens candidate with a Sérsic component using `GASP2D`. An arc-like residual is present on the NW side of the possible lens, although, due to the lack of a clear secondary image, it is not possible to confirm the lensing nature of the candidate.

HATLASJ121334.9−020323: We model this type 1 foreground lens candidate with two Sérsic components using `GASP2D`. Various residuals are present close to the centre of the possible lens. However, due to their complex morphology and faintness, it is impossible to easily interpret them as multiple images of a strongly lensed galaxy.

HATLASJ121542.7−005220 (HerBS62): We model this type 1 foreground lens candidate with a Sérsic component using `GASP2D`. An arc-like residual is present on the SW side of the possible lens, although, due to the lack of a clear secondary image, it is impossible to confirm the lensing nature of the candidate.

HATLASJ130054+260303 (HerBS129): We model this type 1 foreground lens candidate with a Sérsic component using `GASP2D`. No clear residuals are present after the candidate lens surface brightness subtraction.

HATLASJ131322+285836: This type 2 foreground lens candidate is possibly formed by a group of two galaxies, which we deblended by simultaneously modelling them with `GALFIT` using a Sérsic component for each (labelled as '1' and '2' in Figure 5.2). Various residuals are present, although, due to the system complexity, it is impossible to easily interpret them as multiple images of a strongly lensed galaxy.

HATLASJ134159+292833: We model this type 1 foreground lens candidate with a Sérsic component using `GASP2D`. An arc-like residual is present on the W side of the possible lens, although, due to the lack of a clear secondary image, it is impossible to confirm the lensing nature of the candidate.

HATLASJ141833+010212 (HerBS110): This type 2 foreground lens candidate is possibly formed by a group of two galaxies, which we deblended by simultaneously modelling them with `GALFIT` using a de Vaucouleurs component (labelled as '1' and '2' in Figure 5.2). No clear residuals are present after the candidate lens surface brightness subtraction.

HERMESJ142201+533214 (HEGS01): This type 2 foreground lens candidate is possibly formed by a group of three galaxies which we deblended by simultaneously modelling them with `GALFIT` using a Sérsic component and a PSF for the first two (labelled as '1' and '2' in Figure 5.2) and a PSF for the third (labelled as '3'). No clear residuals are present after the candidate lens surface brightness subtraction.

HATLASJ142318.3+013913: We model this type 1 foreground lens candidate with a Sérsic and an exponential disk component using `GALFIT` to include a spiral structure. Various residuals are present around the possible lens. The shape and distribution of the residuals

are consistent with the spiral structure viewed nearly face-on. These residuals are not enough to confirm the lensing nature of the candidate.

HATLASJ143203−005219: We model this type 1 foreground lens candidate with two Sérsic components using `GALFIT` to include a spiral structure. Various residuals are present around the possible lens. The shape and distribution of the residuals are consistent with the spiral structure viewed nearly face-on. These residuals are not enough to confirm the lensing nature of the candidate.

HERMESJ143331+345440 (HBootes01): It is unclear whether this background source at $z^{\rm spec} = 3.27$ (Wardlow et al., 2013) is strongly lensed. It was detected by the *SMA* (340 GHz, Bussmann et al., 2013) and shows one elongated component. Due to the ~ 0.6 arcsec resolution, it is impossible to exclude the presence of background lensed sources with very low angular separation. we model a potential lensing system at $z^{\rm phot} = 0.59$ with one Sérsic component.

HATLASJ144243+015506 (HerBS153): We model this type 1 foreground lens candidate with a Sérsic component using `GASP2D`. Various residuals are present close to the centre of the possible lens. However, due to their complex morphology and faintness, it is impossible to easily interpret them as multiple images of a strongly lensed galaxy.

HATLASJ144715−012114: This type 2 foreground lens candidate is possibly formed by a group of three galaxies, which we deblended by simultaneously modelling them with `GALFIT` using two Sérsic components for the first two (labelled as '1' and '2' in Figure 5.2) and a Sérsic component for the third (labelled as '3'). Faint lens-shaped residuals are present after the lens subtraction, but their morphology is not easily associated with strong lensing.

HATLASJ223942.4−333304 (HerBS111): We model this type 1 foreground lens candidate with a Sérsic component using `GASP2D`. An arc-like residual is present on the SW side of the possible lens, although, due to the lack of a clear secondary image, it is impossible to confirm the lensing nature of the candidate.

HATLASJ224026.5−315154 (HerBS148): We model this type 1 foreground lens candidate with a Sérsic component using `GASP2D`. Various residuals are present close to the centre of the possible lens. However, due to their complex morphology and faintness, it is impossible to easily interpret them as multiple images of a strongly lensed galaxy.

HATLASJ224759.6−310134 (HerBS141): We model this type 1 foreground lens candidate with two Sérsic components using `GASP2D`. Various residuals are present close to the centre of the possible lens. However, due to their complex morphology and faintness, it is impossible to easily interpret them as multiple images of a strongly lensed galaxy. The shape of the residuals suggests the presence of a dust lane extending from the NE to the SW side of the lens.

HATLASJ224805.3−335820 (HerBS33): We model this type 1 foreground lens candidate with two Sérsic components using `GASP2D`. A compact possible lensed image is present on the W side of the possible lens. However, the lack of a clear secondary image makes it impossible to confirm the candidate's lensing nature.

HATLASJ225045.5−304719 (HerBS168): We model this type 1 foreground lens candidate with two Sérsic components using `GASP2D`. Various residuals are present around the possible lens. The shape and distribution of the residuals are consistent with the spiral structure viewed nearly edge-on; hence, these residuals are not enough to confirm the lensing

nature of the candidate.

HATLASJ230546.2−331038 (HerBS49): This type 3 foreground lens candidate is possibly formed by two galaxies which we model separately with GASP2D using a Sérsic and an exponential disk component for first galaxy (labelled as '1' in Figure 5.2) and a Sersic component for the second (labelled as '2'). A possible multiple image is present on the NW side of galaxy '1'. However, the lack of a clear secondary image makes it impossible to confirm the candidate lensing nature.

HELMSJ231447.5−045658 (HELMS44): We model this type 1 foreground lens candidate with two Sérsic components using GALFIT to account for the different locations of their centres. Various residuals are present close to the centre of the possible lens. However, due to the complexity of the system, it is impossible to easily interpret them as multiple images of a strongly lensed galaxy.

HATLASJ232210.9−333749 (HerBS146): We model this type 1 foreground lens candidate with a Sérsic component using GALFIT to include spiral structure. No clear residuals are present after the candidate lens surface brightness subtraction.

HATLASJ232531.3−302235 (HerBS17): This type 2 foreground lens candidate is formed by a group of possibly two galaxies which we deblended by simultaneously modelling them with GALFIT using a Sérsic component each (labelled as '1' and '2' in Figure 5.2). Various residuals are present close to both possible lenses. However, due to the complexity of the system, it is impossible to easily interpret them as multiple images of a strongly lensed galaxy.

HELMSJ232617.5−025319 (HELMS51): We model this type 1 foreground lens candidate with a Sérsic component using GASP2D. Various residuals are present close to the centre of the possible lens. However, due to the complexity of the system, it is impossible to easily interpret them as multiple images of a strongly lensed galaxy.

HELMSJ232831.8−004035 (HELMS55): We model this type 1 foreground lens candidate with a Sérsic and an exponential disk component using GASP2D. Various residuals are present close to the centre of the possible lens. However, due to their complex morphology and faintness, it is impossible to easily interpret them as multiple images of a strongly lensed galaxy. The shape of the residuals suggests the presence of sub-structures in the surface brightness distribution of the lens.

HELMSJ232833.6−031416 (HELMS48): We model this type 1 foreground lens candidate with a Sérsic component using GASP2D. No clear residuals are present after the candidate lens surface brightness subtraction.

HELMSJ233420.4−003458 (HELMS43): The candidate foreground lens is a type 1 edge-on galaxy, which we model with ISOFIT. Irregular residuals are present towards the NE side of the possible lens. The irregularity of these residuals and lack of a secondary image make it impossible to confirm the candidate lensing nature.

HELMSJ233721.9−064740 (HELMS49): We model this type 1 foreground lens candidate with a Sérsic component using GASP2D. Various residuals are present close to the centre of the possible lens. However, due to their complex morphology and faintness, it is impossible to easily interpret them as multiple images of a strongly lensed galaxy. The shape of the residuals suggests the presence of sub-structures in the surface brightness distribution of the lens.

HELMS233728.8−045106 (HELMS20): We model this type 1 foreground lens candidate with two Sérsic components and a de Vaucouleurs component using `GALFIT` to account for the different location of their centres. No clear residuals are present after the candidate lens surface-brightness subtraction.

HELMSJ234314.0+012152 (HELMS36): This type 3 foreground lens candidate is possibly formed by two galaxies which we model separately with `GASP2D` using a Sérsic component for first galaxy (labelled as '1' in Figure 5.2) and two Sersic components for the second (labelled as '2'). A possible multiple image is present on the SE side of galaxy '1'. However, the lack of a clear secondary image makes it impossible to confirm the candidate lensing nature.

HATLASJ234955.7−330833 (HerBS184): We model this type 1 foreground lens candidate with two Sérsic components using `GASP2D`. Various residuals are present very close to the centre of the possible lens. However, due to the complexity of the system, it is impossible to easily interpret them as multiple images of a strongly lensed galaxy.

HELMSJ235101.7−024425 (HELMS50): We model this type 1 foreground lens candidate with three Sérsic components using `GASP2D`. Various residuals are present very close to the centre of the possible lens. However, due to the complexity of the system, it is impossible to easily interpret them as multiple images of a strongly lensed galaxy. The shape of the residuals suggests the presence of a dust lane extending from the NW to the SE side of the lens.

HATLASJ235121.9−332902 (HerBS159): This type 2 foreground lens candidate is formed by a group of possibly two galaxies which we deblended by simultaneously modelling them with `GALFIT` using two Sérsic components each (labelled as '1' and '2' in Figure 5.2). No clear residuals are present after the candidate lens surface brightness subtraction.

HELMSJ235331.7+031717 (HELMS40): It is unclear whether this source located at $z_{\rm s}^{\rm spec}$ = (Cox et al., 2023) is strongly lensed. The source is detected by *ALMA* (Band 7, Amvrosiadis et al., 2018). It forms two pairs of compact sources. The first pair (on the SE side of the cutout) shows a possible near-IR detection but no foreground lens candidate. The members of the second pair are located on the N and S sides of a possible lensing galaxy, respectively, and they do not show any *HST* counterpart. We model the potential lensing system with two Sérsic components and a Gaussian using `GALFIT` to account for the different locations of their centres. This system was studied in detail by Maresca et al. (2022), who modelled the SE pair and measured an Einstein radius of $\theta_{\rm E} = 0.21 \pm 0.01$. We note that the lens redshift adopted by Maresca et al. (2022) is likely associated with a close-by spiral galaxy on the SE side of the SE pair.

HATLASJ011014.5−314813 (HerBS160): It is unclear whether this background source at $z^{\rm spec} = 3.96$ (Urquhart et al., 2022) is strongly lensed. It is detected by *ALMA* (Band 6, Prop. ID 2018.1.00526.S, PI I. Oteo) and forms an elongated arc-like structure near a faint *HST* counterpart. We found no secondary image.

HERMESJ023006−034153 (HXMM12): This system was proposed to be a weakly lensed DSFG by a group of foreground galaxies (Bussmann et al., 2015). It was detected by *ALMA* (Band 7, Bussmann et al., 2015) and forms an arc-like structure near a faint *HST* counterpart. We found no secondary image.

HERMESJ043341−540338 (HADFS04): This system was proposed to be a system

of three DSFGs that is weakly lensed by a foreground group of galaxies (Bussmann et al., 2015). It was detected by *ALMA* (Band 7, Bussmann et al., 2015). The two DSFGs are located on the SE and NE sides of the foreground galaxy. This system was studied in detail by Bussmann et al. (2015), who assumed an Einstein radius of 0.5 arcsec. A near-IR counterpart of the *ALMA* southernmost source is visible.

HATLASJ144556.1−004853 (HERBS46): Whether this background source is strongly lensed is unclear. It was detected by the *SMA* (340 GHz, Bussmann et al., 2013), and shows one elongated component near a faint *HST* counterpart. Due to the ~ 0.6 arcsec resolution, it is impossible to exclude the presence of background lensed sources with very low angular separation.

HATLASJ224207.2−324159 (HerBS67): It is unclear whether this background source at $z^{\rm phot} = 3.57$ (Bakx et al., 2018) is strongly lensed. It was detected by *ALMA* (Band 6, Prop. ID 2018.1.00526.S, PI I. Oteo) and shows one elongated component. Due to the ~ 0.6 arcsec resolution, it is impossible to exclude the presence of background lensed sources with very low angular separation.

5.1.1 Plots and tables

In Figure 5.1, we show the best-fitting surface brightness models for the candidates that were classified as A through the visual classification, multiwavelength follow-up observations, or after the subtraction of the lens surface brightness model.

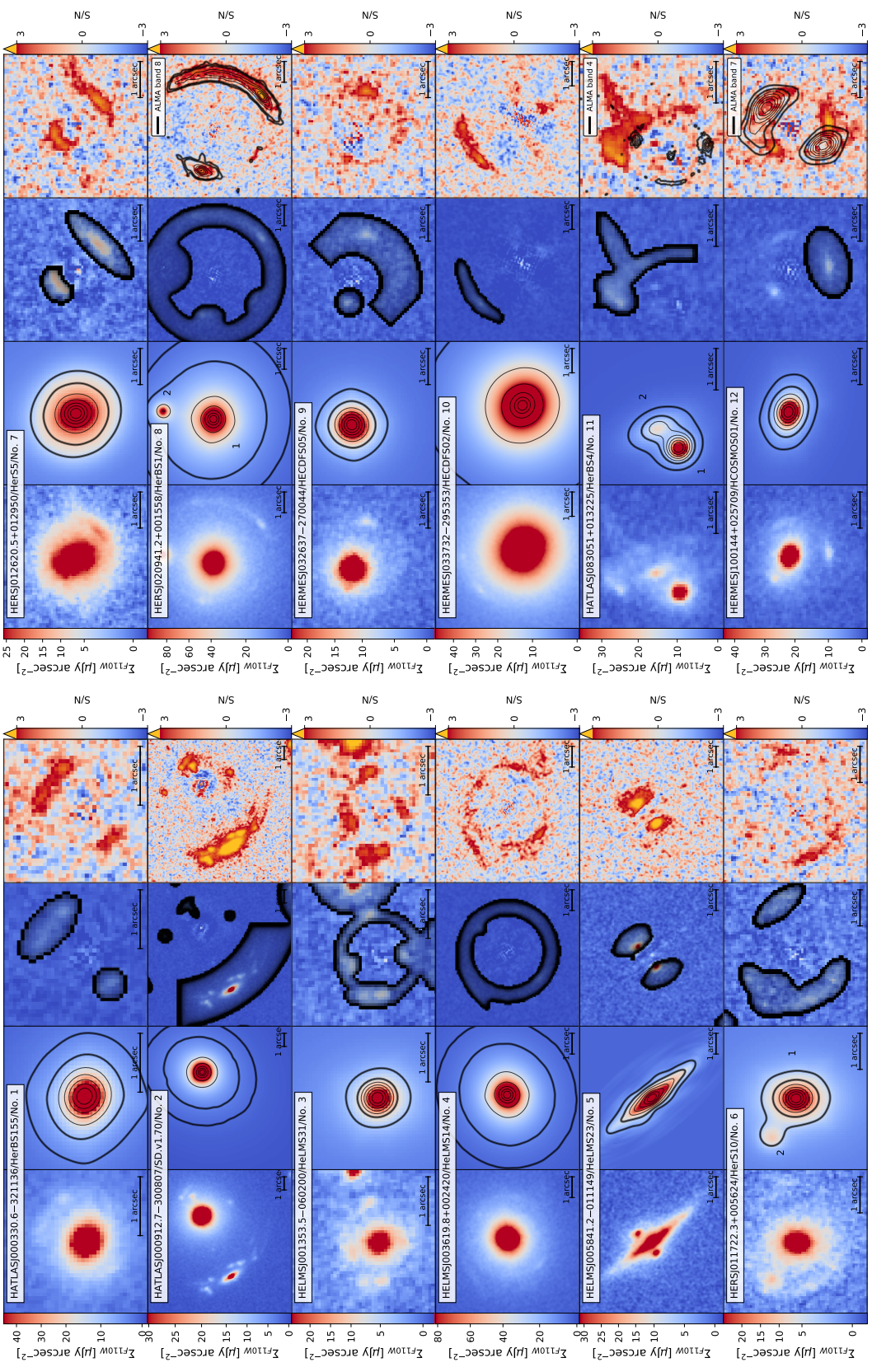

Figure 5.1: *From left to right panels:* Observed *HST* F110W image, best-fitting surface-brightness model of the lens, residual obtained after the subtraction of the lens model from the image, and SNR map of the residuals for the A class candidates. The contours in the model images are taken at two levels corresponding to $SNR = 5$ and 10 (thick curves), and five uniformly spaced levels between the $SNR = 10$ and the maximum SNR in the model image (thin curves). The residual map shows the pixel mask (corresponding to the black-shaded regions) adopted for the surface brightness modelling. The residual maps show the contours of available high-resolution multiwavelength data taken at two levels corresponding to $SNR = 5$ and 10 (thick curves), and five uniformly spaced levels between the $SNR = 10$ and the maximum SNR in the multiwavelength image (thin black curves). The images are oriented such that N is up and E is to the left.

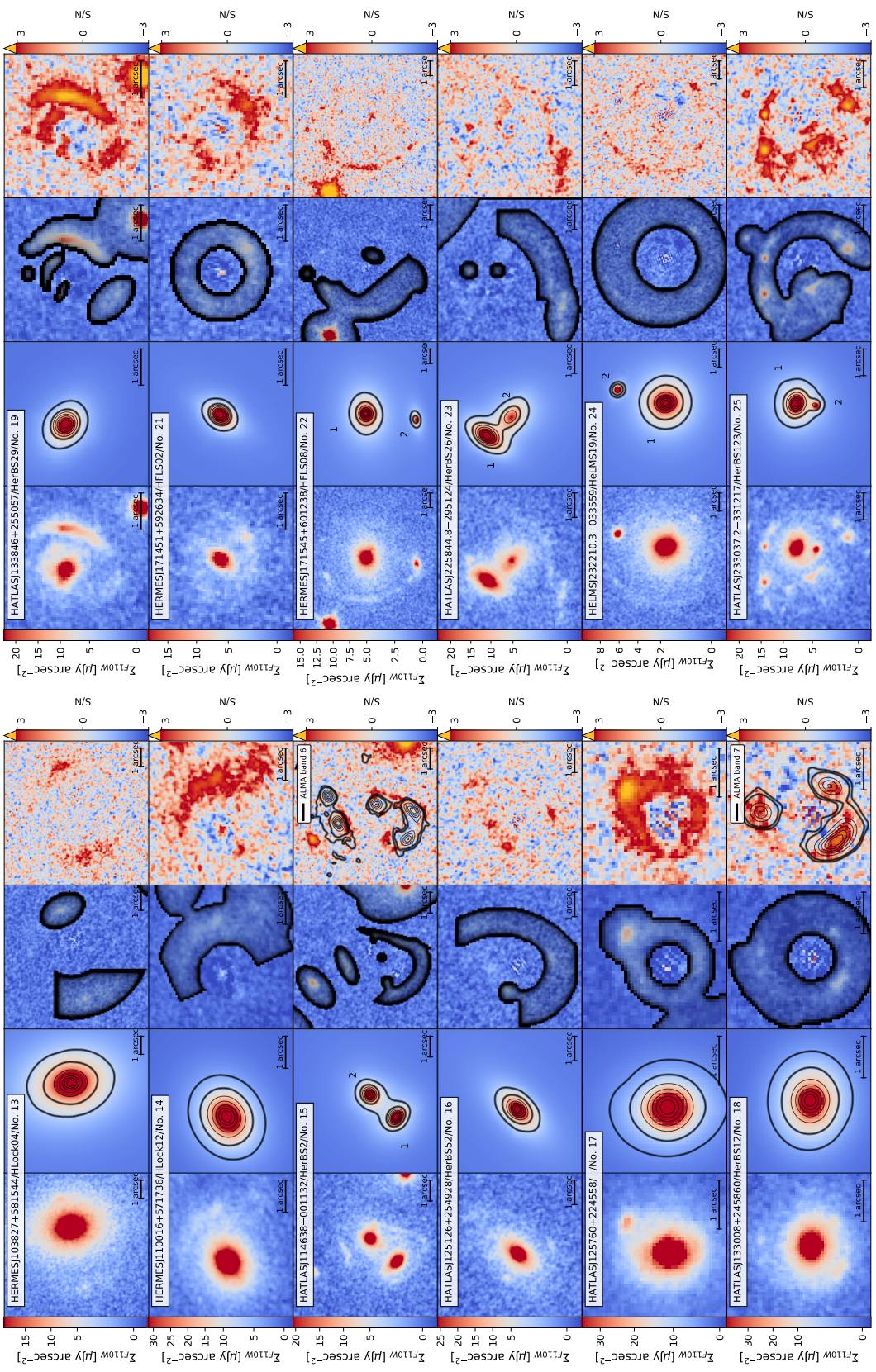

Figure 5.1 (cont.)

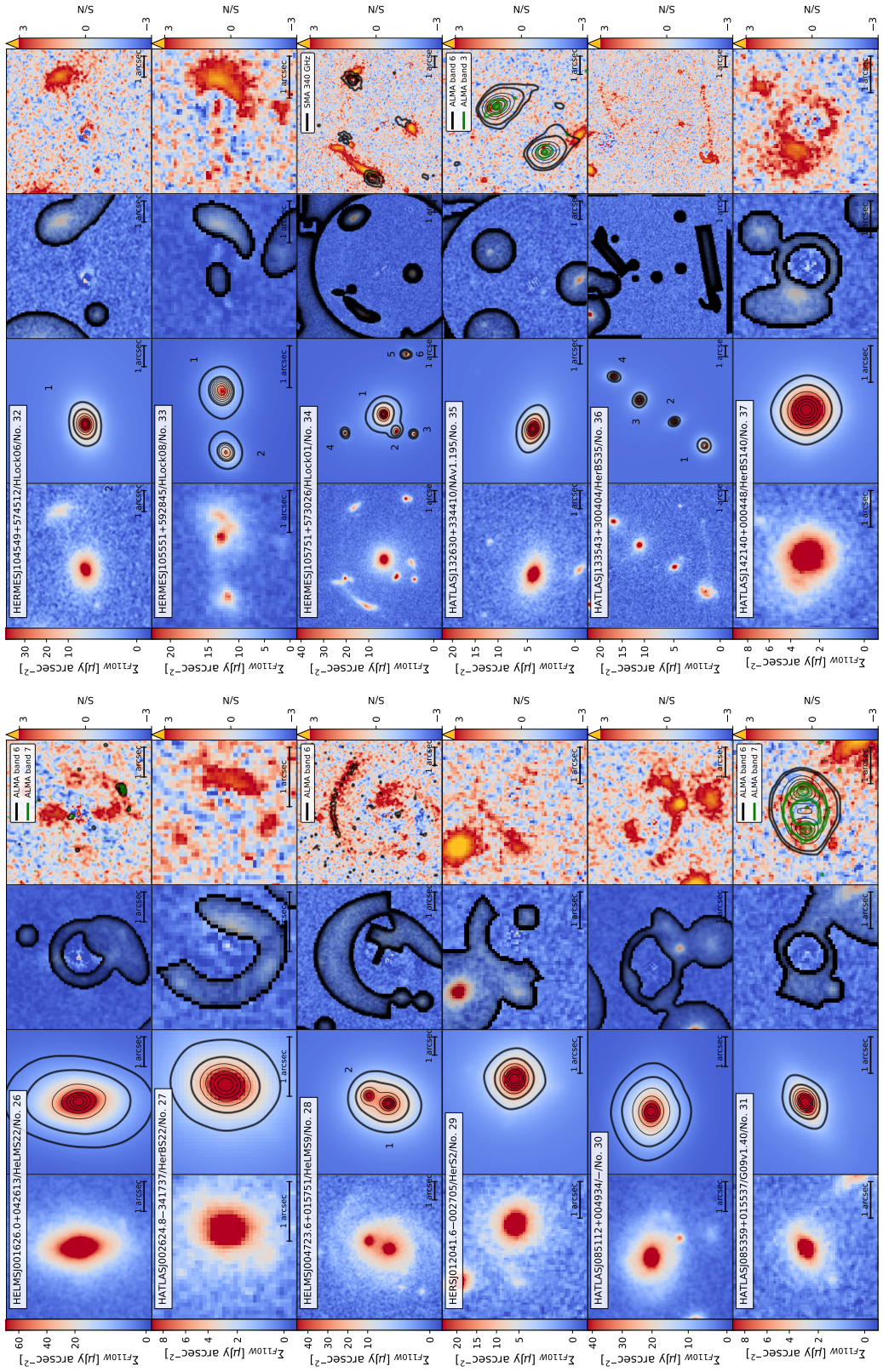

Figure 5.1 (cont.)

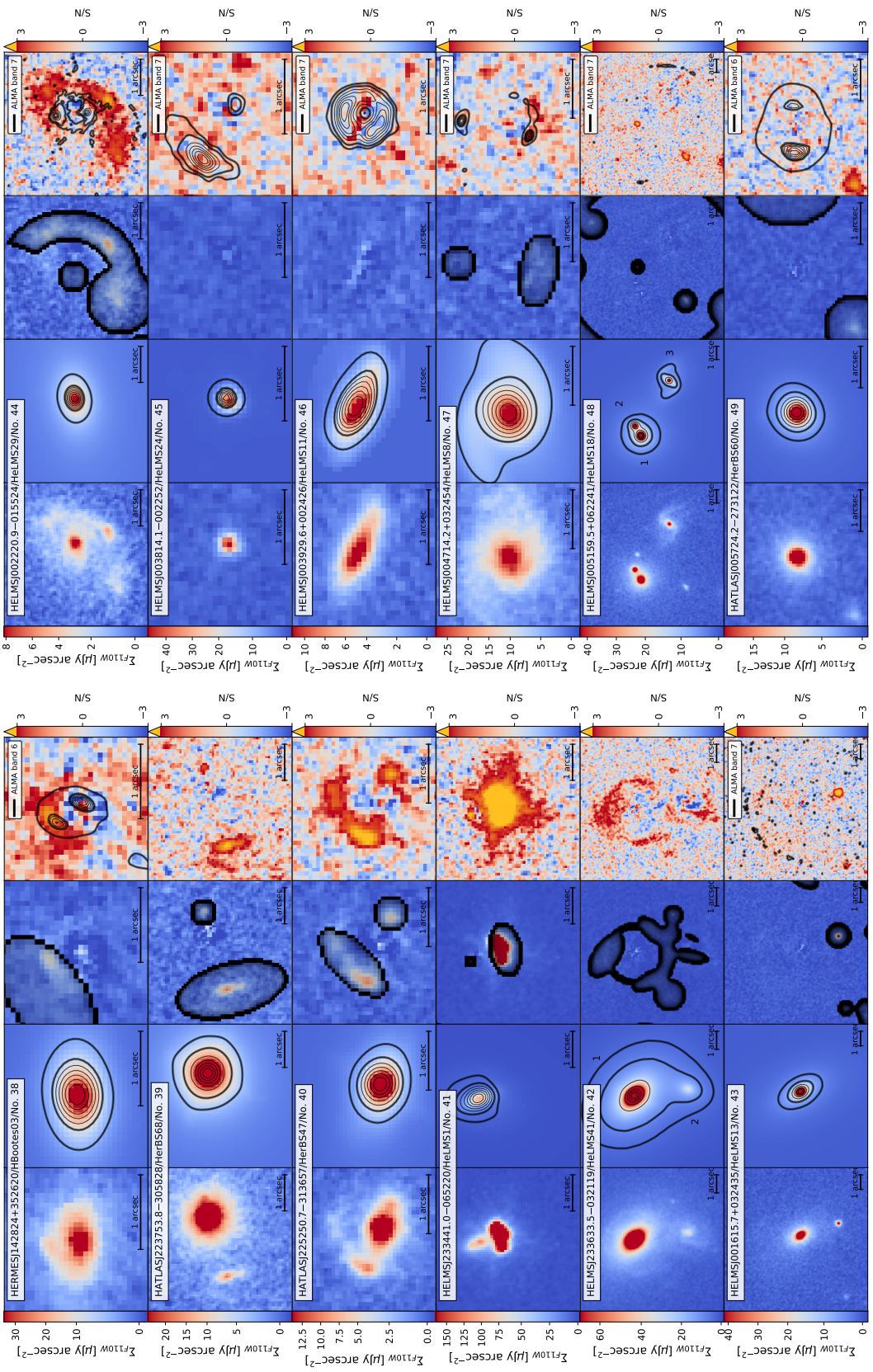

Figure 5.1 (cont.)

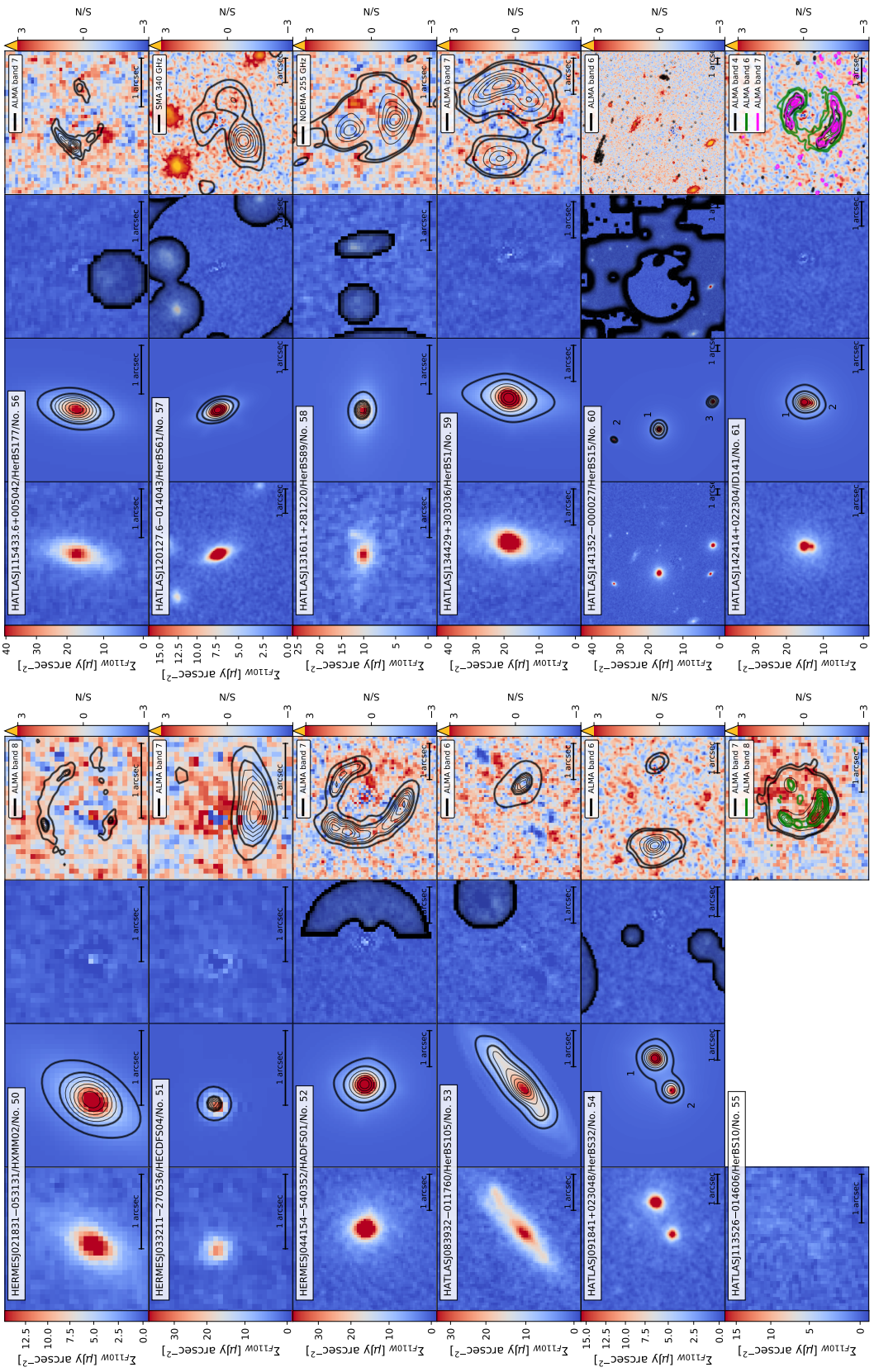

Figure 5.1 (cont.)

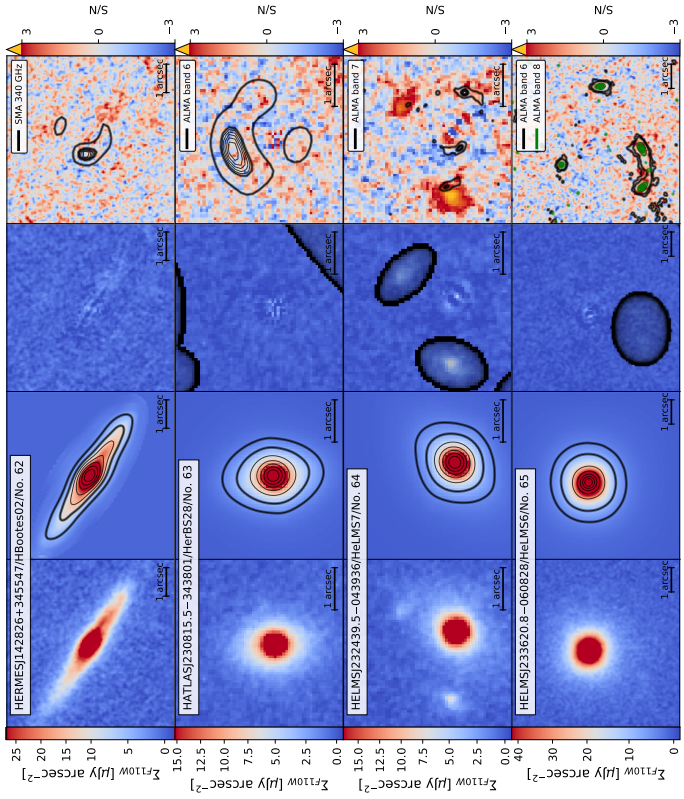

Figure 5.1 (cont.)

In Figure 5.2, we show the best-fitting surface brightness models for the candidates classified as B.

The best-fitting parameters for the surface brightness modelling can be found in Table 5.1 and Table 5.2 for the confirmed lenses. Whereas, in Table 5.3 and Table 5.4, we present the best-fitting parameters for the surface brightness modelling for the B candidates.

In Figure 5.3, we show the results of the lens modelling for some of the candidates classified as A. For the complete modelled candidates, we refer the reader to Chapter 5 or the source-by-source description. In Table 5.5, we report the results of the lens modelling.

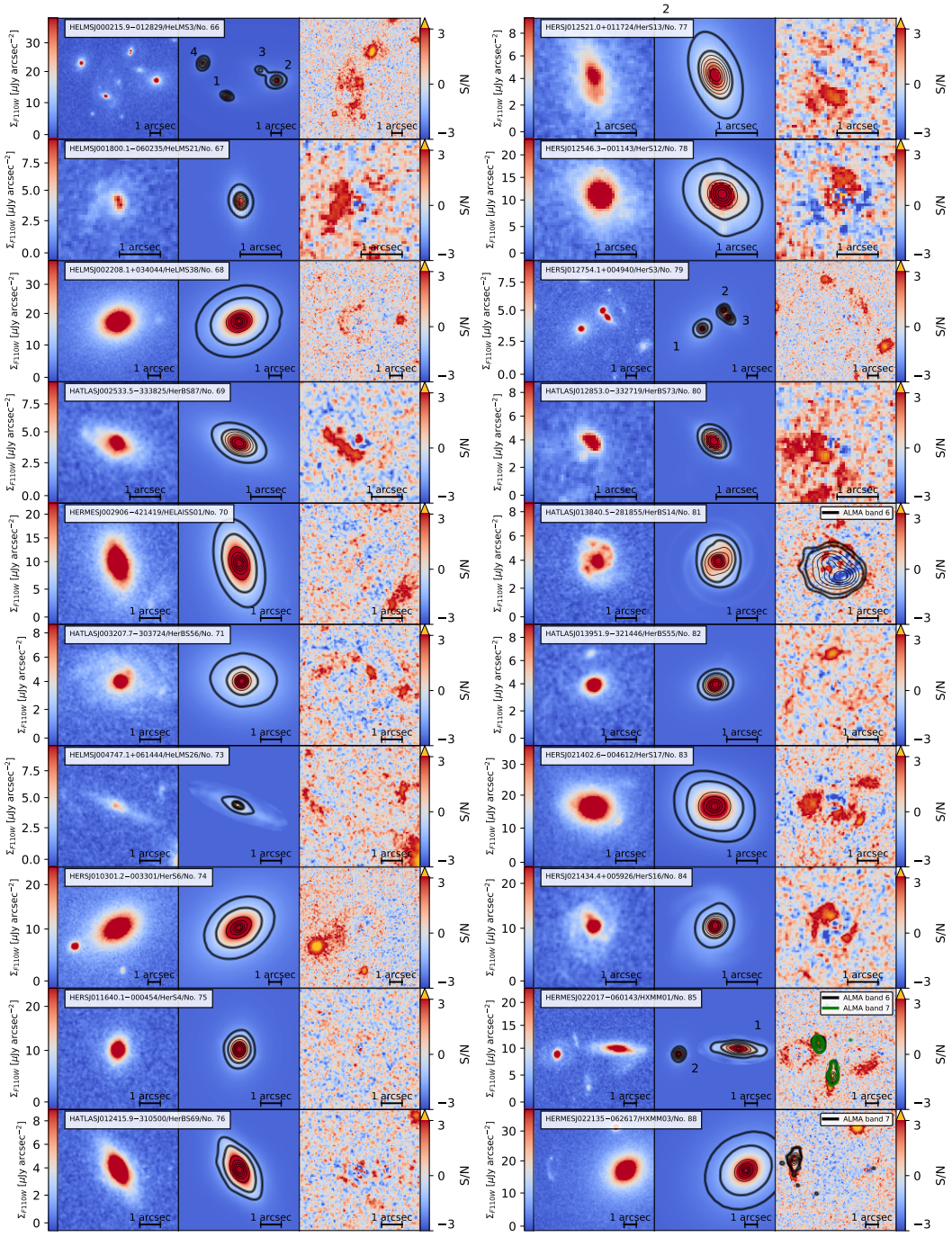

Figure 5.2: *From left to right panels:* Observed *HST* F110W image, best-fitting surface-brightness model of the lens, residual obtained after the subtraction of the lens model from the image, and SNR map of the residuals for the B class candidates. The contours in the model images are taken at two levels corresponding to $SNR = 5$ and 10 (thick curves), and five uniformly spaced levels between the $SNR = 10$ and the maximum SNR in the model image (thin curves). The residual map shows the pixel mask (corresponding to the black-shaded regions) adopted for the surface brightness modelling. The residual maps show the contours of available high-resolution multiwavelength data taken at two levels corresponding to $SNR = 5$ and 10 (thick curves), and five uniformly spaced levels between the $SNR = 10$ and the maximum SNR in the multiwavelength image (thin black curves). The images are oriented such that N is up and E is to the left.

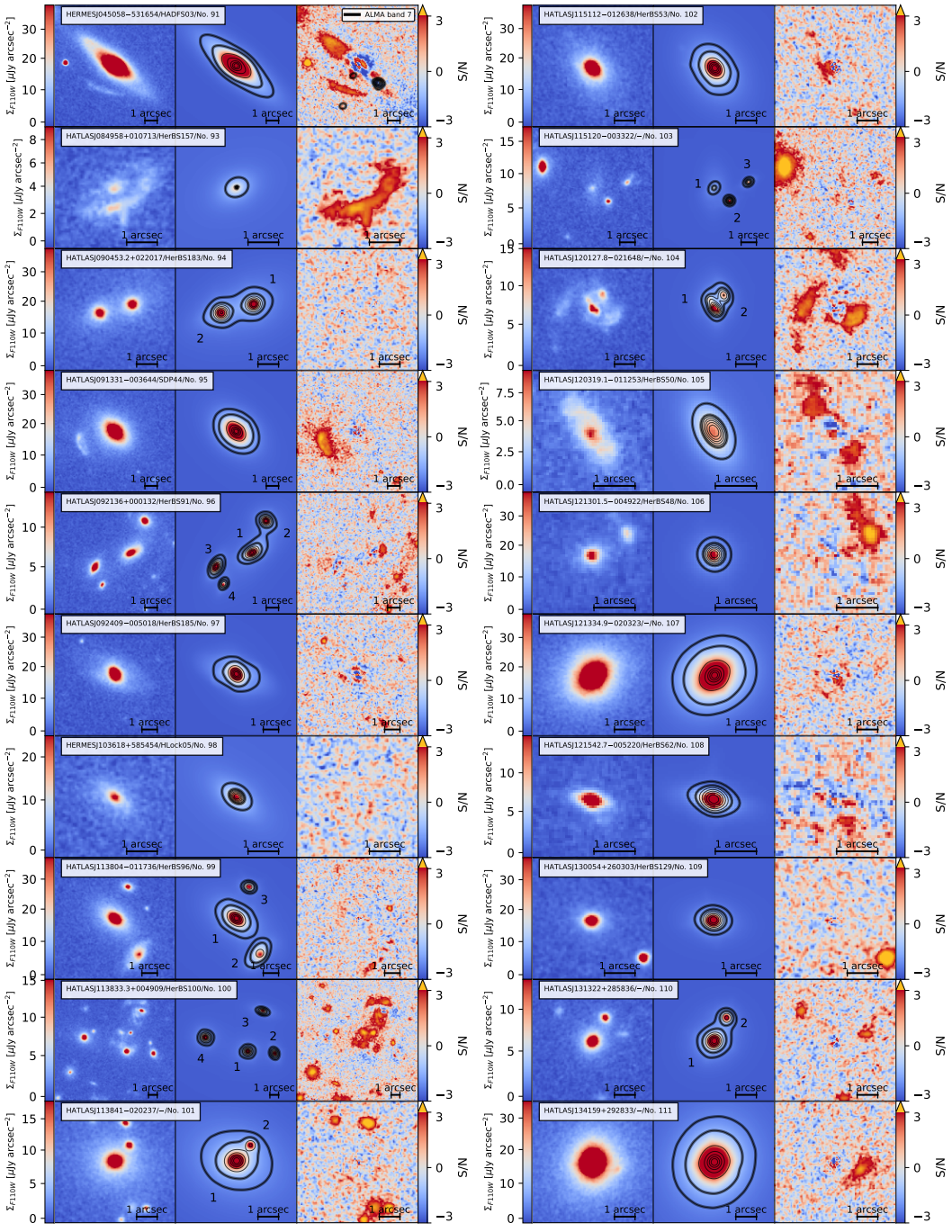

Figure 5.2 (cont.)

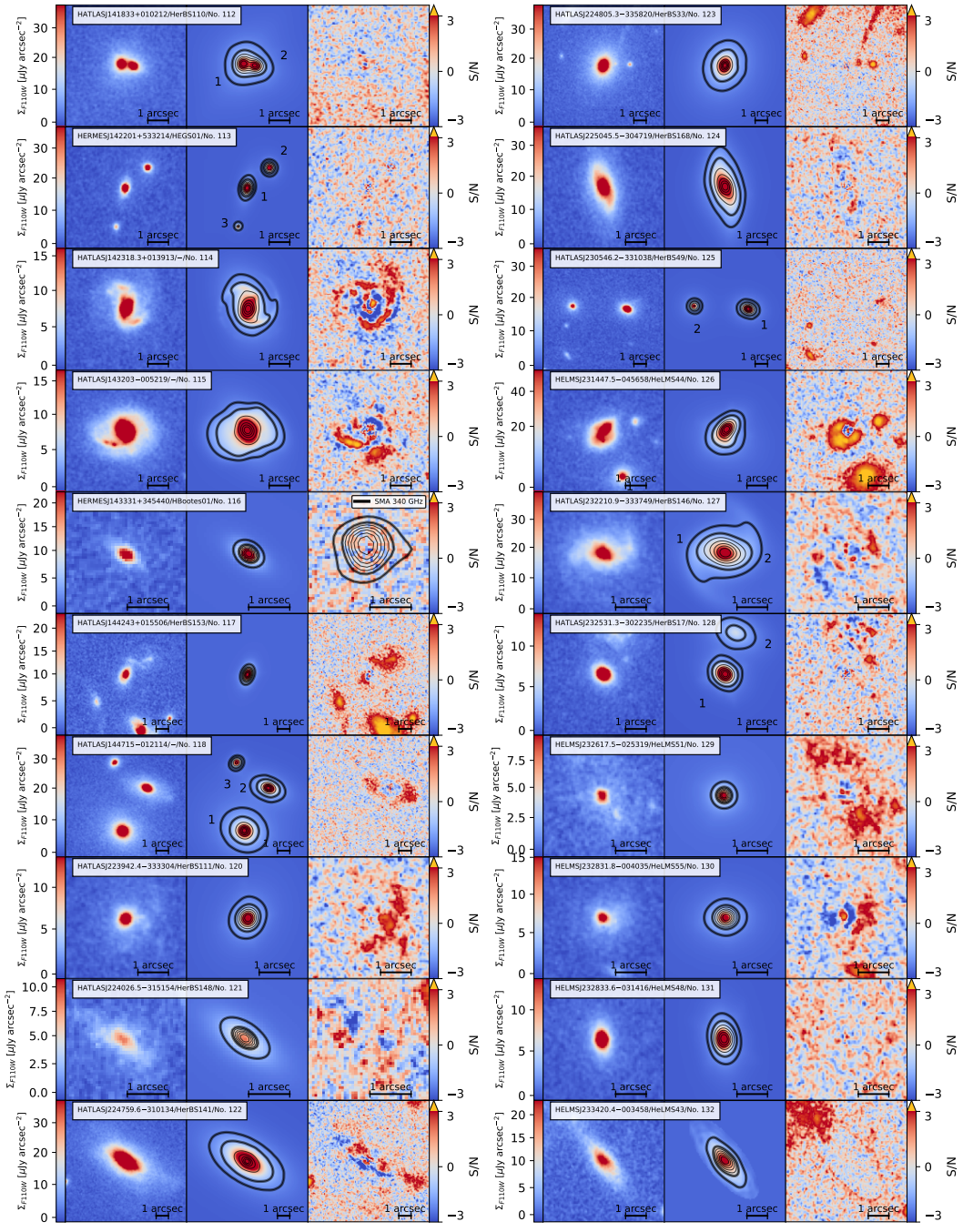

Figure 5.2 (cont.)

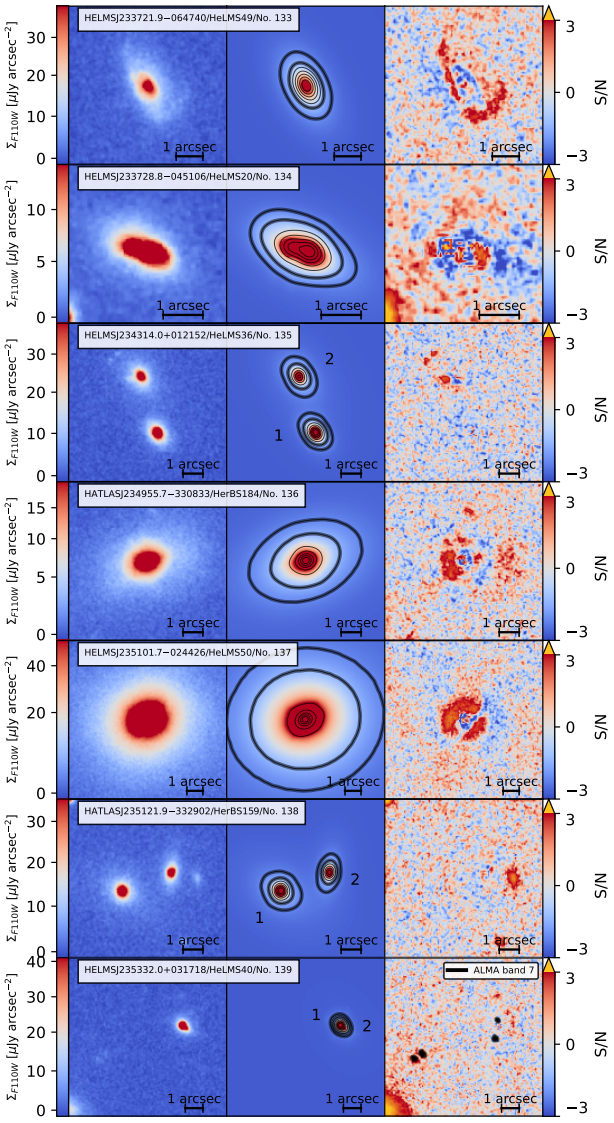

Figure 5.2 (cont.)

Table 5.1: Structural parameters of the systems classified as A obtained from a parametric fit of their surface brightness distributions.

No.	IAU Name	Type	Components	μ_e [mag arcsec^{-2}]	R_e [arcsec]	n	q	PA [deg]	m_{PSF} [mag]	C/T	χ^2	N_{dof}
(1)	(2)	(3)	(4)	(5)	(6)	(7)	(8)	(9)	(10)	(11)	(12)	(13)
1	HATLASJ000330.6−321136	1	Sérsic	$20.69^{+0.12}_{-0.11}$	0.36 ± 0.02	$4.52^{+0.28}_{-0.27}$	0.803 ± 0.009	$73.05^{+0.96}_{-0.95}$	–	0.71 ± 0.05	1.03	35501
			Sérsic	$23.39^{+0.15}_{-0.13}$	1.17 ± 0.06	0.57 ± 0.05	0.96 ± 0.02	$0.003^{+1.933}_{-1.884}$	–	0.29 ± 0.05		
2	HATLASJ000912.7−300807	1	Sérsic	$21.63^{+0.23}_{-0.20}$	$1.16^{+0.17}_{-0.18}$	3.96 ± 0.27	0.929 ± 0.006	$34.92^{+1.39}_{-1.42}$	–	$0.42^{+0.09}_{-0.10}$	1.03	135697
			Sérsic	$26.24^{+0.14}_{-0.12}$	$5.24^{+0.19}_{-0.18}$	0.80 ± 0.07	0.27 ± 0.03	$121.76^{+6.00}_{-6.17}$	–	$0.018^{+0.005}_{-0.004}$		
			Sérsic	$23.31^{+0.14}_{-0.12}$	3.93 ± 0.11	1.54 ± 0.13	0.78 ± 0.02	$139.43^{+3.96}_{-3.97}$	–	$0.56^{+0.10}_{-0.09}$		
3	HELMSJ001353.5−060200	1	Sérsic	$21.21^{+0.28}_{-0.22}$	$0.26^{+0.04}_{-0.03}$	4.03 ± 0.60	0.90 ± 0.02	$20.44^{+3.85}_{-3.82}$	–	0.45 ± 0.11	1.03	61093
			Exp. disk	$24.41^{+0.22}_{-0.18}$	2.02 ± 0.19	[1]	0.66 ± 0.05	$2.58^{+4.59}_{-4.42}$	–	0.55 ± 0.11		
4	HELMSJ003619.8+002420	1	Sérsic	$20.59^{+0.23}_{-0.19}$	1.35 ± 0.17	1.26 ± 0.07	0.905 ± 0.005	$109.96^{+1.05}_{-1.06}$	–	$0.46^{+0.08}_{-0.09}$	1.01	171928
			Sérsic	$17.78^{+0.16}_{-0.14}$	$0.177^{+0.006}_{-0.005}$	1.54 ± 0.15	0.90 ± 0.02	$159.86^{+2.55}_{-2.57}$	–	$0.11^{+0.03}_{-0.02}$		
			Sérsic	$23.65^{+0.14}_{-0.13}$	5.68 ± 0.17	$0.88^{+0.08}_{-0.07}$	0.92 ± 0.02	$128.85^{+4.37}_{-4.42}$	–	$0.42^{+0.08}_{-0.07}$		
6	HERSJ011722.3+005624$_1$	3	Sérsic	$21.64^{+0.29}_{-0.23}$	$0.60^{+0.08}_{-0.07}$	$5.19^{+0.42}_{-0.41}$	0.70 ± 0.02	$2.90^{+1.96}_{-1.92}$	–	$0.85^{+0.05}_{-0.07}$	1.01	55924
			Gauss	$24.97^{+0.21}_{-0.17}$	1.79 ± 0.16	[0.5]	$0.83^{+0.10}_{-0.11}$	$180.53^{+36.51}_{-36.53}$	–	$0.15^{+0.07}_{-0.05}$		
	HERSJ011722.3+005624$_2$		Sérsic	$22.52^{+0.17}_{-0.15}$	0.25 ± 0.02	1.12 ± 0.15	0.93 ± 0.03	$-0.001^{+3.108}_{-3.000}$	–	[1]	1.01	56315
7	HERSJ012620.5+012950	1	Sérsic	$22.23^{+0.31}_{-0.24}$	0.89 ± 0.12	$5.86^{+0.48}_{-0.47}$	0.70 ± 0.02	$13.18^{+1.91}_{-1.92}$	–	$0.66^{+0.08}_{-0.11}$	1.04	66653
			Gauss	$21.72^{+0.09}_{-0.08}$	0.76 ± 0.05	[0.5]	0.88 ± 0.05	74.75 ± 3.74	–	$0.34^{+0.11}_{-0.08}$		
8	HERSJ020941.2+001558$_1$	3	Sérsic	$21.13^{+0.19}_{-0.16}$	1.54 ± 0.18	5.11 ± 0.23	0.916 ± 0.004	$82.42^{+0.93}_{-0.99}$	–	$0.56^{+0.07}_{-0.08}$	0.97	121439
			Sérsic	$23.16^{+0.13}_{-0.12}$	5.03 ± 0.13	$0.75^{+0.07}_{-0.06}$	0.75 ± 0.02	$81.91^{+1.29}_{-1.26}$	–	$0.31^{+0.06}_{-0.05}$		
			Sérsic	$22.28^{+0.15}_{-0.13}$	$2.10^{+0.06}_{-0.07}$	0.47 ± 0.04	0.92 ± 0.02	$66.03^{+3.11}_{-3.18}$	–	$0.13^{+0.03}_{-0.02}$		
	HERSJ020941.2+001558$_2$		Sérsic	20.49 ± 0.06	$0.315^{+0.010}_{-0.009}$	2.86 ± 0.07	0.969 ± 0.007	$156.46^{+0.93}_{-0.92}$	–	[1]	0.97	124612
9	HERMESJ032637−270044	1	Sérsic	22.70 ± 0.05	$1.01^{+0.02}_{-0.03}$	5.73 ± 0.11	$0.997^{+0.002}_{-0.003}$	$46.45^{+0.69}_{-0.70}$	–	[1]	1.04	58583
10	HERMESJ033732−295353	1	Sérsic	$20.23^{+0.25}_{-0.21}$	0.50 ± 0.09	$4.51^{+0.37}_{-0.38}$	0.804 ± 0.009	$53.64^{+1.65}_{-1.68}$	–	$0.15^{+0.06}_{-0.05}$	1.05	177156
			Sérsic	$22.12^{+0.13}_{-0.11}$	$2.96^{+0.08}_{-0.07}$	1.73 ± 0.15	0.96 ± 0.02	$149.69^{+1.32}_{-1.33}$	–	$0.71^{+0.05}_{-0.06}$		
			Sérsic	$20.61^{+0.16}_{-0.14}$	0.83 ± 0.03	0.69 ± 0.06	0.90 ± 0.02	$54.94^{+2.84}_{-2.94}$	–	$0.14^{+0.03}_{-0.02}$		
11	HATLASJ083051+013225$_1$	2	Sérsic	$22.60^{+0.13}_{-0.12}$	0.36 ± 0.02	4.86 ± 0.36	0.84 ± 0.01	$33.02^{+1.44}_{-1.45}$	–	[1]	1.04	32063
	HATLASJ083051+013225$_2$		Sérsic	$23.28^{+0.15}_{-0.13}$	0.69 ± 0.04	$1.34^{+0.13}_{-0.12}$	0.48 ± 0.02	$22.24^{+1.87}_{-1.83}$	–	[1]		
12	HERMESJ100144+025709	1	Sérsic	21.74 ± 0.05	0.82 ± 0.02	$5.35^{+0.11}_{-0.10}$	0.606 ± 0.005	$71.89^{+0.73}_{-0.76}$	–	[1]	1.05	43906

Notes: Col. (1): Source reference number. Col. (2): IAU name of the *Herschel* detection. Indices 1 and 2 refer to the two components of the lens candidate. Col. (3): System type. Col. (4): Adopted model for the lens components. Col. (5): Effective surface brightness, i.e., the surface brightness at the effective radius. Col. (6): Effective radius, i.e., the semi-major axis of the isophote containing half of the light of the component. Col. (7): Sérsic index. Values fixed in the fit are bracketed. Col. (8): Axis ratio. Col. (9): Position angle. Col. (10): Magnitude of the unresolved component. Col. (11): Relative flux density of the components C/T. Col. (12): Reduced χ^2 of the fit. Col. (13): Number of degrees of freedom of the fit.

Table 5.1 (cont.)

No.	IAU Name	Type	Components	μ_e [mag arcsec^{-2}]	R_e [arcsec]	n	q	PA [deg]	m_{PSF} [mag]	C/T	χ^2	N_{dof}
(1)	(2)	(3)	(4)	(5)	(6)	(7)	(8)	(9)	(10)	(11)	(12)	(13)
13	HERMESJ103827+581544	1	Sérsic	$20.25^{+0.10}_{-0.09}$	0.47 ± 0.03	1.56 ± 0.07	0.762 ± 0.008	6.07 ± 0.82	–	0.27 ± 0.03	1.02	107445
			Sérsic	$22.65^{+0.07}_{-0.06}$	$2.56^{+0.07}_{-0.08}$	1.07 ± 0.05	0.74 ± 0.01	$12.31^{+1.06}_{-1.07}$	–	0.73 ± 0.03		
14	HERMESJ110016+571736	1	Sérsic	21.76 ± 0.04	1.01 ± 0.02	2.68 ± 0.04	0.807 ± 0.004	$120.78^{+0.60}_{-0.59}$	–	[1]	1.06	46997
15	HATLASJ114638−001132$_1$	2	Sérsic	$20.30^{+0.24}_{-0.20}$	0.19 ± 0.02	1.36 ± 0.17	0.53 ± 0.03	$50.27^{+1.72}_{-1.69}$	–	$0.58^{+0.08}_{-0.09}$	1.03	44201
			Sérsic	$24.52^{+0.16}_{-0.13}$	1.14 ± 0.07	$0.45^{+0.07}_{-0.08}$	$0.81^{+0.05}_{-0.04}$	$53.88^{+2.83}_{-2.87}$	–	$0.42^{+0.09}_{-0.08}$		
	HATLASJ114638−001132$_2$		Sérsic	$21.17^{+0.25}_{-0.21}$	0.18 ± 0.02	3.26 ± 0.43	0.81 ± 0.03	$128.86^{+1.77}_{-1.75}$	–	$0.29^{+0.08}_{-0.07}$		
			Sérsic	$25.49^{+0.14}_{-0.12}$	2.29 ± 0.10	$1.73^{+0.15}_{-0.14}$	0.86 ± 0.03	$132.15^{+1.64}_{-1.66}$	–	$0.71^{+0.07}_{-0.08}$		
16	HATLASJ125126+254928	1	Sérsic	$23.11^{+0.06}_{-0.05}$	1.50 ± 0.04	7.96 ± 0.16	0.504 ± 0.005	135.36 ± 0.77	–	[1]	1.07	50036
17	HATLASJ125760+224558	1	Sérsic	22.33 ± 0.04	1.13 ± 0.02	4.63 ± 0.08	0.814 ± 0.004	$6.39^{+0.58}_{-0.61}$	–	[1]	1.07	50512
18	HATLASJ133008+245860	1	Sérsic	$21.81^{+0.30}_{-0.24}$	0.69 ± 0.09	$6.34^{+0.49}_{-0.50}$	0.80 ± 0.01	$81.56^{+1.97}_{-1.95}$	–	$0.83^{+0.05}_{-0.07}$	1.04	44862
			Gauss	$22.85^{+0.11}_{-0.10}$	0.83 ± 0.05	[0.5]	$0.91^{+0.05}_{-0.06}$	$96.76^{+10.85}_{-11.16}$	–	$0.17^{+0.07}_{-0.05}$		
19	HATLASJ133846+255057	1	Sérsic	$23.46^{+0.07}_{-0.06}$	1.11 ± 0.04	$5.25^{+0.15}_{-0.16}$	0.696 ± 0.007	$50.61^{+0.87}_{-0.90}$	–	[1]	1.04	57037
21	HERMESJ171451+592634	1	de Vauc.	$22.05^{+0.05}_{-0.04}$	0.45 ± 0.01	[4]	0.55 ± 0.01	$144.39^{+1.69}_{-1.64}$	–	[1]	1.10	31356
22	HERMESJ171545+601238$_1$	3	Sérsic	$22.47^{+0.17}_{-0.15}$	0.56 ± 0.04	$4.43^{+0.33}_{-0.34}$	$0.992^{+0.006}_{-0.009}$	$180.00^{+1.08}_{-1.07}$	–	$0.17^{+0.04}_{-0.03}$	1.05	55119
			PSF	–	–	–	–	–	[24.97]	0.0023 ± 0.0002		
			Sérsic	24.43 ± 0.08	$4.10^{+0.14}_{-0.13}$	2.72 ± 0.16	0.69 ± 0.01	$96.24^{+1.29}_{-1.27}$	–	$0.83^{+0.03}_{-0.04}$		
	HERMESJ171545+601238$_2$		Sérsic	$23.87^{+0.10}_{-0.09}$	1.23 ± 0.06	3.76 ± 0.20	0.39 ± 0.01	$99.53^{+1.02}_{-0.99}$	–	[1]	1.05	54970
23	HATLASJ225844.8−295124$_1$	2	Sérsic	$20.69^{+0.07}_{-0.06}$	$0.44^{+0.01}_{-0.02}$	1.84 ± 0.06	0.448 ± 0.008	$145.47^{+0.87}_{-0.83}$	–	[1]	1.05	15053
	HATLASJ225844.8−295124$_2$		Sérsic	$22.59^{+0.24}_{-0.20}$	0.61 ± 0.07	1.12 ± 0.15	0.39 ± 0.03	58.30 ± 1.77	–	0.10 ± 0.03		
			Sérsic	$24.93^{+0.10}_{-0.09}$	$3.29^{+0.15}_{-0.14}$	$2.83^{+0.27}_{-0.28}$	$0.69^{+0.03}_{-0.02}$	$26.28^{+3.28}_{-3.25}$	–	0.90 ± 0.03		
24	HELMSJ232210.3−033559$_1$	3	Sérsic	$23.38^{+0.10}_{-0.09}$	1.42 ± 0.08	2.25 ± 0.14	$0.963^{+0.008}_{-0.009}$	$80.29^{+0.86}_{-0.89}$	–	0.81 ± 0.03	1.08	54469
			Sérsic	$19.99^{+0.13}_{-0.12}$	0.214 ± 0.008	1.29 ± 0.12	0.57 ± 0.03	$7.88^{+1.32}_{-1.33}$	–	0.19 ± 0.03		
	HELMSJ232210.3−033559$_2$		de Vauc.	21.44 ± 0.06	0.134 ± 0.006	[4]	0.74 ± 0.03	$64.64^{+4.21}_{-4.33}$	–	[1]	1.07	50334
25	HATLASJ233037.2−331217$_1$	3	Sérsic	$20.79^{+0.23}_{-0.19}$	0.25 ± 0.02	$7.05^{+0.58}_{-0.57}$	0.58 ± 0.02	$75.25^{+1.03}_{-1.05}$	–	$0.32^{+0.07}_{-0.06}$	1.05	47114
			Sérsic	$23.71^{+0.12}_{-0.10}$	1.66 ± 0.06	1.44 ± 0.14	0.89 ± 0.03	$139.93^{+3.41}_{-3.29}$	–	$0.68^{+0.06}_{-0.07}$		
	HATLASJ233037.2−331217$_2$		PSF	–	–	–	–	–	[23.14]	[1]		
Confirmed after the lens subtraction												
26	HELMSJ001626.0+042613	1	Sérsic	19.39 ± 0.05	0.52 ± 0.01	4.23 ± 0.09	0.467 ± 0.004	$7.10^{+0.26}_{-0.25}$	–	0.59 ± 0.03	1.05	55249
			Sérsic	$22.22^{+0.09}_{-0.08}$	1.83 ± 0.06	1.27 ± 0.08	0.63 ± 0.01	$162.98^{+1.24}_{-1.26}$	–	0.41 ± 0.03		
27	HATLASJ002624.8−341737	1	Sérsic	$21.92^{+0.25}_{-0.20}$	0.31 ± 0.03	$4.94^{+0.51}_{-0.52}$	0.63 ± 0.02	$172.06^{+1.73}_{-1.74}$	–	$0.54^{+0.08}_{-0.09}$	1.05	52636
			Sérsic	$24.33^{+0.13}_{-0.12}$	1.08 ± 0.04	$0.69^{+0.09}_{-0.08}$	$0.97^{+0.02}_{-0.03}$	180.01 ± 1.36	–	$0.46^{+0.09}_{-0.08}$		
28	HELMSJ004723.6+015751$_1$	2	de Vauc.	$18.60^{+0.30}_{-0.23}$	0.09 ± 0.01	[4]	$0.84^{+0.04}_{-0.03}$	$43.47^{+4.28}_{-4.38}$	–	$0.11^{+0.04}_{-0.03}$	1.03	58679
			Sérsic	21.92 ± 0.02	1.57 ± 0.02	$1.37^{+0.08}_{-0.07}$	0.851 ± 0.004	$165.60^{+1.09}_{-1.13}$	–	$0.89^{+0.03}_{-0.04}$		
	HELMSJ004723.6+015751$_2$		Sérsic	22.17 ± 0.06	0.80 ± 0.02	3.14 ± 0.07	$0.856^{+0.006}_{-0.007}$	$79.44^{+0.83}_{-0.82}$	–	[1]		

Table 5.1 (cont.)

No.	IAU Name	Type	Components	μ_e [mag arcsec^{-2}]	R_e [arcsec]	n	q	PA [deg]	m_{PSF} [mag]	C/T	χ^2	N_{dof}
(1)	(2)	(3)	(4)	(5)	(6)	(7)	(8)	(9)	(10)	(11)	(12)	(13)
29	HERSJ012041.6−002705	1	Sérsic	$19.91^{+0.20}_{-0.17}$	0.19 ± 0.02	4.39 ± 0.34	0.71 ± 0.01	86.79 ± 1.04	–	0.44 ± 0.07	1.03	50744
			Sérsic	$23.67^{+0.13}_{-0.12}$	$1.37^{+0.05}_{-0.06}$	1.98 ± 0.18	0.79 ± 0.02	$3.03^{+2.85}_{-2.88}$	–	0.56 ± 0.07		
30	HATLASJ085112+004934	1	Sérsic	$20.24^{+0.41}_{-0.30}$	0.27 ± 0.06	$4.45^{+0.72}_{-0.71}$	0.61 ± 0.02	$81.52^{+1.84}_{-1.83}$	–	$0.25^{+0.12}_{-0.10}$	1.06	40914
			Sérsic	$21.51^{+0.17}_{-0.14}$	0.78 ± 0.02	0.44 ± 0.04	0.94 ± 0.03	$158.68^{+6.02}_{-6.11}$	–	0.37 ± 0.07		
			Sérsic	$22.35^{+0.14}_{-0.12}$	1.39 ± 0.04	0.72 ± 0.07	0.55 ± 0.02	$81.26^{+1.61}_{-1.71}$	–	0.38 ± 0.07		
31	HATLASJ085359+015537	1	Sérsic	$22.69^{+0.26}_{-0.20}$	0.45 ± 0.05	6.78 ± 0.96	0.30 ± 0.03	$117.52^{+1.82}_{-1.81}$	–	$0.30^{+0.08}_{-0.07}$	1.13	22254
			Sérsic	$26.34^{+0.14}_{-0.12}$	2.34 ± 0.09	5.14 ± 0.48	0.85 ± 0.03	$156.50^{+1.28}_{-1.29}$	–	$0.70^{+0.07}_{-0.08}$		
32	HERMESJ104549+574512	1	Sérsic	$19.59^{+0.23}_{-0.19}$	0.16 ± 0.02	$3.86^{+0.40}_{-0.39}$	0.37 ± 0.02	$121.59^{+1.47}_{-1.38}$	–	$0.22^{+0.06}_{-0.05}$	1.04	60465
			Sérsic	$21.54^{+0.12}_{-0.11}$	0.64 ± 0.03	1.74 ± 0.17	0.68 ± 0.03	$89.59^{+3.16}_{-3.13}$	–	$0.78^{+0.05}_{-0.06}$		
33	HERMESJ105551+592845$_1$	2	Sérsic	22.62 ± 0.08	0.66 ± 0.03	1.82 ± 0.08	0.762 ± 0.009	92.59 ± 0.85	–	[1]	1.15	6328
	HERMESJ105551+592845$_2$		Sérsic	$21.85^{+0.15}_{-0.13}$	0.28 ± 0.02	1.25 ± 0.12	0.79 ± 0.02	$123.08^{+1.84}_{-1.82}$	–	[1]		
34	HERMESJ105751+573026$_1$	2	Sérsic	20.36 ± 0.09	0.41 ± 0.02	3.90 ± 0.18	0.752 ± 0.008	$91.89^{+0.83}_{-0.84}$	–	0.27 ± 0.03	1.11	31547
			Sérsic	24.58 ± 0.07	5.16 ± 0.15	$2.63^{+0.13}_{-0.12}$	0.74 ± 0.01	$30.55^{+1.03}_{-1.05}$	–	0.73 ± 0.03		
	HERMESJ105751+573026$_2$		de Vauc.	$19.30^{+0.27}_{-0.22}$	0.10 ± 0.02	[4]	0.37 ± 0.04	$32.23^{+4.35}_{-4.53}$	–	$0.42^{+0.36}_{-0.24}$		
			Sérsic	$22.80^{+0.67}_{-0.42}$	$0.43^{+0.23}_{-0.21}$	$5.95^{+2.42}_{-2.72}$	$0.76^{+0.12}_{-0.13}$	$94.68^{+7.37}_{-7.46}$	–	$0.58^{+0.24}_{-0.36}$		
	HERMESJ105751+573026$_3$		Sérsic	$20.72^{+0.15}_{-0.13}$	0.137 ± 0.009	$3.63^{+0.31}_{-0.32}$	0.82 ± 0.02	$74.54^{+1.82}_{-1.84}$	–	[1]		
	HERMESJ105751+573026$_4$		de Vauc.	21.16 ± 0.05	0.220 ± 0.007	[4]	0.61 ± 0.02	$100.13^{+2.05}_{-2.07}$	–	[1]		
	HERMESJ105751+573026$_5$		Sérsic	$20.30^{+0.13}_{-0.12}$	$0.131^{+0.008}_{-0.007}$	3.11 ± 0.23	0.89 ± 0.01	$175.89^{+1.42}_{-1.45}$	–	[1]		
	HERMESJ105751+573026$_6$		PSF	–	–	–	–	–	[23.60]	[1]		
35	HATLASJ132630+334410	1	Sérsic	23.80 ± 0.04	2.53 ± 0.05	5.73 ± 0.09	0.595 ± 0.004	$72.04^{+0.57}_{-0.59}$	–	[1]	1.05	39273
36	HATLASJ133543+300404$_1$	2	Sérsic	22.42 ± 0.08	0.65 ± 0.03	0.88 ± 0.04	0.902 ± 0.009	127.84 ± 0.89	–	0.954 ± 0.005	1.03	41523
			PSF	–	–	–	–	–	[24.11]	0.046 ± 0.005		
	HATLASJ133543+300404$_2$		Sérsic	$21.90^{+0.09}_{-0.08}$	0.41 ± 0.02	$4.97^{+0.23}_{-0.24}$	0.567 ± 0.010	$24.77^{+0.94}_{-0.95}$	–	[1]		
	HATLASJ133543+300404$_3$		Sérsic	23.50 ± 0.06	1.10 ± 0.03	5.58 ± 0.15	0.844 ± 0.007	$64.17^{+0.92}_{-0.94}$	–	[1]		
	HATLASJ133543+300404$_4$		Sérsic	$23.58^{+0.07}_{-0.06}$	1.02 ± 0.04	6.21 ± 0.21	0.609 ± 0.008	$165.10^{+0.80}_{-0.84}$	–	[1]		
37	HATLASJ142140+000448	1	Sérsic	$21.27^{+0.07}_{-0.06}$	0.38 ± 0.01	2.28 ± 0.05	0.925 ± 0.005	0.67 ± 0.77	–	[1]	1.11	44658
38	HERMESJ142824+352620	1	Sérsic	$21.47^{+0.08}_{-0.07}$	0.49 ± 0.02	$2.43^{+0.10}_{-0.09}$	0.487 ± 0.008	$92.76^{+0.89}_{-0.91}$	–	[1]	1.17	7204
39	HATLASJ223753.8−305828	1	Sérsic	21.81 ± 0.05	0.72 ± 0.02	$5.03^{+0.10}_{-0.09}$	0.940 ± 0.005	$87.28^{+0.70}_{-0.71}$	–	[1]	1.03	63365
40	HATLASJ225250.7−313657	1	Sérsic	$22.23^{+0.12}_{-0.10}$	0.40 ± 0.02	6.21 ± 0.40	0.53 ± 0.01	$75.70^{+1.21}_{-1.25}$	–	[1]	1.04	34943
41	HELMSJ233441.0−065220	1	Sérsic	$19.47^{+0.20}_{-0.17}$	0.28 ± 0.02	1.14 ± 0.09	0.38 ± 0.01	$22.16^{+1.00}_{-1.01}$	–	$0.49^{+0.07}_{-0.08}$	1.57	35357
			Sérsic	$22.59^{+0.15}_{-0.13}$	1.00 ± 0.06	0.62 ± 0.06	0.68 ± 0.03	$167.72^{+2.29}_{-2.37}$	–	$0.51^{+0.08}_{-0.07}$		

Table 5.1 (cont.)

No.	IAU Name	Type	Components	μ_e [mag arcsec^{-2}]	R_e [arcsec]	n	q	PA [deg]	m_{PSF} [mag]	C/T	χ^2	N_{dof}
(1)	(2)	(3)	(4)	(5)	(6)	(7)	(8)	(9)	(10)	(11)	(12)	(13)
42	HELMSJ233633.5−032119$_1$	2	Sérsic	18.38 ± 0.05	0.332 ± 0.009	2.82 ± 0.06	$0.577^{+0.004}_{-0.003}$	$42.72^{+0.24}_{-0.25}$	–	0.34 ± 0.02	1.06	58206
			Sérsic	21.94 ± 0.04	$2.55^{+0.03}_{-0.04}$	1.25 ± 0.04	0.738 ± 0.006	46.04 ± 0.84	–	0.66 ± 0.02		
	HELMSJ233633.5−032119$_2$		Sérsic	$23.16^{+0.06}_{-0.05}$	1.79 ± 0.04	2.21 ± 0.04	0.723 ± 0.005	$160.63^{+0.74}_{-0.75}$	–	[1]		
Confirmed through sub-mm/mm follow-up												
43	HELMSJ001615.7+032435	1	Sérsic	$24.18^{+0.31}_{-0.25}$	$3.46^{+0.45}_{-0.44}$	$7.32^{+0.38}_{-0.39}$	$0.579^{+0.007}_{-0.006}$	$31.91^{+0.67}_{-0.65}$	–	$0.86^{+0.04}_{-0.06}$	1.09	57290
			Gauss	24.61 ± 0.09	3.25 ± 0.21	[0.5]	0.50 ± 0.07	$17.05^{+3.68}_{-3.72}$	–	$0.14^{+0.06}_{-0.04}$		
44	HELMSJ002220.9−015524	1	Sérsic	$25.43^{+0.10}_{-0.09}$	2.09 ± 0.10	$3.77^{+0.19}_{-0.20}$	0.58 ± 0.01	98.62 ± 0.99	–	[1]	1.13	37251
45	HELMSJ003814.1−002252	1	PSF	–	–	–	–	–	[22.45]	[1]	1.04	18416
47	HELMSJ004714.2+032454	1	Sérsic	$20.79^{+0.18}_{-0.15}$	0.20 ± 0.02	0.60 ± 0.10	0.75 ± 0.03	$103.11^{+4.11}_{-4.17}$	–	$0.17^{+0.06}_{-0.05}$	1.01	26442
			Exp. disk	$23.42^{+0.19}_{-0.17}$	$1.47^{+0.14}_{-0.13}$	[1]	$0.60^{+0.04}_{-0.05}$	$111.21^{+4.52}_{-4.42}$	–	$0.83^{+0.05}_{-0.06}$		
48	HELMSJ005159.5+062241$_1$	2	Sérsic	$18.59^{+0.21}_{-0.17}$	$0.113^{+0.009}_{-0.010}$	2.28 ± 0.18	0.77 ± 0.01	119.44 ± 1.05	–	0.14 ± 0.03	1.03	48792
			Sérsic	$23.10^{+0.08}_{-0.07}$	2.10 ± 0.06	$1.95^{+0.10}_{-0.09}$	0.96 ± 0.01	$9.11^{+1.24}_{-1.22}$	–	0.86 ± 0.03		
	HELMSJ005159.5+062241$_2$		de Vauc.	20.48 ± 0.03	0.201 ± 0.004	[4]	0.76 ± 0.01	$173.86^{+1.76}_{-1.70}$	–	[1]		
	HELMSJ005159.5+062241$_3$		Sérsic	$24.00^{+0.07}_{-0.06}$	1.92 ± 0.06	1.33 ± 0.04	$0.703^{+0.007}_{-0.008}$	$37.42^{+0.90}_{-0.87}$	–	$0.899^{+0.008}_{-0.009}$		
			PSF	–	–	–	–	–	[22.52]	$0.101^{+0.009}_{-0.008}$		
49	HATLASJ005724.2−273122	1	Sérsic	$24.83^{+0.07}_{-0.06}$	1.46 ± 0.05	9.11 ± 0.30	0.858 ± 0.008	$126.93^{+0.84}_{-0.83}$	–	[1]	1.05	37643
50	HERMESJ021831−053131	1	Sérsic	$23.60^{+0.13}_{-0.12}$	0.83 ± 0.05	5.12 ± 0.38	0.38 ± 0.01	$148.55^{+1.47}_{-1.43}$	–	[1]	1.07	49835
51	HERMESJ033211−270536	1	PSF	–	–	–	–	–	[23.01]	[1]	1.07	9735
52	HERMESJ044154−540352	1	Sérsic	21.75 ± 0.06	0.54 ± 0.02	7.49 ± 0.17	0.783 ± 0.007	9.27 ± 0.86	–	[1]	1.03	44932
54	HATLASJ091841+023048$_1$	2	Sérsic	$20.11^{+0.34}_{-0.27}$	0.11 ± 0.02	$1.83^{+0.30}_{-0.31}$	0.69 ± 0.03	$152.52^{+1.94}_{-1.93}$	–	$0.19^{+0.07}_{-0.06}$	1.07	43760
			Sérsic	$25.92^{+0.14}_{-0.12}$	2.99 ± 0.14	2.44 ± 0.20	0.76 ± 0.02	$70.78^{+1.87}_{-1.88}$	–	$0.81^{+0.06}_{-0.07}$		
	HATLASJ091841+023048$_2$		de Vauc.	21.80 ± 0.06	0.155 ± 0.006	[4]	0.91 ± 0.03	$115.92^{+4.12}_{-4.11}$	–	[1]		
56	HATLASJ115433.6+005042	1	Sérsic	$21.10^{+0.08}_{-0.07}$	0.48 ± 0.02	1.83 ± 0.08	0.337 ± 0.009	$169.27^{+0.85}_{-0.87}$	–	[1]	1.01	34603
57	HATLASJ120127.6−014043	1	Sérsic	$25.61^{+0.35}_{-0.26}$	1.51 ± 0.23	1.00 ± 0.18	0.74 ± 0.03	$42.98^{+1.91}_{-1.83}$	–	$0.25^{+0.09}_{-0.08}$	1.06	28398
			Sérsic	$19.56^{+0.14}_{-0.12}$	0.225 ± 0.009	2.12 ± 0.20	0.27 ± 0.03	$20.79^{+1.31}_{-1.29}$	–	$0.75^{+0.08}_{-0.09}$		
58	HATLASJ131611+281220	1	Sérsic	$22.68^{+0.15}_{-0.13}$	0.45 ± 0.03	$5.08^{+0.44}_{-0.43}$	0.40 ± 0.02	$1.47^{+1.77}_{-1.73}$	–	[1]	1.02	28595
59	HATLASJ134429+303036	1	Sérsic	$19.44^{+0.37}_{-0.28}$	0.20 ± 0.03	2.50 ± 0.29	0.65 ± 0.01	$161.16^{+2.23}_{-2.21}$	–	$0.54^{+0.13}_{-0.14}$	1.04	48806
			Exp. disk	$22.71^{+0.20}_{-0.16}$	1.64 ± 0.15	[1]	$0.26^{+0.04}_{-0.05}$	$173.10^{+4.55}_{-4.49}$	–	$0.46^{+0.14}_{-0.13}$		
60	HATLASJ141352−000027$_1$	3	Sérsic	$20.47^{+0.18}_{-0.15}$	0.51 ± 0.05	$3.36^{+0.21}_{-0.22}$	0.825 ± 0.006	83.00 ± 1.08	–	$0.55^{+0.07}_{-0.08}$	1.01	73852
			Exp. disk	23.99 ± 0.11	2.87 ± 0.17	[1]	0.96 ± 0.03	$-0.01^{+4.33}_{-4.12}$	–	$0.45^{+0.08}_{-0.07}$		
	HATLASJ141352−000027$_2$		Sérsic	21.05 ± 0.08	0.31 ± 0.01	$3.64^{+0.17}_{-0.16}$	0.536 ± 0.010	$148.77^{+0.88}_{-0.89}$	–	[1]	1.01	63073
	HATLASJ141352−000027$_3$		Sérsic	21.69 ± 0.05	0.68 ± 0.02	4.91 ± 0.10	0.866 ± 0.005	$41.57^{+0.79}_{-0.75}$	–	[1]	1.01	64764

Table 5.1 (cont.)

No.	IAU Name	Type	Components	μ_e [mag arcsec^{-2}]	R_e [arcsec]	n	q	PA [deg]	m_{PSF} [mag]	C/T	χ^2	N_{dof}
(1)	(2)	(3)	(4)	(5)	(6)	(7)	(8)	(9)	(10)	(11)	(12)	(13)
61	HATLASJ142414+022304$_1$	2	Sérsic	$24.20^{+0.07}_{-0.06}$	1.49 ± 0.05	3.76 ± 0.11	0.910 ± 0.007	$15.97^{+0.94}_{-0.89}$	–	$0.880^{+0.009}_{-0.010}$	1.04	22914
			PSF	–	–	–	–	–	[22.25]	$0.120^{+0.010}_{-0.009}$		
	HATLASJ142414+022304$_2$		Sérsic	$24.59^{+0.10}_{-0.09}$	1.13 ± 0.06	7.02 ± 0.36	0.68 ± 0.01	$149.22^{+1.02}_{-0.98}$	–	[1]		
62	HATLASJ230815.5−343801	1	Sérsic	$22.86^{+0.21}_{-0.17}$	0.56 ± 0.05	$8.73^{+0.65}_{-0.69}$	0.89 ± 0.01	157.26 ± 1.05	–	$0.76^{+0.05}_{-0.06}$	1.13	21244
			Sérsic	$22.89^{+0.14}_{-0.13}$	0.75 ± 0.03	0.52 ± 0.07	$0.56^{+0.03}_{-0.04}$	$7.75^{+1.49}_{-1.48}$	–	$0.24^{+0.06}_{-0.05}$		
63	HELMSJ232439.5−043936	1	Sérsic	$21.14^{+0.22}_{-0.18}$	$0.27^{+0.02}_{-0.03}$	3.26 ± 0.24	0.98 ± 0.01	$89.07^{+1.07}_{-1.03}$	–	$0.67^{+0.06}_{-0.08}$	1.06	53698
			Sérsic	$23.95^{+0.13}_{-0.12}$	1.10 ± 0.04	1.61 ± 0.18	0.52 ± 0.03	$129.07^{+1.13}_{-1.16}$	–	$0.33^{+0.08}_{-0.06}$		
64	HELMSJ233620.8−060828	1	Sérsic	20.53 ± 0.05	0.64 ± 0.02	$4.76^{+0.10}_{-0.09}$	0.878 ± 0.004	52.62 ± 0.24	–	0.85 ± 0.02	1.04	27656
			Sérsic	$22.22^{+0.12}_{-0.10}$	0.96 ± 0.04	0.87 ± 0.08	0.73 ± 0.03	$127.25^{+3.16}_{-3.17}$	–	0.15 ± 0.02		

Table 5.2: Derived properties of the lensing systems.

No.	IAU Name	m_{F110W} [mag] M_{F110W} [mag]	μ_{50} [mag arcsec^{-2}] $\mu_{50,0}$ [mag kpc^{-2}]	R_{50} [arcsec] $R_{50,0}$ [kpc]	C_{31}	$\mu S_{1.1}$ [μJy]
(1)	(2)	(3)	(4)	(5)	(6)	(7)
1	HATLASJ000330.6−321136	19.30 ± 0.14 $-17.78^{+0.73}_{-0.59}$	$21.49^{+0.21}_{-0.20}$ $20.10^{+0.37}_{-0.35}$	0.56 ± 0.05 $2.99^{+0.52}_{-0.55}$	$7.24^{+0.43}_{-0.40}$	1.81 ± 0.06
2	HATLASJ000912.7−300807	17.09 ± 0.19 $-19.26^{+0.83}_{-0.68}$	22.18 ± 0.26 $21.10^{+0.38}_{-0.37}$	$2.38^{+0.20}_{-0.17}$ $10.49^{+2.19}_{-2.36}$	$5.34^{+0.38}_{-0.40}$	45.35 ± 0.12
3	HELMSJ001353.5−060200	19.99 ± 0.24 $-18.29^{+0.92}_{-0.72}$	$23.16^{+0.41}_{-0.50}$ $21.09^{+0.67}_{-0.64}$	$0.90^{+0.25}_{-0.21}$ $5.98^{+1.98}_{-1.57}$	$7.26^{+1.15}_{-1.34}$	3.00 ± 0.10
4	HELMSJ003619.8+002420	16.41 ± 0.18 $-19.72^{+0.18}_{-0.17}$	$21.29^{+0.46}_{-0.36}$ $20.29^{+0.46}_{-0.36}$	$2.07^{+0.26}_{-0.20}$ $8.55^{+1.06}_{-0.84}$	$6.38^{+1.30}_{-0.97}$	13.58 ± 0.25
5	HELMSJ005841.2−011149	$18.910^{+0.001}_{-0.001}$ $-18.15^{+0.57}_{-0.48}$	$20.26^{+0.02}_{-0.02}$ $18.88^{+0.25}_{-0.24}$	$0.478^{+0.005}_{-0.006}$ $2.54^{+0.31}_{-0.35}$	$3.05^{+0.04}_{-0.04}$	$14.55^{+0.10}_{-0.10}$
6	HERSJ011722.3+005624$_1$ HERSJ011722.3+005624$_2$	$19.45^{+0.34}_{-0.31}$ $-19.82^{+0.37}_{-0.36}$ $22.87^{+0.23}_{-0.22}$ –	$22.10^{+0.47}_{-0.34}$ $19.38^{+0.47}_{-0.37}$ $22.52^{+0.17}_{-0.15}$ –	$0.67^{+0.08}_{-0.07}$ $5.33^{+0.66}_{-0.55}$ 0.24 ± 0.02 –	$8.68^{+0.74}_{-0.68}$ 2.95 ± 0.18	2.23 ± 0.10
7	HERSJ012620.5+012950	$18.86^{+0.29}_{-0.28}$ $-18.55^{+0.42}_{-0.40}$	$21.22^{+0.13}_{-0.11}$ $19.67^{+0.20}_{-0.19}$	0.74 ± 0.05 $4.27^{+0.43}_{-0.42}$	$4.64^{+1.03}_{-0.76}$	5.72 ± 0.09
8	HERSJ020941.2+001558$_1$ HERSJ020941.2+001558$_2$	$16.15^{+0.18}_{-0.17}$ $-19.38^{+0.18}_{-0.17}$ $19.82^{+0.09}_{-0.09}$ $-15.71^{+0.09}_{-0.09}$	$21.27^{+0.19}_{-0.17}$ $20.47^{+0.19}_{-0.17}$ $20.49^{+0.06}_{-0.06}$ $19.69^{+0.06}_{-0.06}$	$2.47^{+0.13}_{-0.12}$ $8.48^{+0.46}_{-0.40}$ $0.310^{+0.010}_{-0.009}$ $1.06^{+0.03}_{-0.03}$	$5.35^{+0.45}_{-0.47}$ $5.24^{+0.10}_{-0.10}$	$18.72^{+0.34}_{-0.34}$
9	HERMESJ032637−270044	19.10 ± 0.07 –	22.70 ± 0.05 –	$1.01^{+0.02}_{-0.03}$ –	10.12 ± 0.22	3.81 ± 0.13
10	HERMESJ033732−295353	$16.47^{+0.13}_{-0.12}$ $-18.89^{+0.68}_{-0.55}$	$21.15^{+0.19}_{-0.20}$ $20.40^{+0.25}_{-0.27}$	1.91 ± 0.16 6.15 ± 1.32	$5.36^{+0.33}_{-0.32}$	2.93 ± 0.07
11	HATLASJ083051+013225$_1$ HATLASJ083051+013225$_2$	$21.54^{+0.18}_{-0.18}$ $-16.86^{+0.18}_{-0.18}$ $22.05^{+0.21}_{-0.19}$ $-17.59^{+0.21}_{-0.20}$	$22.60^{+0.13}_{-0.12}$ $20.48^{+0.13}_{-0.12}$ $23.28^{+0.15}_{-0.13}$ $20.27^{+0.15}_{-0.13}$	$0.33^{+0.02}_{-0.02}$ $2.30^{+0.13}_{-0.13}$ $0.48^{+0.03}_{-0.03}$ $3.94^{+0.26}_{-0.25}$	$8.47^{+0.66}_{-0.64}$ $3.21^{+0.16}_{-0.15}$	$6.79^{+0.11}_{-0.11}$
12	HERMESJ100144+025709	$19.17^{+0.08}_{-0.08}$ $-20.17^{+0.08}_{-0.08}$	$21.74^{+0.05}_{-0.05}$ $18.96^{+0.05}_{-0.05}$	$0.64^{+0.02}_{-0.02}$ $5.10^{+0.13}_{-0.13}$	$9.37^{+0.20}_{-0.20}$	$10.14^{+0.17}_{-0.17}$
13	HERMESJ103827+581544	$17.86^{+0.09}_{-0.08}$ $-20.38^{+0.09}_{-0.08}$	$21.95^{+0.12}_{-0.13}$ $19.93^{+0.12}_{-0.13}$	1.53 ± 0.11 $10.48^{+0.76}_{-0.72}$	$4.75^{+0.19}_{-0.20}$	10.12 ± 0.23
14	HERMESJ110016+571736	18.78 ± 0.06 -20.19 ± 0.06	21.76 ± 0.04 19.25 ± 0.04	0.91 ± 0.02 6.97 ± 0.15	4.99 ± 0.06	12.71 ± 0.19
15	HATLASJ114638−001132$_1$ HATLASJ114638−001132$_2$	$21.15^{+0.21}_{-0.20}$ $-19.03^{+0.21}_{-0.20}$ $20.52^{+0.16}_{-0.15}$ $-19.66^{+0.16}_{-0.15}$	$21.97^{+1.01}_{-0.70}$ $18.50^{+1.01}_{-0.70}$ $24.52^{+0.29}_{-0.37}$ $21.05^{+0.29}_{-0.37}$	$0.29^{+0.10}_{-0.05}$ $2.51^{+0.86}_{-0.42}$ 1.28 ± 0.24 $10.90^{+2.06}_{-2.09}$	$7.50^{+0.98}_{-1.17}$ $8.90^{+1.82}_{-1.84}$	6.33 ± 0.14
16	HATLASJ125126+254928	19.21 ± 0.08 $-19.16^{+0.46}_{-0.40}$	$23.11^{+0.06}_{-0.05}$ $21.02^{+0.27}_{-0.26}$	1.07 ± 0.03 $7.46^{+0.52}_{-0.61}$	$15.14^{+0.42}_{-0.41}$	4.18 ± 0.15
17	HATLASJ125760+224558	18.83 ± 0.06 -19.25 ± 0.06	22.33 ± 0.04 20.42 ± 0.04	1.02 ± 0.02 6.76 ± 0.15	8.05 ± 0.13	10.13 ± 0.12
18	HATLASJ133008+245860	$19.05^{+0.35}_{-0.32}$ $-18.36^{+0.35}_{-0.32}$	$21.55^{+0.23}_{-0.20}$ $20.01^{+0.23}_{-0.20}$	0.68 ± 0.05 3.95 ± 0.31	$7.33^{+1.09}_{-1.03}$	3.54 ± 0.11

Notes: Col. (1): Source reference number. Col. (2): IAU name of the *Herschel* detection. Indices 1 and 2 refer to the two components of the lens candidate. Col. (3): Apparent magnitude of the model (first row), and absolute magnitude of the model (second row). Col. (4): Total effective radius in arcsec (first row) and in kpc (second row). Col. (5): Total effective surface brightness before (first row) and after correcting for cosmological dimming (second row). Col. (6): C_{31} of the model.

Table 5.2 (cont.)

No.	IAU Name	m_{F110W} [mag] M_{F110W} [mag]	μ_{50} [mag arcsec^{-2}] $\mu_{50,0}$ [mag kpc^{-2}]	R_{50} [arcsec] $R_{50,0}$ [kpc]	C_{31}	$\mu S_{1.1}$ [μJy]
(1)	(2)	(3)	(4)	(5)	(6)	(7)
19	HATLASJ133846+255057	$20.09^{+0.10}_{-0.09}$ $-17.25^{+0.70}_{-0.55}$	$23.46^{+0.07}_{-0.06}$ $21.94^{+0.32}_{-0.30}$	0.93 ± 0.03 $5.27^{+0.68}_{-0.84}$	9.19 ± 0.29	12.23 ± 0.12
21	HERMESJ171451+592634	21.03 ± 0.08 -19.17 ± 0.08	$22.05^{+0.05}_{-0.04}$ $18.56^{+0.05}_{-0.04}$	$0.336^{+0.010}_{-0.009}$ 2.87 ± 0.08	$6.9887^{+0.0005}_{-0.0003}$	7.00 ± 0.13
22	HERMESJ171545+601238$_1$	$18.38^{+0.11}_{-0.10}$ $-18.78^{+0.64}_{-0.53}$	23.86 ± 0.12 $22.43^{+0.30}_{-0.29}$	2.68 ± 0.17 $14.54^{+2.11}_{-2.40}$	$6.51^{+0.37}_{-0.35}$	6.65 ± 0.14
	HERMESJ171545+601238$_2$	$21.09^{+0.15}_{-0.14}$ –	$23.87^{+0.10}_{-0.09}$ –	0.77 ± 0.04 –	6.60 ± 0.32	
23	HATLASJ225844.8−295124$_1$	20.37 ± 0.10 $-18.28^{+0.93}_{-0.69}$	$20.69^{+0.07}_{-0.06}$ $18.41^{+0.57}_{-0.49}$	0.29 ± 0.01 $2.13^{+0.22}_{-0.33}$	3.86 ± 0.08	1.41 ± 0.08
	HATLASJ225844.8−295124$_2$	19.43 ± 0.14 $-19.18^{+0.92}_{-0.73}$	$24.60^{+0.12}_{-0.14}$ $22.33^{+0.56}_{-0.52}$	$2.32^{+0.19}_{-0.20}$ $16.60^{+2.34}_{-2.76}$	$6.47^{+0.56}_{-0.53}$	
24	HELMSJ232210.3−033559$_1$	$19.33^{+0.14}_{-0.13}$ $-15.46^{+1.76}_{-1.08}$	$22.74^{+0.13}_{-0.14}$ 22.13 ± 0.33	$1.00^{+0.11}_{-0.12}$ $2.64^{+1.20}_{-1.30}$	$7.18^{+0.50}_{-0.53}$	3.47 ± 0.08
	HELMSJ232210.3−033559$_2$	22.74 ± 0.12 –	21.44 ± 0.06 –	$0.116^{+0.006}_{-0.005}$ –	$6.982^{+0.004}_{-0.001}$	
25	HATLASJ233037.2−331217$_1$	$19.45^{+0.14}_{-0.13}$ $-19.07^{+0.82}_{-0.63}$	$22.91^{+0.19}_{-0.21}$ $20.71^{+0.52}_{-0.47}$	1.08 ± 0.12 $7.66^{+1.16}_{-1.32}$	$6.58^{+1.32}_{-1.03}$	19.93 ± 0.21
	HATLASJ233037.2−331217$_2$	[23.14] $-15.40^{+0.80}_{-0.60}$	– –	– –	–	
Confirmed after the lens subtraction						
26	HELMSJ001626.0+042613	17.63 ± 0.07 -18.06 ± 0.07	20.35 ± 0.11 19.50 ± 0.11	0.73 ± 0.04 $2.63^{+0.16}_{-0.15}$	7.11 ± 0.17	1.46 ± 0.08
27	HATLASJ002624.8−341737	$20.82^{+0.20}_{-0.19}$ $-18.61^{+1.20}_{-0.88}$	$23.13^{+0.30}_{-0.31}$ $20.28^{+0.88}_{-0.78}$	$0.62^{+0.08}_{-0.07}$ $4.88^{+0.81}_{-0.85}$	$6.69^{+0.86}_{-0.94}$	0.90 ± 0.03
28	HELMSJ004723.6+015751$_1$	18.14 ± 0.06 -18.86 ± 0.06	$21.67^{+0.09}_{-0.11}$ $20.32^{+0.09}_{-0.11}$	$1.27^{+0.06}_{-0.07}$ $6.65^{+0.33}_{-0.38}$	$4.10^{+0.49}_{-0.35}$	10.99 ± 0.18
	HELMSJ004723.6+015751$_2$	$19.58^{+0.09}_{-0.08}$ –	22.17 ± 0.06 –	0.74 ± 0.02 –	5.65 ± 0.10	
29	HERSJ012041.6−002705	19.59 ± 0.15 $-19.21^{+0.21}_{-0.20}$	$21.97^{+0.34}_{-0.37}$ $19.59^{+0.35}_{-0.38}$	$0.58^{+0.10}_{-0.09}$ $4.36^{+0.75}_{-0.66}$	$9.37^{+0.72}_{-0.85}$	2.57 ± 0.10
30	HATLASJ085112+004934	$18.68^{+0.17}_{-0.19}$ $-19.86^{+1.58}_{-1.07}$	$20.81^{+0.18}_{-0.20}$ $18.60^{+0.88}_{-0.79}$	0.75 ± 0.06 $5.27^{+0.91}_{-1.47}$	$3.25^{+0.66}_{-0.47}$	9.37 ± 0.15
31	HATLASJ085359+015537	$20.77^{+0.16}_{-0.15}$ $-19.26^{+0.58}_{-0.49}$	$24.92^{+0.36}_{-0.38}$ 21.58 ± 0.57	$1.22^{+0.20}_{-0.18}$ $10.17^{+1.76}_{-1.54}$	$14.19^{+1.47}_{-1.44}$	0.87 ± 0.03
32	HERMESJ104549+574512	19.69 ± 0.14 $-15.81^{+0.29}_{-0.28}$	$20.94^{+0.17}_{-0.18}$ $20.15^{+0.18}_{-0.19}$	0.41 ± 0.04 $1.39^{+0.17}_{-0.16}$	$5.16^{+0.46}_{-0.43}$	7.20 ± 0.10
33	HERMESJ105551+592845$_1$	20.84 ± 0.12 $-16.26^{+0.85}_{-0.66}$	22.62 ± 0.08 $21.22^{+0.37}_{-0.33}$	0.58 ± 0.02 $3.09^{+0.51}_{-0.63}$	3.83 ± 0.10	5.60 ± 0.08
	HERMESJ105551+592845$_2$	$22.06^{+0.21}_{-0.20}$ –	$21.86^{+0.15}_{-0.13}$ –	0.25 ± 0.02 –	3.10 ± 0.14	
34	HERMESJ105751+573026$_1$	17.82 ± 0.08 $-20.47^{+0.20}_{-0.19}$	$23.48^{+0.15}_{-0.17}$ $21.43^{+0.19}_{-0.20}$	2.64 ± 0.24 $18.16^{+1.76}_{-1.72}$	$9.89^{+0.72}_{-0.71}$	43.86 ± 0.21
	HERMESJ105751+573026$_2$	$20.98^{+0.70}_{-0.81}$ –	$20.67^{+0.99}_{-1.12}$ –	$0.16^{+0.19}_{-0.08}$ –	$11.33^{+4.02}_{-2.77}$	
	HERMESJ105751+573026$_3$	$21.93^{+0.22}_{-0.20}$ –	$20.72^{+0.15}_{-0.13}$ –	0.124 ± 0.008 –	6.39 ± 0.49	
	HERMESJ105751+573026$_4$	$21.59^{+0.10}_{-0.09}$ –	21.16 ± 0.05 –	0.172 ± 0.006 –	$6.987^{+0.002}_{-0.001}$	
	HERMESJ105751+573026$_5$	$21.58^{+0.19}_{-0.18}$ –	$20.30^{+0.13}_{-0.12}$ –	0.124 ± 0.007 –	5.60 ± 0.34	
	HERMESJ105751+573026$_6$	[23.60] –	– –	– –	–	

Table 5.2 (cont.)

No.	IAU Name	m_{F110W} [mag] M_{F110W} [mag]	μ_{50} [mag arcsec^{-2}] $\mu_{50,0}$ [mag kpc^{-2}]	R_{50} [arcsec] $R_{50,0}$ [kpc]	C_{31}	$\mu S_{1.1}$ [μJy]
(1)	(2)	(3)	(4)	(5)	(6)	(7)
35	HATLASJ132630+334410	18.76 ± 0.06 -20.23 ± 0.06	23.80 ± 0.04 21.28 ± 0.04	1.95 ± 0.04 $15.00^{+0.32}_{-0.31}$	$10.11^{+0.19}_{-0.18}$	1.34 ± 0.06
36	HATLASJ133543+300404$_1$	$20.76^{+0.12}_{-0.11}$ $-18.83^{+0.12}_{-0.11}$	$22.35^{+0.08}_{-0.07}$ $19.38^{+0.08}_{-0.07}$	0.60 ± 0.03 4.90 ± 0.22	$2.88^{+0.06}_{-0.05}$	15.09 ± 0.23
	HATLASJ133543+300404$_2$	20.98 ± 0.13 -18.62 ± 0.13	$21.90^{+0.09}_{-0.08}$ $18.92^{+0.09}_{-0.08}$	0.31 ± 0.01 $2.50^{+0.12}_{-0.11}$	$8.66^{+0.43}_{-0.42}$	
	HATLASJ133543+300404$_3$	19.92 ± 0.09 -19.67 ± 0.09	23.50 ± 0.06 20.53 ± 0.06	1.01 ± 0.03 $8.27^{+0.25}_{-0.26}$	9.81 ± 0.30	
	HATLASJ133543+300404$_4$	$20.45^{+0.11}_{-0.10}$ $-19.18^{+0.11}_{-0.10}$	$23.58^{+0.07}_{-0.06}$ $20.58^{+0.07}_{-0.06}$	0.80 ± 0.03 6.56 ± 0.23	$11.10^{+0.45}_{-0.44}$	
37	HATLASJ142140+000448	20.34 ± 0.10 $-19.62^{+1.19}_{-0.80}$	$21.27^{+0.07}_{-0.06}$ $18.00^{+0.91}_{-0.73}$	0.36 ± 0.01 $3.08^{+0.17}_{-0.34}$	4.44 ± 0.10	3.24 ± 0.05
38	HERMESJ142824+352620	$20.69^{+0.12}_{-0.11}$ $-19.04^{+0.12}_{-0.11}$	$21.47^{+0.08}_{-0.07}$ $18.38^{+0.08}_{-0.07}$	0.34 ± 0.01 2.81 ± 0.11	4.64 ± 0.13	1.93 ± 0.05
39	HATLASJ223753.8−305828	$19.09^{+0.08}_{-0.07}$ $-18.92^{+0.79}_{-0.63}$	21.81 ± 0.05 $19.93^{+0.43}_{-0.39}$	0.70 ± 0.02 $4.55^{+0.53}_{-0.72}$	$8.77^{+0.18}_{-0.17}$	3.56 ± 0.08
40	HATLASJ225250.7−313657	$21.31^{+0.17}_{-0.16}$ $-17.32^{+1.21}_{-0.86}$	$22.23^{+0.12}_{-0.10}$ $19.97^{+0.72}_{-0.63}$	0.29 ± 0.02 $2.09^{+0.27}_{-0.43}$	$11.10^{+0.86}_{-0.81}$	2.04 ± 0.03
41	HELMSJ233441.0−065220	$19.79^{+0.17}_{-0.16}$ $-18.09^{+0.17}_{-0.16}$	21.04 ± 0.51 19.23 ± 0.51	$0.38^{+0.08}_{-0.05}$ $2.44^{+0.53}_{-0.35}$	$5.13^{+0.39}_{-0.40}$	172.09 ± 0.22
42	HELMSJ233633.5−032119$_1$	$16.99^{+0.05}_{-0.04}$ –	20.94 ± 0.08 –	1.29 ± 0.06 –	$7.24^{+0.28}_{-0.29}$	14.41 ± 0.21
	HELMSJ233633.5−032119$_2$	19.16 ± 0.08 –	$23.16^{+0.06}_{-0.05}$ –	1.53 ± 0.04 –	4.34 ± 0.06	
Confirmed through sub-mm/mm follow-up						
43	HELMSJ001615.7+032435	$18.24^{+0.36}_{-0.34}$ $-20.31^{+0.36}_{-0.34}$	$23.64^{+0.18}_{-0.16}$ $21.43^{+0.18}_{-0.16}$	$2.54^{+0.24}_{-0.22}$ $18.25^{+1.76}_{-1.62}$	$9.16^{+1.47}_{-1.63}$	< 0.04
44	HELMSJ002220.9−015524	$21.07^{+0.15}_{-0.14}$ $-18.27^{+0.50}_{-0.44}$	$25.43^{+0.10}_{-0.09}$ $22.66^{+0.36}_{-0.34}$	1.59 ± 0.08 $12.62^{+0.82}_{-0.90}$	6.62 ± 0.31	< 0.04
45	HELMSJ003814.1−002252	[22.45] $-12.66^{+1.43}_{-0.95}$	– –	– –	–	< 0.04
46	HELMSJ003929.6+002426	22.398 ± 0.003 $-16.34^{+0.99}_{-0.73}$	$22.17^{+0.02}_{-0.01}$ $19.83^{+0.61}_{-0.53}$	0.256 ± 0.003 $1.90^{+0.18}_{-0.31}$	$2.38^{+0.08}_{-0.09}$	< 0.04
47	HELMSJ004714.2+032454	$20.25^{+0.24}_{-0.23}$ $-17.43^{+0.54}_{-0.48}$	$23.07^{+0.17}_{-0.16}$ $21.38^{+0.31}_{-0.30}$	0.92 ± 0.14 $5.57^{+1.05}_{-1.04}$	$4.40^{+0.61}_{-0.60}$	< 0.04
48	HELMSJ005159.5+062241$_1$	18.36 ± 0.09 -19.94 ± 0.09	$22.71^{+0.10}_{-0.12}$ $20.66^{+0.10}_{-0.12}$	$1.67^{+0.11}_{-0.12}$ $11.54^{+0.74}_{-0.80}$	$5.95^{+0.91}_{-0.64}$	< 0.04
	HELMSJ005159.5+062241$_2$	20.87 ± 0.06 –	20.48 ± 0.03 –	0.176 ± 0.004 –	$6.987^{+0.001}_{-0.002}$	
	HELMSJ005159.5+062241$_3$	20.03 ± 0.09 -18.24 ± 0.09	23.78 ± 0.05 21.75 ± 0.05	1.42 ± 0.06 $9.78^{+0.41}_{-0.42}$	$4.08^{+0.13}_{-0.11}$	
49	HATLASJ005724.2−273122	20.36 ± 0.10 $-19.00^{+1.52}_{-0.99}$	$24.83^{+0.07}_{-0.06}$ $22.05^{+1.01}_{-0.83}$	1.35 ± 0.05 $10.76^{+0.88}_{-2.22}$	$18.23^{+0.86}_{-0.84}$	< 0.05
50	HERMESJ021831−053131	$21.55^{+0.19}_{-0.18}$ $-18.89^{+0.19}_{-0.18}$	$23.60^{+0.13}_{-0.12}$ $19.89^{+0.13}_{-0.12}$	$0.51^{+0.03}_{-0.03}$ $4.40^{+0.27}_{-0.26}$	$8.95^{+0.71}_{-0.69}$	< 0.04
51	HERMESJ033211−270536	[23.01] –	– –	– –	–	< 0.03
52	HERMESJ044154−540352	$19.64^{+0.09}_{-0.08}$ –	21.75 ± 0.06 –	0.48 ± 0.01 –	$13.98^{+0.40}_{-0.41}$	< 0.03
53	HATLASJ083932−011760	19.992 ± 0.002 $-17.34^{+0.84}_{-0.65}$	21.16 ± 0.01 $19.65^{+0.38}_{-0.35}$	0.458 ± 0.005 $2.60^{+0.38}_{-0.50}$	2.18 ± 0.03	< 0.03

Table 5.2 (cont.)

No.	IAU Name	m_{F110W} [mag] M_{F110W} [mag]	μ_{50} [mag arcsec^{-2}] $\mu_{50,0}$ [mag kpc^{-2}]	R_{50} [arcsec] $R_{50,0}$ [kpc]	C_{31}	
(1)	(2)	(3)	(4)	(5)	(6)	
54	HATLASJ091841+023048$_1$	$20.48^{+0.17}_{-0.16}$ $-18.92^{+1.12}_{-0.80}$	$25.27^{+0.24}_{-0.30}$ $22.43^{+0.82}_{-0.71}$	$1.85^{+0.30}_{-0.34}$ $14.30^{+2.89}_{-3.32}$	$9.93^{+5.55}_{-2.95}$	< 0.04
	HATLASJ091841+023048$_2$	22.56 ± 0.11 $-16.84^{+1.12}_{-0.80}$	21.80 ± 0.06 $18.97^{+0.78}_{-0.67}$	0.148 ± 0.006 $1.18^{+0.09}_{-0.17}$	$6.9849^{+0.0029}_{-0.0010}$	
56	HATLASJ115433.6+005042	20.89 ± 0.13 $-17.03^{+0.62}_{-0.51}$	$21.10^{+0.08}_{-0.07}$ $19.28^{+0.33}_{-0.31}$	0.28 ± 0.01 $1.79^{+0.19}_{-0.23}$	$3.83^{+0.10}_{-0.11}$	< 0.03
57	HATLASJ120127.6−014043	20.85 ± 0.19 $-18.43^{+1.34}_{-0.91}$	$20.44^{+0.60}_{-0.42}$ $17.81^{+1.06}_{-0.91}$	$0.18^{+0.04}_{-0.03}$ $1.37^{+0.36}_{-0.29}$	$8.27^{+3.41}_{-1.67}$	< 0.04
58	HATLASJ131611+281220	$21.87^{+0.22}_{-0.20}$ $-17.48^{+0.46}_{-0.42}$	$22.68^{+0.15}_{-0.13}$ $19.91^{+0.34}_{-0.33}$	0.29 ± 0.02 $2.31^{+0.18}_{-0.19}$	$8.86^{+0.84}_{-0.78}$	< 0.03
59	HATLASJ134429+303036	$19.57^{+0.32}_{-0.30}$ $-19.01^{+0.32}_{-0.30}$	$20.85^{+0.73}_{-0.69}$ $18.61^{+0.73}_{-0.69}$	$0.38^{+0.14}_{-0.08}$ $2.74^{+1.00}_{-0.58}$	$6.09^{+0.69}_{-0.68}$	< 0.04
60	HATLASJ141352−000027$_1$	$18.19^{+0.18}_{-0.17}$ $-19.85^{+0.18}_{-0.17}$	$22.11^{+0.43}_{-0.42}$ $20.21^{+0.43}_{-0.42}$	$1.22^{+0.23}_{-0.18}$ $8.01^{+1.52}_{-1.17}$	7.67 ± 0.48	
	HATLASJ141352-000027$_2$	$20.91^{+0.13}_{-0.12}$ –	21.05 ± 0.08 –	0.229 ± 0.010 –	$6.40^{+0.27}_{-0.26}$	< 0.04
	HATLASJ141352−000027$_3$	19.18 ± 0.08 -18.87 ± 0.08	21.69 ± 0.05 19.79 ± 0.05	0.64 ± 0.02 $4.20^{+0.10}_{-0.11}$	8.56 ± 0.18	
61	HATLASJ142414+022304$_1$	$19.95^{+0.09}_{-0.08}$ -18.31 ± 0.09	23.04 ± 0.09 21.68 ± 0.05	1.11 ± 0.06 $7.65^{+0.39}_{-0.40}$	$10.30^{+0.64}_{-0.53}$	< 0.03
	HATLASJ142414+022304$_2$	$21.05^{+0.15}_{-0.14}$ $-17.21^{+0.15}_{-0.14}$	$24.59^{+0.10}_{-0.09}$ $22.56^{+0.10}_{-0.09}$	0.93 ± 0.05 $6.41^{+0.31}_{-0.30}$	$12.87^{+0.84}_{-0.80}$	
62	HERMESJ142826+345547	19.254 ± 0.001 -18.065 ± 0.001	20.801 ± 0.007 19.297 ± 0.007	0.542 ± 0.003 3.07 ± 0.02	2.56 ± 0.03	< 0.03
63	HATLASJ230815.5−343801	$20.18^{+0.21}_{-0.20}$ $-18.58^{+0.93}_{-0.72}$	$22.15^{+0.13}_{-0.11}$ $19.80^{+0.59}_{-0.52}$	$0.55^{+0.02}_{-0.03}$ $4.05^{+0.42}_{-0.60}$	$7.71^{+1.59}_{-1.35}$	< 0.04
64	HELMSJ232439.5−043936	$20.34^{+0.21}_{-0.20}$ $-18.21^{+1.27}_{-0.89}$	$21.64^{+0.31}_{-0.26}$ $19.44^{+0.77}_{-0.67}$	0.40 ± 0.03 $2.86^{+0.43}_{-0.65}$	$5.96^{+0.32}_{-0.29}$	< 0.04
65	HELMSJ233620.8−060828	17.97 ± 0.07 -19.24 ± 0.07	20.39 ± 0.05 18.94 ± 0.05	0.66 ± 0.02 3.62 ± 0.09	$6.58^{+0.20}_{-0.19}$	< 0.04

Table 5.3: Structural parameters of the systems classified as B obtained from a parametric fit of their surface brightness distributions.

No.	IAU Name	Type	Components	μ_e [mag arcsec^{-2}]	R_e [arcsec]	n	q	PA [deg]	m_{PSF} [mag]	C/T	χ^2	N_{dof}
(1)	(2)	(3)	(4)	(5)	(6)	(7)	(8)	(9)	(10)	(11)	(12)	(13)
	HELMSJ00215.9−012829$_1$		Sérsic	23.76 ± 0.07	1.32 ± 0.04	9.15 ± 0.26	0.454 ± 0.007	$71.45^{+0.67}_{-0.70}$	–	[1.00]		
	HELMSJ00215.9−012829$_2$		Sérsic	21.94 ± 0.07	0.56 ± 0.02	1.92 ± 0.06	0.766 ± 0.007	$158.48^{+0.72}_{-0.70}$	–	[1.00]		
66		2									1.06	36859
	HELMSJ00215.9−012829$_3$		Sérsic	$20.72^{+0.17}_{-0.15}$	0.27 ± 0.02	$3.14^{+0.24}_{-0.25}$	0.83 ± 0.01	$1.57^{+1.15}_{-1.13}$	–	0.26 ± 0.05		
			Sérsic	$24.46^{+0.11}_{-0.10}$	3.55 ± 0.17	1.65 ± 0.13	0.57 ± 0.02	$1.82^{+2.52}_{-2.48}$	–	0.74 ± 0.05		
	HELMSJ00215.9−012829$_4$		de Vauc.	25.01 ± 0.03	2.18 ± 0.03	[4.00]	0.51 ± 0.01	1.25 ± 1.05	–	[1.00]		
67	HELMSJ001800.1−060235	1	Sérsic	$22.48^{+0.18}_{-0.15}$	0.28 ± 0.02	1.97 ± 0.27	0.45 ± 0.03	$8.63^{+2.96}_{-3.04}$	–	[1.00]	1.09	5692
68	HELMSJ002208.1+034044	1	Sérsic	22.39 ± 0.01	3.48 ± 0.02	5.62 ± 0.02	0.774 ± 0.001	112.08 ± 0.11	–	[1.00]	1.04	179985
69	HATLASJ002533.5−333825	1	Sérsic	22.67 ± 0.07	0.79 ± 0.03	2.67 ± 0.10	0.495 ± 0.008	$65.31^{+0.75}_{-0.72}$	–	[1.00]	1.03	49556
70	HERMESJ002906−421419	1	Sérsic	21.82 ± 0.07	$1.38^{+0.06}_{-0.05}$	$5.90^{+0.14}_{-0.13}$	0.462 ± 0.004	15.42 ± 0.29	–	$0.84^{+0.02}_{-0.03}$	1.03	57088
			Sérsic	$23.28^{+0.13}_{-0.12}$	1.60 ± 0.09	0.70 ± 0.06	0.66 ± 0.02	$9.99^{+2.61}_{-2.60}$	–	$0.16^{+0.03}_{-0.02}$		
71	HATLASJ003207.7−303724	1	Sérsic	$20.66^{+0.25}_{-0.20}$	0.17 ± 0.02	2.51 ± 0.28	0.87 ± 0.02	$2.02^{+1.84}_{-1.83}$	–	$0.24^{+0.07}_{-0.06}$	1.20	16024
			Sérsic	$23.61^{+0.14}_{-0.12}$	1.72 ± 0.10	0.57 ± 0.05	0.76 ± 0.02	$1.42^{+2.44}_{-2.42}$	–	$0.76^{+0.06}_{-0.07}$		
73	HERSJ010301.2−003301	1	Sérsic	$19.66^{+0.24}_{-0.20}$	0.55 ± 0.09	2.02 ± 0.16	0.611 ± 0.008	$2.08^{+1.32}_{-1.28}$	–	$0.28^{+0.09}_{-0.08}$	1.02	97861
			Sérsic	$23.30^{+0.17}_{-0.15}$	4.61 ± 0.17	0.77 ± 0.07	0.71 ± 0.03	$2.29^{+4.69}_{-4.77}$	–	$0.54^{+0.07}_{-0.08}$		
			Gauss	$21.86^{+0.12}_{-0.11}$	1.41 ± 0.04	[0.50]	0.73 ± 0.02	$2.12^{+3.08}_{-3.11}$	–	0.17 ± 0.03		
74	HERSJ011640.1−000454	1	Sérsic	20.89 ± 0.06	0.46 ± 0.01	3.98 ± 0.09	0.734 ± 0.006	173.26 ± 0.67	–	[1.00]	1.03	39846
75	HATLASJ012415.9−310500	1	Sérsic	$18.91^{+0.17}_{-0.15}$	0.16 ± 0.01	1.80 ± 0.14	0.54 ± 0.01	$0.41^{+1.18}_{-1.17}$	–	$0.69^{+0.05}_{-0.06}$	1.07	56335
			Sérsic	$23.62^{+0.13}_{-0.12}$	0.91 ± 0.03	0.74 ± 0.09	0.83 ± 0.03	$0.96^{+2.13}_{-2.14}$	–	$0.31^{+0.06}_{-0.05}$		
76	HERSJ012521.0+011724$_1$	3	Sérsic	$20.36^{+0.18}_{-0.16}$	0.19 ± 0.02	$0.51^{+0.11}_{-0.10}$	0.37 ± 0.03	169.97 ± 1.95	–	0.49 ± 0.10	1.05	46470
			Sérsic	$23.85^{+0.19}_{-0.16}$	0.72 ± 0.07	1.16 ± 0.26	0.50 ± 0.06	$154.46^{+4.80}_{-4.95}$	–	0.51 ± 0.10		
	HERSJ012521.0+011724$_2$		Sérsic	23.66 ± 0.08	1.25 ± 0.04	2.18 ± 0.09	$0.457^{+0.008}_{-0.009}$	$19.79^{+0.79}_{-0.77}$	–	[1.00]		
	HERSJ012754.1+004940$_1$		Sérsic	$20.93^{+0.12}_{-0.11}$	$0.193^{+0.009}_{-0.010}$	$2.31^{+0.17}_{-0.16}$	0.63 ± 0.02	141.54 ± 1.45	–	[1.00]	1.06	35456
78	HERSJ012754.1+004940$_2$	2	de Vauc.	$22.10^{+0.20}_{-0.17}$	0.25 ± 0.03	[4.00]	0.92 ± 0.03	$97.35^{+5.46}_{-5.37}$	–	$0.18^{+0.07}_{-0.05}$	1.06	35456
			Sérsic	$25.38^{+0.17}_{-0.15}$	3.43 ± 0.32	$1.77^{+0.22}_{-0.23}$	0.66 ± 0.01	$135.40^{+1.35}_{-1.32}$	–	$0.82^{+0.05}_{-0.07}$		
	HERSJ012754.1+004940$_3$		Sérsic	22.08 ± 0.09	0.46 ± 0.02	3.29 ± 0.17	0.44 ± 0.01	$42.45^{+1.00}_{-0.95}$	–	[1.00]	1.06	35456

Notes: Col. (1): Source reference number. Col. (2): IAU name of the *Herschel* detection. Indices 1 and 2 refer to the two components of the lens candidate. Col. (3): System type. Col. (4): Adopted model for the lens components. Col. (5): Effective surface brightness, i.e., the surface brightness at the effective radius. Col. (6): Effective radius, i.e., the semi-major axis of the isophote containing half of the light of the component. Col. (7): Sérsic index. Values fixed in the fit are bracketed. Col. (8): Axis ratio. Col. (9): Position angle. Col. (10): Magnitude of the unresolved component. Col. (11): Relative flux density of the components C/T. Col. (12): Reduced χ^2 of the fit. Col. (13): Number of degrees of freedom of the fit.

Table 5.3 (cont.)

No.	IAU Name	Type	Components	μ_e [mag arcsec^{-2}]	R_e [arcsec]	n	q	PA [deg]	m_{PSF} [mag]	C/T	χ^2	N_{dof}
(1)	(2)	(3)	(4)	(5)	(6)	(7)	(8)	(9)	(10)	(11)	(12)	(13)
79	HATLASJ012853.0−332719	1	Sérsic	$20.29^{+0.14}_{-0.13}$	0.171 ± 0.010	1.17 ± 0.12	0.30 ± 0.02	$44.73^{+2.14}_{-2.10}$	–	[1.00]	1.11	8522
80	HATLASJ013840.5−281855	2	Sérsic	$22.89^{+0.08}_{-0.07}$	0.88 ± 0.03	1.00 ± 0.03	0.854 ± 0.007	2.83 ± 0.74	–	$0.963^{+0.003}_{-0.004}$	1.75	10783
			PSF	–	–	–	–	–	[24.19]	$0.037^{+0.004}_{-0.003}$		
81	HATLASJ013951.9−321446	1	Sérsic	$22.12^{+0.11}_{-0.10}$	0.30 ± 0.01	$3.96^{+0.27}_{-0.26}$	0.68 ± 0.01	$109.05^{+1.31}_{-1.32}$	–	[1.00]	1.04	16354
82	HERSJ021402.6−004612	1	Sérsic	$19.18^{+0.26}_{-0.21}$	0.33 ± 0.06	$2.57^{+0.24}_{-0.25}$	0.742 ± 0.010	$95.19^{+1.43}_{-1.42}$	–	$0.43^{+0.10}_{-0.11}$	1.07	48476
			Sérsic	$21.46^{+0.15}_{-0.13}$	1.08 ± 0.03	0.46 ± 0.04	0.70 ± 0.02	$63.54^{+2.08}_{-2.00}$	–	$0.27^{+0.06}_{-0.05}$		
			Sérsic	$23.58^{+0.14}_{-0.13}$	2.63 ± 0.10	$0.57^{+0.05}_{-0.06}$	0.83 ± 0.03	$22.74^{+4.65}_{-4.70}$	–	0.29 ± 0.06		
83	HERSJ021434.4+005926	1	Sérsic	$21.65^{+0.08}_{-0.07}$	0.283 ± 0.010	$7.19^{+0.27}_{-0.28}$	0.874 ± 0.008	2.96 ± 0.74	–	[1.00]	1.01	59738
84	HERMESJ022017−060143$_1$	3	Sérsic	21.23 ± 0.07	0.34 ± 0.01	6.62 ± 0.19	0.755 ± 0.007	$160.35^{+0.71}_{-0.70}$	–	[1.00]	1.04	78534
85	HERMESJ022135−062617	1	Sérsic	$18.75^{+0.11}_{-0.10}$	0.23 ± 0.01	0.85 ± 0.06	0.63 ± 0.01	150.18 ± 0.89	–	$0.041^{+0.010}_{-0.008}$	1.10	44199
			Sérsic	$23.02^{+0.13}_{-0.12}$	$4.64^{+0.27}_{-0.26}$	$4.89^{+0.49}_{-0.47}$	0.829 ± 0.007	$128.03^{+0.71}_{-0.69}$	–	$0.959^{+0.008}_{-0.010}$		
87	HATLASJ084958+010713	1	Sérsic	$24.32^{+0.15}_{-0.13}$	0.64 ± 0.04	$2.22^{+0.24}_{-0.23}$	0.67 ± 0.02	$115.56^{+2.10}_{-2.19}$	–	[1.00]	1.07	19834
88	HATLASJ90453.2+022017$_1$	2	Sérsic	$21.49^{+0.22}_{-0.18}$	0.22 ± 0.02	2.70 ± 0.37	0.90 ± 0.02	$113.00^{+1.96}_{-1.89}$	–	0.18 ± 0.05	1.03	34113
			Sérsic	$25.52^{+0.13}_{-0.11}$	3.95 ± 0.23	1.76 ± 0.17	0.62 ± 0.02	$116.57^{+2.66}_{-2.72}$	–	0.82 ± 0.05		
	HATLASJ90453.2+022017$_2$		Sérsic	$21.37^{+0.19}_{-0.16}$	0.21 ± 0.02	$1.46^{+0.23}_{-0.24}$	0.85 ± 0.03	$0.43^{+1.90}_{-1.83}$	–	0.46 ± 0.09		
			Sérsic	$24.35^{+0.14}_{-0.13}$	1.13 ± 0.06	1.54 ± 0.24	0.51 ± 0.03	$2.05^{+3.65}_{-3.52}$	–	0.54 ± 0.09		
89	HATLASJ091331−003644	1	Sérsic	20.65 ± 0.06	0.80 ± 0.03	$5.10^{+0.10}_{-0.11}$	0.600 ± 0.004	44.44 ± 0.26	–	0.70 ± 0.03	1.09	43112
			Sérsic	$21.45^{+0.10}_{-0.09}$	1.02 ± 0.04	0.68 ± 0.05	0.83 ± 0.01	$54.57^{+1.76}_{-1.79}$	–	0.30 ± 0.03		
90	HATLASJ092136+000132$_1$	2	Sérsic	21.68 ± 0.08	0.32 ± 0.01	$4.23^{+0.18}_{-0.17}$	0.784 ± 0.009	$0.88^{+0.80}_{-0.81}$	–	[1.00]	1.13	23289
	HATLASJ092136+000132$_2$		de Vauc.	22.41 ± 0.06	0.29 ± 0.01	[4.00]	0.48 ± 0.02	$2.65^{+3.32}_{-3.33}$	–	[1.00]		
	HATLASJ092136+000132$_3$		Sérsic	$21.51^{+0.20}_{-0.16}$	0.47 ± 0.04	1.73 ± 0.15	0.50 ± 0.02	$2.02^{+1.30}_{-1.22}$	–	0.35 ± 0.07	1.13	
			Sérsic	$25.47^{+0.13}_{-0.12}$	4.35 ± 0.24	$1.56^{+0.15}_{-0.14}$	0.43 ± 0.02	$2.49^{+2.49}_{-2.47}$	–	0.65 ± 0.07		
	HATLASJ092136+000132$_4$		Sérsic	$21.28^{+0.08}_{-0.07}$	0.39 ± 0.01	2.15 ± 0.09	0.492 ± 0.009	$2.66^{+0.81}_{-0.84}$	–	[1.00]		
91	HATLASJ092409−005018		Sérsic	$20.15^{+0.05}_{-0.04}$	$0.424^{+0.009}_{-0.010}$	$3.79^{+0.07}_{-0.06}$	0.676 ± 0.005	$0.61^{+0.61}_{-0.62}$	–	[1.00]	1.07	52167
92	HERMESJ103618+585454	1	Sérsic	$23.86^{+0.08}_{-0.07}$	1.26 ± 0.04	4.17 ± 0.15	0.479 ± 0.008	51.82 ± 0.73	–	[1.00]	1.05	49688
93	HATLASJ113804−011736$_1$	2	Sérsic	21.63 ± 0.03	1.06 ± 0.02	4.65 ± 0.06	0.603 ± 0.004	54.87 ± 0.50	–	[1.00]	1.00	36845
	HATLASJ113804−011736$_2$		de Vauc.	$26.10^{+0.06}_{-0.05}$	$2.97^{+0.10}_{-0.09}$	[4.00]	0.31 ± 0.02	$2.94^{+1.99}_{-2.02}$	–	[1.00]		
	HATLASJ113804−011736$_3$		Sérsic	$21.78^{+0.13}_{-0.12}$	0.22 ± 0.01	$2.99^{+0.27}_{-0.29}$	0.59 ± 0.02	$1.24^{+1.83}_{-1.81}$	–	[1.00]		
94	HATLASJ113833.3+004909$_1$	2	Sérsic	23.99 ± 0.08	1.15 ± 0.04	$6.17^{+0.24}_{-0.26}$	0.426 ± 0.009	$74.69^{+0.82}_{-0.80}$	–	[1.00]	1.30	29339
	HATLASJ113833.3+004909$_2$		Sérsic	$22.14^{+0.09}_{-0.08}$	0.39 ± 0.02	$4.27^{+0.20}_{-0.21}$	0.66 ± 0.01	$17.48^{+0.89}_{-0.90}$	–	[1.00]		
	HATLASJ113833.3+004909$_3$		Sérsic	23.08 ± 0.07	0.76 ± 0.02	5.10 ± 0.15	0.931 ± 0.007	$66.67^{+0.70}_{-0.71}$	–	[1.00]		
	HATLASJ113833.3+004909$_4$		Sérsic	$25.16^{+0.07}_{-0.06}$	2.05 ± 0.06	9.18 ± 0.24	0.861 ± 0.006	$96.05^{+0.70}_{-0.71}$	–	[1.00]		

Table 5.3 (cont.)

No.	IAU Name	Type	Components	μ_e [mag arcsec^{-2}]	R_e [arcsec]	n	q	PA [deg]	m_{PSF} [mag]	C/T	χ^2	N_{dof}
(1)	(2)	(3)	(4)	(5)	(6)	(7)	(8)	(9)	(10)	(11)	(12)	(13)
95	HATLASJ113841−020237$_1$	2	Sérsic	$20.21^{+0.14}_{-0.12}$	0.087 ± 0.005	3.22 ± 0.32	0.76 ± 0.02	$42.46^{+1.96}_{-1.91}$	–	[1.00]	1.09	29078
	HATLASJ113841−020237$_2$		Sérsic	$24.45^{+0.11}_{-0.10}$	3.06 ± 0.18	0.99 ± 0.06	0.63 ± 0.01	$63.03^{+0.91}_{-0.87}$	–	0.48 ± 0.06		
			Sérsic	$22.69^{+0.13}_{-0.11}$	0.81 ± 0.04	5.62 ± 0.50	0.86 ± 0.02	$99.89^{+2.83}_{-2.78}$	–	0.52 ± 0.06		
96	HATLASJ115112−012638	1	Sérsic	$22.46^{+0.09}_{-0.08}$	$1.28^{+0.07}_{-0.06}$	1.39 ± 0.06	$0.720^{+0.009}_{-0.008}$	$35.26^{+0.65}_{-0.66}$	–	0.57 ± 0.05	1.05	26365
			Sérsic	$18.15^{+0.13}_{-0.12}$	0.143 ± 0.008	$3.37^{+0.29}_{-0.30}$	0.54 ± 0.02	40.24 ± 2.84	–	0.43 ± 0.05		
97	HATLASJ115120−003322$_1$	2	Sérsic	$20.85^{+0.13}_{-0.12}$	0.088 ± 0.005	$6.89^{+0.71}_{-0.70}$	0.87 ± 0.02	62.31 ± 2.06	–	[1.00]	1.07	29074
	HATLASJ115120−003322$_2$		Sérsic	$24.40^{+0.20}_{-0.17}$	0.61 ± 0.05	$3.60^{+0.82}_{-0.84}$	0.56 ± 0.04	$139.38^{+1.87}_{-1.81}$	–	0.43 ± 0.10		
			Sérsic	$24.82^{+0.17}_{-0.15}$	1.44 ± 0.13	0.55 ± 0.11	0.45 ± 0.06	$0.43^{+4.77}_{-4.74}$	–	0.57 ± 0.10		
	HATLASJ115120−003322$_3$		Sérsic	$21.69^{+0.17}_{-0.15}$	0.20 ± 0.01	2.17 ± 0.28	0.46 ± 0.03	$126.80^{+2.93}_{-2.89}$	–	[1.00]		
98	HATLASJ120319.1−011253	1	Sérsic	$22.77^{+0.12}_{-0.11}$	0.57 ± 0.03	1.00 ± 0.08	0.50 ± 0.02	27.77 ± 1.56	–	[1.00]	1.06	20030
99	HATLASJ121301.5−004922	1	Sérsic	$21.99^{+0.09}_{-0.08}$	0.27 ± 0.01	$5.18^{+0.25}_{-0.26}$	$0.993^{+0.005}_{-0.008}$	$128.44^{+0.95}_{-0.92}$	–	[1.00]	0.99	33097
100	HATLASJ121334.9−020323$_1$	1	Sérsic	20.12 ± 0.05	0.58 ± 0.02	6.53 ± 0.12	0.670 ± 0.003	142.91 ± 0.25	–	0.63 ± 0.03	1.03	63123
			Sérsic	$21.44^{+0.09}_{-0.08}$	1.16 ± 0.04	0.88 ± 0.05	0.84 ± 0.01	$101.65^{+1.69}_{-1.70}$	–	0.37 ± 0.03		
101	HATLASJ121542.7−005220	1	Sérsic	$20.44^{+0.12}_{-0.11}$	0.20 ± 0.01	3.40 ± 0.25	0.30 ± 0.02	74.97 ± 1.46	–	[1.00]	1.06	25007
103	HATLASJ131322+285836$_1$	2	Sérsic	$22.46^{+0.08}_{-0.07}$	0.49 ± 0.02	5.00 ± 0.18	$0.867^{+0.007}_{-0.008}$	$127.06^{+0.73}_{-0.77}$	–	[1.00]	1.04	32562
	HATLASJ131322+285836$_2$		Sérsic	$21.78^{+0.14}_{-0.12}$	0.176 ± 0.009	$3.51^{+0.34}_{-0.33}$	0.82 ± 0.02	45.50 ± 1.87	–	[1.00]		
104	HATLASJ134159+292833	1	Sérsic	21.24 ± 0.01	1.26 ± 0.01	5.10 ± 0.02	0.888 ± 0.001	160.98 ± 0.27	–	[1.00]	1.05	60370
105	HATLASJ141833+010212$_1$	2	de Vauc.	23.15 ± 0.01	1.45 ± 0.02	[4.00]	0.868 ± 0.008	158.42 ± 1.19	–	[1.00]	1.05	26010
	HATLASJ141833+010212$_2$		de Vauc.	20.36 ± 0.03	0.232 ± 0.004	[4.00]	0.55 ± 0.01	$68.16^{+1.20}_{-1.21}$	–	[1.00]		
106	HERMESJ142201+533214$_1$	2	Sérsic	$20.04^{+0.08}_{-0.07}$	0.255 ± 0.009	5.00 ± 0.17	0.381 ± 0.007	$167.01^{+0.69}_{-0.70}$	–	[1.00]	1.07	26208
	HERMESJ142201+533214$_2$		Sérsic	$22.44^{+0.11}_{-0.10}$	0.36 ± 0.02	2.11 ± 0.14	0.89 ± 0.01	177.85 ± 1.21	–	[1.00]		
	HERMESJ142201+533214$_3$		PSF	–	–	–	–	–	[23.04]	[1.00]		
107	HATLASJ142318.3+013913	1	Sérsic	22.44 ± 0.11	0.67 ± 0.05	$4.86^{+0.31}_{-0.32}$	0.616 ± 0.010	$176.30^{+0.86}_{-0.85}$	–	$0.62^{+0.05}_{-0.06}$	1.87	18237
			Exp. disk	$23.19^{+0.11}_{-0.10}$	$1.11^{+0.07}_{-0.06}$	[1.00]	0.57 ± 0.03	$32.97^{+2.12}_{-2.13}$	–	$0.38^{+0.06}_{-0.05}$		
108	HATLASJ143203−005219	1	Sérsic	$20.48^{+0.06}_{-0.05}$	0.46 ± 0.01	3.31 ± 0.07	0.625 ± 0.005	$0.59^{+0.62}_{-0.65}$	–	[1.00]	1.26	28559
109	HERMESJ143331+345440$_1$		Sérsic	$21.19^{+0.12}_{-0.11}$	0.23 ± 0.01	$2.64^{+0.20}_{-0.19}$	0.48 ± 0.02	$0.93^{+1.47}_{-1.45}$	–	[1.00]	1.04	21511
110	HATLASJ144243+015506	1	Sérsic	20.82 ± 0.07	$0.44^{+0.02}_{-0.01}$	1.37 ± 0.04	0.546 ± 0.007	$160.16^{+0.72}_{-0.69}$	–	[1.00]	1.05	40321
111	HATLASJ144715−012114$_1$	2	Sérsic	$20.67^{+0.11}_{-0.10}$	0.33 ± 0.02	5.63 ± 0.38	0.65 ± 0.01	$0.56^{+1.01}_{-1.00}$	–	0.78 ± 0.04	1.07	66426
			Sérsic	$22.01^{+0.13}_{-0.12}$	0.58 ± 0.02	0.48 ± 0.06	0.60 ± 0.03	$0.81^{+1.95}_{-1.94}$	–	0.22 ± 0.04		
	HATLASJ144715−012114$_2$		Sérsic	$20.66^{+0.08}_{-0.07}$	0.268 ± 0.010	2.10 ± 0.08	$0.782^{+0.008}_{-0.007}$	$140.19^{+0.72}_{-0.74}$	–	[1.00]		
	HATLASJ144715−012114$_3$		Sérsic	$24.47^{+0.09}_{-0.08}$	4.17 ± 0.21	$0.302^{+0.003}_{-0.002}$	$0.758^{+0.008}_{-0.009}$	$51.40^{+0.64}_{-0.66}$	–	0.47 ± 0.05		
			Sérsic	$19.88^{+0.10}_{-0.09}$	0.34 ± 0.01	2.09 ± 0.16	0.93 ± 0.02	$57.71^{+2.30}_{-2.28}$	–	0.53 ± 0.05		

Table 5.3 (cont.)

No.	IAU Name	Type	Components	μ_e [mag arcsec^{-2}]	R_e [arcsec]	n	q	PA [deg]	m_{PSF} [mag]	C/T	χ^2	N_{dof}
(1)	(2)	(3)	(4)	(5)	(6)	(7)	(8)	(9)	(10)	(11)	(12)	(13)
112	HATLASJ223942.4−333304	1	Sérsic	$25.55^{+0.08}_{-0.07}$	1.81 ± 0.06	$9.69^{+0.21}_{-0.29}$	0.771 ± 0.008	$152.58^{+0.76}_{-0.74}$	–	[1.00]	1.07	52942
113	HATLASJ224026.5−315154	1	Sérsic	$23.13^{+0.12}_{-0.11}$	0.68 ± 0.03	$1.51^{+0.11}_{-0.12}$	0.40 ± 0.02	$54.75^{+1.53}_{-1.50}$	–	[1.00]	2.33	12126
114	HATLASJ224759.6−310134	1	Sérsic	$22.16^{+0.09}_{-0.08}$	1.13 ± 0.05	4.81 ± 0.20	0.489 ± 0.008	0.85 ± 0.60	–	0.45 ± 0.04	1.22	77939
			Sérsic	$23.08^{+0.09}_{-0.08}$	2.29 ± 0.09	$2.16^{+0.14}_{-0.13}$	0.50 ± 0.01	$1.10^{+1.72}_{-1.80}$	–	0.55 ± 0.04		
115	HATLASJ224805.3−335820	1	Sérsic	19.81 ± 0.08	0.38 ± 0.02	2.63 ± 0.10	0.706 ± 0.007	$163.60^{+0.59}_{-0.60}$	–	0.30 ± 0.03	1.02	41417
			Sérsic	23.02 ± 0.06	$2.67^{+0.08}_{-0.07}$	1.51 ± 0.08	0.83 ± 0.01	$154.57^{+1.18}_{-1.15}$	–	0.70 ± 0.03		
116	HATLASJ225045.5−304719	1	Sérsic	$20.59^{+0.17}_{-0.15}$	0.30 ± 0.02	5.42 ± 0.41	0.43 ± 0.01	$2.84^{+1.18}_{-1.13}$	–	0.56 ± 0.07	1.02	60134
			Sérsic	$23.15^{+0.15}_{-0.14}$	1.01 ± 0.06	0.55 ± 0.06	0.87 ± 0.03	$3.15^{+2.22}_{-2.21}$	–	0.44 ± 0.07		
117	HATLASJ230546.2−331038$_1$	3	Sérsic	$18.99^{+0.12}_{-0.11}$	0.18 ± 0.01	2.04 ± 0.13	$0.567^{+0.009}_{-0.010}$	70.35 ± 0.87	–	0.54 ± 0.06	1.02	57738
			Exp. disk	22.80 ± 0.10	0.91 ± 0.05	[1.00]	0.85 ± 0.03	$78.70^{+2.19}_{-2.18}$	–	0.46 ± 0.06		
	HATLASJ230546.2−331038$_2$		Sérsic	$24.11^{+0.07}_{-0.06}$	1.32 ± 0.04	5.65 ± 0.15	$0.996^{+0.003}_{-0.005}$	$179.98^{+0.69}_{-0.68}$	–	[1.00]	1.03	58443
118	HELMSJ231447.5−045658	1	Sérsic	$19.03^{+0.10}_{-0.09}$	0.28 ± 0.02	$2.00^{+0.11}_{-0.12}$	0.429 ± 0.010	$135.82^{+0.89}_{-0.88}$	–	0.50 ± 0.05	1.06	48942
			Sérsic	$23.64^{+0.13}_{-0.12}$	1.59 ± 0.08	$2.55^{+0.22}_{-0.23}$	0.81 ± 0.02	$65.31^{+2.89}_{-2.88}$	–	0.50 ± 0.05		
119	HATLASJ232210.9−333749	1	Sérsic	22.81 ± 0.07	0.98 ± 0.03	4.34 ± 0.13	0.460 ± 0.007	$87.36^{+0.71}_{-0.72}$	–	[1.00]	1.10	23362
120	HELMSJ232617.5−025319	1	Sérsic	$25.28^{+0.11}_{-0.10}$	$0.98^{+0.05}_{-0.04}$	6.48 ± 0.41	$0.991^{+0.007}_{-0.010}$	-0.01 ± 1.17	–	[1.00]	1.06	45836
121	HELMSJ232831.8−004035	1	Sérsic	$21.39^{+0.11}_{-0.10}$	$0.173^{+0.008}_{-0.009}$	2.42 ± 0.34	0.57 ± 0.02	$55.35^{+2.35}_{-2.36}$	–	$0.26^{+0.05}_{-0.04}$	1.14	44945
			Exp. disk	$24.14^{+0.11}_{-0.10}$	$1.27^{+0.08}_{-0.07}$	[1.00]	0.56 ± 0.03	$115.14^{+2.04}_{-2.02}$	–	$0.74^{+0.04}_{-0.05}$		
122	HELMSJ232833.6−031416	1	Sérsic	$21.51^{+0.09}_{-0.08}$	0.36 ± 0.01	3.37 ± 0.16	0.49 ± 0.01	7.40 ± 0.87	–	[1.00]	1.21	58769
124	HELMSJ233721.9−064740	1	Sérsic	$21.53^{+0.06}_{-0.05}$	0.92 ± 0.02	1.56 ± 0.03	$0.550^{+0.006}_{-0.005}$	$27.09^{+0.66}_{-0.65}$	–	[1.00]	1.09	41430
126	HELMSJ234314.0+012152$_1$	3	Sérsic	$23.40^{+0.05}_{-0.04}$	1.73 ± 0.04	5.08 ± 0.09	0.657 ± 0.005	$34.26^{+0.65}_{-0.66}$	–	[1.00]	1.06	64023
			Sérsic	$20.68^{+0.11}_{-0.10}$	0.33 ± 0.02	5.62 ± 0.38	0.65 ± 0.01	$0.56^{+1.00}_{-0.99}$	–	0.78 ± 0.04	1.02	75193
	HELMSJ234314.0+012152$_1$		Sérsic	$22.01^{+0.13}_{-0.12}$	0.58 ± 0.02	0.48 ± 0.06	0.60 ± 0.03	$0.82^{+1.94}_{-1.97}$	–	0.22 ± 0.04		
127	HATLASJ234955.7−330833	1	Sérsic	22.37 ± 0.09	0.68 ± 0.04	6.81 ± 0.34	$0.994^{+0.004}_{-0.007}$	$3.15^{+0.72}_{-0.73}$	–	$0.30^{+0.04}_{-0.03}$	1.17	32161
			Sérsic	23.91 ± 0.07	3.17 ± 0.10	$3.93^{+0.23}_{-0.22}$	0.57 ± 0.01	$1.96^{+1.49}_{-1.50}$	–	$0.70^{+0.03}_{-0.04}$		
128	HELMSJ235101.7−024426	1	Sérsic	$21.87^{+0.22}_{-0.18}$	2.65 ± 0.34	$1.72^{+0.10}_{-0.11}$	0.746 ± 0.008	160.02 ± 1.46	–	0.29 ± 0.07	1.04	73079
			Sérsic	$18.22^{+0.17}_{-0.15}$	0.46 ± 0.02	3.04 ± 0.25	0.70 ± 0.02	$112.92^{+3.39}_{-3.43}$	–	0.32 ± 0.05		
			Sérsic	$22.37^{+0.18}_{-0.16}$	4.27 ± 0.17	1.24 ± 0.09	0.68 ± 0.02	$81.12^{+1.57}_{-1.63}$	–	0.38 ± 0.06		
129	HATLASJ235121.9−332902$_1$	2	Sérsic	$19.90^{+0.20}_{-0.17}$	0.20 ± 0.02	2.02 ± 0.17	0.60 ± 0.02	$171.89^{+1.27}_{-1.25}$	–	$0.15^{+0.04}_{-0.03}$	1.05	20220
			Sérsic	$24.16^{+0.10}_{-0.09}$	2.66 ± 0.10	3.33 ± 0.24	0.72 ± 0.01	$54.63^{+1.84}_{-1.86}$	–	$0.85^{+0.03}_{-0.04}$		
	HATLASJ235121.9−332902$_2$		Sérsic	22.20 ± 0.07	0.80 ± 0.03	5.03 ± 0.14	$0.461^{+0.007}_{-0.006}$	171.81 ± 0.70	–	[1.00]		
130	HELMSJ235332.0+031718	1	Sérsic	24.51 ± 0.08	1.14 ± 0.04	7.31 ± 0.29	$0.700^{+0.008}_{-0.009}$	34.24 ± 0.75	–	[1.00]	1.02	26066
			Sérsic	$18.05^{+0.48}_{-0.33}$	0.07 ± 0.01	$4.99^{+0.53}_{-0.55}$	0.87 ± 0.02	17.37 ± 1.45	–	$0.95^{+0.04}_{-0.10}$		
			Gauss	$23.20^{+0.89}_{-0.52}$	$0.29^{+0.14}_{-0.13}$	[0.50]	$0.81^{+0.13}_{-0.20}$	$135.51^{+91.78}_{-81.60}$	–	$0.05^{+0.10}_{-0.04}$		

Table 5.4: Derived properties of the candidate lensing systems classified as B.

No.	IAU Name	m_{F110W} [mag]	μ_{50} [mag arcsec^{-2}]	R_{50} [arcsec]	C_{31}
(1)	(2)	(3)	(4)	(5)	(6)
66	HELMSJ00215.9−012829$_1$	20.19 ± 0.10	23.76 ± 0.07	0.89 ± 0.03	18.34 ± 0.74
	HELMSJ00215.9−012829$_2$	$20.47^{+0.11}_{-0.10}$	21.94 ± 0.07	0.49 ± 0.02	3.95 ± 0.08
	HELMSJ00215.9−012829$_3$	$19.06^{+0.13}_{-0.12}$	$23.66^{+0.17}_{-0.20}$	$1.78^{+0.23}_{-0.22}$	$7.12^{+0.96}_{-0.93}$
	HELMSJ00215.9−012829$_4$	20.66 ± 0.05	25.01 ± 0.03	1.56 ± 0.03	$6.98945^{+0.00003}_{-0.00001}$
67	HELMSJ001800.1−060235	$23.09^{+0.26}_{-0.24}$	$22.48^{+0.18}_{-0.15}$	0.19 ± 0.01	$4.02^{+0.35}_{-0.34}$
68	HELMSJ002208.1+034044	16.39 ± 0.02	22.39 ± 0.01	3.06 ± 0.02	9.89 ± 0.04
69	HATLASJ002533.5−333825	20.77 ± 0.11	$22.67^{+0.08}_{-0.07}$	0.56 ± 0.02	4.98 ± 0.14
70	HERMESJ002906−421419	18.17 ± 0.10	21.66 ± 0.07	1.04 ± 0.04	7.49 ± 0.36
71	HATLASJ003207.7−303724	$19.98^{+0.16}_{-0.15}$	23.27 ± 0.15	$1.18^{+0.14}_{-0.15}$	$4.26^{+1.22}_{-0.87}$
72	HELMSJ004747.1+061444	21.849 ± 0.003	23.309 ± 0.009	0.514 ± 0.004	2.61 ± 0.04
73	HERSJ010301.2−003301	17.11 ± 0.16	$21.75^{+0.40}_{-0.46}$	$1.87^{+0.36}_{-0.32}$	$5.76^{+0.56}_{-0.70}$
74	HERSJ011640.1−000454	19.55 ± 0.08	20.89 ± 0.06	0.39 ± 0.01	6.95 ± 0.15
75	HATLASJ012415.9−310500	20.20 ± 0.17	$19.97^{+0.45}_{-0.36}$	0.19 ± 0.02	$6.74^{+1.06}_{-0.91}$
76	HERSJ012521.0+011724	$21.85^{+0.22}_{-0.21}$	$21.44^{+0.95}_{-0.57}$	$0.20^{+0.06}_{-0.03}$	$4.74^{+0.84}_{-1.08}$
	HERSJ012521.0+011724$_2$	$20.95^{+0.12}_{-0.11}$	$23.65^{+0.08}_{-0.07}$	0.84 ± 0.03	$4.30^{+0.11}_{-0.12}$
78	HERSJ012754.1+004940$_1$	$21.90^{+0.17}_{-0.16}$	$20.93^{+0.12}_{-0.11}$	0.154 ± 0.008	$4.47^{+0.23}_{-0.22}$
	HERSJ012754.1+004940$_2$	$19.97^{+0.23}_{-0.21}$	$24.86^{+0.19}_{-0.20}$	$2.16^{+0.33}_{-0.34}$	$5.67^{+0.99}_{-0.75}$
	HERSJ012754.1+004940$_3$	$21.39^{+0.14}_{-0.13}$	22.08 ± 0.09	0.30 ± 0.01	$5.87^{+0.26}_{-0.25}$
79	HATLASJ012853.0−332719	$22.67^{+0.22}_{-0.21}$	$20.29^{+0.14}_{-0.13}$	$0.094^{+0.007}_{-0.006}$	$3.00^{+0.16}_{-0.15}$
80	HATLASJ013840.5−281855	20.60 ± 0.10	22.83 ± 0.07	0.79 ± 0.03	2.99 ± 0.05
81	HATLASJ013951.9−321446	$21.77^{+0.16}_{-0.15}$	$22.12^{+0.11}_{-0.10}$	0.25 ± 0.01	$6.93^{+0.46}_{-0.43}$
82	HERSJ021402.6−004612	$17.89^{+0.20}_{-0.21}$	$20.66^{+0.41}_{-0.42}$	$0.81^{+0.14}_{-0.11}$	$5.48^{+0.53}_{-0.57}$
83	HERSJ021434.4+005926	20.84 ± 0.11	$21.65^{+0.08}_{-0.07}$	$0.264^{+0.010}_{-0.009}$	13.28 ± 0.64
84	HERMESJ022017−060143$_1$	20.23 ± 0.10	21.23 ± 0.07	$0.294^{+0.010}_{-0.009}$	$11.98^{+0.42}_{-0.41}$
	HERMESJ022017−060143$_2$	19.799 ± 0.002	21.308 ± 0.006	0.529 ± 0.003	2.56 ± 0.02
85	HERMESJ022135−062617	$16.36^{+0.18}_{-0.17}$	$22.84^{+0.11}_{-0.10}$	3.87 ± 0.27	$9.72^{+1.07}_{-0.99}$
87	HATLASJ084958+010713	$22.67^{+0.20}_{-0.19}$	$24.32^{+0.15}_{-0.12}$	0.52 ± 0.03	4.36 ± 0.32
88	HATLASJ90453.2+022017$_1$	$19.89^{+0.17}_{-0.16}$	$25.01^{+0.17}_{-0.19}$	$2.37^{+0.29}_{-0.32}$	$6.22^{+1.33}_{-0.97}$
	HATLASJ90453.2+022017$_2$	21.26 ± 0.18	$22.46^{+0.43}_{-0.39}$	$0.39^{+0.06}_{-0.05}$	$5.20^{+0.46}_{-0.49}$
89	HATLASJ091331−003644	17.79 ± 0.08	20.38 ± 0.06	0.76 ± 0.02	$5.34^{+0.23}_{-0.22}$
90	HATLASJ092136+000132$_1$	21.02 ± 0.11	21.68 ± 0.08	0.28 ± 0.01	$7.36^{+0.30}_{-0.29}$
	HATLASJ092136+000132$_2$	22.48 ± 0.11	22.41 ± 0.06	0.204 ± 0.009	$6.9872^{+0.0015}_{-0.0008}$
	HATLASJ092136+000132$_3$	$19.83^{+0.16}_{-0.15}$	$24.22^{+0.36}_{-0.47}$	$1.46^{+0.34}_{-0.30}$	$8.11^{+0.60}_{-0.72}$
	HATLASJ092136+000132$_4$	21.05 ± 0.11	$21.28^{+0.08}_{-0.07}$	0.27 ± 0.01	4.26 ± 0.12
91	HATLASJ092409−005018	19.08 ± 0.07	20.15 ± 0.04	0.349 ± 0.008	6.65 ± 0.10
92	HERMESJ103618+585454	20.74 ± 0.11	$23.86^{+0.08}_{-0.07}$	0.87 ± 0.03	$7.26^{+0.26}_{-0.25}$

Notes: Col. (1): Source reference number. Col. (2): IAU name of the *Herschel* detection. Indices 1 and 2 refer to the two components of the lens candidate. Col. (3): Apparent magnitude of the model and absolute magnitude of the model. Col. (4): Total effective radius in arcsec and in kpc. Col. (5): Total effective surface brightness before and after correcting for cosmological dimming. Col. (6): C_{31} of the model.

Table 5.4 (cont.)

No.	IAU Name	m_{F110W} [mag]	μ_{50} [mag arcsec^{-2}]	R_{50} [arcsec]	C_{31}
(1)	(2)	(3)	(4)	(5)	(6)
	HATLASJ113804−011736$_1$	18.59 ± 0.05	21.63 ± 0.03	0.82 ± 0.01	8.10 ± 0.10
93	HATLASJ113804−011736$_2$	21.61 ± 0.11	$26.09^{+0.06}_{-0.05}$	1.66 ± 0.07	$6.98946^{+0.00002}_{-0.00001}$
	HATLASJ113804−011736$_3$	22.44 ± 0.18	$21.78^{+0.13}_{-0.12}$	0.167 ± 0.009	5.43 ± 0.41
	HATLASJ113833.3+004909$_1$	21.00 ± 0.11	$23.99^{+0.08}_{-0.07}$	0.75 ± 0.03	$11.02^{+0.53}_{-0.51}$
94	HATLASJ113833.3+004909$_2$	$21.23^{+0.13}_{-0.12}$	$22.14^{+0.09}_{-0.08}$	0.32 ± 0.01	$7.41^{+0.35}_{-0.34}$
	HATLASJ113833.3+004909$_3$	20.23 ± 0.10	23.08 ± 0.07	0.74 ± 0.02	$8.90^{+0.28}_{-0.26}$
	HATLASJ113833.3+004909$_4$	19.94 ± 0.09	$25.16^{+0.07}_{-0.06}$	1.90 ± 0.06	$18.44^{+0.71}_{-0.69}$
95	HATLASJ113841−020237$_1$	$22.54^{+0.19}_{-0.18}$	$20.21^{+0.14}_{-0.12}$	0.076 ± 0.004	$5.77^{+0.48}_{-0.46}$
	HATLASJ113841−020237$_2$	19.03 ± 0.12	23.35 ± 0.14	$1.63^{+0.15}_{-0.13}$	$6.04^{+0.55}_{-0.52}$
96	HATLASJ115112−012638	$18.82^{+0.12}_{-0.11}$	$20.92^{+0.28}_{-0.34}$	$0.50^{+0.09}_{-0.08}$	$10.16^{+0.66}_{-0.80}$
	HATLASJ115120−003322$_1$	$22.60^{+0.20}_{-0.18}$	$20.85^{+0.14}_{-0.12}$	0.082 ± 0.005	$12.51^{+1.66}_{-1.50}$
97	HATLASJ115120−003322$_2$	$21.85^{+0.22}_{-0.21}$	24.24 ± 0.16	$0.80^{+0.11}_{-0.10}$	$3.50^{+0.45}_{-0.36}$
	HATLASJ115120−003322$_3$	$23.01^{+0.24}_{-0.23}$	$21.69^{+0.17}_{-0.15}$	$0.133^{+0.009}_{-0.010}$	4.29 ± 0.37
	HATLASJ120127.8−021648$_1$	$21.94^{+0.36}_{-0.34}$	21.90 ± 0.58	$0.18^{+0.07}_{-0.05}$	$13.05^{+3.47}_{-2.80}$
98	HATLASJ120127.8−021648$_2$	$21.78^{+0.16}_{-0.15}$	$25.96^{+0.11}_{-0.10}$	1.41 ± 0.07	$7.77^{+0.53}_{-0.51}$
	HATLASJ120127.8−021648$_3$	$22.52^{+0.19}_{-0.18}$	$22.62^{+0.14}_{-0.12}$	0.27 ± 0.02	$3.86^{+0.24}_{-0.23}$
99	HATLASJ120319.1−011253	$22.07^{+0.18}_{-0.17}$	$22.77^{+0.12}_{-0.11}$	0.40 ± 0.02	$2.80^{+0.09}_{-0.10}$
100	HATLASJ121301.5−004922	21.32 ± 0.13	$21.99^{+0.09}_{-0.08}$	0.27 ± 0.01	$9.03^{+0.50}_{-0.48}$
101	HATLASJ121334.9−020323	17.60 ± 0.07	$20.29^{+0.06}_{-0.07}$	0.75 ± 0.03	$6.52^{+0.31}_{-0.30}$
102	HATLASJ121542.7−005220	$21.91^{+0.18}_{-0.16}$	$20.43^{+0.12}_{-0.11}$	0.111 ± 0.006	6.04 ± 0.37
103	HATLASJ130054+260303$_1$	18.92 ± 0.12	$23.55^{+0.16}_{-0.18}$	$1.67^{+0.17}_{-0.18}$	$9.47^{+1.16}_{-1.10}$
104	HATLASJ131322+285836$_1$	20.65 ± 0.11	$22.46^{+0.08}_{-0.07}$	0.46 ± 0.02	8.71 ± 0.33
	HATLASJ131322+285836$_2$	$22.46^{+0.19}_{-0.18}$	$21.78^{+0.14}_{-0.12}$	0.159 ± 0.009	$6.21^{+0.54}_{-0.49}$
105	HATLASJ134159+292833	17.36 ± 0.02	21.24 ± 0.01	1.182 ± 0.010	8.90 ± 0.04
106	HATLASJ141833+010212$_1$	19.11 ± 0.03	23.15 ± 0.01	1.35 ± 0.02	$6.98944^{+0.00003}_{-0.00002}$
	HATLASJ141833+010212$_2$	20.80 ± 0.05	20.36 ± 0.03	0.172 ± 0.003	6.987 ± 0.002
	HERMESJ142201+533214$_1$	$20.54^{+0.11}_{-0.10}$	$20.04^{+0.08}_{-0.07}$	0.158 ± 0.006	$8.71^{+0.31}_{-0.30}$
107	HERMESJ142201+533214$_2$	$21.72^{+0.16}_{-0.14}$	$22.44^{+0.11}_{-0.10}$	0.34 ± 0.02	4.21 ± 0.18
	HERMESJ142201+533214$_3$	[23.04]	–	–	–
108	HATLASJ142318.3+013913	$19.82^{+0.14}_{-0.13}$	22.17 ± 0.10	0.68 ± 0.04	$5.18^{+0.35}_{-0.33}$
109	HATLASJ143203−005219	19.40 ± 0.08	$20.48^{+0.06}_{-0.05}$	0.362 ± 0.009	5.90 ± 0.10
110	HERMESJ143331+345440$_1$	$21.99^{+0.17}_{-0.16}$	$21.19^{+0.12}_{-0.11}$	0.161 ± 0.008	$4.93^{+0.28}_{-0.27}$
111	HATLASJ144243+015506	20.41 ± 0.10	20.82 ± 0.07	0.33 ± 0.01	3.26 ± 0.05
	HATLASJ144715−012114$_1$	19.70 ± 0.14	$20.65^{+0.12}_{-0.11}$	0.34 ± 0.01	$6.47^{+0.52}_{-0.47}$
112	HATLASJ144715−012114$_2$	$20.73^{+0.12}_{-0.11}$	$20.66^{+0.08}_{-0.07}$	0.237 ± 0.008	4.19 ± 0.10
	HATLASJ144715−012114$_3$	18.58 ± 0.10	$22.79^{+0.57}_{-0.67}$	$1.09^{+0.28}_{-0.21}$	$12.03^{+0.60}_{-0.61}$

Table 5.4 (cont.)

No.	IAU Name	m_{F110W} [mag]	μ_{50} [mag arcsec^{-2}]	R_{50} [arcsec]	C_{31}
(1)	(2)	(3)	(4)	(5)	(6)
113	HATLASJ223942.4−333304	20.69 ± 0.11	$25.56^{+0.08}_{-0.07}$	1.59 ± 0.06	$19.94^{+0.63}_{-0.86}$
114	HATLASJ224026.5−315154	22.07 ± 0.17	$23.13^{+0.12}_{-0.11}$	0.43 ± 0.02	$3.43^{+0.14}_{-0.15}$
115	HATLASJ224759.6−310134	18.32 ± 0.09	22.08 ± 0.08	1.25 ± 0.05	5.97 ± 0.22
116	HATLASJ224805.3−335820	$17.81^{+0.08}_{-0.07}$	$22.08^{+0.13}_{-0.14}$	$1.53^{+0.12}_{-0.11}$	$6.55^{+0.32}_{-0.36}$
117	HATLASJ225045.5−304719	$19.97^{+0.16}_{-0.15}$	$22.01^{+0.23}_{-0.26}$	$0.53^{+0.08}_{-0.07}$	$7.48^{+0.89}_{-0.98}$
118	HATLASJ230546.2−331038$_1$	19.63 ± 0.13	$20.60^{+0.40}_{-0.36}$	$0.32^{+0.05}_{-0.04}$	$6.98^{+0.44}_{-0.47}$
	HATLASJ230546.2−331038$_2$	19.95 ± 0.09	$24.11^{+0.07}_{-0.06}$	1.31 ± 0.04	$9.96^{+0.30}_{-0.29}$
119	HELMSJ231447.5−045658	18.95 ± 0.12	$20.72^{+0.39}_{-0.35}$	$0.44^{+0.07}_{-0.05}$	$9.10^{+0.81}_{-0.92}$
120	HATLASJ232210.9−333749	20.27 ± 0.10	22.81 ± 0.07	0.66 ± 0.02	7.55 ± 0.21
121	HATLASJ232531.3−302235$_1$	$21.26^{+0.13}_{-0.12}$	23.51 ± 0.08	0.81 ± 0.03	2.86 ± 0.06
	HATLASJ232531.3−302235$_2$	20.56 ± 0.11	$20.81^{+0.08}_{-0.07}$	0.244 ± 0.009	6.14 ± 0.18
122	HELMSJ232617.5−025319	$21.71^{+0.15}_{-0.14}$	$25.28^{+0.11}_{-0.10}$	$0.97^{+0.05}_{-0.04}$	$11.67^{+0.91}_{-0.88}$
123	HELMSJ232831.8−004035	$21.24^{+0.13}_{-0.14}$	$23.55^{+0.13}_{-0.14}$	0.69 ± 0.08	$4.98^{+0.48}_{-0.45}$
124	HELMSJ232833.6−031416	21.23 ± 0.12	$21.50^{+0.09}_{-0.08}$	0.25 ± 0.01	$5.99^{+0.25}_{-0.24}$
125	HELMSJ233420.4−003458	20.154 ± 0.002	$21.273^{+0.006}_{-0.005}$	0.473 ± 0.003	2.41 ± 0.02
126	HELMSJ233721.9−064740	19.45 ± 0.08	$21.54^{+0.06}_{-0.05}$	0.68 ± 0.02	3.50 ± 0.04
128	HELMSJ34314.0+012152$_1$	19.70 ± 0.14	$20.65^{+0.11}_{-0.10}$	0.34 ± 0.01	$6.46^{+0.53}_{-0.47}$
	HELMSJ34314.0+012152$_2$	19.04 ± 0.02	$23.40^{+0.02}_{-0.01}$	1.73 ± 0.01	4.93 ± 0.02
129	HATLASJ234955.7−330833	18.24 ± 0.08	22.99 ± 0.10	$1.76^{+0.09}_{-0.08}$	$9.11^{+0.42}_{-0.41}$
130	HELMSJ235101.7−024426	15.80 ± 0.14	$20.46^{+0.19}_{-0.20}$	$1.81^{+0.24}_{-0.23}$	$6.90^{+0.69}_{-0.72}$
131	HATLASJ235121.9−332902$_1$	18.92 ± 0.12	$23.55^{+0.16}_{-0.18}$	$1.66^{+0.17}_{-0.18}$	$9.47^{+1.21}_{-1.10}$
	HATLASJ235121.9−332902$_2$	20.01 ± 0.10	22.20 ± 0.07	0.55 ± 0.02	$8.78^{+0.26}_{-0.25}$
132	HELMSJ235332.0+031718	$20.91^{+0.12}_{-0.11}$	24.51 ± 0.08	0.95 ± 0.03	$13.54^{+0.70}_{-0.67}$

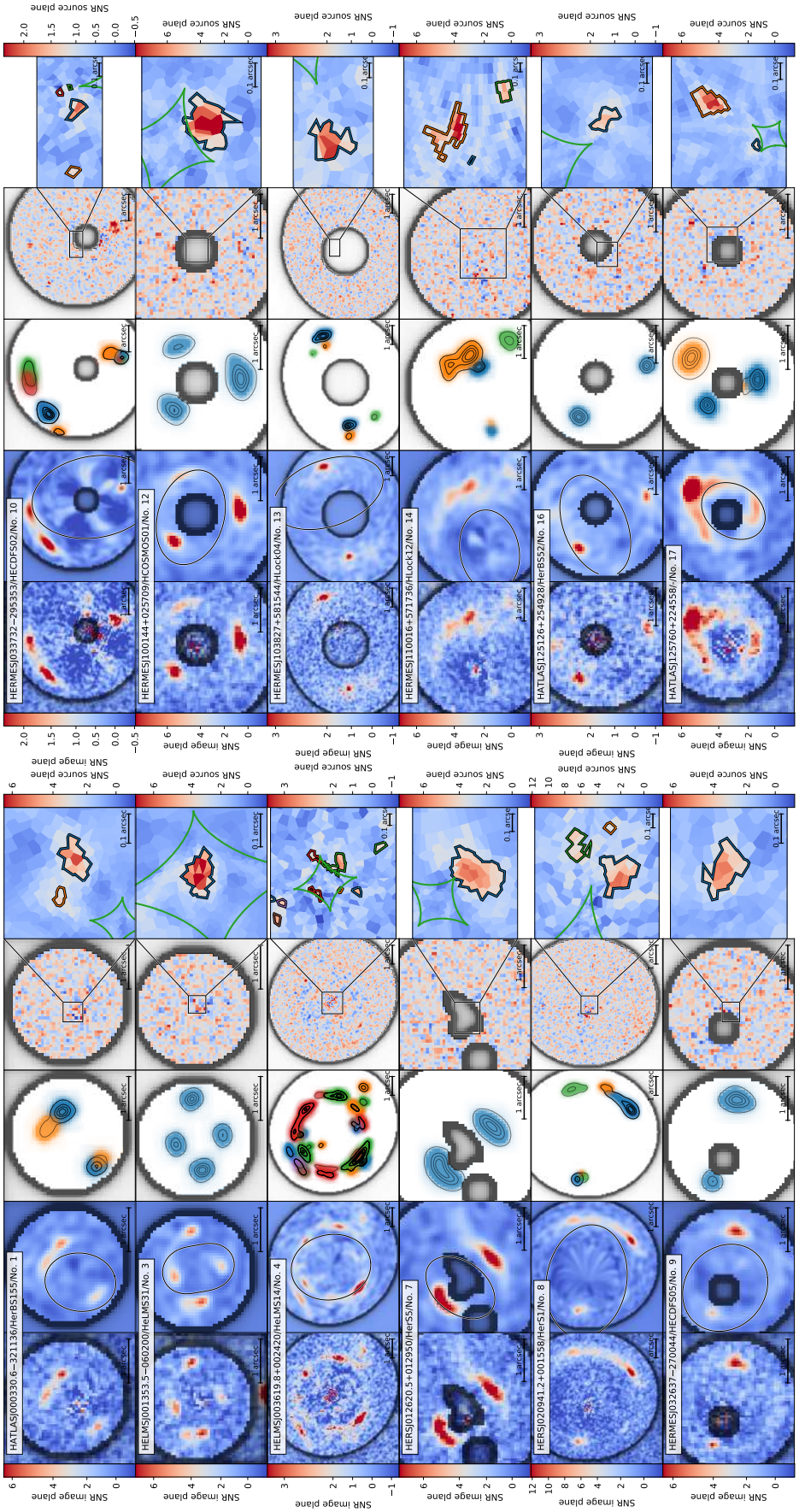

Figure 5.3: *From left to right panels:* Lens subtracted image, best-fitting model of the lensed source, SNR > 3 regions of the reconstructed source plane lensed back to the image plane, SNR map of the residuals obtained after subtracting the model lensed source from the input lens-subtracted image, and the reconstructed background source with caustics curves (green line). Each of the first three panels shows the pixel mask (black-shaded region) adopted for the lens modelling. The second panel from the left also shows the critical curves (black curve). In the source plane image, we highlighted with black contours the *SNR* > 3 region adopted for computing the magnification and source size.

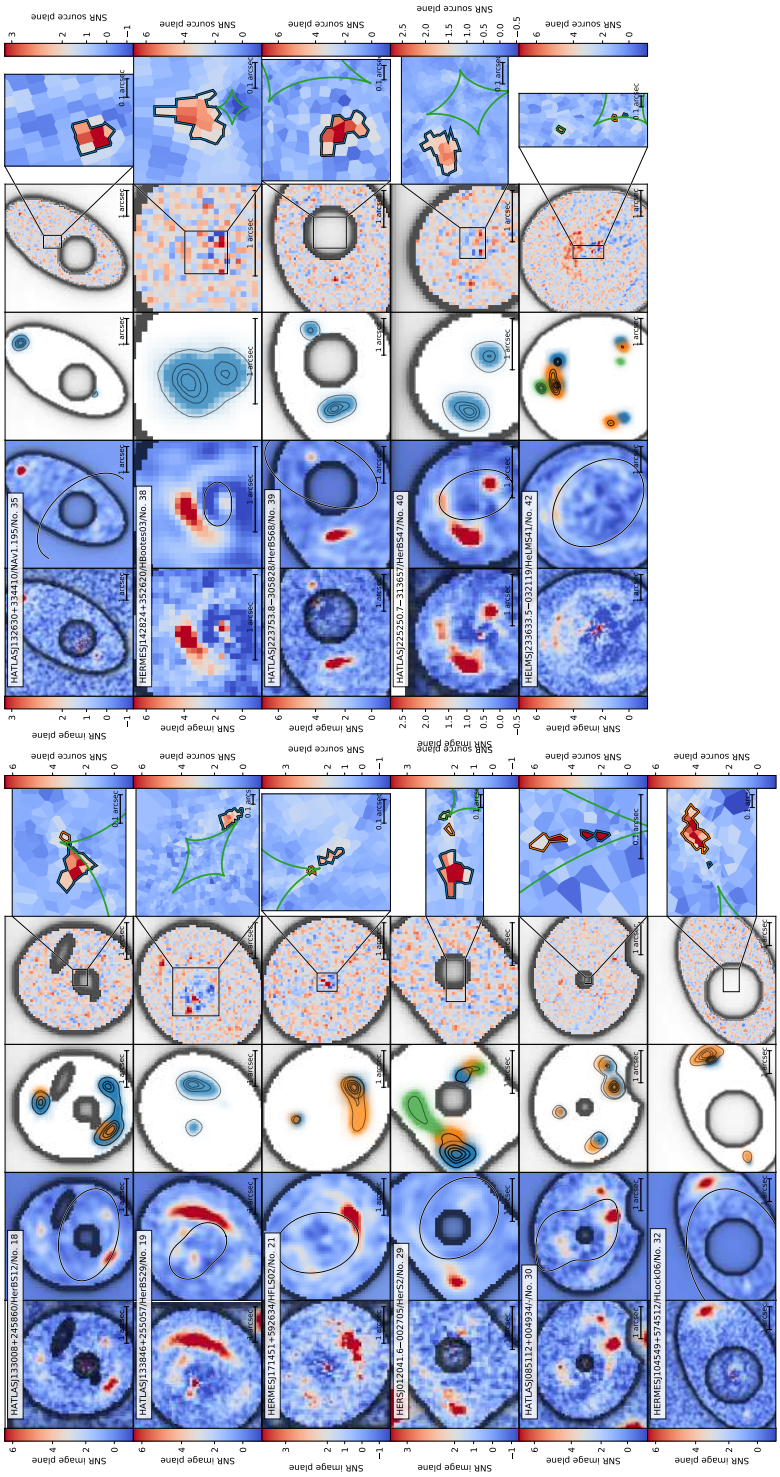

Figure 5.3 (cont.)

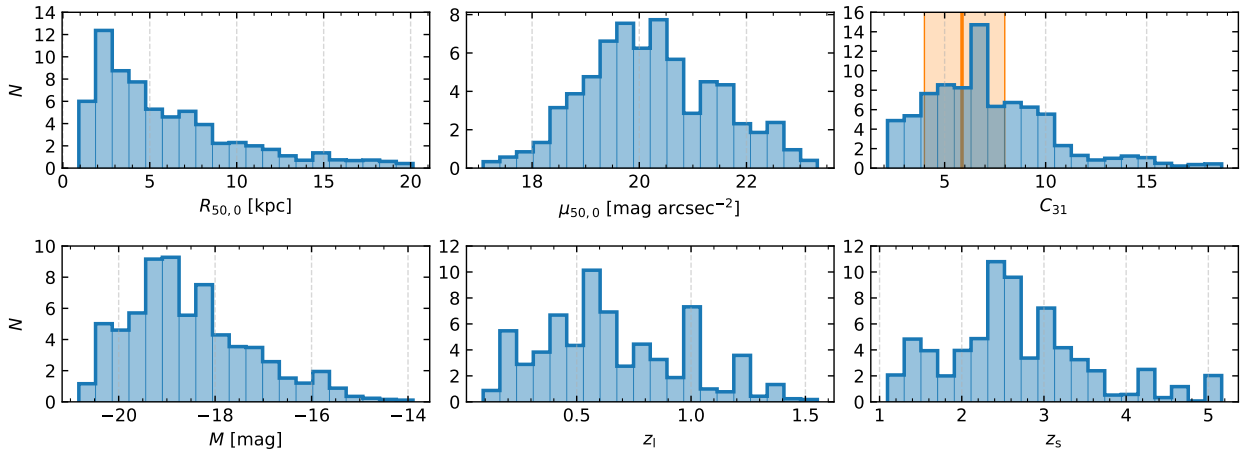

Figure 5.4: Distribution of the total effective radii $R_{50,0}$ (top left panel), total effective surface brightnesses $\mu_{50,0}$ (top central panel), concentrations C_{31} (top right panel), total absolute magnitudes M_{F110W} (bottom left panel), redshifts z_l of the foreground lenses (bottom central panel), and redshifts z_s of the background sources (bottom right panel). All the foreground lenses and background sources with a measured redshift are included. The orange line corresponds to the median of the values of C_{31} of the ETGs sample of Watkins et al. (2022), while the orange shaded region marks the corresponding $\pm 1\sigma$ confidence interval.

5.2 Properties of the confirmed lensing galaxies

We can now focus on the general properties of the population of confirmed strong lenses. In Figure 5.4, we show the C_{31} distribution of our lenses. The peak at $C_{31} \simeq 7$ is due to the systems that we model with a de Vaucouleurs profile and have all the same concentration. We measure a median $\langle C_{31} \rangle = 6.8 \pm 0.4$, which is slightly larger than the median value $\langle C_{31} \rangle = 5.2 \pm 0.1$ measured by Watkins et al. (2022) for a sample of nearby ETGs observed with *Spitzer* at $3.6\,\mu$m. This finding and the observed morphology of smooth and featureless elliptical systems provide further evidence that our lenses are mostly ETGs. Lastly, we measure the flux density $S_{1.1}$ of the background sources at $1.1\,\mu$m by taking the aperture photometry in the regions dominated by the lensing features on the lens subtracted residuals. The uncertainties $\sigma_{S_{1.1}}$ are computed as $\sigma^2_{S_{1.1}} = \sum_{ij} \sigma^2_{i,j}$, where $\sigma_{i,j}$ is the pixel standard deviation associated with the total noise. The values of $S_{1.1}$ and their uncertainties are given in Table 5.2.

For the 68 foreground lensing galaxies with known photometric or spectroscopic redshift, we convert the size of the total effective radius from arcsec to kpc through the angular diameter distance and the total magnitude to absolute magnitude M_{F110W} through the luminosity distance. We also correct the total effective surface brightness for cosmological dimming by multiplying the *F110W* flux density by $(1+z)^4$. when converting from observed to physical quantities, to take into account the uncertainties on the photometric redshift, we sample a truncated normal distribution centred on the redshift measurement with standard deviation being the quoted uncertainty and extending within the range $[0, \infty)$. Then, we perform the corresponding correction for each sampled redshift.

Table 5.5: Results of the lens modelling.

No.IAU Name	δx [arcsec] δx_0 [kpc]	δy [arcsec] δy_0 [kpc]	θ_E [arcsec] $\theta_{E,0}$ [kpc]	q	PA	$\epsilon_{shear,1}$	$\epsilon_{shear,2}$	$x_{\rm pix}$	$y_{\rm pix}$	λ	μ	$R_{\rm bkg,\,circ}$ [arcsec] $R_{\rm bkg,\,circ,\,0}$ [kpc]	κ_0 [] M [10^{11} M$_\odot$]	M/L
(1) (2)	(3)	(4)	(5)	(6)	(7)	(8)	(9)	(10)	(11)	(12)	(13)	(14)	(15)	(16)
1 HATLASJ000330.6−321136	$-0.13^{+0.03}_{-0.02}$ $-0.65^{+0.19}_{-0.16}$	$-0.05^{+0.01}_{-0.02}$ $-0.24^{+0.08}_{-0.12}$	$0.733^{+0.006}_{-0.009}$ $3.85^{+0.61}_{-0.85}$	0.85 ± 0.03	$80.11^{+3.78}_{-10.85}$	–	–	39^{+3}_{-9}	33^{+8}_{-7}	$0.0101^{+0.0011}_{-0.0009}$	$5.48^{+0.62}_{-0.48}$	$0.052^{+0.006}_{-0.004}$ $0.41^{+0.04}_{-0.03}$	$1.68^{+0.03}_{-0.04}$ $0.92^{+0.23}_{-0.28}$	– $2.93^{+1.65}_{-0.98}$
3 HELMSJ001353.5−060200	$-0.038^{+0.004}_{-0.003}$ $-0.26^{+0.05}_{-0.04}$	$0.066^{+0.004}_{-0.006}$ $0.45^{+0.07}_{-0.08}$	$0.658^{+0.004}_{-0.003}$ $4.56^{+0.50}_{-0.74}$	$0.85^{+0.03}_{-0.04}$	$-49.56^{+8.51}_{-8.32}$	$0.017^{+0.008}_{-0.010}$	0.191 ± 0.009	40 ± 4	31 ± 9	0.0084 ± 0.0006	$10.37^{+0.47}_{-0.56}$	0.052 ± 0.002 0.45 ± 0.02	$1.49^{+0.02}_{-0.01}$ $1.48^{+0.52}_{-0.44}$	– $4.19^{+3.00}_{-1.48}$
4 HELMSJ003619.8+002420	$-0.015^{+0.002}_{-0.001}$ $-0.063^{+0.007}_{-0.005}$	$0.122^{+0.001}_{-0.002}$ $0.504^{+0.006}_{-0.008}$	$1.9349^{+0.0017}_{-0.0008}$ $7.977^{+0.007}_{-0.004}$	$0.813^{+0.001}_{-0.003}$	$-79.38^{+0.23}_{-0.21}$	–	–	36	40	$0.0164^{+0.0009}_{-0.0008}$ $1.25^{+0.06}_{-0.07}$	$15.82^{+1.23}_{-0.72}$ 5.234 ± 0.001	$0.143^{+0.006}_{-0.008}$ $3.40^{+0.68}_{-0.54}$	12.16 ± 0.3	–
7 HERSJ012620.5+012950	$-0.006^{+0.015}_{-0.007}$ $-0.04^{+0.08}_{-0.04}$	$0.14^{+0.01}_{-0.02}$ $0.79^{+0.09}_{-0.13}$	0.766 ± 0.004 $4.44^{+0.28}_{-0.32}$	$0.60^{+0.07}_{-0.03}$	$52.13^{+0.85}_{-0.58}$	–	–	31^{+4}_{-0}	40^{+4}_{-7}	0.0114 ± 0.0006	$5.19^{+0.56}_{-0.20}$	$0.142^{+0.003}_{-0.010}$ $1.23^{+0.03}_{-0.08}$	$1.73^{+0.02}_{-0.01}$ $1.32^{+0.18}_{-0.17}$	– $2.36^{+0.73}_{-0.54}$
8 HERSJ020941.2+001558$_1$	$-0.259^{+0.005}_{-0.010}$ $-0.89^{+0.02}_{-0.03}$	$0.046^{+0.008}_{-0.002}$ $0.159^{+0.028}_{-0.006}$	$2.579^{+0.002}_{-0.003}$ $8.844^{+0.007}_{-0.011}$	$0.704^{+0.003}_{-0.004}$	$-10.81^{+0.55}_{-0.21}$	–	–	43	43	0.0093 ± 0.0004	$7.29^{+0.30}_{-0.10}$	0.158 ± 0.003 1.30 ± 0.03	$18.61^{+0.08}_{-0.19}$ $5.99^{+0.03}_{-0.06}$	– $4.96^{+0.95}_{-0.77}$
9 HERMESJ032637−270044	$0.024^{+0.009}_{-0.013}$ –	-0.12 ± 0.01 –	$0.981^{+0.005}_{-0.006}$ –	0.87 ± 0.01	$-40.54^{+1.64}_{-2.25}$	–	–	42^{+0}_{-9}	28^{+11}_{-5}	$0.0110^{+0.0010}_{-0.0009}$	$6.15^{+0.32}_{-0.38}$	0.072 ± 0.004 –	$3.01^{+0.03}_{-0.04}$ –	– –
10 HERMESJ033732−295353	$0.1754^{+0.0007}_{-0.0005}$ $0.57^{+0.11}_{-0.12}$	$0.0576^{+0.0012}_{-0.0008}$ $0.18^{+0.04}_{-0.05}$	$1.9718^{+0.0003}_{-0.0006}$ $6.40^{+1.18}_{-1.30}$	$0.6495^{+0.0003}_{-0.0006}$	$-80.49^{+0.04}_{-0.15}$	–	–	41	38	$0.0057^{+0.0002}_{-0.0003}$	$6.27^{+0.50}_{-0.05}$	$0.0801^{+0.0045}_{-0.0002}$ –	$11.662^{+0.004}_{-0.007}$ –	– –
12 HERMESJ100144+025709	$-0.033^{+0.003}_{-0.004}$ $-0.26^{+0.02}_{-0.03}$	$0.042^{+0.009}_{-0.003}$ $0.34^{+0.08}_{-0.02}$	0.930 ± 0.002 $7.44^{+0.02}_{-0.01}$	$0.686^{+0.006}_{-0.008}$	$-16.66^{+0.39}_{-0.56}$	–	–	33^{+11}_{-10}	30^{+9}_{-0}	$0.0076^{+0.0004}_{-0.0003}$	$6.33^{+0.15}_{-0.17}$ –	$0.094^{+0.002}_{-0.001}$ –	2.63 ± 0.02 –	–
13 HERMESJ103827+581544	$0.228^{+0.016}_{-0.006}$ $1.56^{+0.11}_{-0.04}$	0.27 ± 0.01 $1.84^{+0.09}_{-0.10}$	2.408 ± 0.010 16.47 ± 0.07	0.582 ± 0.007	$-70.47^{+0.76}_{-0.47}$	–	–	44	44	0.025 ± 0.002	$4.29^{+0.15}_{-0.25}$ –	$0.17^{+0.02}_{-0.01}$ –	15.68 ± 0.4 –	–
14 HERMESJ110016+571736	$-0.324^{+0.007}_{-0.009}$ $-2.48^{+0.05}_{-0.07}$	$-0.251^{+0.007}_{-0.011}$ $-1.92^{+0.05}_{-0.08}$	1.081 ± 0.003 $8.28^{+0.02}_{-0.03}$	0.71 ± 0.01	$11.63^{+1.13}_{-0.88}$	–	–	32^{+5}_{-7}	42^{+1}_{-0}	$0.0151^{+0.0008}_{-0.0009}$	$2.43^{+0.03}_{-0.04}$	$0.211^{+0.004}_{-0.006}$ $1.84^{+0.04}_{-0.06}$	3.56 ± 0.02 $5.39^{+0.03}_{-0.04}$	– $1.95^{+0.10}_{-0.09}$
16 HATLASJ125126+254928	-0.40 ± 0.02 $-2.75^{+0.24}_{-0.23}$	$0.056^{+0.009}_{-0.014}$ $0.38^{+0.08}_{-0.09}$	$1.133^{+0.016}_{-0.007}$ $7.94^{+0.50}_{-0.66}$	$0.58^{+0.01}_{-0.02}$	$20.05^{+2.41}_{-3.88}$	–	–	39 ± 3	37^{+5}_{-9}	0.015 ± 0.002	$5.10^{+0.37}_{-0.67}$	$0.052^{+0.006}_{-0.005}$ 0.39 ± 0.04	$3.73^{+0.13}_{-0.04}$ $3.20^{+0.45}_{-0.46}$	– $3.29^{+1.07}_{-0.72}$
17 HATLASJ125760+224558	$0.104^{+0.012}_{-0.007}$ $0.69^{+0.08}_{-0.04}$	$-0.06^{+0.01}_{-0.04}$ $-0.40^{+0.08}_{-0.30}$	$0.681^{+0.005}_{-0.006}$ $4.52^{+0.03}_{-0.04}$	$0.70^{+0.07}_{-0.02}$	$60.10^{+1.21}_{-2.50}$	–	–	38	43	0.0059 ± 0.0004	$4.46^{+0.56}_{-0.52}$	$0.081^{+0.006}_{-0.005}$ $0.70^{+0.05}_{-0.04}$	$1.41^{+0.04}_{-0.03}$ $1.43^{+0.22}_{-0.13}$	– $1.74^{+0.28}_{-0.17}$
18 HATLASJ133008+245860	$0.037^{+0.003}_{-0.010}$ $0.21^{+0.02}_{-0.06}$	$-0.287^{+0.010}_{-0.005}$ $-1.65^{+0.06}_{-0.03}$	$1.037^{+0.001}_{-0.002}$ $5.974^{+0.009}_{-0.011}$	$0.616^{+0.009}_{-0.007}$	$-14.02^{+0.61}_{-0.43}$	–	–	39^{+2}_{-5}	36^{+7}_{-5}	0.0084 ± 0.0006	$12.31^{+1.10}_{-0.72}$	0.055 ± 0.003 0.43 ± 0.02	$3.184^{+0.009}_{-0.008}$ $1.990^{+0.006}_{-0.005}$	– $3.47^{+1.14}_{-0.80}$
19 HATLASJ133846+255057	$0.0905^{+0.0005}_{-0.0028}$ $0.51^{+0.07}_{-0.08}$	$-0.1092^{+0.0001}_{-0.0008}$ $-0.63^{+0.10}_{-0.08}$	$0.6697^{+0.0004}_{-0.0002}$ $3.83^{+0.48}_{-0.62}$	$0.895^{+0.002}_{-0.011}$	$79.56^{+0.59}_{-0.58}$	$0.281^{+0.008}_{-0.001}$	$-0.0560^{+0.0024}_{-0.0002}$	42	41	$0.0046^{+0.0003}_{-0.0002}$	$3.78^{+0.04}_{-0.02}$	$0.0963^{+0.0006}_{-0.0008}$ 0.80 ± 0.03	$1.706^{+0.012}_{-0.002}$ 1.12 ± 0.26	– $7.95^{+3.82}_{-2.14}$
21 HERMESJ171451+592634	$-0.23^{+0.05}_{-0.01}$ $-2.01^{+0.39}_{-0.09}$	$0.21^{+0.03}_{-0.01}$ $1.80^{+0.27}_{-0.09}$	$0.976^{+0.006}_{-0.007}$ $8.35^{+0.05}_{-0.06}$	0.72 ± 0.02	$-76.63^{+1.34}_{-0.90}$	–	–	42^{+1}_{-6}	35^{+5}_{-2}	0.012 ± 0.001	$8.40^{+5.93}_{-6.00}$	$0.053^{+0.053}_{-0.009}$ $0.41^{+0.41}_{-0.07}$	$2.46^{+0.02}_{-0.01}$ 4.1435 ± 0.0008	– $2.83^{+0.18}_{-0.17}$
29 HERSJ012041.6−002705	-0.07 ± 0.01 $-0.55^{+0.08}_{-0.09}$	$-0.095^{+0.010}_{-0.011}$ -0.71 ± 0.08	$0.928^{+0.005}_{-0.006}$ 6.94 ± 0.15	$0.76^{+0.02}_{-0.01}$	$-41.77^{+2.16}_{-2.17}$	–	–	38^{+5}_{-6}	35 ± 6	0.022 ± 0.002	$3.91^{+0.43}_{-0.34}$	$0.124^{+0.008}_{-0.006}$ –	2.65 ± 0.03 –	– –
30 HATLASJ085112+004934	$0.03406^{+0.00009}_{-0.00014} 10^{-2}$ $0.24^{+0.03}_{-0.07}$	$0.1967^{+0.0010}_{-0.0002}$ $1.41^{+0.20}_{-0.39}$	$1.24359^{+0.00004}_{-0.00003}$ $8.90^{+1.26}_{-2.45}$	$0.34221^{+0.00034}_{-0.00007}$	$-41.033^{+0.008}_{-0.033}$	$-0.29461^{+0.00011}_{-0.00006}$	$0.28098^{+0.00005}_{-0.00043}$	44	44	$0.00112^{+0.00004}_{-0.00005}$	$27.80^{+0.50}_{-0.59}$	$0.01863^{+0.00004}_{-0.00009}$ $0.161^{+0.001}_{-0.004}$	$4.0578^{+0.0014}_{-0.0903}$ $4.60^{+3.73}_{-2.22}$	– $1.86^{+2.07}_{-0.72}$
32 HERMESJ104549+574512	$-0.47^{+0.03}_{-0.04}$ $-1.59^{+0.15}_{-0.17}$	$-0.129^{+0.006}_{-0.009}$ -0.44 ± 0.04	$2.631^{+0.007}_{-0.012}$ $8.97^{+0.67}_{-0.73}$	$0.677^{+0.005}_{-0.003}$	$18.85^{+0.69}_{-0.23}$	–	–	41	40 ± 4	0.014 ± 0.001	$8.63^{+0.37}_{-0.21}$	0.108 ± 0.002 0.85 ± 0.02	$17.23^{+0.21}_{-0.12}$ $5.45^{+0.50}_{-0.52}$	– $63.80^{+12.97}_{-10.76}$
35 HATLASJ132630+334410	$0.004^{+0.004}_{-0.006}$ $0.03^{+0.03}_{-0.05}$	$-0.057^{+0.009}_{-0.013}$ $-0.44^{+0.07}_{-0.10}$	$1.684^{+0.005}_{-0.004}$ $12.92^{+0.04}_{-0.03}$	$0.577^{+0.008}_{-0.006}$	$-47.54^{+0.42}_{-0.40}$	–	–	42^{+2}_{-4}	34^{+8}_{-2}	0.0095 ± 0.0006	1.89 ± 0.02	$0.0938^{+0.0079}_{-0.0004}$ $0.743^{+0.063}_{-0.003}$	$8.26^{+0.03}_{-0.02}$ 9.09 ± 0.03	– $3.83^{+0.20}_{-0.19}$
38 HERMESJ142824+352620	$-0.0008^{+0.0065}_{-0.0074}$ $-0.007^{+0.054}_{-0.061}$	$0.016^{+0.005}_{-0.006}$ $0.13^{+0.04}_{-0.05}$	$0.215^{+0.006}_{-0.003}$ $1.78^{+0.05}_{-0.03}$	$0.66^{+0.06}_{-0.05}$	$-5.44^{+5.95}_{-8.75}$	–	–	42^{+1}_{-8}	25^{+5}_{-4}	$0.0064^{+0.0006}_{-0.0004}$	$2.64^{+0.15}_{-0.14}$	$0.090^{+0.003}_{-0.004}$ 0.78 ± 0.03	$0.137^{+0.010}_{-0.005}$ $0.58^{+0.04}_{-0.02}$	– $0.98^{+0.11}_{-0.09}$
39 HATLASJ223753.8−305828	$0.19^{+0.02}_{-0.01}$ $1.24^{+0.18}_{-0.20}$	$-0.091^{+0.010}_{-0.017}$ $-0.60^{+0.11}_{-0.13}$	$1.26^{+0.02}_{-0.01}$ $8.28^{+0.90}_{-1.31}$	$0.54^{+0.01}_{-0.03}$	$65.49^{+0.77}_{-0.62}$	–	–	44	20	$0.0098^{+0.0006}_{-0.0005}$	$2.65^{+0.04}_{-0.10}$	$0.1281^{+0.0032}_{-0.0010}$ 1.10 ± 0.03	$4.53^{+0.07}_{-0.05}$ $3.88^{+1.15}_{-1.02}$	– $4.00^{+2.08}_{-1.12}$
40 HATLASJ225250.7−313657	$0.182^{+0.012}_{-0.005}$ $1.33^{+0.17}_{-0.27}$	$0.08^{+0.01}_{-0.02}$ $0.54^{+0.14}_{-0.18}$	$0.605^{+0.008}_{-0.004}$ $4.41^{+0.51}_{-0.89}$	$0.633^{+0.020}_{-0.009}$	$-73.84^{+2.35}_{-0.69}$	–	–	41^{+3}_{-9}	40^{+4}_{-14}	$0.0031^{+0.0002}_{-0.0003}$	$3.44^{+0.18}_{-0.11}$	$0.078^{+0.002}_{-0.003}$ 0.65 ± 0.02	$1.09^{+0.03}_{-0.01}$ $1.12^{+0.47}_{-0.40}$	– $4.89^{+4.71}_{-1.81}$
41 HELMSJ233633.5−032119$_1$	$0.051^{+0.001}_{-0.005}$ –	$-0.0851^{+0.0106}_{-0.0004}$ –	$1.7281^{+0.0130}_{-0.0007}$ –	$0.7347^{+0.0008}_{-0.0196}$	$-48.44^{+1.47}_{-0.11}$	–	–	39	43	$0.0084^{+0.0005}_{-0.0004}$	$12.39^{+2.16}_{-2.48}$	$0.036^{+0.011}_{-0.005}$ $0.30^{+0.10}_{-0.05}$	$9.161^{+0.105}_{-0.006}$ –	– –

Notes: Col. (1): Source reference number. Col. (2): IAU name of the *Herschel* detection. Col. (3) and (4): RA and Dec. offsets between the surface brightness model and lens mass model in arcsec (first row) and kpc (second row). Col. (5): Einstein radius in arcsec (first row) and kpc (second row). Col. (6): Axis ratio of the mass profile. Col. (7): Position angle of the mass profile. Col. (8) and (9): Shear elliptical components of the mass profile. Col. (10) and (11): Number of pixels in the source plane pixelization. Col. (12): Regularization constant. Col. (13): Magnification computed for the region of the source plane with $SNR > 3$. Col. (14): Circularized radius equivalent to the region of the source plane with $SNR > 3$. Col. (15): Mass within the Einstein radius. Col. (16): Mass-to-light ratio at 1.1 μm within the Einstein radius.

When more than one potential lens is present (i.e. for type 2 and 3 systems), we correct for the redshift only if the secondary potential lens had a spectroscopic redshift (HERSJ020941.2+001558, HATLASJ083051+013225, HATLASJ114638−001132, HATLASJ133543+300404) or none of the blended lenses dominate the available photometric redshift (HATLASJ225844.7−295124, HELMSJ004723.6+015751, HERMESJ105551+592845). To denote the parameters that have been corrected for the lens redshift, we add to them a subscript '0'. In Table 5.2, we list the measured values of m_{F110W}, M_{F110W}, R_{50}, $R_{50,0}$, μ_{50}, $\mu_{50,0}$, C_{31} for the modelled lensing galaxies.

Figure 5.4 shows the distribution of $R_{50,0}$ in kpc, $\mu_{50,0}$ in mag arcsec^{-2}, C_{31}, M_{F110W} in mag, z_l and z_s. We stack all the single-system parameter distributions for each parameter to account for the varying uncertainties between different systems. We bin them together and normalise them for the total number of realisations (i.e., 10^4 for each system).

Consistently with expectations (Perrotta et al., 2002; Lapi et al., 2012; Negrello et al., 2017) our 65 lensing systems mainly comprise systems where the lens is a single galaxy (HERMESJ033211−270536). Only four are made of spectroscopically-confirmed groups or clusters (HATLASJ133543+300404, HELMSJ005159.4+062240, HATLASJ141352−000027, and HATLASJ142414+022304), and nine systems have a morphology consistent with a group (HERSJ011722.3+005624, HATLASJ114638−001132, HATLASJ225844.7−295124, HATLASJ233037.2−331217, HELMSJ004723.6+015751, HERMESJ105551+592845, HERMESJ105751+573026, HATLASJ091841+023048, and HATLASJ230815.5−343801). The lensing galaxies are nearly all ETGs, with the exceptions of HELMSJ004714.2+032454 and of one of the galaxies in the lensing cluster of HELMSJ005159.4+062240. Both of them show a clear spiral structure. The ETG nature of the lensing galaxies is further confirmed by their concentrations, with 92% of the sample lenses being more concentrated than expected for an exponential disk.

Comparing the distribution of the μ_{50}, R_{50}, C_{31} and m_{F110W} of the confirmed lenses with those of the B candidates, we find no significative difference. This suggests that the detection of the background sources does not depend on the photometric properties of the lensing galaxies in a straightforward manner. Since this comparison is performed on the observed quantities, some differences could arise from the redshift distributions of the two populations.

A comparison between our Einstein radii and those available in the literature (Bussmann et al., 2013, 2015; Calanog et al., 2014; Geach et al., 2015; Enia et al., 2018; Dye et al., 2022; Maresca et al., 2022; Kamieneski et al., 2023a) is shown in Table 5.6 and Figure 5.5. Our values are consistent with those found in the literature, with only two exceptions: HERMESJ142824+352620, which Bussmann et al. (2013) did not resolve with the *SMA* due to the very low angular separation of the multiple images and assumed to have Einstein radius of 0.1 ± 0.3 arcsec and HERMESJ033732−295353, for which Calanog et al. (2014) fixed the flattening and position angle of the mass model to be circular and aligned with the lens.

It is worth noticing that our uncertainties on the mass model parameters are a factor of ~ 10 smaller than what is usually reported in the literature. This could be due to the different models adopted for the background source since most of the literature uses parametric profiles, whereas we adopt pixelisation. Indeed, we find the same discrepancy for HerS5 (Table 4.2), which we analyze by adopting the two different modelling approaches. Moreover, as noted

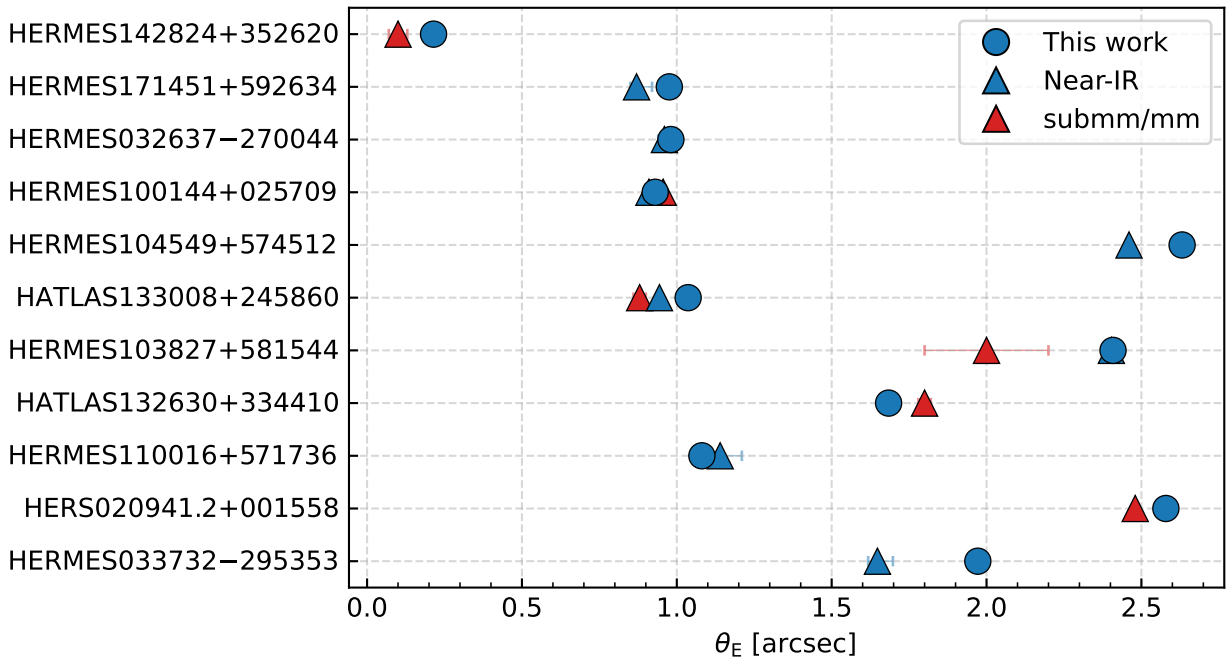

Figure 5.5: Comparison between our estimated Einstein radii (blue circles) and the ones from literature measured either in near-IR (blue triangles) or sub-mm/mm (red triangles).

before, this analysis is missing a complete treatment of any systematic error arising from the choice of prior pixelization and regularization. We expect that including these systematics would reduce the discrepancies in the mass model uncertainties.

Table 5.6: Comparison between our Einstein radii and/or those available in the literature in the near-IR and in the sub-mm/mm.

No.	IAU Name	$\theta_{\rm E}$ [arcsec]	$\theta_{\rm E,near-IRlit.}$ [arcsec]	Ref.	$\theta_{\rm E,sub-mm/mm.lit.}$ [arcsec]	Ref.	Multiw.	Ref
(1)	(2)	(3)	(4)	(5)	(6)	(7)	(8)	(9)
8	HERSJ020941.2+001558	$2.579^{+0.002}_{-0.003}$	$2.48^{+0.02}_{-0.01}$	Ge15	$2.55^{+0.14}_{-0.20}$	Ka23	*ALMA* band 6	Li22
9	HERMESJ032637−270044	$0.981^{+0.005}_{-0.006}$	$0.96^{+0.02}_{-0.03}$	Ca14	–	–	–	–
10	HERMESJ033732−295353	$1.9718^{+0.0004}_{-0.0005}$	$1.65^{+0.03}_{-0.054}$	Ca14	–	–	–	–
12	HERMESJ100144−025709	0.930 ± 0.002	0.91 ± 0.01	Ca14	0.956 ± 0.005	Bu15	*ALMA* band 7	Bu15
13	HERMESJ103827+581544	2.408 ± 0.010	$2.40^{+0.01}_{-0.05}$	Ca14	2.0 ± 0.2	Bu13	*SMA* 340 GHz	Bu13
14	HERMESJ110016+571736	1.081 ± 0.003	$1.14^{+0.04}_{-0.07}$	Ca14	–	–	–	–
18	HATLASJ133008+24586	1.037 ± 0.002	$0.944^{+0.002}_{-0.001}$	Ca14	0.88 ± 0.02	Bu13	*SMA* 340 GHz	Bu13
21	HERMESJ171451+592634	$0.976^{+0.006}_{-0.007}$	$0.87^{+0.02}_{-0.05}$	Ca14	–	–	–	–
32	HERMESJ104549+574512	$2.631^{+0.008}_{-0.012}$	2.46 ± 0.01	Ca14	–	–	–	–
35	HATLASJ132630+334410	$1.684^{+0.005}_{-0.004}$	–	–	1.80 ± 0.02	Bu13	*SMA* 340 GHz	Bu13
38	HERMESJ142824+35262	0.37 ± 0.02	–	–	0.10 ± 0.03	Bu13	*SMA* 340 GHz	Bu13

Notes: Col. (1): Source reference number. Col. (2): IAU name of the *Herschel* detection. Col. (3): Value of the Einstein radius measured in this work. Col. (4) and (5): Value of the Einstein radius measured in the literature from the near-IR observations with the corresponding reference. Col. (6) and (7): Value of the Einstein radius measured in the literature from the sub-mm/mm observations with the corresponding reference. Col. (8) and (9): Multiwavelength observations and corresponding reference.

The mass within the Einstein radius of the lenses ranges between 9.9×10^{10} $M_\odot$ (1% percentile) and 6.4×10^{11} $M_\odot$ (99% percentile). The mass-to-light ratio in the F110W filter within the Einstein radius ranges between 1.25 and 8.86 $M_\odot$ $L_\odot^{-1}$. As detailed in the source-by-source description, the background sources have a variety of morphologies, including single compact sources (e.g. HERMESJ100144+025709), more diffuse sources (e.g. HATLASJ133008+245900), and multiple clumps (e.g. HATLASJ125760+224558). We find that 14 of the 23 reconstructed background sources are single sources, whereas the remaining 8 are multiple sources. Due to the incompleteness of the sample of reconstructed sources, the present analysis alone is not enough to allow us to make any definitive claim on the typical stellar morphologies of DSFGs. The physical size of the background sources, measured as the circularised radius of the circles equivalent to the region of the source plane with SNR > 3, ranges between 0.34 kpc (1% percentile) and 1.30 kpc (99% percentile). We compare our stellar sizes with the ones of the dust emitting region by Enia et al. (2018), who modelled the *SMA* sub-mm/mm emission of a sample of 12 lensed galaxies similarly selected and partially included in the sample analysed in this thesis. They found dust sizes between 1.52 kpc (1% percentile) and 4.07 kpc (99% percentile). We can understand this result by considering that the *HST* observations, by sampling the optical/near-UV rest-frame emission, are expected to pick up only the intrinsically brightest and more compact regions of the background sources, whose light passes through the dust. This observation is consistent with an inside-out growth and later inside-out quenching, a scenario where the central regions of these DSFGs begin to clear out the dust first, causing the more compact stellar emission to shine through (e.g., Kamieneski et al., 2023b). Interestingly, the *HST* sizes are comparable to bright nuclei and off-nuclear knots in local ULIRGs (Surace et al., 1998; Farrah et al., 2001).

These findings are somewhat in contrast with previous literature (e.g., Pantoni et al., 2021), that argued for dust emission to be more compact than the stellar one. Recently, Kamieneski et al. (2023b) have studied a $z \sim 2.3$ lensed galaxy with properties similar to those of the lensed DSFGs in this sample. They have found rest frame near-UV/optical/near-IR emitting regions comparable or even slightly smaller in size than the ones measured in the sub-mm, thus providing evidence for an inside-out quenching scenario. It is worth noticing that Kamieneski et al. (2023b) has also considered another possible, but less likely, explanation related to inclination effects and uneven dust distribution. We also want to point out that the difference in sizes we observe between the stellar emitting region, as sampled by *HST*, and the dust emitting region, as probed by *SMA*, may be affected by the lower angular resolution of the *SMA* observations compared to the *HST* data. In fact, by projecting the half width at half maximum (HWHM) of the *SMA* beam to the redshift of the source and then dividing it by the square root of the total magnification within the $> 3\sigma$ regions, we get a physical resolution (once averaged over the whole sample) of 0.85 kpc, which is larger than what we get for near-IR size for $\sim$ 50% of the sample. While Enia et al. (2018) sources are resolved ($R_{\mathrm{bkg,\,circ}}/\mathrm{PSF}_{\mathrm{HWHM}} > 1$), any emission coming from regions smaller than the projected HWHM would inevitably be broadened. Moreover, the depth of our observations does not allow us to exclude that other, more obscured and undetected, star-forming knots are present throughout the disk, implying that mass buildup could happen disk-wide. Additionally, it is not unlikely for the sub-mm and near-IR emissions to trace different regions of the background source (e.g., Negrello et al., 2014), weakening the claim of an

inside-out quenching scenario that requires them to be co-spatial. These differences should be visible as offsets or changes in morphology in the lensed images. For the background sources presented in this sample, these offsets and changes in morphology are generally small, except for HATLASJ083051+013225, where both are visible. Unfortunately, we do not have enough overlap between the high-resolution *HST* and sub-mm observations to drive conclusive claims. Finally, the optical/near-IR sizes quoted in the literature are often measured through the effective radius obtained by fitting a Sérsic profile to the surface brightness distribution of the background sources. For lensed galaxies, this is usually done directly during the lens modelling by adopting a parametric model for the background source (e.g. Calanog et al., 2014). Such an estimate of the size models the concentration of the source and averages out the surface brightness distribution in the case of clumpy emission. In contrast, our measure is SNR-dependent and is not affected by the smoothness of the surface brightness distribution. We remark that the relation between the observed-frame near-IR sizes and sub-mm ones is still open to debate and could depend on additional factors we do not discuss here, like the stellar mass of the galaxy (see, Liu et al., 2023, for details) or its evolutionary stage.

Allen et al. (2017) measured the redshift-size relation for a sample of ~ 70000 unlensed star-forming galaxies from the ZFOURGE sample (Spitler et al., 2012). These galaxies, distributed in the redshift range $1 < z < 7$, were observed in the near-IR with the *HST*/F160W filter. In the redshift bin $2.5 < z < 3.0$, which brackets the median redshift of our background sources, Allen et al. (2017) found a median effective radius of 2.34 ± 0.13 kpc kpc. Since this value refers to the measurements obtained along major-axis profiles, it can be considered as an upper limit compared to our circularised radii.

More recently, Gillman et al. (2023) have analysed 45 unlensed *SCUBA*-selected DSFGs with archival *HST* and *JWST* observations as part of the Cosmic Evolution Early Release Science Survey (CEERS; Prop. ID 1345, PI: S. Finkelstein). They measured circularised effective radii of 3.10 ± 1.67 kpc in the rest-frame optical range and of 1.64 ± 0.97 kpc in the rest-frame near-IR range. These estimates are closer to our measurements, with a partial overlap between the two samples. They are consistent with or smaller than the sub-mm ones measured by Enia et al. (2018). Nevertheless, the tension between the sub-mm and observed-frame near-IR sizes remains with Gullberg et al. (2019). They found a typical effective radius of 1.2 ± 0.4 kpc with ALMA observations smaller than the optical and near-IR sizes by Gillman et al. (2023). The sizes presented in Allen et al. (2017), Gillman et al. (2023), and Gullberg et al. (2019) are measured by parametric surface-brightness profile fitting.

At the same time, we find magnifications ranging between 2.4 (1% percentile) and 15.8 (99% percentile), with a median of 5.5 for this sample. The magnifications by Enia et al. (2018) range between 3.20 (1% percentile) and 8.35 (1% percentile) with a median of 5.7. This comparison suggests a minor, or even negligible, differential magnification.

We compare the properties of our lenses (i.e., total effective radii, Einstein radii, and total effective surface brightnesses) to those of the SLACS sample of confirmed lenses (Bolton et al., 2008). SLACS is the most significant sample of strong lenses followed up by *HST* and with available lens modelling results. The SLACS lensing candidates were identified from archival SDSS spectroscopic data as all the systems that showed the presence of two separate redshift estimates in the same spectrum: a lower absorption-line redshift for the foreground galaxy and a higher emission-line redshift for the background source. These candidates were

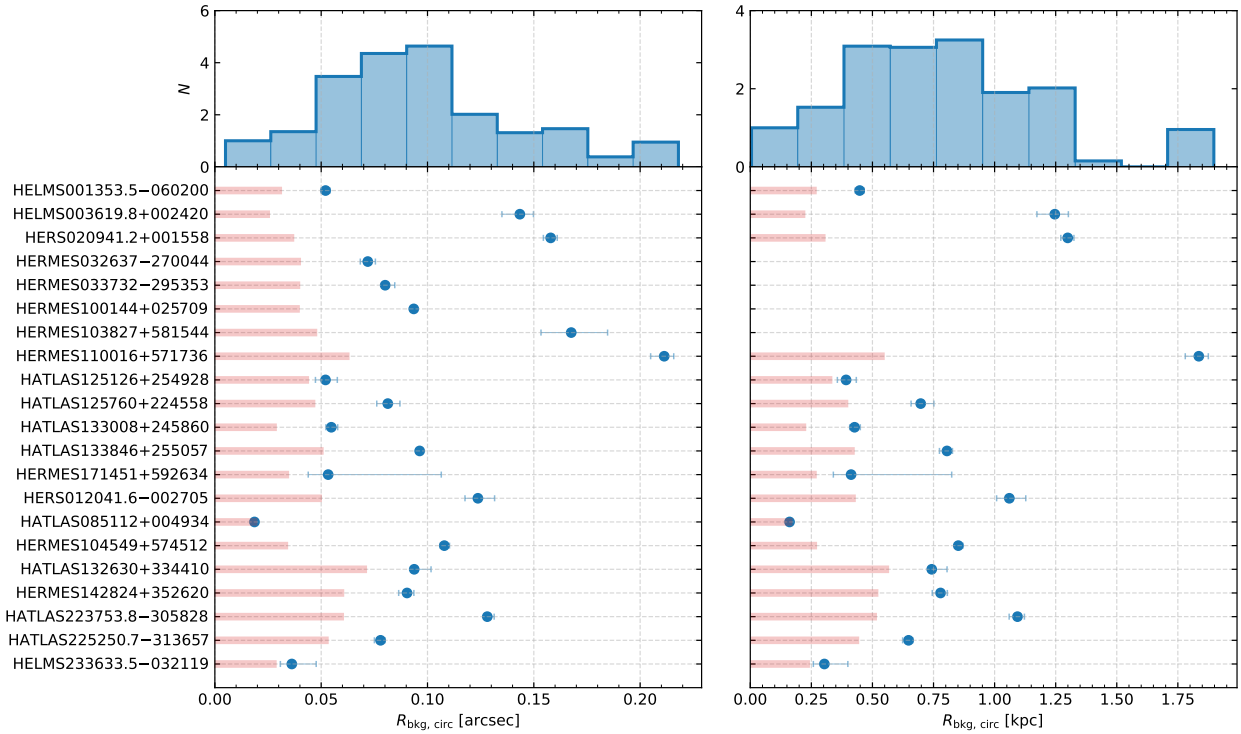

Figure 5.6: *Top panels:* Distribution of the circularised radius in arcseconds (left panel) and kpc (right panel) of the background sources derived from the lens modelling. *Bottom panels*: Circularised radius in arcseconds (left panel) and kpc (right panel) of the individual background sources (blue circles). The HWHM of the PSF of the image corrected for the lensing magnification (pink line) is also shown for comparison.

then followed up and confirmed by means of *HST*/ACS F814W imaging. We consider the 63 confirmed lenses out of 131 candidates, for which Bolton et al. (2008) could subtract the foreground lens surface brightness distribution and perform the lens modelling. They modelled the surface brightness distribution of the lens by adopting a de Vaucouleurs profile. We perform a K-correction of the total effective surface brightness of all the galaxies of our and SLACS samples with available redshifts. As a template for the ETG SED, we use the 17 local elliptical galaxies available in the Brown Atlas (Brown et al., 2014). To estimate the *F110W* magnitude of the SLACS lenses, we redshift and normalise the template to match the measured *F814W* magnitude using `PySynphot` package[1]. Then, we compute the *F110W* magnitude of each template at $z = 0$ and at the redshift of the foreground lenses of both samples. Finally, we adopt the *F110W* magnitude difference as the K-correction term. This correction does not take into account possible differences between the SEDs of the templates and the ones of the lenses. The median K-correction terms for this sample and SLACS are 0.04 mag and 0.03 mag, respectively.

From Figure 5.7, it is possible to see that this sample shows different R_{50} and θ_E distributions than SLACS. This sample reflects a wider distribution in θ_E, and predominantly selects systems with smaller radii than SLACS, with a median value of 4.65 kpc for this sample and 6.95 kpc for SLACS. Moreover, at similar Einstein radii, the effective radii of our lenses are significantly smaller than the SLACS, making our background sources less contaminated by the emission of the lenses. Figure 5.8 shows that the two samples have similar $R_{50,0}$ and absolute magnitude distributions, although our lenses show a tail for smaller and fainter galaxies. At the same time, our lenses have lower $\mu_{50,0,\mathrm{K_{corr}}}$ for the same radii, which implies that our lenses either are fainter or more concentrated than the de Vaucouleurs profiles. The increased scatter we find in both the $R_{50,0} - M_{F110W}$, and $R_{50,0} - \mu_{50,0,\mathrm{K_{corr}}}$ distributions can be accounted for by considering the variation in concentration and wide range of foreground lens redshifts we observed. We can further explain these differences by considering the different selections of the two samples. The SLACS sample, constructed from SDSS spectroscopic data and needing a robust detection of both the foreground lens and background source, is limited in magnitude to brighter lenses located prevalently at lower redshift. In particular, the SLACS spectroscopic selection is done through 3 arcsec diameter fibres and comprises either local galaxies or massive ETGs at $z \lesssim 0.6$.

5.3 Summary

We model and subtract the surface brightness distribution for the candidate lensing galaxies of the 132 A and B systems. Then, we perform lens modelling and source reconstruction on all the systems in which we could confidently identify in the *HST* images a galaxy acting as the main lens as well as the background source (34 systems). We obtain successful results for 23 systems. The main results of our analysis are as follows.

- The overall surface brightness distribution of the lenses and their morphology follows the relations expected for ETGs; however, the foreground lensing galaxies often needed mul-

[1] https://pysynphot.readthedocs.io/en/latest/

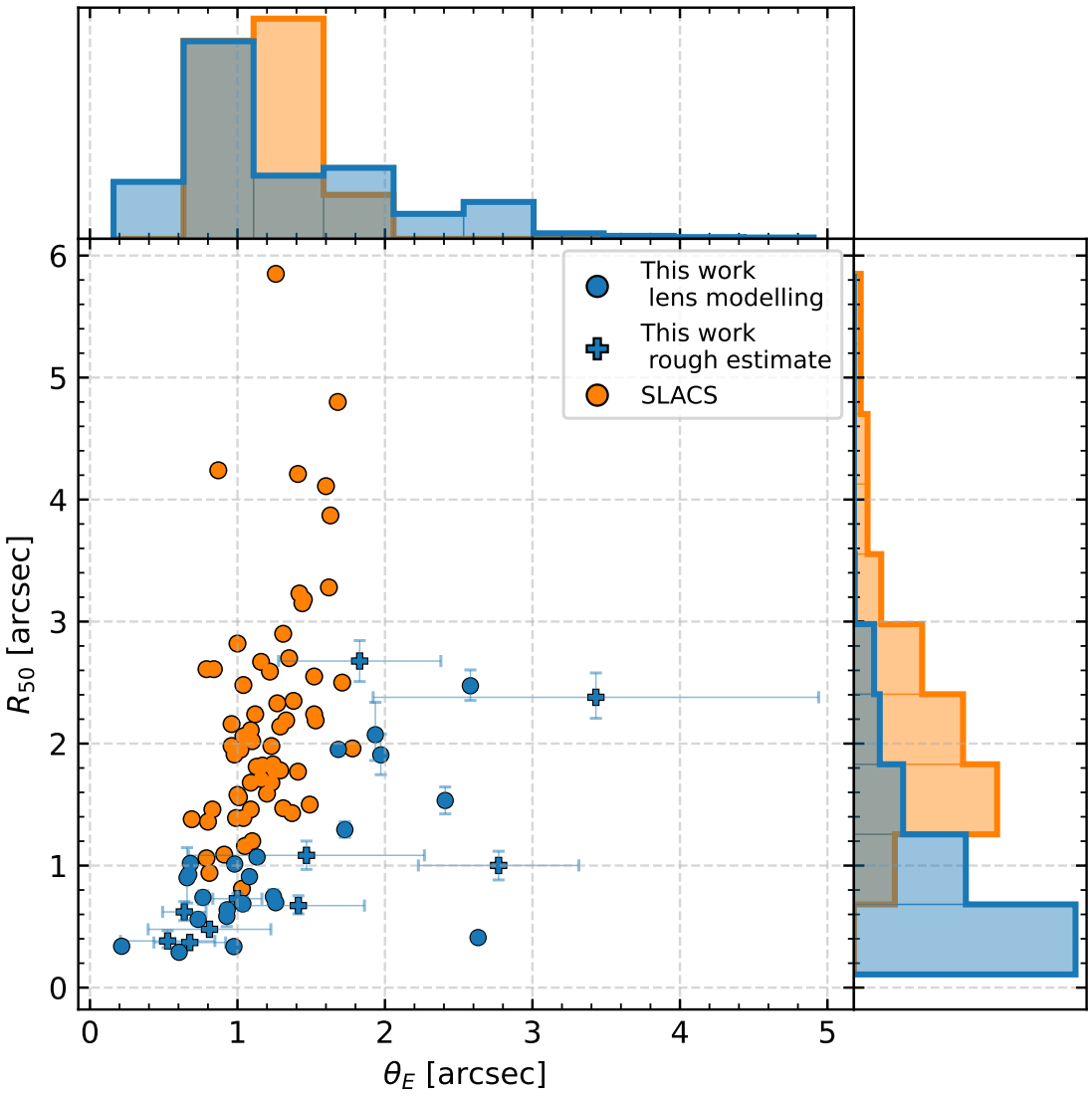

Figure 5.7: *Top panel:* Normalised distribution of the values of the Einstein radius of the lenses in our (blue histogram) and in the SLACS samples (orange histogram). *Bottom left panel:* Total effective radius as a function of Einstein radius of the lenses in our (blue symbols) and in the SLACS sample (orange circles). The blue circles and crosses correspond to systems for which we derived the Einstein radius from the lens modelling or the separation between multiple images, respectively. *Bottom right panel* Normalised distribution of the values of the total effective radius of the lenses.

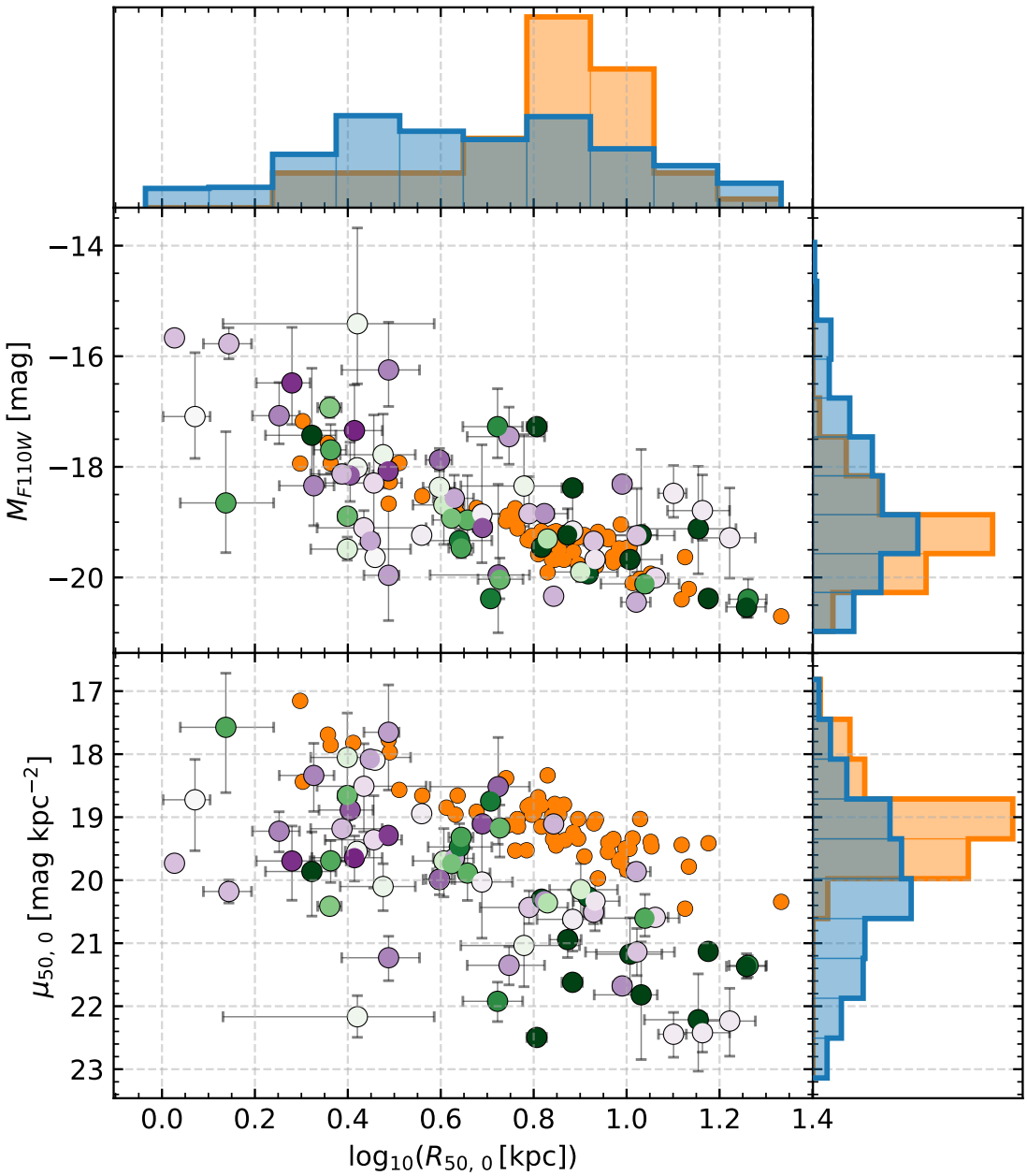

Figure 5.8: *Top panel:* Normalised distribution of the total effective radii in kpc of our (blue histogram) and SLACS sample (orange histogram). *Central left panel:* Absolute magnitude corrected for K correction against the total effective radii in kpc of the two samples. *Central right panel:* Normalised distribution of the absolute magnitude of the two samples with the K-correction applied. Our lensing galaxies are colour-coded according to their concentration, with purple corresponding to the less-concentrated systems and green to the most-concentrated ones. White marks the concentration of a de Vaucouleurs profile. *Bottom left panel:* Kormendy relation of the two samples. Our lensing galaxies are colour-coded according to their concentration. *Bottom right panel:* Normalised distribution of the total effective surface brightness of the two samples with the K-correction applied.

tiple surface brightness components, with properties significantly varying from galaxy to galaxy.

- Most of the lensing systems are consistent with having a single galaxy acting as a lens, with only $\sim 7\%$ of them being confirmed as group or cluster lenses.
- The estimated magnifications and Einstein radii are consistent with previous analysis at different wavelengths; however, the inferred size of the background sources is about three times smaller than the ones measured in the sub-mm/mm with the *SMA* by Enia et al. (2018) for a similarly selected (and partially overlapping sample). This difference in size between the stellar and dust-emitting regions is indicative of an inside-out quenching scenario as long as they are both co-spatial.
- The sub-mm selection used to build this sample revealed lensing systems with fainter lenses and larger Einstein radii than SLACS.

Chapter 6

Spitzer deblending and SED fitting

The measure of the stellar mass of a galaxy is of great importance in understanding its evolutionary stage and mode of star formation. Most star-forming galaxies follow a tight linear relation between the stellar mass and SFR. A systematic study of the location of lensed DSFGs in the SFR versus stellar mass plane is still missing. This is mainly due to the intrinsic faintness of these galaxies in the rest frame UV/optical and contamination from the lens surface brightness distribution. In this chapter, we provide a working example of how to constrain the stellar mass for one of the confirmed lensed galaxies in the sample. i.e., HATLASJ142414+022304. In Section 6.1, we discuss how to estimate the flux density of lensed sources in low-resolution *Spitzer* observations, which are crucial to the SED fitting and the measure of the stellar mass. Lastly, in Section 6.2, we give a brief summary of the possible implications of the same methodology to the full sample.

The shallow *HST* snapshots often cannot detect the emission from the background sources, allowing only an upper limit to be set for the 1.1 μm flux density. Indeed, even when the source is detected, a single photometric data point is hardly enough to adequately constrain the DSFG stellar emission. These SED constraints can be improved by adding further observations in the near-IR/mid-IR where the lower-mass, redder stars dominate the emission and effects of dust extinction are negligible.

One of the few facilities capable of providing such observations that was available before the launch of *JWST* is *Spitzer*. Unfortunately, the angular resolution of *Spitzer* is 1.95 arcsec and 2.02 arcsec for the IRAC channel 1 (3.6 μm) and 2 (4.5 μm), respectively. This is not high enough to resolve the lensing features and considerably suffers from blending between the lens and background source.

6.1 Test case for ID 141

HATLASJ142414+022304, hereafter ID 141, was discovered by Cox et al. (2011) in the H-ATLAS survey and is a very luminous DSFG located at $z = 4.24$. This system was studied in detail (Dye et al., 2022) due to its remarkable luminosity ($L_{\rm FIR} = 1.6 \times 10^{13}\,{\rm L}_{\odot}$). Moreover, ID 141 has a very high star formation rate $SFR = 2400 \pm 500\,{\rm M}_{\odot}\,{\rm yr}^{-1}$ and ISM mass

ranging between $3.2 - 3.8 \times 10^{11}\,M_{\odot}$, making it an exceptional system. The morphology of the reconstructed background source shows the presence of various clumps in the sub-mm. At the same time, a dynamical analysis supports the idea that ID 141 is a disturbed disk consisting of a main regular component and possibly two clumps in a minor merger (Dye et al., 2022). A chemical evolution model combined with the dynamical timescales and an instability analysis suggests that ID 141 might be the progenitor of $z \sim 3$ massive quiescent ETGs.

6.1.1 *Spitzer*/IRAC deblending

ID 141 has both *HST* (Chapter 2) and *Keck* observations (Bussmann et al., 2012). The high-resolution image was taken with the NIRC-II camera in the K_s band at 2.1 μm mounted on the *Keck* II telescope. The observations were obtained in April 2011 (Prop. ID C213N2L, PI: H. Fu). The FOV and angular scale are $0.78 \times 0.78\,\mathrm{arcmin}^2$ and $0.04\,\mathrm{arcsec\,pixel}^{-1}$, respectively. The observations have a total exposure time of 2155.78 s and were taken with the *Keck* II laser guide-star adaptive optics system (LGSAO, Wizinowich et al., 2006).

We decided to base the *Spitzer* model on the *Keck* observations, which are closer in wavelength to the IRAC channels 1 and 2. The IRAC channel data we used were taken in September 2012 (Prop. ID 80156, PI: A. Cooray). The channel 1 (3.6 μm) image has a FOV and an angular scale of $24.32 \times 11.24\,\mathrm{arcmin}^2$ and $0.6\,\mathrm{arcsec\,pixel}^{-1}$, respectively. Channel 2 (4.5 μm) covers the same FOV and has the same angular scale. The two observations have total exposure times of 23.6 s and 26.8 s at 3.6 μm and 4.5 μm, respectively.

Given the low angular resolution and high blending that affect the IRAC observations, disentangling the lens from the background source is not straightforward. A reasonable approach is to utilise a surface brightness model for the lens derived from higher-resolution observation, such as *HST* or *Keck*, fix some structural parameters of the lens surface brightness model, fit it to the IRAC data, and then subtract it from the image to reveal any residuals associated with the background source. This technique reduces the parameters needed to describe the lens surface brightness distribution, keeping part of its complexity. This method was first developed by Hopwood et al. (2011), who modelled the IRAC data of SDP.81 and SDP.130 (Negrello et al., 2010). Bothwell et al. (2013) and Ma et al. (2015) later improved this approach by applying it to one lensed *SPT* DSFG and six lensed HerMES DSFGs, respectively. Bothwell et al. (2013), in particular, included a Gaussian ring to the surface brightness model to include the contribution of the background source and obtain better residuals for the lens.

The approach by Hopwood et al. (2011) works as follows. First, a high-resolution model of the lens surface brightness is obtained from either the *HST* or *Keck* images. This model is convolved with the IRAC PSF and resampled with the IRAC pixel scale. Then, the lower resolution and resampled model is fitted to the *Spitzer* observation, leaving only the centre and normalisation as free parameters. Hopwood et al. (2011) further improved the fitting by modelling and subtracting the residuals related to the background source with Gaussian profiles and repeating the lens surface brightness fitting. This second time, they adopted a Sérsic and an exponential model for SDP.130 and a single Sérsic for SDP.81 following Negrello et al. (2010). As before, the structural parameters of the lens are fixed, with the

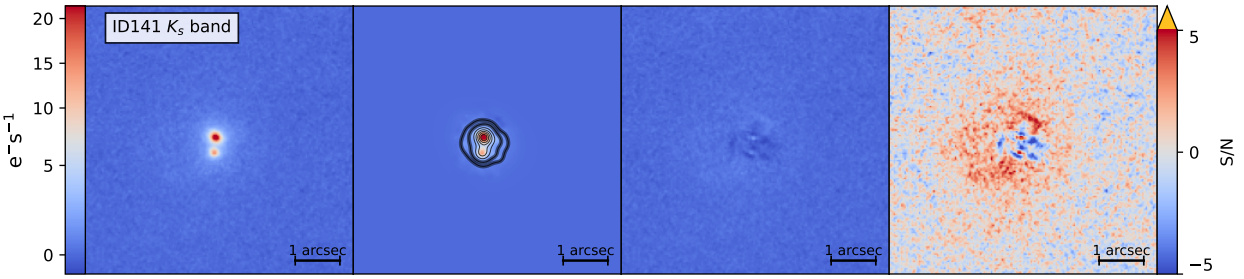

Figure 6.1: *From left to right panels:* Observed *Keck* K_s band image, lens surface brightness model, residual, and SNR residual map of ID 141. Contours in the model images are taken at two levels corresponding to $SNR = 5$ and 10 (thicker curves), and five uniformly spaced levels between the $SNR = 10$ and the maximum SNR in the model image (thinner curves).

only exception being its position and the surface brightness normalisation.

In Figure 6.1, we show the *Keck* K_s band for ID 141 (for the *HST* data see Figure 5.1 and Tables 5.1 and 5.2). The best-fitting *Keck* model is obtained using a de Vaucouleurs profile for both lensing galaxies. The resulting parameters are K_s band magnitude $m_{K_s} = 18.32$ mag, effective radius $R_e = 3.20$ arcsec, axis ratio $q = 0.71$, and position angle $PA = 61.50$ deg for the first lens, and $m_{K_s} = 19.11$ mag, $R_e = 3.51$ arcsec, $q = 0.92$, and $PA = -51.34$ deg for the second one. The same *Keck* data were modelled by Bussmann et al. (2012), finding consistent residuals and parameters.

In Figure 6.2, we show the *Spitzer* observations, lens surface brightness model, and residuals of ID 141. Instead of modelling the background source, we mask it with a circular annulus using the available high-resolution ALMA data as reference (Figure 6.3). We then fit to the IRAC data the normalisation and position of the *Keck* model, obtaining the deblended IRAC images of the lenses and background source.

We then use the same circular annulus mask as an aperture to retrieve the flux densities of the background sources (Figure 6.3). This results in values of $8.7 \pm 2.2\,\mu$Jy and $8.1 \pm 2.2\,\mu$Jy at $3.6\,\mu$m and $4.5\,\mu$m, respectively. The quoted errors are estimated from the image noise by randomly placing the aperture onto background-dominated regions of the image and taking the standard deviation of the resulting distribution. It is important to note that these errors do not include any uncertainty arising from lens light removal but only from the aperture measure. Figure 6.3 shows the IRAC residuals overplotted with the circular annulus aperture and ALMA contours. The location and shape of the residuals are consistent with the ALMA band 4 continuum observations of the background source.

To further investigate whether the residuals we obtained are related to the background source and not to the fitting process, or to some SED variation in the lens between the K_s band and the two IRAC bands, we apply the same procedure to three galaxies with a similar magnitude and morphology to the lenses of ID 141. The resulting models fit the data well, leaving no evident residuals. This test strengthens the idea that the residuals we see on the IRAC images are related to the background source and are not the spurious features left over by the fitting process.

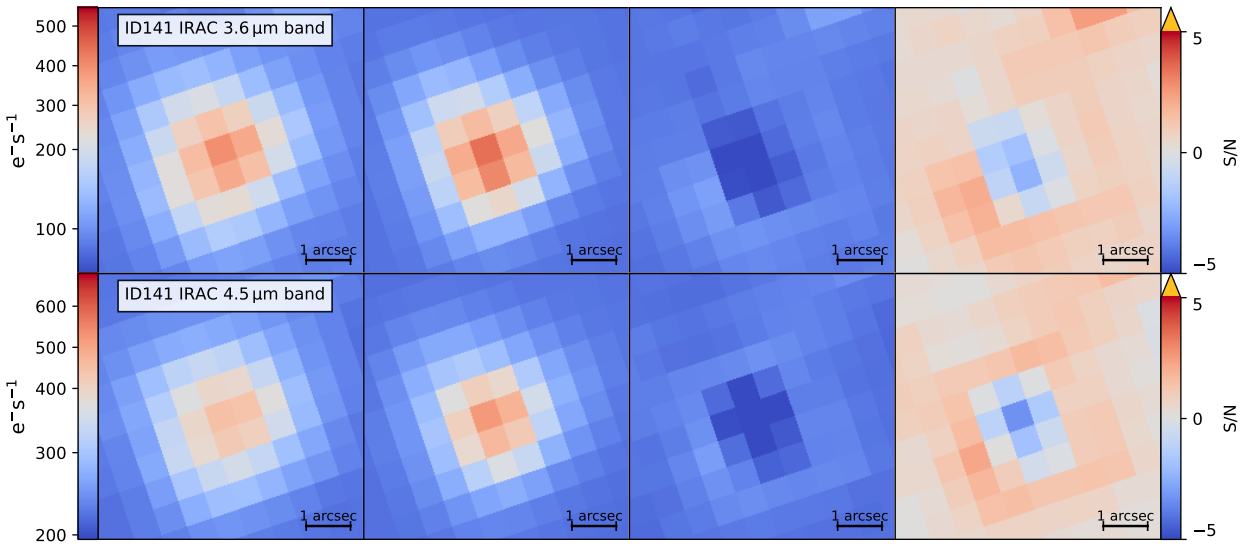

Figure 6.2: *From left to right panels:* Observed 3.6 μm (top row) and 4.5 μm (bottom row) *Spitzer* images, lens surface brightness models, residuals, and SNR residual maps of ID 141.

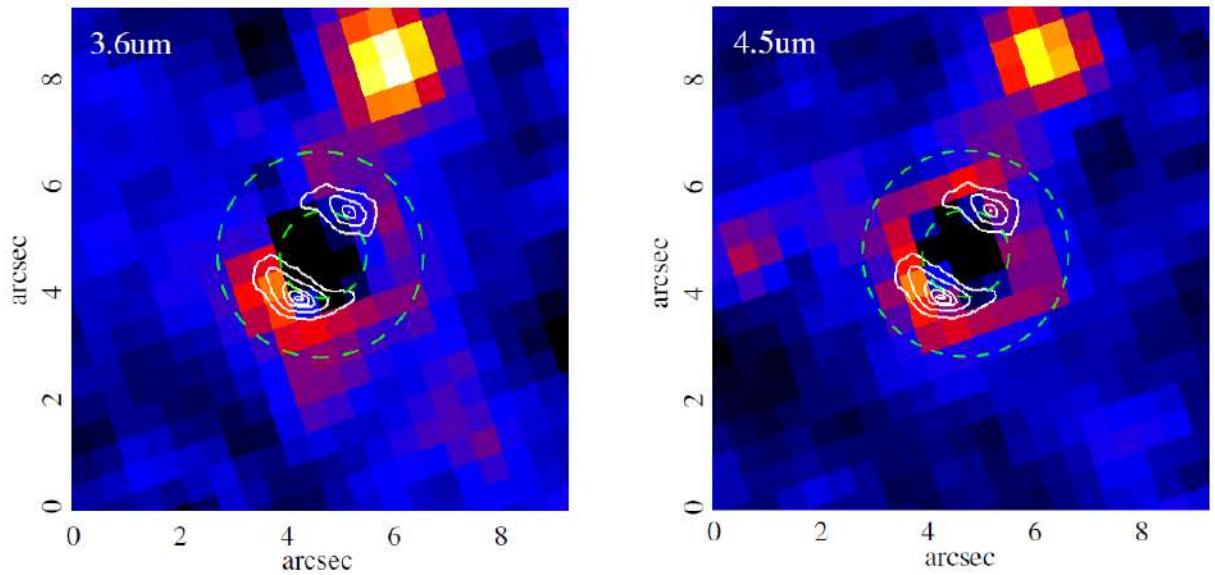

Figure 6.3: *Left panel:* Lens subtracted residuals for the 3.6 μm *Spitzer* observations. *Right panel:* Lens subtracted residuals for the 4.5 μm. We show the circular annulus aperture used both as a mask during the surface brightness fitting of the lenses and as an aperture for the estimate of the background source flux density (green dashed line). Furthermore, we plot the ALMA band 4 continuum contours with the white continuous line. This image is from Dye et al. (2022).

6.1.2 SED fitting

The most common way to recover the stellar mass of a galaxy is to model the full SED through fitting algorithms. These codes combine a series of templates describing the stellar populations, nebular emission, and dust content of the galaxy, predicting its observed flux density at any given wavelengths (e.g., Lower et al., 2020).

To model the SED of ID 141, we use version 2 of the SED fitting code MAGPHYS (da Cunha et al., 2008; Battisti et al., 2020). We supply MAGPHYS with flux densities coming from the *Keck* K_s band, IRAC, and *Wide-field Infrared Survey Explorer* (*WISE*, Lang et al., 2016) observation in the near-IR/mid-IR. Whereas, for the far-IR/sub-mm, we use the flux densities reported in Section 4.2 of Dye et al. (2022). We adopt an upper limit for flux density from the *Keck* image. Some residuals are visible after subtracting the lenses, although their location and shape suggest that these residuals are related to the lens subtraction. We set the K_s flux to be three times the standard deviation of the background and assume a 1σ error equal to this value. Since the WISE flux densities are an unknown combination of the lens and the background source light due to the poor angular resolution, we assign half of the flux density in each band to the background source and half to the lens. We then take a 1σ error equal to this value, so we have some upper limits again.

To convert the properties of ID 141 derived by MAGPHYS from observed (i.e., lensed) to intrinsic, we assume a magnification of 5.8, equal to the mean of the magnifications given by Dye et al. (2022) as derived from continuum ALMA data in Band 4. The resulting stellar mass is $3.4^{+1.8}_{-1.7} \times 10^{11}\,\mathrm{M}_\odot$ where the quoted errors are derived from the posterior distribution on of the MAGPHYS fit. Since MAGPHYS assumes a Chabrier initial mass function (Chabrier, 2003), we scale the stellar mass, dust mass and SFR output by MAGPHYS by a factor of 1.41 for comparison with the other estimates determined by Dye et al. (2022) using a Kroupa IMF (Kroupa &Weidner, 2003). The factor of 1.41 we adopted is determined from the scalings derived by Madau &Dickinson (2014). The resulting stellar mass is $4.8^{+2.5}_{-2.3} \times 10^{11}\,\mathrm{M}_\odot$.

In Figure 6.4, we show the best-fitting SED model, observed flux densities, and residuals between the observed flux density and model of ID 141.

The stellar mass we derive puts ID 141 in the high-mass range of the SFMS at $z \sim 4.24$ as derived by Pearson et al. (2018) for the COSMOS field (Figure 6.5). Pearson et al. (2018) adopted a Chabrier IMF that we convert to a Kroupa IMF by scaling the stellar mass and SFR by the same factor of 1.41 used before. This is consistent with the minor merger scenario suggested by the study of the morphology and dynamics of ID 141.

6.2 Conclusions

We provide a working example of constraining the stellar mass for ID 141. Specifically, we discuss how to estimate the flux density of lensed sources in low-resolution *Spitzer* observations measuring the stellar mass. The stellar mass we derive of $3.4^{1.8}_{-1.7} \times 10^{11}\,\mathrm{M}_\odot$ puts ID 141 in the high-mass/high-SFR range of the SFMS at the candidate redshift. This measurement, coupled with dynamical studies presented in Dye et al. (2022), suggests that the system is a minor merger onto a massive disk-like galaxy.

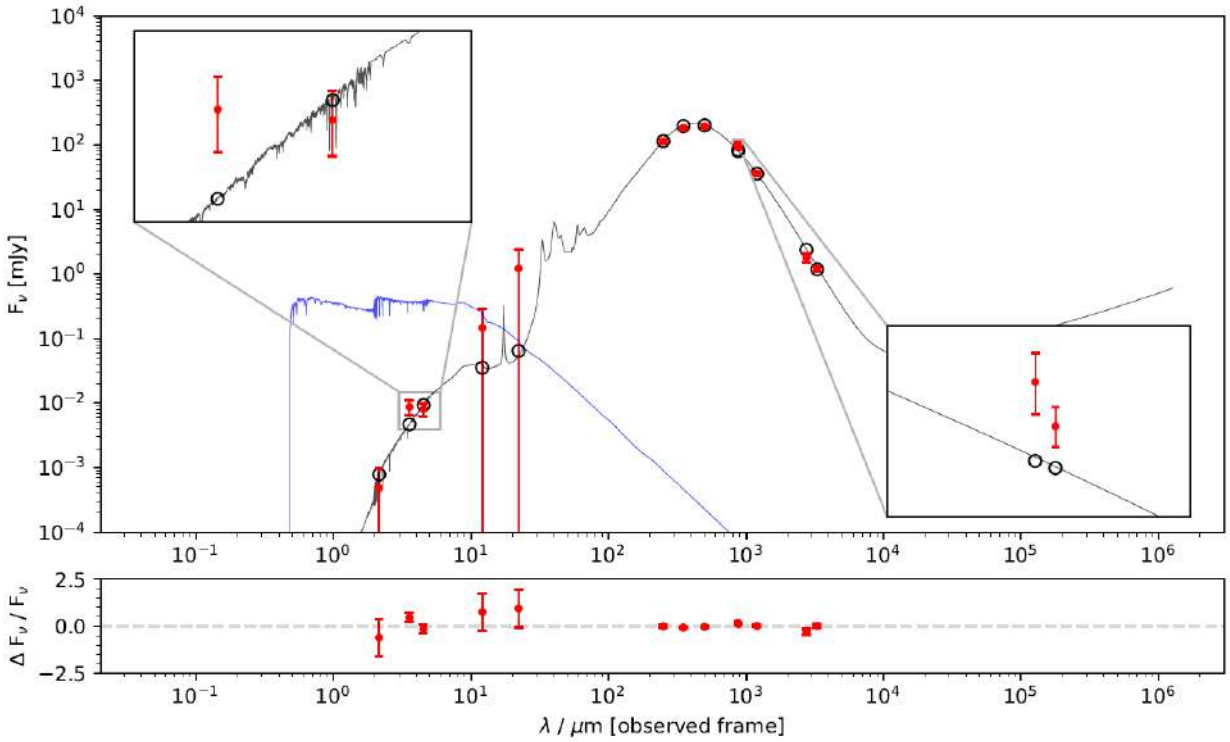

Figure 6.4: *Top panel:* Results of the SED fitting for ID 141. The black line is the best-fitting dust-attenuated SED, whereas the blue line is the unattenuated SED. The red dots are the observations, and the empty black circles are the best-fitting SED predictions. *Bottom panel:* observed - best-fitting SED relative residuals. The data points from the *Keck* K_s band and *WISE* are used as upper limits.

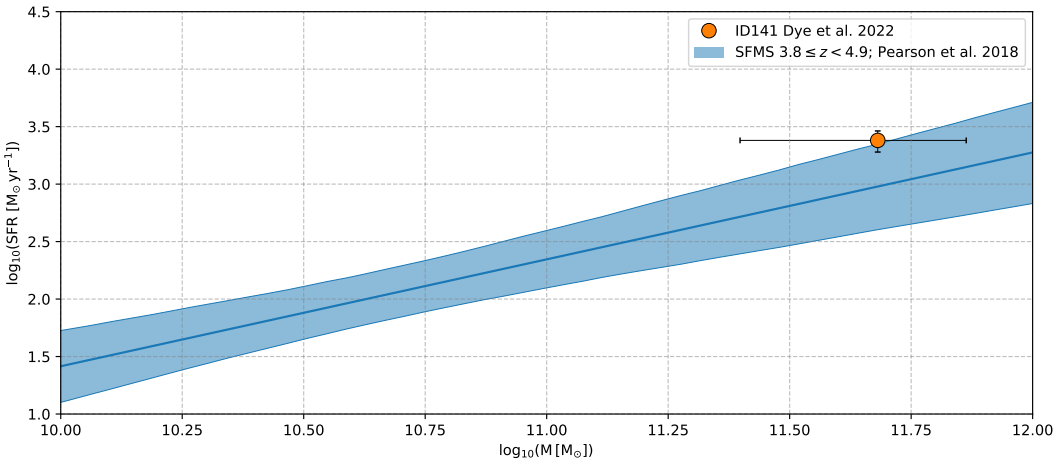

Figure 6.5: SFR versus stellar mass of ID 141 (orange circle) compared to the best-fitting SFMS from Pearson et al. (2018) between $3.8 \leq z < 4.9$ (blue strip). The best-fitting parameters for a linear fit of the SFMS are $(0.93 \pm 0.22) \cdot [\log_{10}(\mathrm{M}\,[\mathrm{M}_\odot]) - 10.5] + (1.82 \pm 0.20)$ and intrinsic scatter $\sigma_{\mathrm{intr}} = 0.15 \pm 0.07$ (Pearson et al., 2018).

The availability of both high-resolution *HST* surface brightness models for all the candidate lenses presented in this thesis and of *Spitzer*/IRAC observations for $\sim 60\%$ of the whole sample galaxies (Prop. ID 61508, PI S. Eales) opens the possibility of constraining the stellar masses for 65 confirmed lensed DSFGs and a further 67 likely lensed candidates. This would allow us to locate these DSFGs in the SFR versus stellar mass plane and, combined with the high-resolution studies of many of these lensed systems, would add useful constraints on their evolutionary stage and mode of star formation.

Moreover, this work can be the foundation for possible *JWST* proposals that would likely detect and resolve the background sources constraining the spatial distribution of stars in the lensed DSFGs.

Chapter 7

Conclusions

In this thesis, we study a sample of 281 strongly-lensed candidate DSFGs identified with *Herschel* and followed up with *HST*. These *HST* observations, presented in Chapter 2, consist of shallow snapshots taken at 1.1 μm with the WFC3 camera. In Chapter 3, we classify the candidates on their likelihood of being lensed. In Chapter 4, we outline the methods to characterise the lensing galaxies and the background sources. The results are reported in Chapter 5. Lastly, we give a working example of constraining the stellar mass for one of the confirmed lenses in the sample in Chapter 6.

More specifically, we tried to address the following key questions.

1. *Given a sample of strongly lensed candidates identified with Herschel, how can one distinguish the truly lensed systems from intrinsically bright, unlensed sources?* – We present and utilise a combination of high-resolution data coming from *HST* in the near-IR and ALMA and SMA in the sub-mm. A visual inspection of these observations confirms that 65 out of the 281 systems are strongly lensed. While the background source flux density distribution of the fraction of confirmed candidates agrees with predictions (e.g., Negrello et al., 2010; Wardlow et al., 2013), the total number does not. We argue that this is primarily due to two factors: (i) the highly-obscured background sources are faint in the observed frame near-IR observed by the shallow *HST* snapshot observations, and (ii) the partial coverage ($\sim 20\%$ of the sample candidates) of the high-resolution sub-mm observations that nevertheless are much more effective at confirming strongly lensed DSFGs thanks to the bright dust emission characteristic of these sources.

2. *How should one proceed to study the lensing galaxies and the background sources?* – We discuss the first necessary step is to disentangle the lens emission from that of the background source. This comes with the advantage of simultaneously being able to characterise some photometric properties of the lensing galaxies and removing their contamination to the background sources. With the lens surface brightness distribution subtracted, it is possible to apply lens modelling techniques to reconstruct the unlensed background source and access its rest frame optical emission. To model the surface brightness of the lensing galaxies, we adopt three different algorithms, `GASP2D` (Méndez-Abreu et al., 2008, 2017) for the isolated galaxies, `GALFIT` (Peng et al., 2002, 2010) for blended groups and spiral galaxies, and `ISOFIT` (Ciambur, 2015) for edge-on

disk galaxies. The first two codes model the surface brightness distribution through parametric models (e.g., Sérsic profiles), whereas the latter model the galaxy isophotes, which then interpolate to derive the 2D surface brightness distribution. For the lens modelling, we used `PyAutoLens` (Nightingale et al., 2018) adopting a SIE profile and external shear (if necessary) for the lenses and a magnification-based Voronoi pixelisation plus a regularisation constant for the background sources.

3. *What properties do we find for our lensing galaxies and background sources?* – We perform the modelling and subtraction of the surface brightness for the 65 class A and 67 class B candidates. The lenses are primarily single galaxies, with only $\sim 7\%$ confirmed as group lenses. When we look at each lensing galaxy morphology, we find that the majority are ETGs, with only a few of them being disks. This finding is also strengthened by the distribution of the lens concentration. This is consistent with $\sim 92\%$ them being more concentrated than an exponential profile commonly used to model disk galaxies. For the 23 confirmed systems for which (i) the background sources are well detected in the *HST* snapshots, (ii) the lenses are adequately fitted by a SIE and shear combination, we find the following. The magnifications and mass profiles are consistent with similarly selected samples in the literature. The background source morphology is heterogeneous. More than half of the DSFGs (14 out of 23) show a single component, but a non-negligible fraction of them show multiple separated clumps that, in a few cases, are arranged in a complex morphology. We measure the background source size by applying the procedure presented in Enia et al. (2018) for SMA observations of a similarly selected sample of lensed DSFGs, finding that our near-IR estimate is ~ 3 times lower. While we measure a median value of 0.75 kpc, Enia et al. (2018) found 2.47 kpc. We argue that this might be an indication of early inside-out quenching that clears the innermost regions of these galaxies first, letting the stellar emission through. Although, further investigation into the spatial distribution of the two components and the adopted techniques for size measurement is necessary to strengthen this claim. Interestingly, these sizes are similar to those of local found in star-forming knots of local ULIRGs (e.g., Farrah et al., 2001). We can not exclude this effect being, at least in part, related to the shallow depth of our observations or how we measure our sizes.

4. *How does this sample compare with optically selected ones like SLACS?* – We compare the F110W magnitude, effective surface brightness, effective radius, and Einstein radius of our lenses to the SLACS sample (Bolton et al., 2008). SLACS lenses are selected through optical spectroscopy and followed up with the ACS camera in *HST*. We find that the two samples show different distributions for all the compared parameters. Specifically, we find significantly fainter lenses with these sub-mm selected lenses having effective surface brightness between 23.04 mag arcsec^{-2} and 17.41 mag arcsec^{-2} (median of 20.14 mag arcsec^{-2}), and the SLACS between 20.39 mag arcsec^{-2} and 17.49 mag arcsec^{-2} (median of 19.10 mag arcsec^{-2}). It is possible to see a tail of less luminous sources with absolute magnitude distributed within -14.73 mag and -20.66 mag (median of -18.78 mag) for this sample and within -17.42 mag and -20.43 mag (median of -19.31 mag) for SLACS. This *Herschel*-selected sample also

has a tail of more extended galaxies with effective radii ranging between 1.03 kpc and 17.30 kpc (median of 4.65 kpc) in contrast with SLACS that shows values distributed within 1.99 kpc and 17.46 kpc (median of 6.95 kpc) for SLACS. At the same time, our Einstein radii span a wider range of values distributed within 0.21 arcsec and 2.64 arcsec (median of 1.04 arcsec) and the SLACS between 0.75 arcsec and 1.74 arcsec (median of 1.17 arcsec). We argue that this is due to both the different redshift distributions of the lenses and selection techniques. The lenses presented in this work are distributed between a redshift of 0.13 and 1.43, whereas the SLACS ones are between a redshift of 0.07 and 0.48. The median values are 0.60 and 0.20, respectively. While SLACS is constructed to follow up classical ETG lenses, the sub-mm selection identifies candidates based on background source properties and lens magnifications. This allows the second to construct samples containing more peculiar lenses, such as LTGs or groups of galaxies.

5. *How can we use this sample to address the broader picture of galaxy formation and evolution?* – These strongly lensed DSFGs have been studied in detail in the literature with various works focusing on spatially resolving their dust properties, molecular gas content, metallicity, gaseous outflows or inflows and dynamics. Constraining the stellar content of these galaxies would greatly complement the above works by addressing how evolved these systems already are, hence characterising their evolutionary stage and mode of star formation. Most star-forming galaxies follow a tight linear relation between the stellar mass and SFR. A systematic study of the location of lensed DSFGs in the SFR versus stellar mass plane is still missing. A common way to measure the stellar mass of a galaxy is through SED fitting techniques. For an effective constraint on the stellar mass, it is necessary to cover the rest-frame optical/near-IR portion of the SED. We provide a working example of how to constrain the stellar mass for one of the confirmed lensed galaxies in the sample. i.e., HATLASJ142414+022304. Specifically, we discuss how to estimate the flux density of lensed sources in low-resolution *Spitzer* observations, which are crucial to the SED fitting and the measure of the stellar mass. We measured a stellar mass of $3.4^{1.8}_{-1.7} \times 10^{11}\,\mathrm{M}_{\odot}$ assuming a Kroupa IMF. This estimate locates HATLASJ142414+022304 in the high-mass/high-SFR region of the $z \sim 4$ SFMS. The study presented in this thesis can be expanded by extending the SED fitting applied to HATLASJ142414+022304 to the whole sample.

The availability of both high-resolution *HST* surface brightness models for all the candidate lenses presented in this thesis and of *Spitzer*/IRAC observations for $\sim 60\%$ of the whole sample galaxies (Prop. ID 61508, PI S. Eales) opens the possibility of constraining the stellar masses for 65 confirmed lensed DSFGs and a further 67 likely lensed candidates. This would allow us to locate these DSFGs in the SFR versus stellar mass plane and, combined with the high-resolution studies of many of these lensed systems, would add useful constraints on their evolutionary stage and mode of star formation.

Moreover, this work can be the foundation for possible *JWST* proposals that would likely detect and resolve the background sources constraining the spatial distribution of stars in the lensed DSFGs (e.g., Amvrosiadis et al., MNRAS submitted).

List of Figures

List of Tables

Bibliography

Abazajian K. N., et al., 2009, ApJS, 182, 543

Aguerri J. A. L., Méndez-Abreu J., Corsini E. M., 2009, A&A, 495, 491

Albareti F. D., et al., 2017, ApJS, 233, 25

Allen R. J., et al., 2017, ApJ, 834, L11

Amvrosiadis A., et al., 2018, MNRAS, 475, 4939

Asboth V., et al., 2016, MNRAS, 462, 1989

Auger M. W., Treu T., Bolton A. S., Gavazzi R., Koopmans L. V. E., Marshall P. J., Bundy K., Moustakas L. A., 2009, ApJ, 705, 1099

Bakx T. J. L. C., et al., 2018, MNRAS, 473, 1751

Bakx T. J. L. C., et al., 2020, MNRAS, 496, 2372

Barnabè M., Czoske O., Koopmans L. V. E., Treu T., Bolton A. S., Gavazzi R., 2009, MNRAS, 399, 21

Battisti A. J., da Cunha E., Grasha K., Cosmos Collaboration 2020, in American Astronomical Society Meeting Abstracts #236. p. 110.05

Bell E. F., de Jong R. S., 2001, ApJ, 550, 212

Berman D. A., et al., 2022, MNRAS, 515, 3911

Berta S., et al., 2021, A&A, 646, A122

Binney J., Tremaine S., 1987, Galactic Dynamics. Princeton University Press, Princeton, NJ, US

Blumenthal G. R., Faber S. M., Primack J. R., Rees M. J., 1984, Nature, 311, 517

Bolton A. S., Burles S., Schlegel D. J., Eisenstein D. J., Brinkmann J., 2004, AJ, 127, 1860

Bolton A. S., Burles S., Koopmans L. V. E., Treu T., Gavazzi R., Moustakas L. A., Wayth R., Schlegel D. J., 2008, ApJ, 682, 964

Borsato E., et al., 2023, MNRAS,

Borys C., et al., 2006, ApJ, 636, 134

Bothwell M. S., et al., 2013, ApJ, 779, 67

Bourne N., et al., 2016, MNRAS, 462, 1714

Bradley L., et al., 2021, astropy/photutils: 1.1.0, doi:10.5281/zenodo.4624996, https://doi.org/10.5281/zenodo.4624996

Brown M. J. I., et al., 2014, ApJS, 212, 18

Buat V., et al., 2010, MNRAS, 409, L1

Bussmann R. S., et al., 2012, ApJ, 756, 134

Bussmann R. S., et al., 2013, ApJ, 779, 25

Bussmann R. S., et al., 2015, ApJ, 812, 43

Butler K. M., et al., 2021, ApJ, 919, 5

Cañameras R., et al., 2017, A&A, 604, A117

Calanog J. A., et al., 2014, ApJ, 797, 138

Caputi K. I., et al., 2007, ApJ, 660, 97

Carrasco M., et al., 2017, ApJ, 834, 210

Carter D., 1978, MNRAS, 182, 797

Casey C. M., 2012, MNRAS, 425, 3094

Casey C. M., Narayanan D., Cooray A., 2014, Phys. Rep., 541, 45

Chabrier G., 2003, PASP, 115, 763

Ciambur B. C., 2015, ApJ, 810, 120

Corsini E. M., et al., 1999, A&A, 342, 671

Cox P., et al., 2011, ApJ, 740, 63

Cox P., et al., 2023, ApJ, in press, (arXiv:2307.15732),

Daddi E., et al., 2007, ApJ, 670, 156

Dalla Bontà E., Davies R. L., Houghton R. C. W., D'Eugenio F., Méndez-Abreu J., 2018, MNRAS, 474, 339

Danielson A. L. R., et al., 2017, ApJ, 840, 78

Davis M., Efstathiou G., Frenk C. S., White S. D. M., 1985, ApJ, 292, 371

De Breuck C., et al., 2019, A&A, 631, A167

Dressel L., 2022, WFC3 Instrument Handbook for Cycle 30 v. 14. STScI, Baltimore, MD, US

Driver S. P., et al., 2009, Astronomy and Geophysics, 50, 5.12

Dudzevičiūtė U., et al., 2020, MNRAS, 494, 3828

Dye S., et al., 2014, MNRAS, 440, 2013

Dye S., et al., 2015, MNRAS, 452, 2258

Dye S., et al., 2018, MNRAS, 476, 4383

Dye S., et al., 2022, MNRAS, 510, 3734

Eddington A. S., 1913, MNRAS, 73, 359

Edge A., Sutherland W., Kuijken K., Driver S., McMahon R., Eales S., Emerson J. P., 2013, The Messenger, 154, 32

Elbaz D., et al., 2007, A&A, 468, 33

Enia A., et al., 2018, MNRAS, 475, 3467

Falgarone E., et al., 2017, Nature, 548, 430

Farrah D., et al., 2001, MNRAS, 326, 1333

Freeman K. C., 1966, MNRAS, 133, 47

Fu H., et al., 2012, ApJ, 753, 134

Furlanetto C., et al., 2018, MNRAS, 476, 961

Gaia Collaboration et al., 2021, A&A, 649, A1

Galliano F., Galametz M., Jones A. P., 2018, ARA&A, 56, 673

Gavazzi R., et al., 2011, ApJ, 738, 125

Geach J. E., et al., 2015, MNRAS, 452, 502

Gillman S., et al., 2023, A&A, 676, A26

Giulietti M., et al., 2022, MNRAS, 511, 1408

Giulietti M., et al., 2023, ApJ, 943, 151

González-Nuevo J., et al., 2012, ApJ, 749, 65

Gullberg B., et al., 2019, MNRAS, 490, 4956

Harrington K. C., et al., 2016, MNRAS, 458, 4383

Harris A. I., et al., 2012, ApJ, 752, 152

Hatziminaoglou E., Farrah D., Humphreys E., Manrique A., Pérez-Fournon I., Pitchford L. K., Salvador-Solé E., Wang L., 2018, MNRAS, 480, 4974

Hernán-Caballero A., Spoon H. W. W., Lebouteiller V., Rupke D. S. N., Barry D. P., 2016, MNRAS, 455, 1796

Hodge J. A., da Cunha E., 2020, Royal Society Open Science, 7, 200556

Hodge J. A., et al., 2013, ApJ, 768, 91

Hoffmann S. L., Mack J., Avila R., Martlin C., Cohen Y., Bajaj V., 2021, New Drizzlepac Handbook Version 2.0 Released In Hdox: Updated Documentation For HST Image Analysis. American Astronomical Society Meeting Abstracts Vol. 53, STScI, Baltimore, MD, US

Hopkins A. M., Beacom J. F., 2006, ApJ, 651, 142

Hopkins P. F., Hernquist L., Cox T. J., Kereš D., 2008, ApJS, 175, 356

Hopkins P. F., Murray N., Thompson T. A., 2009, MNRAS, 398, 303

Hopkins P. F., Hayward C. C., Narayanan D., Hernquist L., 2012a, MNRAS, 420, 320

Hopkins P. F., Hernquist L., Hayward C. C., Narayanan D., 2012b, MNRAS, 425, 1121

Hopwood R., et al., 2011, ApJ, 728, L4

Ikarashi S., et al., 2011, MNRAS, 415, 3081

Ismail D., et al., 2023, ApJ, in press (arXiv.2307.15747),

Ivison R. J., et al., 2013, ApJ, 772, 137

Jarugula S., et al., 2021, ApJ, 921, 97

Jedrzejewski R. I., 1987, MNRAS, 226, 747

Jiang G., Kochanek C. S., 2007, ApJ, 671, 1568

Kamieneski P. S., et al., 2023b, A&A, in press,

Kamieneski P. S., et al., 2023a, A&A, in press,

King I., 1962, AJ, 67, 471

Kochanek C. S., 2004, ApJ, 605, 58

Kroupa P., Weidner C., 2003, ApJ, 598, 1076

Lang D., Hogg D. W., Schlegel D. J., 2016, AJ, 151, 36

Lapi A., Negrello M., González-Nuevo J., Cai Z. Y., De Zotti G., Danese L., 2012, ApJ, 755, 46

Lasker B. M., Sturch C. R., McLean B. J., Russell J. L., Jenkner H., Shara M. M., 1990, AJ, 99, 2019

Le Floc'h E., et al., 2005, ApJ, 632, 169

Liu B., et al., 2022, ApJ, 929, 41

Liu Z., Morishita T., Kodama T., 2023, ApJ, 955, 29

Lower S., Narayanan D., Leja J., Johnson B. D., Conroy C., Davé R., 2020, ApJ, 904, 33

Ma B., et al., 2015, ApJ, 814, 17

Ma J., et al., 2019, ApJS, 244, 30

Madau P., Dickinson M., 2014, ARA&A, 52, 415

Maddox S. J., et al., 2018, ApJS, 236, 30

Magnelli B., Elbaz D., Chary R. R., Dickinson M., Le Borgne D., Frayer D. T., Willmer C. N. A., 2011, A&A, 528, A35

Magnelli B., et al., 2013, A&A, 553, A132

Maller A. H., Flores R. A., Primack J. R., 1997, ApJ, 486, 681

Manjón-García A., Herranz D., Diego J. M., Bonavera L., González-Nuevo J., 2019, A&A, 622, A106

Maresca J., et al., 2022, MNRAS, 512, 2426

Marshall P. J., et al., 2007, ApJ, 671, 1196

Méndez-Abreu J., Aguerri J. A. L., Corsini E. M., Simonneau E., 2008, A&A, 478, 353

Méndez-Abreu J., et al., 2017, A&A, 598, A32

Meneghetti M., 2021, Introduction to Gravitational Lensing; With Python Examples. Springer Cham, Cham, Switzerland

Messias H., et al., 2014, A&A, 568, A92

Meštrić U., et al., 2022, MNRAS, 516, 3532

Michałowski M. J., 2015, A&A, 577, A80

Moffat A. F. J., 1969, A&A, 3, 455

Murphy E. J., Chary R. R., Dickinson M., Pope A., Frayer D. T., Lin L., 2011, ApJ, 732, 126

Nadadur D., Haralick R. M., 2000, IEEE Transactions on Image Processing, 9, 749

Nanni A., Burgarella D., Theulé P., Côté B., Hirashita H., 2020, A&A, 641, A168

Navarro J. F., Frenk C. S., White S. D. M., 1996, ApJ, 462, 563

Nayyeri H., et al., 2016, ApJ, 823, 17

Nayyeri H., et al., 2017, ApJ, 844, 82

Negrello M., Perrotta F., González-Nuevo J., Silva L., de Zotti G., Granato G. L., Baccigalupi C., Danese L., 2007, MNRAS, 377, 1557

Negrello M., et al., 2010, Science, 330, 800

Negrello M., et al., 2014, MNRAS, 440, 1999

Negrello M., et al., 2017, MNRAS, 465, 3558

Neri R., et al., 2020, A&A, 635, A7

Nightingale J. W., Dye S., 2015, MNRAS, 452, 2940

Nightingale J. W., Dye S., Massey R. J., 2018, MNRAS, 478, 4738

Nightingale J. W., Hayes R. G., Griffiths M., 2021a, Journal of Open Source Software, 6, 2550

Nightingale J., et al., 2021b, The Journal of Open Source Software, 6, 2825

Nightingale J. W., et al., 2023, MNRAS, 521, 3298

Nulsen P. E. J., Powell S. L., Vikhlinin A., 2010, ApJ, 722, 55

Oguri M., Diego J. M., Kaiser N., Kelly P. L., Broadhurst T., 2018, Phys. Rev. D, 97, 023518

Okido D. H., Furlanetto C., Trevisan M., Tergolina M., 2021, in Storchi Bergmann T., Forman W., Overzier R., Riffel R., eds, Proceedings of the International Astronomical Union Vol. 359, Galaxy Evolution and Feedback across Different Environments. Cambridge University Press, Cambridge, England, pp 188–189

Oliver S. J., et al., 2012, MNRAS, 424, 1614

Omont A., et al., 2013, A&A, 551, A115

Pantoni L., et al., 2021, MNRAS, 507, 3998

Pearson E. A., et al., 2013, MNRAS, 435, 2753

Pearson W. J., et al., 2018, A&A, 615, A146

Peng C. Y., Ho L. C., Impey C. D., Rix H.-W., 2002, AJ, 124, 266

Peng C. Y., Impey C. D., Rix H.-W., Kochanek C. S., Keeton C. R., Falco E. E., Lehár J., McLeod B. A., 2006, ApJ, 649, 616

Peng C. Y., Ho L. C., Impey C. D., Rix H.-W., 2010, AJ, 139, 2097

Pérez-González P. G., et al., 2005, ApJ, 630, 82

Perrotta F., Baccigalupi C., Bartelmann M., De Zotti G., Granato G. L., 2002, MNRAS, 329, 445

Perrotta F., et al., 2023, ApJ, 952, 90

Pohlen M., Trujillo I., 2006, A&A, 454, 759

Press W. H., Teukolsky S. A., Vetterling W. T., Flannery B. P., 1992, Numerical Recipes in C. The Art of Scientific Computing. Cambridge University Press, Cambridge, England

Prieto M., Gottesman S. T., Aguerri J.-A. L., Varela A.-M., 1997, AJ, 114, 1413

Ratzlaff K. L., Johnson J. T., 1989, Analytical Chemistry, 61, 1303

Riechers D. A., Walter F., Brewer B. J., Carilli C. L., Lewis G. F., Bertoldi F., Cox P., 2008, ApJ, 686, 851

Rigby E. E., et al., 2011, MNRAS, 415, 2336

Rizzo F., Vegetti S., Fraternali F., Stacey H. R., Powell D., 2021, MNRAS, 507, 3952

Rizzo F., Kohandel M., Pallottini A., Zanella A., Ferrara A., Vallini L., Toft S., 2022, A&A, 667, A5

Rybak M., Hodge J. A., Vegetti S., van der Werf P., Andreani P., Graziani L., McKean J. P., 2020, MNRAS, 494, 5542

Saintonge A., et al., 2013, ApJ, 778, 2

Sanders D. B., Mirabel I. F., 1996, ARA&A, 34, 749

Sanders D. B., Soifer B. T., Elias J. H., Neugebauer G., Matthews K., 1988, ApJ, 328, L35

Scoville N., et al., 2017, ApJ, 837, 150

Shirley R., et al., 2019, MNRAS, 490, 634

Shirley R., et al., 2021, MNRAS, 507, 129

Simpson J. M., et al., 2014, ApJ, 788, 125

Simpson J. M., et al., 2017, ApJ, 839, 58

Smith M. W. L., et al., 2017, ApJS, 233, 26

Speagle J. S., 2020, MNRAS, 493, 3132

Spitler L. R., et al., 2012, ApJ, 748, L21

Stanford S. A., Gonzalez A. H., Brodwin M., Gettings D. P., Eisenhardt P. R. M., Stern D., Wylezalek D., 2014, ApJS, 213, 25

Stark D. P., Swinbank A. M., Ellis R. S., Dye S., Smail I. R., Richard J., 2008, Nature, 455, 775

Su T., et al., 2017, MNRAS, 464, 968

Sun F., et al., 2021, ApJ, 908, 192

Surace J. A., Sanders D. B., Vacca W. D., Veilleux S., Mazzarella J. M., 1998, ApJ, 492, 116

Suyu S. H., Marshall P. J., Hobson M. P., Blandford R. D., 2006, MNRAS, 371, 983

Swinbank A. M., et al., 2014, MNRAS, 438, 1267

Sérsic J. L., 1968, Atlas de Galaxias Australes. Observatorio Astronomico de Cordoba, Cordoba, Argentina

Tacconi L. J., et al., 2018, ApJ, 853, 179

Tacconi L. J., Genzel R., Sternberg A., 2020, ARA&A, 58, 157

Thomas J., Saglia R. P., Bender R., Thomas D., Gebhardt K., Magorrian J., Corsini E. M., Wegner G., 2007, MNRAS, 382, 657

Thomas J., Saglia R. P., Bender R., Thomas D., Gebhardt K., Magorrian J., Corsini E. M., Wegner G., 2009, ApJ, 691, 770

Treu T., Auger M. W., Koopmans L. V. E., Gavazzi R., Marshall P. J., Bolton A. S., 2010, ApJ, 709, 1195

Urquhart S. A., et al., 2022, MNRAS, 511, 3017

Valiante E., et al., 2016, MNRAS, 462, 3146

Vanzella E., et al., 2023, ApJ, 945, 53

Viero M. P., et al., 2014, ApJS, 210, 22

Walsh D., Carswell R. F., Weymann R. J., 1979, Nature, 279, 381

Walter F., et al., 2020, ApJ, 902, 111

Wang S. X., et al., 2013, ApJ, 778, 179

Ward B. A., et al., 2022, MNRAS, 510, 2261

Wardlow J. L., et al., 2013, ApJ, 762, 59

Warren S. J., Dye S., 2003, ApJ, 590, 673

Watkins A. E., et al., 2022, A&A, 660, A69

Welch B., et al., 2022, Nature, 603, 815

White S. D. M., Rees M. J., 1978, MNRAS, 183, 341

Wizinowich P. L., et al., 2006, PASP, 118, 297

Yang C., et al., 2016, A&A, 595, A80

Yang C., et al., 2017, A&A, 608, A144

Yang C., et al., 2019, A&A, 624, A138

Yang C., González-Alfonso E., Omont A., Pereira-Santaella M., Fischer J., Beelen A., Gavazzi R., 2020, A&A, 634, L3

Zackrisson E., Bergvall N., Marquart T., Östlin G., 2006, A&A, 452, 857

Zhang Z.-Y., et al., 2018, MNRAS, 481, 59

Zwicky F., 1937, ApJ, 86, 217

da Cunha E., Charlot S., Elbaz D., 2008, MNRAS, 388, 1595

da Cunha E., Charmandaris V., Díaz-Santos T., Armus L., Marshall J. A., Elbaz D., 2010, A&A, 523, A78

da Cunha E., et al., 2015, ApJ, 806, 110

da Cunha E., et al., 2021, ApJ, 919, 30

de Blok W. J. G., Walter F., Brinks E., Trachternach C., Oh S. H., Kennicutt R. C. J., 2008, AJ, 136, 2648

de Vaucouleurs G., 1948, Annales d'Astrophysique, 11, 247

van Albada T. S., Sancisi R., 1986, Philosophical Transactions of the Royal Society of London Series A, 320, 447